AD-A273 772

DTIC
S ELECTE
DEC 16 1993
A

A NONLINEAR THREE-DIMENSIONAL

MICROMECHANICS MODEL FOR FIBER-

REINFORCED LAMINATED COMPOSITES

DISSERTATION

David D. Robertson
Captain, USAF

AFIT/DS/AA/93-3

93-30478

Approved for public release; distribution unlimited

93 12 15 09 1

AFIT/DS/AA/93-3

A NONLINEAR THREE-DIMENSIONAL MICROMECHANICS MODEL
FOR FIBER-REINFORCED LAMINATED COMPOSITES

DISSERTATION

Presented to the Faculty of the School of Engineering

of the Air Force Institute of Technology

Air University

In Partial Fulfillment of the

Requirements for the Degree of

Doctor of Philosophy

David D. Robertson

Captain, USAF

November 1993

A NONLINEAR THREE-DIMENSIONAL MICROMECHANICS MODEL

FOR FIBER-REINFORCED LAMINATED COMPOSITES

David D. Robertson, B.S., M.S.

Captain, USAF

Approved:

Mall   Oct. 28, 1993
Dr. Shankar Mall

Peter S. Torvik   Nov 2 1993
Dr. Peter Torvik

Mark Oxley   Oct 28, 1993
Dr. Mark Oxley

Anthony Palazotto   Nov. 2, 1993
Dr. Anthony Palazotto

Accepted:

Przemieniecki   Nov. 5, 1993
Dr. J.S. Przemieniecki
Institute Senior Dean

Acknowledgements

I am greatly indebted to many who have given freely of their time, resources, and knowledge throughout this work. My sincere and deepest thanks goes to Dr. Shankar Mall for his calm instruction, patience, and help. He has truly been an inspiration from the beginning to the end of this entire experience. In addition, I am grateful to Dr. T. Nicholas, R. Neu, and others of the Material Directorate, Wright Laboratory, WPAFB, for their time and experimental resources, and my gratitude also goes out to the Air Force Office of Scientific Research for their sponsorship of this venture.

Likewise, I wish to thank Dr. Peter Torvik and Dr. Mark Oxley for their time and effort in pouring over this research to ensure its quality. Their suggestions and comments have been greatly appreciated. I am also thankful to Dr. Jim Sherwood and Dr. Mark Tuttle for their willingness to gather and send helpful information, and to many others who deserve thanks but due to the lapse of time and my memory have unfortunately gone unmentioned. For this I greatly apologize.

To my wife, Diane, who has spent the majority of our married life patiently putting up with the academic demands of schooling, I cannot repay, but only be grateful for her love and understanding. Finally, I am the most thankful to my God who has blessed such an undeserving man as myself so completely.

Table of Contents

List of Figures

List of Tables

List of Symbols

a	Characteristic Unit Cell Dimension (Figure 8)
α	Coefficient of Thermal Expansion
b	Characteristic Unit Cell Dimension (Figure 8)
c	Characteristic Unit Cell Dimension (Figure 8)
D_o	Inelastic Material Parameter for the Bodner-Partom Model (Limiting Strain Rate)
δ	Displacement at Interface, Kronecker Delta, or Signifies a Small Change in Given Quantity
Δ	Signifies Change in Given Quantity
e	Engineering Strain in Ply Coordinate System
E	Elastic Modulus
ε	Tensorial Strain or Engineering Strain for Normal Directions
$_o\varepsilon$	Strain at Midplane of Laminate
f	Forcing Vector of Applied Load in Micromechanics Formulation
γ	Engineering Shear Strain
h_D	Specifies Percent of Hardening Due to Kinematic Effects
H	Matrix That Relates Applied Forces and Moments on Laminate to Ply Stresses
H'	Strain Hardening Parameter
J_2	Second Invariant of the Deviatoric Stress Tensor
K_2	Second Invariant of the Deviatoric Stress Tensor for Inelastic Models Containing a Back Stress

κ	Curvature of Laminate Surface
λ	Plastic Multiplier
M	Laminate Moments Applied at the Edges
n	Inelastic Exponential Material Parameter for the Bodner-Partom Model
N	Laminate In-Plane Per Unit Length Force
P	Final Matrix in Unidirectional Formulation Which Must Be Inverted to Solve for the Region Stresses
P_I	Final Matrix in Unidirectional Formulation Which Premultiplies the Inelastic Strains
s	Engineering Stress in Ply Coordinate System
S	Material Compliance or Standard Deviation of the Interfacial Stress Distribution
σ	Tensorial or Engineering Stress
σ'	Deviatoric Stress
t	Time
T	Temperature or Transformation Matrix Between Laminate and Ply Coordinate Systems
τ	Engineering Shear Stress
u	Displacement
V	Volumn Fraction
W_p	Plastic Work
Ω	Back Stress
Z	Drag Stress in Bodner-Partom Model
z	Distance the Given Point Is From the Midplane of the Laminate (If Subscripted, Then Number Denotes Ply)

Subscripts

AVG	Average Interfacial Stress or Displacement in Composite
c	Stress Axis Intercept Point of Interfacial Stress-Displacement Curve
eff	Effective Stress or Strain
f	Fiber Property or Failure Strength of Interface
ij	Tensorial or Indicial Notation
I	Interface Property
I1, I2	Signifies Interface Region
m	Matrix Property or Mean of the Interfacial Stress Distribution
m1, m2, m3	Signifies Matrix Region
n	Normal to Interface
r	Signifies Equation Applies for All Regions, r, Specified
s	Signifies Equation Applies for All Interface Regions
sep	Signifies Value After Fiber/Matrix Separation
t	Tangent to Interface
ys	Yield Stress

Superscripts

c	Critical Interfacial Stress or Displacement Beyond Which Further Interfacial Failure Will Occur
δ	Signifies Interfacial Compliance
E	Elastic Component
I	Inelastic Component
reg	Denotes Vector Region Stresses of Given Ply
TH	Thermal Component
TOT	Total of all Components

-T   The Inverse-Transpose of the Given Matrix

Ascenders

$\bar{x}$ Composite Property

$\dot{x}$ Rate of Change of x

$\hat{x}$ Shorthand for $\left\{ \begin{array}{c} x_{11} \\ x_{22} \\ x_{33} \end{array} \right\}$

$\tilde{z}$ Distance from Center of Given Ply to the Midplane of the Laminate

Abstract

In order to provide improved capabilities for predicting nonlinear composite material behavior, a new three-dimensional micromechanical model is presented. The model formulation is based on a unit cell or representative volume element approach where the coupling effects between normal and shear stresses within the unit cell are relaxed. The formulation lends itself very well to the inclusion of nonlinear behavior while maintaining the three-dimensional effects.

The present capabilities of the model include both unidirectional and laminated composite layups with various types of nonlinear analysis such as a thermoelastic-plastic analysis employing the Prandtl-Reuss flow relations, a thermoviscoplastic analysis using Bodner-Partom unified constitutive theory, and an interfacial damage progression scheme based on a statistical interfacial failure criteria. Such nonlinearities are critical factors during thermomechanical fatigue (TMF) loading of high temperature composites.

Solutions were obtained and extensive comparisons performed with existing micromechanics models, finite element analysis, and experiment with excellent results. In addition, the analysis was developed to require minimal computer resources. For instance, the majority of problems may be accomplished on a personal computer in a matter of seconds. Therefore, the present analysis represents a formulation that accounts for many nonlinearities that heretofore have been very difficult or in some cases impossible to perform with previous micromechanics models or the finite element method.

A NONLINEAR THREE-DIMENSIONAL MICROMECHANICS MODEL FOR FIBER-REINFORCED LAMINATED COMPOSITES

I. Overview

1.1 Introduction

Composite materials have been in the forefront of materials research for many years. As a result, there has been much effort devoted to understanding the mechanics of composite materials at their constituent level. This is usually referred to in the literature as micromechanics. Some examples where micromechanics have been utilized or proved useful are in examining the stress field surrounding a fiber, or in modeling the propagation of cracks through both matrix and fiber. Also, many efforts have been made to calculate the constituent microstresses during processing of these materials. Such studies have done much to advance science and technology, resulting in improved composite materials. Also, a thorough understanding of the basic mechanisms underlying their behavior and response under different loading conditions has been achieved. In addition, such understanding has led to micromechanical models which can predict a composite material's behavior from the properties of its constituents. The complexity of these models generally increases with the complexity of constituent properties and applied loading.

Over the last several years, attention has shifted from the epoxy based fiber reinforced composites, which are primarily used for low temperature applications, to metal and ceramic based composites which possess greater promise for high temperature applications. In contrast to the epoxy based composites, these high temperature materials present unique challenges for micromechanical modeling. For example, in metal matrix composites the matrix may carry a relatively large percentage of the load, and the thermal effects between fiber and matrix become significant due to a mismatch of the thermal expansion coefficients along with greater processing and usage temperatures. Also, nonlinear behavior in such materials is likely to occur, and the loading experienced by them during application is, in general, highly cyclic both mechanically and thermally. Hence, fatigue failure is of primary importance.

The presence of all these mechanisms creates a difficult problem in mathematical modeling. A micromechanical model that incorporates these and other characteristics would be highly beneficial since it would provide a means of predicting the behavior of this class of composite. Of equal importance, such a model would furnish the ability for explaining observed behavior in the laboratory and in predicting a composite material's response under practical situations.

1.2 Background

Several micromechanical models have been proposed over the years, but the majority of them possess the capability to model linear behavior only. However, in recent years, a few nonlinear models have been pro-

posed that include elastic-plastic and viscoplastic matrix properties, e.g. see Reference 1. These models are available as simple computer programs which can run on a personal computer and provide reasonable predictions for the nonlinear behavior of a given composite. The accuracy of each of these models is dependent on their assumptions and the loading conditions. In addition, the plasticity formulations employed in each of these models generally consider only isotropic hardening.

However, only a single type of nonlinearity, such as plasticity with isotropic hardening, does not provide enough flexibility for the complete characterization of the material, especially in metal matrix composites (MMCs), since different hardening characteristics are commonly observed in these composites. Further, the available micromechanical analyses do not consider any form of damage mechanisms. Such damage mechanisms are of great concern in high temperature MMCs, and it would be advantageous to develop a model that could incorporate many of these types of nonlinearities (due to damage or material behavior). At present there is a lack of such an analytical tool. Even the finite element method is lacking in this area. This is partly due to its computational intensity which excludes all but very simple loading sequences. Also, it is very difficult to go beyond the unidirectional composite laminates due to the extremely complex grids required for multidirectional laminates. In addition, most finite element programs do not allow for complex material hardening or viscoplasticity.

1.3 Approach

The main objective of the present study was to formulate, develop, and validate a nonlinear three-dimensional micromechanics model for fiber reinforced composites which incorporates many nonlinearities previously unavailable with existing micromechanics models. Some of the capabilities of the proposed model include the effects of plastic and viscoplastic characteristics with various types of hardening, the effects of fiber/matrix interfacial failure and damage progression, and the effects of various types of laminated composite layups. Also, the proposed model calculates the three-dimensional stresses of the constituents by preserving the three-dimensional Poisson effects. Therefore, a more accurate approximation of the stress field is obtained in the present formulation than if the Poisson effects were ignored as in some of the previous models, e.g. see Reference 1.

The capability to predict the effects of various types of elastic-plastic or viscoplastic matrix material behavior on a composite's characteristics is important when modeling MMCs. Many metal matrix composites show promise for high temperature applications, and since most metals exhibit elastic-plastic or viscoplastic behavior, it is important to understand these effects.

In addition, the fiber/matrix interface is the first region where damage is often observed during loading, especially in MMCs. Hence, a micromechanics approach, that properly models interfacial damage, will be very useful in predicting the response of these composites. Also, an accurate micromechanics model which incorporates the fatigue will greatly en-

4

hance life prediction techniques of these composites for aerospace applications.

Furthermore, the present micromechanics formulation is extended to include a nonlinear laminated composite analysis by employing the classical laminated plate theory assumptions . Although classical laminated plate theory is a linear theory, the underlying assumptions may be extended in a nonlinear formulation that combines these assumptions with the micromechanics relations.

Additionally, the proposed model is computationally efficient. This is, no doubt, a subjective statement, but most of the analyses in this study were performed on an Apple Macintosh IIx computer in a matter of seconds. Only some of the more extensive analyses involving fatigue of several hundred or thousand cycles required the use of a workstation. Hence, a computationally efficient general purpose nonlinear micromechanics model that possesses much of the capabilities which are required to model high temperature titanium-based MMCs is proposed.

A reliable micromechanical model with the ability to simulate various nonlinearities and thermal effects would provide a useful tool for the technical community by furnishing the capacity to predict the response and behavior of metal matrix composites. The present study is focussed in this direction. It will serve a useful role and provide relevant information towards the efficient usage of the new class of titanium based composites in advanced aerospace structures and engines such as are targeted for the advanced tactical fighter and the national aerospace plane.

The formulation of a new micromechanical model, possessing the above mentioned characteristics, is presented in the forthcoming chapters.

Its accuracy and potential for greater use is demonstrated, and the complete development of this model which includes the above mentioned capabilities is established.

II. Perspective

2.1 Motivation

Reliable prediction of a material's behavior is closely tied to a strong understanding of what occurs at the microscopic level. The mechanisms acting and degree to which they effect a given composite must be ascertained if the overall material's characteristics are to be understood.

The recent technological push for improved high temperature materials has resulted in new classes of composites (e.g. fiber reinforced titanium matrix composites) being brought to the forefront of composite research. Such composites are subjected to severe thermal as well as mechanical loads. Further, due to the mismatch of the thermal expansion coefficient between the fiber and matrix, thermal residual stresses are present in the composite which become a significant factor in the composite material behavior. In addition, the higher temperatures will have a strong effect on the viscoplastic behavior of metal matrix composites.

Phenomena such as these produce many questions. For example, how does the progression of damage along the interface affect the composite, and how can it be modeled? Also, how does the viscoplastic characteristics of the matrix affect the relaxation of the thermal stresses both during processing and usage? Questions such as these can only be answered after extensive analytical and experimental work.

Accurate micromechanical models will provide the analytical tools needed to address the characteristics of high temperature composites and make it possible to explain laboratory observations. This will provide a

better understanding of high temperature composites, which will in turn lead to improved materials.

2.2 General Micromechanics

Many micromechanical theories have been proposed over the years, and before attempting a micromechanical analysis it is beneficial to possess an overall view on both closed form and numerical methods that have been used in the past.

Chamis and Sendeckyj provide a good summary on various techniques in micromechanics (2). They divide the approaches into netting analyses, mechanics of materials approaches, self-consistent models, variational techniques using energy bounding principles, exact solutions, statistical approaches, discrete element methods, semiempirical approaches, and microstructure theories. Many of these approaches are summarized by Jones (3). Except for the first two, all approaches use at least some of the elements of the theory of elasticity.

The self-consistent model is based on two assumptions (4). First, the free strain of an inclusion is linearly related to the constrained strain of the same inclusion embedded in an elastic body. Also, the strain is assumed constant in the inclusion. These two assumptions provide a means of determining the effective material properties. Gramoll, Freed, and Walker provide an excellent summary of self-consistent techniques and how they may be applied to inelastic materials (5).

Energy principles have been used extensively to achieve general bounds on the elastic properties (6). Most new micromechanical models

are compared to these bounds as a means of evaluating their effectiveness. If the model produces properties that lie outside these bounds, then its accuracy in that area is questioned.

Elasticity solutions have also been used to predict material behavior (7). Several simplifying assumptions are generally necessary when using elasticity solutions. For instance, no interaction between the fibers is assumed to exist, and therefore, the problem reduces to a single fiber or inclusion embedded in an infinite matrix as solved by Muskhelishvili (8). Such methods provide insight into the stress and strain field surrounding a fiber, but fail to produce reliable predictions of the overall composite response.

Another example of an elasticity solution is a circular concentric cylinder model proposed by Pagano and Tandon (9-12). With this model a study of interfacial debonding was performed. Complete separation was modeled by replacing the fibers with cylindrical voids, and a slipping condition was simulated by forcing the shear traction at the interface to vanish.

Also, a very useful set of equations for overall stiffness were developed by Halpin and Tsai (13). Their result is a good approximation to the self-consistent model in the transverse direction without the complexity. Overall stiffness properties may be obtained quickly and easily from relatively simple equations. In the Halpin-Tsai equations a single parameter is used to incorporate fiber geometry, packing geometry, and loading conditions. The value of this parameter must be assessed by relating the equations to exact solutions. In addition, no fiber or matrix stresses are determined, only overall stiffness properties.

Micromechanical analysis generally requires assuming a regular array of fibers distributed in the matrix. After assuming a fiber array, a single repeating cell or representative volume element (RVE) is isolated, and the response of the RVE is assumed to represent the overall composite response. In doing this the analyst has taken a completely random distribution of fibers and assumed it to be ordered. The influence of random filament packing on transverse stiffness was examined by Adams and Tsai (14). They studied two types of random arrays: square and hexagonal. The arrays were not entirely random since they still contained repeating units of several fibers. Regardless, res s indicated that a random hexagonal array analysis agrees more closely with experiment than a square random array analysis. This confirms the notion that a hexagonal array seems more physically realistic. On the other hand, with an analysis which is not random, the square fiber array tends to agree more closely with experiment. In addition, a square array possesses greater flexibility by allowing for two independent dimensions in defining a unit cell while the hexagonal array contains only one dimension. Therefore, since most analysis assumes a repeating regular array of fibers that is not random, a square array is more widely used.

Many studies have been done using numerical approaches to obtain discrete approximations to the elasticity equations. Foye was one of the first to use a finite element approach with a regular square array of fibers to analyze the transverse properties of a unidirectional composite (15). Subsequently, Adams and Doner analyzed longitudinal shear as well as transverse normal loading of a unidirectional composite using a finite difference technique (16, 17). Stress concentration and stiffness were ana-

lyzed as functions of fiber volume fraction, constituent stiffness ratio, and fiber shape. Later Adams used a nonlinear material analysis to analyze transverse normal loading (18). A plane strain finite element scheme was incorporated to obtain the stress field throughout the matrix, but the greatly increased computational requirements resulted in only a limited amount of data being produced.

A rudimentary crack propagation scheme utilizing the finite element technique to model failure in the matrix around the fiber during transverse loading was proposed by Adams (19). Once an element reached a critical octahedral shear strain for failure, its stiffness was reduced to zero. Of course, such a scheme is not entirely accurate since it produces relatively large gaps in the material after failure of a matrix element. Also, modeling crack propagation in such a discrete fashion resulted in a highly irregular transverse stress-strain response. However, the results tended to bound the experimental data, but not in a way that could be easily predicted. In addition, it was only capable of a monotonically increasing load.

These and other models have been used in the past to model fibrous composites undergoing simplistic loading and possessing linear or modest nonlinear behavior. However, various nonlinearities can occur in some composites under complex loading conditions that must be accounted for if a reliable prediction of the material behavior is to be achieved.

2.3 Composite Nonlinearities

Many types of nonlinearities can develop in a composite material, and it is convenient to classify them into separate categories as shown in

Figure 1. A micromechanical model that accounts for each effect separately would have the greatest chance of success. However, developing a reasonable model for each type of nonlinearity can be difficult, and accounting for their combined effects on the composite can present a challenging bookkeeping problem. In addition, these analyses are load and time history dependent. Therefore, a balance must be achieved between developing reasonable models for the individual effects and maintaining mathematical simplicity to make the problem a solvable one.

Another characteristic in high temperature composites which must be accounted for is the thermal residual stresses present in the fiber and matrix. These stresses are a result of the coefficient of thermal expansion mismatch between the fiber and matrix. Hence, during cooldown after processing or while experiencing thermal loads the composite will sustain
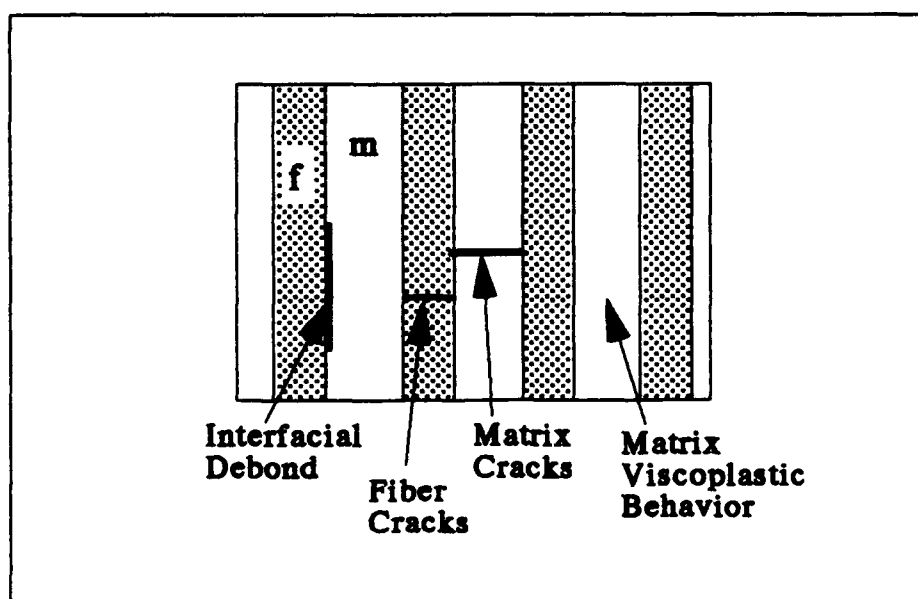
Figure 1. Examples of Nonlinearities that Can Develop in Fibrous Composites

residual stresses both longitudinally and transversely (Figure 2). The residual stresses can at times exceed the matrix yield stress, and must be properly modeled if gross errors are to be avoided (20).

The coefficient of thermal expansion mismatch produces relatively large stresses at the interface which coupled with applied mechanical loading can result in interfacial debond. The integrity of the interface has a profound effect on the composite behavior, and there have been many studies into how it influences the composite. A good sample of some of the previous research in this area is given in references 21-25.

A debonded interface coupled with thermal residual stresses due to cooldown results in a transverse composite response that is bilinear in nature. This was observed experimentally by Johnson et. al. (26). A distinct "knee" in the transverse load-displacement curve occurred. It was postulated that the compressive thermal residual stresses at the interface kept the fiber and matrix in contact until a sufficient load was applied to overcome them, and a weaker modulus existed after fiber/matrix separa-
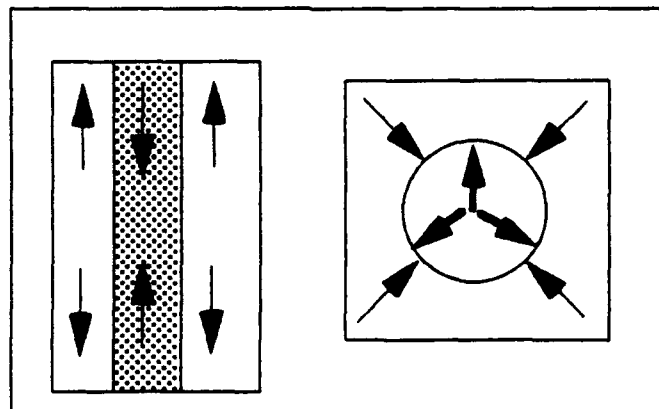
Figure 2.   Residual Thermal Stresses Due to Coefficient of Thermal Expansion Mismatch

13

tion resulting in the approximate bilinear behavior. Some analytical studies have also been performed to confirm this behavior (20, 27).

In actuality, the interface consists of a third phase zone that possesses distinct properties from either the fiber or matrix. This zone comprises imperfections due to absorption and reaction of the two constituents, voids, imperfect adhesion, and microcracks. Some researchers have attempted to model these imperfections by incorporating a thin interphase zone layer that possesses a relatively low yield stress (28). In this method the plastic properties may be varied to match a particular interphase zone's behavior.

Since the load transfer between fiber and matrix depends on the strength of the interface, the thermomechanical properties of the composite are strongly affected by its integrity. However, due to high temperature processing and the constituents involved, the effect of the interphase zone in high temperature metal matrix composites is amplified. Therefore, even though an accurate representation of the zone is very complex, incorporating its effect into a micromechanics model is necessary for such composites.

In addition to the interface, nonlinearities in the composite can result from the plastic or viscoplastic behavior of the matrix (29). There have been several attempts at modeling a composite that exhibits plastic behavior. An orthotropic plasticity model has been proposed by Sun and Chen that assumed negligible plasticity in the longitudinal direction and incorporated a single parameter flow rule (30). Subsequently, Sun and Chen developed a simple micromechanical model to describe the elastic-plastic behavior of fibrous composites (31). The off-axis stress-strain curves

14

from the micromechanical model were used to evaluate the macroscopic orthotropic plasticity model Sun and Chen had earlier developed. In addition, Sherwood and Boyle analyzed viscoplastic behavior using a unified state variable model and the finite element method, and compared the results with that of an elastic-plastic material model (no time dependence) (32).

2.4 Existing Models

In spite of the several previous studies that have been done to analyze the specific aspects of nonlinear behavior of composite materials, only a few nonlinear micromechanical models have been developed to the point of being able to solve broad-based problems of various types of loadings or laminate analysis. These models are available to the scientific community in the form of usable computer programs. Among these are the vanishing fiber diameter model proposed by Bahei-El-Din (33-36), the multi-cell model proposed by Hopkins and Chamis (37, 38), and the method of cells model proposed by Aboudi (39-43). Each of these models possess similar capabilities in that they model the effects of elastic-plastic or viscoplastic matrix behavior on the composite, but they differ greatly in method of approach and complexity.

The vanishing fiber diameter model is the simplest of the three and is essentially the rule of mixtures mechanics of materials approach. However, the additional assumption is made that the fibers possess a vanishingly small diameter even though they occupy a finite volume fraction of the composite. Hence, the fibers will not interfere with matrix deformation in

15

the transverse plane, and therefore the elastic rule of mixtures constitutive relations for stresses and strains may be applied at all times.

This model is pictorially represented in Figure 3 where the unidirectional ply may be regarded as transversely isotropic. The constitutive relations for stress and strain as may be determined from the figure are

$$\bar{\sigma}_{11} = V_f \, \sigma_{11f} + V_m \, \sigma_{11m} \tag{1}$$

$$\bar{\sigma}_{ij} = (\sigma_{ij})_f = (\sigma_{ij})_m \quad \text{for} \quad (ij \neq 11) \tag{2}$$

$$\bar{\varepsilon}_{11} = (\varepsilon_{11})_f = (\varepsilon_{11})_m \tag{3}$$

$$\bar{\varepsilon}_{ij} = V_f \, (\varepsilon_{ij})_f + V_m \, (\varepsilon_{ij})_m \quad \text{for} \quad (ij \neq 11) \tag{4}$$
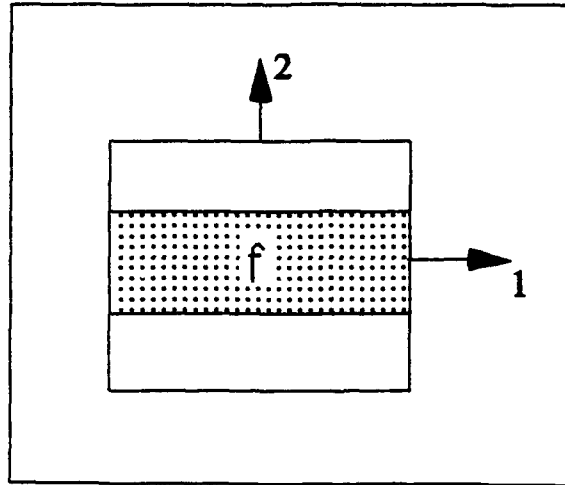
Figure 3.   Vanishing Fiber Diameter Model

where σ represents tensorial stress, and ε the tensorial strains in either the fiber (subscript f), matrix (subscript m), or composite (overbar), and possess the appropriate subscripts denoting direction, and V represents the fiber or matrix's respective volume fraction.

The vanishing fiber diameter model with elastic-plastic matrix characteristics is the basis for the composite laminate computer program AGLPLY (33). Subsequently, Bahei-El-Din extended this model to include thermoviscoplastic behavior. He described the inelastic strain rate with a power law relation as a function of the overstress which is defined as the difference between the current stress and the equilibrium stress (quasi-static). The updated laminate code which includes the thermoviscoplastic behavior is known as VISCOPLY (36).

Some of the drawbacks of the vanishing fiber diameter model are a direct result of its simplifying assumptions. For instance, residual thermal stresses in the transverse plane are not allowed and interfacial debonding cannot be modeled. However, even though the assumptions of this model may seem to oversimplify the problem, it provides a very computationally efficient means of obtaining approximate results.

The multi-cell model proposed by Hopkins and Chamis represents a one-dimensional analysis that unlike the vanishing fiber diameter model still provides for fiber/matrix interaction. In this model it is assumed that the fibers are evenly distributed in the matrix in a regular rectangular array. Hence, a repeating cell or representative volume element (RVE) consists of a single fiber and its surrounding matrix and interphase. The response of the RVE is determined by dividing it into separate regions as shown in Figure 4. Two of the regions contain matrix material only, and

17
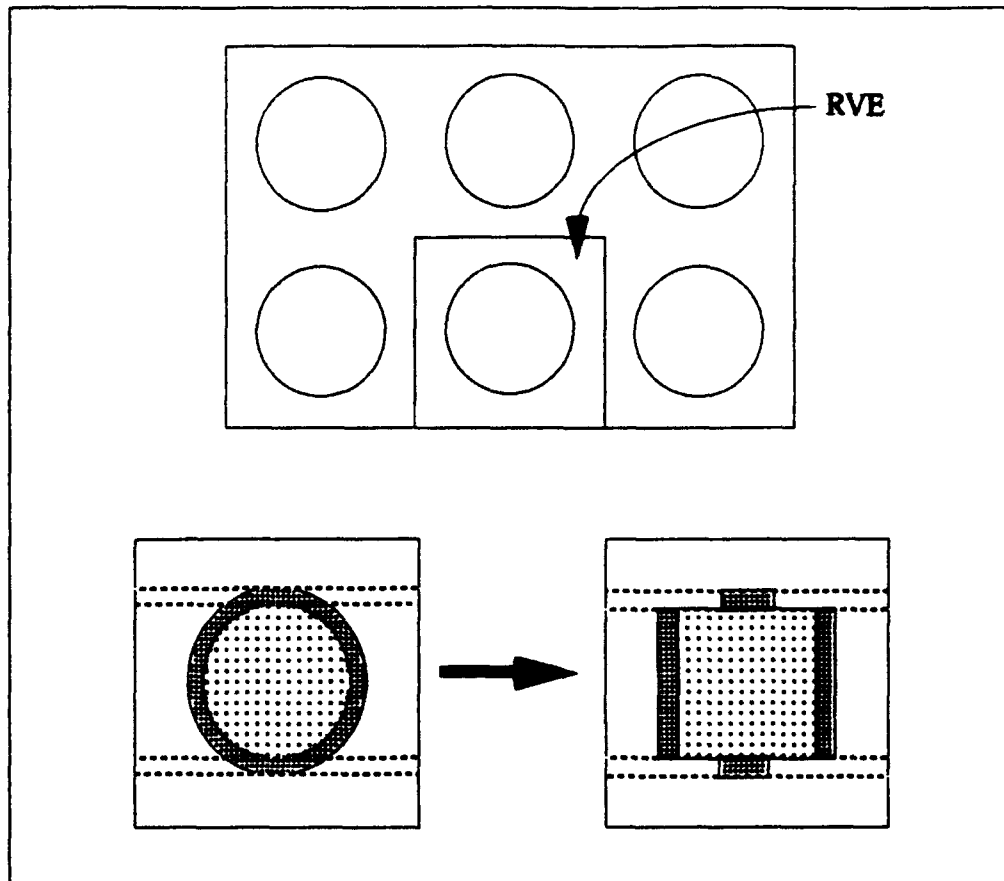
Figure 4.   Multi-Cell Model

two more contain both matrix and interphase material, while a single re-
gion contains all three materials (matrix, interphase, and fiber). Each re-
gion is then modeled as a set of constituent rectangular cells of equivalent
area. No Poisson or shear effect coupling occurs between the regions.
Therefore, the tensorial stresses and strains completely decouple and may
be analyzed one at a time. For instance, solving for the transverse normal
response may be visualized by replacing each rectangle by an equivalent
stiffness. The response would then be modeled by a set of springs in se-
ries and parallel. The constitutive relations are too lengthy to list here,

but a complete set may be found in reference (37).

Hopkins and Chamis's multi-cell model is the basis for the computer code METCAN developed at the NASA Lewis Research Center. Nonlinear thermoviscoplastic behavior is approximated through the use of power law relations. In this method the ratio of the property of interest to a given reference value is set equal to a product of terms with unknown exponents. The terms consist of all values that the desired property might depend on such as temperature, stress, stress rate, loading cycles, etc., and the exponents must be determined either experimentally or estimated. Such an approach does not constitute a true viscoplastic analysis but rather a hypoelastic analysis where the elastic properties are varied to control the nonlinear behavior.

The most complex of the models discussed in this section is the method of cells developed by Aboudi (42). As in the previous model, a regular rectangular array of fibers distributed in the matrix is assumed. In addition, the fibers are assumed to possess a rectangular cross-section. Therefore, the selected RVE positions the fiber in the corner of the RVE as opposed to the center (see Figure 5). The method of cells is a first order theory, and hence, the displacement variation in each subcell is assumed to be linear.

$$u_i = a_i + \sum_{j=1}^{3} b_{ij} x_j \tag{5}$$

where the u_i represent displacements, the a_i and b_{ij} are constants, and the x_j are appropriate coordinates.
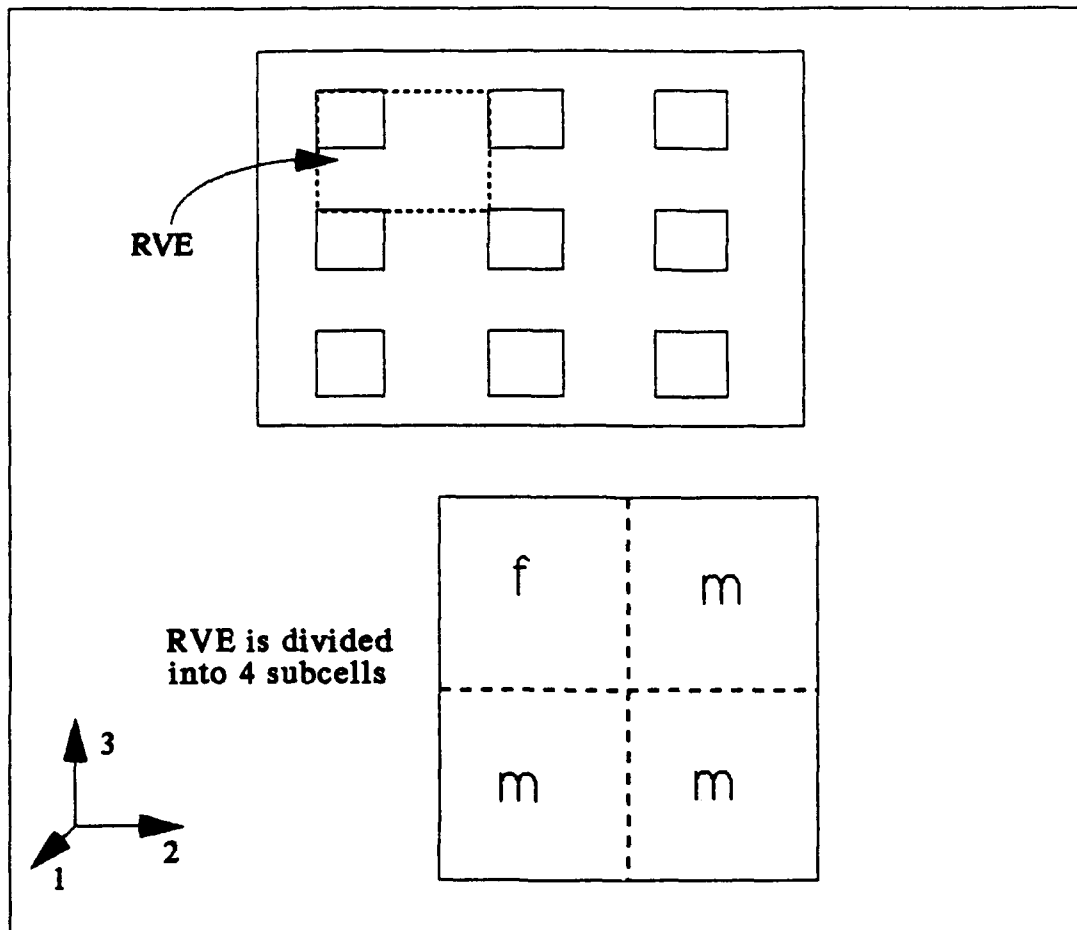
Figure 5.   The Method of Cells Model

Once the general form of the assumed displacement field in each sub-cell is obtained, an appropriate set of equilibrium and continuity conditions are sought. Each subcell possesses a total of twelve degrees of freedom, but in a traditional finite element approach a rectangular parallelepiped element possesses twenty four degrees of freedom. Therefore, the familiar finite element method of satisfying continuity and equilibrium at each node or corner cannot be used. Instead, continuity and equilibrium are chosen to be satisfied on an average basis between subcells and neigh-

boring cells. For instance, the continuity condition at the interface between a fiber and matrix subcell is satisfied when the average displacement of the fiber subcell at the interface matches the average displacement of the matrix subcell at the interface.

The Aboudi model offers many advantages in that it is a full three dimensional analysis where Poisson and shear effects are included, and the total degrees of freedom are half of what a comparable finite element approach would require. The main drawback of this method as opposed to the finite element approach is that continuity and equilibrium are at times violated. For example, overlap may occur between subcells where a portion of the material from each subcell may occupy the same physical space as indicated by the shaded regions in Figure 6, or unwanted gaps
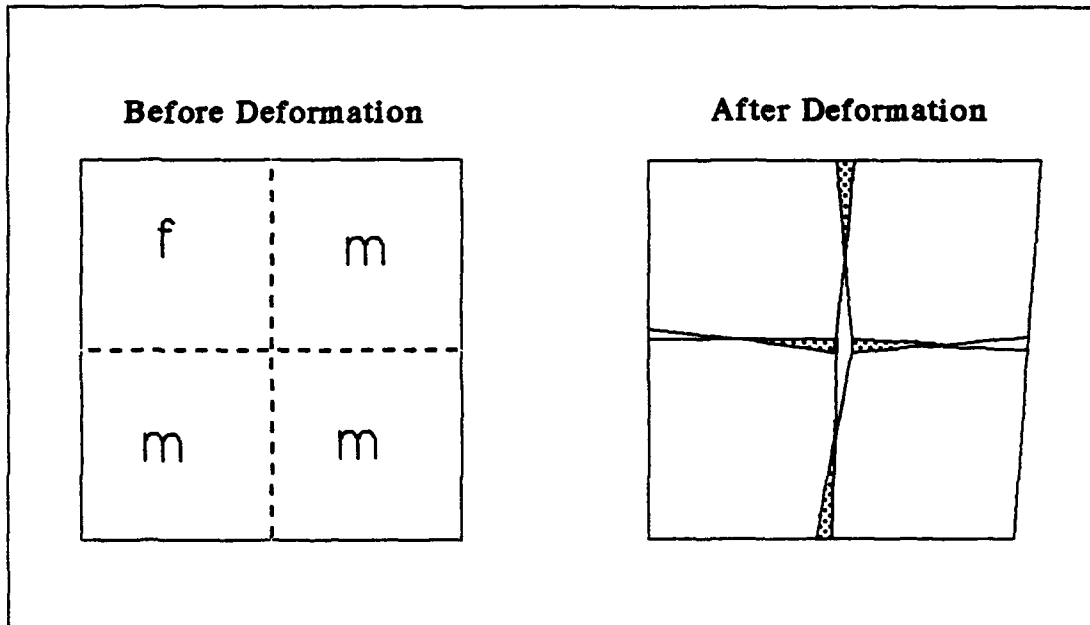
Figure 6. Pictorial Description of Continuity Condition in the Method of Cells Model

may occur.

A strong plus for Aboudi's model is that since it is a full three dimensional analysis, many well known nonlinear material analysis methods may be used such as the Von Mises yielding and Prandtl-Reuss flow rules. Also, the unified viscoplastic theory of Bodner is incorporated to model time dependent behavior (44). The EPC computer code is based on Aboudi's model, and is capable of determining composite yield surfaces and nonlinear response. However, at present, the plasticity analyses are limited to isotropic hardening. Also, interfacial debonding is allowable only if the material is linear.

In summary, the Aboudi model is the most complete in that it is a full three-dimensional analysis, but it's main drawbacks are its mathematical complexity and that it allows material overlap and gaps near the interfaces between neighboring cells and subcells. Bahei-El-Din's vanishing fiber diameter model is a one dimensional analysis and is the simplest of the three where it assumes that no fiber/matrix interaction occurs in the transverse plane. The model proposed by Hopkins and Chamis is also a one dimensional analysis but allows for some transverse fiber/matrix interaction. Also, these last two models fail to account for Poisson effects which can be significant under the generalized plane strain boundary condition and especially during plastic deformation where the Poisson ratio is generally assumed to be one-half. In addition, none of these models at present possess the capability to model progressive interfacial damage.

Therefore, to account properly for interfacial failure and debonding as well as the elimination of some of the main drawbacks of the above models, a new model must be sought. The present study develops such a

22

model and validates its capabilities. The following chapters elucidate the theory and formulation of this model.

III. Basic Micromechanics Formulation for Unidirectional Composites

The basic formulation consists of a set of equations which define how the constituent microstresses and strains are related to the composite stress and strain. Much of the advantages or disadvantages of a particular micromechanics model result from these basic equations. If the equations are overly simplified, then much of the constituent interaction or three-dimensional effects are ignored to reduce the difficulty of the problem. On the other hand, if the equations are too complex, then it may be impossible to perform a laminate analysis or add even rudimentary nonlinearities because of the computational intensity. Therefore, a balance must be sought such that appropriate constituent interaction and three dimensional effects are accounted for while maintaining a formulation that allows for the addition of various nonlinearities and its extension to analyze the laminate.

An essential criterion in the formulation of the proposed model was to maintain the full three-dimensional Poisson effects. In addition, it was desirous to maintain continuity within the constituents of the model as much as possible. In particular, no overlapping of material or unwanted gaps were desired. This last criterion was chosen to ensure proper modeling of fiber/matrix debond which is likely to occur during interfacial damage progression. Also, these capabilities were desired without the complexity of the finite element method or Aboudi's model. Hence, the present model was formulated to include all the major ingredients of a

well balanced micromechanics model from constituent interaction and nonlinearities to laminate analysis.

3.1 Model Description

Many of the assumptions that were used in the present formulation are similar to those of previous models (33-43). For instance, a regular rectangular array of fibers distributed in the matrix is assumed. However, symmetry is further assumed to isolate one-quarter of a unit fiber/matrix cell as shown in Figure 7. Also, it is assumed that the matrix may be adequately represented by a set of rectangular parallelepiped regions and the fiber by a single prismatic region whose various edges are aligned with the coordinate axes. The final assumption is the same as is made in both the vanishing fiber diameter (33) and Hopkins and Chamis (37) models which is that normal and shear stresses decouple in the equilibrium and continuity equations, so any normal applied stress to the composite along any of the three axes shown in Figure 7 will not produce shear stresses in either fiber or matrix regions. These assumptions produce a model that maintains the three-dimensional constituent stress interaction while allowing for the inclusion of various nonlinear effects such as matrix plasticity and interfacial damage.

Although any number of regions could be used in the formulation, only two configurations for the present formulation with 4 and 8 regions were employed in this study as shown in Figure 8. The fiber region dimensions are determined by approximating a quarter circle while maintaining the proper fiber volume fraction. The dimensions of the remaining
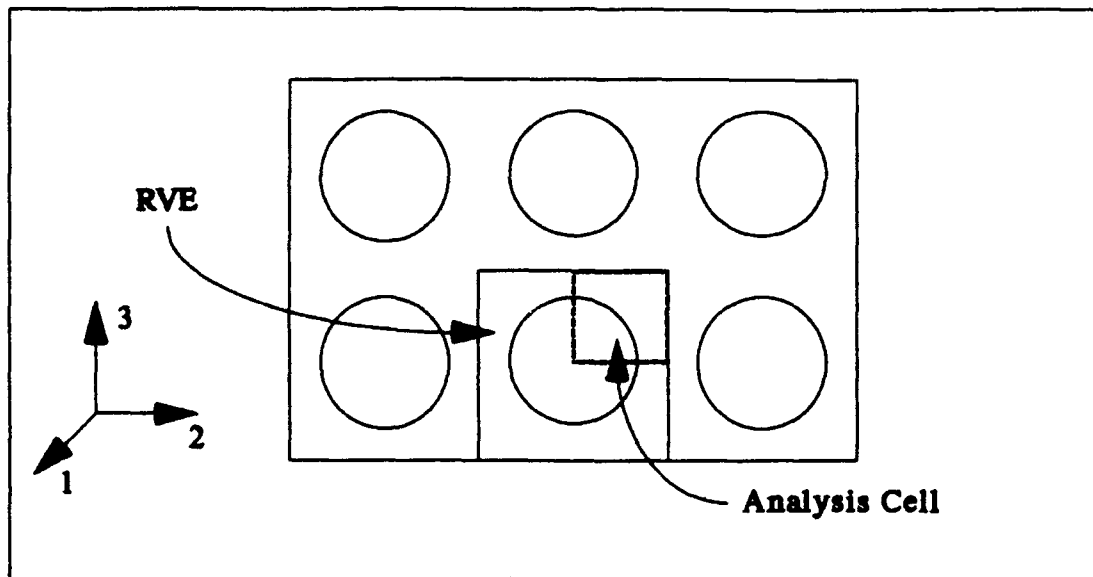
Figure 7. Analysis Cell Used in Present Formulation

4-region model   8-region model
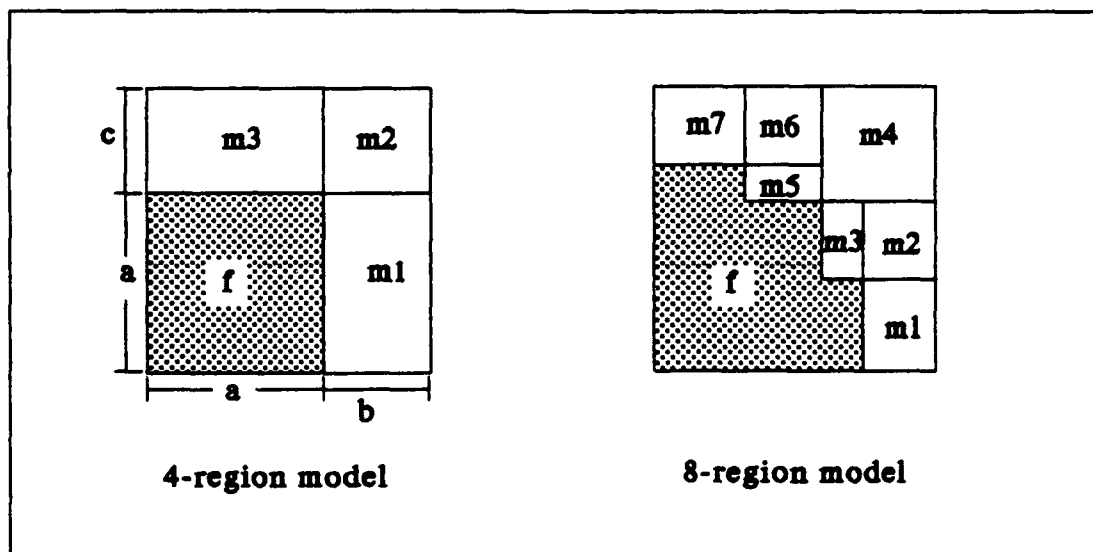
Figure 8. Region Configurations Employed for the Present Formulation

matrix regions may then be determined once the RVE aspect ratio is known. The formulation for the 4-region configuration will be presented in this chapter while the governing equations for the 8-region model are listed in the appendix. The vast majority of the results presented in the later chapters were obtained with the 4-region model although a few results with the 8-region model are also presented for comparison. The formulation becomes much more tedious with the 8-region model, and hence, is too computationally intensive to be effective, especially for fatigue.

If a first order or linear displacement variation is assumed within each region, then a constant stress and strain state exists within each region and the remainder of the formulation may be achieved in terms of the stresses and strains.

In addition, for any solid mechanics analysis, a choice must be made as to whether to formulate the problem in a stress-based, strain-based, or displacement-based system of equations. In the present formulation a stress-based system was chosen. The advantage in choosing a stress-based system is that their associated numerical algorithms tend to be faster than in strain or displacement based systems. This is because calculations of the total strain are not required upon each iteration, but only once the converged solution is achieved. On the other hand, strain-based systems must also calculate the stresses upon each iteration since the deviatoric stress tensor controls the nonlinear behavior. The disadvantages of choosing a stress-based system are that very few stress-based algorithms have been published, and hence, they are not readily available. Also, they are more unstable than strain-based algorithms.

3.2 Governing Equations

The governing equations for the general response of a four-region micromechanics model as described in the previous section are now presented. The model is depicted in Figure 9 where the composite applied stress is indicated with an overbar. Also, in addition to the fiber and matrix regions, two infinitely thin interfacial regions are included in Figure 9 so that interfacial effects can be accounted for. The total strain for each fiber and matrix region may be partitioned into its elastic, thermal, and inelastic components as follows:

$$\varepsilon_{ij} = \varepsilon_{ij}^E + \varepsilon_{ij}^{TH} + \varepsilon_{ij}^I \tag{6}$$

If both the fiber and matrix are assumed to be transversely isotropic, then upon employing the stress-strain and thermal expansion relationships the total strain for each region is be given by

$$\begin{Bmatrix} \varepsilon_{11} \\ \varepsilon_{22} \\ \varepsilon_{33} \end{Bmatrix}_r = \begin{bmatrix} S_{11} & S_{12} & S_{12} \\ S_{12} & S_{22} & S_{23} \\ S_{12} & S_{23} & S_{22} \end{bmatrix}_r \begin{Bmatrix} \sigma_{11} \\ \sigma_{22} \\ \sigma_{33} \end{Bmatrix}_r + \begin{Bmatrix} \alpha_1 \\ \alpha_2 \\ \alpha_3 \end{Bmatrix}_r \Delta T + \begin{Bmatrix} \varepsilon_{11} \\ \varepsilon_{22} \\ \varepsilon_{33} \end{Bmatrix}_r^I \tag{7}$$

$$\varepsilon_{12_r} = \frac{1}{2} S_{44_r} \sigma_{12_r} + \varepsilon_{12_r}^I \tag{8}$$

$$\varepsilon_{13_r} = \frac{1}{2} S_{44_r} \sigma_{13_r} + \varepsilon_{13_r}^I \tag{9}$$

28
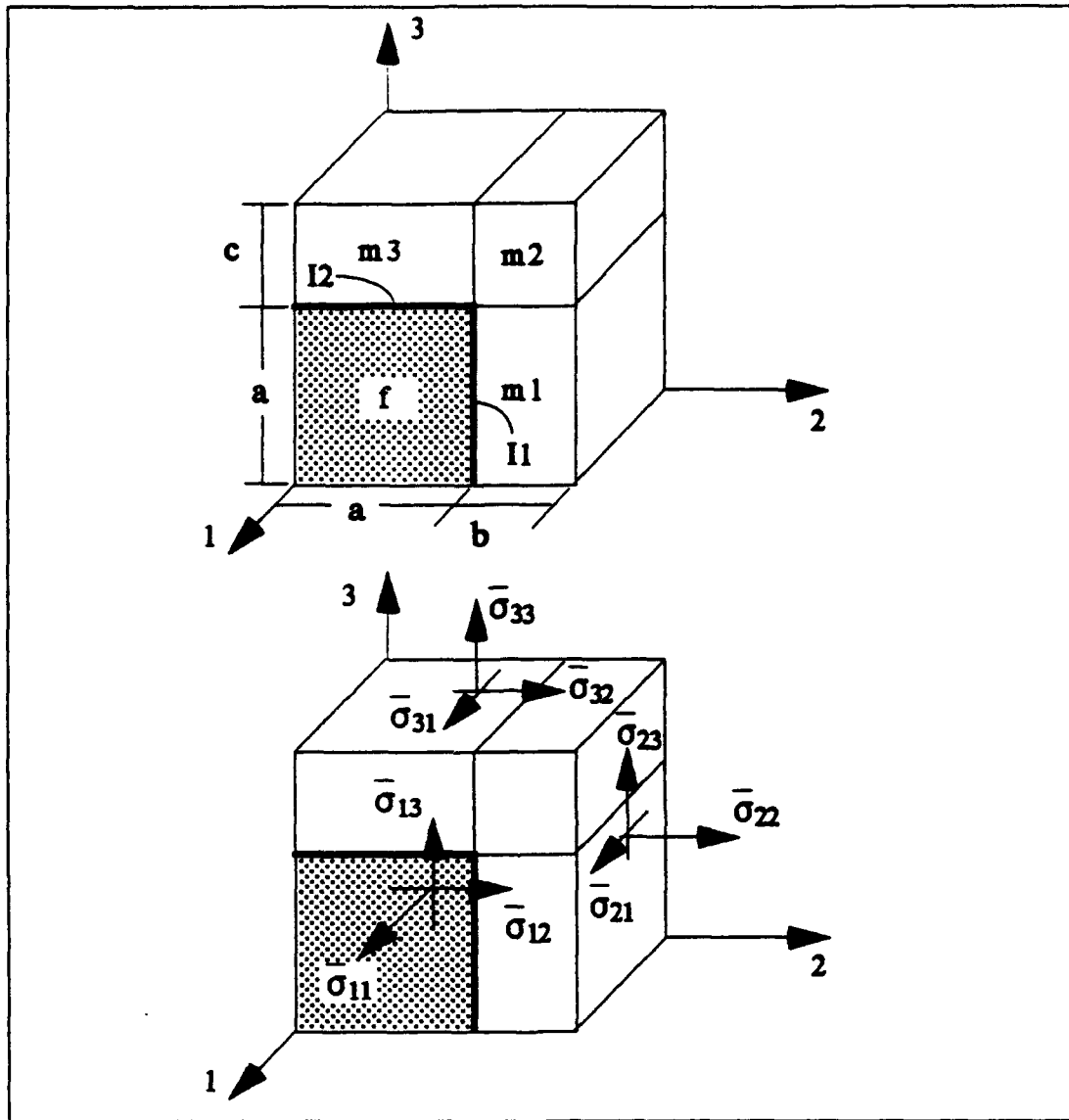
Figure 9. General Loading of the Micromechanics Model

$$\varepsilon_{23_r} = \left(S_{22_r} - S_{23_r}\right)\sigma_{23_r} + \varepsilon_{23_r}^I \tag{10}$$

where the subscript, r, denotes the specified region, S represents the components of the region's compliance matrix that relates engineering stress

to engineering strain, α is the coefficient of thermal expansion, and ΔT is the change in temperature from the reference temperature. The above notation was adopted to allow the usage of tensorial stresses and strains while maintaining the vector transformation capability of the engineering stresses and strains, and it is simply recognized that $\varepsilon_{ij} = \varepsilon_{ji}$.

The effect of debonding on fibrous composite behavior may also be modeled with the present micromechanics approach. Two types of debonding occur at the fiber/matrix interface, separation and slip. The present model accounts for both separation normal to the fiber and slip longitudinally along the fiber by incorporating an interfacial compliance along the two interfacial regions, I1 and I2. The local separation and slip displacement is controlled by the compliance and local interfacial stress as follows:

$$\delta_{n_r} = aS^{\delta}_{n_r}\sigma_{n_r} \qquad S^{\delta}_{n_r} = \begin{cases} 0 & \sigma_{n_r} < 0 \\ S^{\delta}_{sep} & \sigma_{n_r} \geq 0 \end{cases} \qquad (11)$$

$$\delta_{t_r} = aS^{\delta}_{t_r}\sigma_{t_r} \qquad (12)$$

where δ is the displacement, S^{δ} is the interfacial compliance, and a is the characteristic fiber dimension in Figure 9. The subscripts n and t specify either normal (separation) or tangential (slip) directions, and the subscript sep denotes the desired compliance after separation occurs. Also, the subscript r once again represents the appropriate region which in this case is an interface region. Thus, in the normal direction the above equations allow for an infinite stiffness in compression and either approximately

30

zero or any other desired specified stiffness in tension.

The continuity conditions for any deformed body ensures that any curve drawn through the undeformed body remains connected after deformation (i.e. no gap is generated in the undeformed body). To meet these as well as the equilibrium conditions completely would result in more equations than unknowns. Therefore, some of these conditions must be relaxed. In Aboudi's model the continuity conditions are relaxed by requiring only the average displacement between adjacent regions to be equivalent and employing the rule of mixtures to relate the composite strain with the constituent strains. Such conditions allow for overlaps and gaps in the material and couples the normal stresses in the 2-3 plane with the shear stresses (see Figure 6). It is considered appropriate in the present formulation to avoid these contingencies so that interfacial failure and separation may be modeled with no undefined gaps in the material, so instead, the no slip condition in the 2-3 plane between two adjacent regions is relaxed. Therefore, the continuity conditions for the present formulation may be simply stated as the average strain (length average) in any of the three directions through the model regions is equal to the composite strain for all except the shear strain, ε_{23}, where the volumetric average (i.e. rule of mixtures) within the model is set equal to the composite shear strain, ε_{23}. In addition, the normal strain in the fiber direction is assumed to be the same for all regions, so a state similar to generalized plane strain exists in this direction. These requirements lead to the following continuity conditions in terms of the strains:

$$a \, \varepsilon_{22\,f} + \delta_{I1} + b \, \varepsilon_{22\,m1} = a \, \varepsilon_{22\,m3} + b \, \varepsilon_{22\,m2} = (a + b) \, \bar{\varepsilon}_{22} \qquad (13)$$

$$a \, \varepsilon_{33\,f} + \delta_{I2} + c \, \varepsilon_{33\,m3} = a \, \varepsilon_{33\,m1} + c \, \varepsilon_{33\,m2} = (a + c) \, \bar{\varepsilon}_{33} \qquad (14)$$

$$\varepsilon_{11\,f} = \varepsilon_{11\,m1} = \varepsilon_{11\,m2} = \varepsilon_{11\,m3} = \bar{\varepsilon}_{11} \qquad (15)$$

$$\varepsilon_{12\,f} = \varepsilon_{12\,m3} \qquad (16)$$

$$\varepsilon_{12\,m1} = \varepsilon_{12\,m2} \qquad (17)$$

$$a \, \varepsilon_{12\,f} + b \, \varepsilon_{12\,m1} = (a+b) \, \bar{\varepsilon}_{12} \qquad (18)$$

$$\varepsilon_{13\,f} = \varepsilon_{13\,m1} \qquad (19)$$

$$\varepsilon_{13\,m2} = \varepsilon_{13\,m3} \qquad (20)$$

$$a \, \varepsilon_{13\,f} + c \, \varepsilon_{13\,m3} = (a+c) \, \bar{\varepsilon}_{13} \qquad (21)$$

$$a^2 \, \varepsilon_{23\,f} + ab \, \varepsilon_{23\,m1} + bc \, \varepsilon_{23\,m2} + ac \, \varepsilon_{23\,m3} = (a+b)(a+c) \, \bar{\varepsilon}_{23} \qquad (22)$$

where the subscripts f, m1, m2, m3, I1, and I2 specify the respective region and a, b, and c are the characteristic dimensions depicted in Figure 9.

Equilibrium requires that the average stress through any cross section of the unit cell is in equilibrium with the composite applied stress. Also, the stresses normal to the internal faces of the unit cell are equivalent between adjacent regions. These requirements lead to the following conditions for equilibrium:

$$\sigma_{22\,f} = \sigma_{22\,m1} \tag{23}$$

$$\sigma_{22\,f} = \sigma_{m1} \tag{24}$$

$$\sigma_{22\,m2} = \sigma_{22\,m3} \tag{25}$$

$$\sigma_{33\,f} = \sigma_{33\,m3} \tag{26}$$

$$\sigma_{33\,f} = \sigma_{m2} \tag{27}$$

$$\sigma_{33\,m1} = \sigma_{33\,m2} \tag{28}$$

$$a\,\sigma_{22\,m1} + c\,\sigma_{22\,m2} = (a+c)\,\overline{\sigma}_{22} \tag{29}$$

$$a\,\sigma_{33\,m3} + b\,\sigma_{33\,m2} = (a+b)\,\overline{\sigma}_{33} \tag{30}$$

$$a^2\,\sigma_{11\,f} + ab\,\sigma_{11\,m1} + bc\,\sigma_{11\,m2} + ac\,\sigma_{11\,m3} = (a+b)(a+c)\,\overline{\sigma}_{11} \tag{31}$$

$$a\,\sigma_{12\,f} + c\,\sigma_{12\,m3} = a\,\sigma_{12\,m1} + c\,\sigma_{12\,m2} = (a+c)\,\overline{\sigma}_{12} \tag{32}$$

$$a\,\sigma_{13\,f} + b\,\sigma_{13\,m1} = a\,\sigma_{13\,m3} + b\,\sigma_{13\,m2} = (a+b)\,\overline{\sigma}_{13} \tag{33}$$

$$\sigma_{23\,f} = \sigma_{23\,m1} = \sigma_{23\,m2} = \sigma_{23\,m3} = \overline{\sigma}_{23} \tag{34}$$

If Eqs (7) and (11) are substituted into Eqs (13-15), then by also employing Eqs (23-31) a general set of equations which relate the composite applied normal stress to the normal stresses in each region may be obtained. This relationship is given below in its general form for the state of stress.

$$
\begin{bmatrix} \mathbf{M} \\ 14\text{x}23 \end{bmatrix}
\begin{Bmatrix}
\widehat{\sigma}_f \\
\widehat{\sigma}_{m1} \\
\widehat{\sigma}_{m2} \\
\widehat{\sigma}_{m3} \\
\sigma_{n_{I1}} \\
\sigma_{n_{I2}} \\
\widehat{\varepsilon}^I_{m1} \\
\widehat{\varepsilon}^I_{m2} \\
\widehat{\varepsilon}^I_{m3}
\end{Bmatrix}
=
\begin{Bmatrix}
0 \\
0 \\
0 \\
0 \\
0 \\
0 \\
0 \\
0 \\
\left(\alpha_{1_m} - \alpha_{1_f}\right)\Delta T \\
a\left(\alpha_{2_m} - \alpha_{2_f}\right)\Delta T \\
a\left(\alpha_{3_m} - \alpha_{3_f}\right)\Delta T \\
\overline{\sigma}_{11} \\
\overline{\sigma}_{22} \\
\overline{\sigma}_{33}
\end{Bmatrix}
\tag{35}
$$

where,

$$
\widehat{\sigma}_r = \begin{Bmatrix} \sigma_{11} \\ \sigma_{22} \\ \sigma_{33} \end{Bmatrix}_r
\quad \text{and} \quad
\widehat{\varepsilon}^I_r = \begin{Bmatrix} \varepsilon^I_{11} \\ \varepsilon^I_{22} \\ \varepsilon^I_{33} \end{Bmatrix}_r
\tag{36}
$$

Equation (35) may be simplified by recognizing that a portion of the forcing vector on the right hand side of the equation is always zero. Hence, some beneficial matrix manipulations may be used. For instance,

34

given a matrix equation of the following form

$$m \begin{array}{c} m \quad 1 \\ \left[\begin{array}{c|c} A & B \\ \hline C & D \end{array} \right] \end{array} \begin{Bmatrix} x \\ y \end{Bmatrix} = \begin{Bmatrix} 0 \\ f \end{Bmatrix} \tag{37}$$

where $\{x\}$ and $\{0\}$ are of length m, $\{y\}$ is of length 1, and $\{f\}$ is of length n, then

$$[A]\{x\} + [B]\{y\} = \{0\} \tag{38}$$

which implies that

$$\{x\} = -[A]^{-1}[B]\{y\} \tag{39}$$

when the inverse of the matrix A exists. Also, from Eq (37)

$$[C]\{x\} + [D]\{y\} = \{f\} \tag{40}$$

Combining these last two equations yields

$$([D] - [C][A]^{-1}[B])\{y\} = \{f\} \tag{41}$$

Hence, Eq (35) may be reduced to the general form

$$
\begin{bmatrix} & & \\ & M_2 & \\ & 6\text{x}15 & \\ & & \end{bmatrix}
\begin{Bmatrix} \widehat{\sigma}_f \\ \sigma_{11_{ml}} \\ \sigma_{33_{ml}} \\ \sigma_{11_{m2}} \\ \widehat{\varepsilon}^I_{ml} \\ \widehat{\varepsilon}^I_{m2} \\ \widehat{\varepsilon}^I_{m3} \end{Bmatrix}
=
\begin{Bmatrix} (\alpha_{1_m} - \alpha_{1_f})\Delta T \\ a(\alpha_{2_m} - \alpha_{2_f})\Delta T \\ a(\alpha_{3_m} - \alpha_{3_f})\Delta T \\ \overline{\sigma}_{11} \\ \overline{\sigma}_{22} \\ \overline{\sigma}_{33} \end{Bmatrix}
\tag{42}
$$

Separating out the inelastic strain terms and moving them to the right hand side of the equation leads to

$$
\begin{bmatrix} & & \\ & P & \\ & 6\text{x}6 & \\ & & \end{bmatrix}
\begin{Bmatrix} \sigma_{11_f} \\ \sigma_{22_f} \\ \sigma_{33_f} \\ \sigma_{11_{ml}} \\ \sigma_{33_{ml}} \\ \sigma_{11_{m2}} \end{Bmatrix}
=
\begin{Bmatrix} (\alpha_{1_m} - \alpha_{1_f})\Delta T \\ a(\alpha_{2_m} - \alpha_{2_f})\Delta T \\ a(\alpha_{3_m} - \alpha_{3_f})\Delta T \\ \overline{\sigma}_{11} \\ \overline{\sigma}_{22} \\ \overline{\sigma}_{33} \end{Bmatrix}
-
\begin{bmatrix} & & \\ & P_I & \\ & 6\text{x}9 & \\ & & \end{bmatrix}
\begin{Bmatrix} \varepsilon^I_{ml} \\ \varepsilon^I_{m2} \\ \varepsilon^I_{m3} \end{Bmatrix}
\tag{43}
$$

where the matrix P is given by

$$\begin{bmatrix}
S_{11_f} & S_{12_f} - S_{12_m} & S_{12_f} & -S_{11_m} & -S_{12_m} & 0 \\
aS_{12_f} & aU & aV & R - aS_{12_m} & -a\dfrac{S_{12_m}^2}{S_{11_m}} & -R \\
aS_{12_f} & a(S_{23_f} - S_{23_m}) & a(S_{22_f} + S_{m12}^\delta) - Q & -aS_{12_m} & Q - aS_{22_m} & 0 \\
\dfrac{a^2}{A} & 0 & -\dfrac{acS_{12_m}}{AS_{11_m}} & \dfrac{ab}{A} & \dfrac{acS_{12_m}}{AS_{11_m}} & \dfrac{c}{(a+c)} \\
0 & 1 & 0 & \dfrac{cS_{11_m}}{(a+c)S_{12_m}} & 0 & \dfrac{-cS_{11_m}}{(a+c)S_{12_m}} \\
0 & 0 & \dfrac{a}{(a+b)} & 0 & \dfrac{b}{(a+b)} & 0
\end{bmatrix} \tag{44}$$

and the matrix P_I by

$$\begin{bmatrix}
-1 & 0 & 0 & 0 & 0 & 0 & 0 & 0 & 0 \\
-(a+b)\dfrac{S_{22_m}}{S_{12_m}} & b & 0 & (a+b)\dfrac{S_{22_m}}{S_{12_m}} - a\dfrac{S_{12_m}}{S_{11_m}} & -b & 0 & a\dfrac{S_{12_m}}{S_{11_m}} & -a & 0 \\
0 & 0 & -a & c\dfrac{S_{12_m}}{S_{11_m}} & 0 & -c & -c\dfrac{S_{12_m}}{S_{11_m}} & 0 & c \\
0 & 0 & 0 & \dfrac{ac}{AS_{11_m}} & 0 & 0 & \dfrac{-ac}{AS_{11_m}} & 0 & 0 \\
\dfrac{c}{(a+c)S_{12_m}} & 0 & 0 & \dfrac{-c}{(a+c)S_{12_m}} & 0 & 0 & 0 & 0 & 0 \\
0 & 0 & 0 & 0 & 0 & 0 & 0 & 0 & 0
\end{bmatrix} \tag{45}$$

The quantities A, U, V, R, and Q in the above matrices are defined by

$$A = (a + b)(a + c) \qquad U = S_{22_f} - S_{22_m} + S_{n11}^{\delta} \qquad V = \frac{S_{12_m}^2}{S_{11_m}} + S_{23_f} - S_{23_m} \quad (46)$$

$$R = (a + b)\left(S_{12_m} - \frac{S_{11_m} S_{22_m}}{S_{12_m}}\right) \qquad Q = c\left(\frac{S_{12_m}^2}{S_{11_m}} - S_{22_m}\right) \quad (47)$$

Once the region stresses in Equation (43) are determined through matrix inversion, the remaining normal stresses in each region are found from equilibrium between adjacent regions and continuity of the matrix regions in the longitudinal or fiber direction. Thus, the remaining normal stresses are given by

$$\sigma_{22_{m1}} = \sigma_{22_f} \qquad (48)$$

$$\sigma_{22_{m2}} = \sigma_{22_{m1}} + \frac{S_{11_m}}{S_{12_m}}\left(\sigma_{11_{m1}} - \sigma_{11_{m2}}\right) + \frac{1}{S_{12_m}}\left(\epsilon_{11_{m1}}^I - \epsilon_{11_{m2}}^I\right) \qquad (49)$$

$$\sigma_{n\,I1} = \sigma_{22_f} \qquad (50)$$

$$\sigma_{33_{m2}} = \sigma_{33_{m1}} \qquad (51)$$

$$\sigma_{22_{m3}} = \sigma_{22_{m2}} \qquad (52)$$

$$\sigma_{33_{m3}} = \sigma_{33_f} \qquad (53)$$

$$\sigma_{n\,I2} = \sigma_{33_f} \qquad (54)$$

38

$$\sigma_{11_{m3}} = \sigma_{11_{m2}} + \frac{S_{12_m}}{S_{11_m}}\left(\sigma_{33_{m2}} - \sigma_{33_{m3}}\right) + \frac{1}{S_{11_m}}\left(\varepsilon^I_{11_{m2}} - \varepsilon^I_{11_{m3}}\right) \qquad (55)$$

The normal strains for each region are determined from Equation (7), and the composite normal strains are determined from the continuity relations along the external faces of the analysis cell which results in

$$\bar{\varepsilon}_{11} = \varepsilon_{11_f} \qquad (56)$$

$$\bar{\varepsilon}_{22} = \frac{1}{(a+b)}\left(a\,\varepsilon_{22_{m3}} + b\,\varepsilon_{22_{m2}}\right) \qquad (57)$$

$$\bar{\varepsilon}_{33} = \frac{1}{(a+c)}\left(a\,\varepsilon_{33_{m1}} + c\,\varepsilon_{33_{m2}}\right) \qquad (58)$$

The shear effects decouple from the normal stresses and strains and from one another. Therefore, each set of shear stresses in a single direction may be solved separately. As mentioned, the equilibrium condition requires that the average stress through any cross-section of the analysis cell be equal to the composite stress. This along with the continuity condition that requires the length average strain in any of the three directions to be equal to the composite strain except for the shear strain, ε_{23}, where the volumetric average is taken results in a set of equations which may be solved explicitly. Hence, upon solving Eqs (8-10), (12), (16-22), and (32-34) the resulting equations for the shear stresses in each region may be written as follows:

$$\sigma_{12_{m3}} = \frac{\left(1 + \frac{c}{a}\right)\left(S_{44_f} + S_{t_{11}}^{\delta}\right)}{\left[S_{44_m} + \frac{c}{a}\left(S_{44_f} + S_{t_{11}}^{\delta}\right)\right]} \, \overline{\sigma}_{12} - \frac{2\,\varepsilon_{12_{m3}}^{I}}{\left[S_{44_m} + \frac{c}{a}\left(S_{44_f} + S_{t_{11}}^{\delta}\right)\right]} \tag{59}$$

$$\sigma_{12_f} = \left(1 + \frac{c}{a}\right)\overline{\sigma}_{12} - \frac{c}{a}\,\sigma_{12_{m3}} \tag{60}$$

$$\sigma_{12_{m2}} = \overline{\sigma}_{12} + \frac{2\left(\varepsilon_{12_{m1}}^{I} - \varepsilon_{12_{m2}}^{I}\right)}{S_{44_m}\left(1 + \frac{c}{a}\right)} \tag{61}$$

$$\sigma_{12_{m1}} = \left(1 + \frac{c}{a}\right)\overline{\sigma}_{12} - \frac{c}{a}\,\sigma_{12_{m2}} \tag{62}$$

$$\sigma_{t_{I1}} = \sigma_{12_f} \tag{63}$$

$$\sigma_{13_{m1}} = \frac{\left(1 + \frac{b}{a}\right)\left(S_{44_f} + S_{t_{12}}^{\delta}\right)}{\left[S_{44_m} + \frac{b}{a}\left(S_{44_f} + S_{t_{12}}^{\delta}\right)\right]} \, \overline{\sigma}_{13} - \frac{2\,\varepsilon_{13_{m1}}^{I}}{\left[S_{44_m} + \frac{b}{a}\left(S_{44_f} + S_{t_{12}}^{\delta}\right)\right]} \tag{64}$$

$$\sigma_{13_f} = \left(1 + \frac{b}{a}\right)\overline{\sigma}_{13} - \frac{b}{a}\,\sigma_{13_{m1}} \tag{65}$$

$$\sigma_{13_{m2}} = \overline{\sigma}_{13} + \frac{2\left(\varepsilon_{13_{m3}}^{I} - \varepsilon_{13_{m2}}^{I}\right)}{S_{44_m}\left(1 + \frac{b}{a}\right)} \tag{66}$$

$$\sigma_{13_{m3}} = \left(1 + \frac{b}{a}\right)\overline{\sigma}_{13} - \frac{b}{a}\,\sigma_{13_{m2}} \tag{67}$$

$$\sigma_{t_{I2}} = \sigma_{13_f} \tag{68}$$

$$\sigma_{23_f} = \sigma_{23_{m1}} = \sigma_{23_{m2}} = \sigma_{23_{m3}} = \bar{\sigma}_{23} \tag{69}$$

The shear strains for each region are found from Eqs (8-10), and the composite shear strains from Eqs (18) and (21-22). Hence,

$$\bar{\varepsilon}_{12} = \frac{1}{(a+b)} \left(a\, \varepsilon_{12_{m3}} + b\, \varepsilon_{12_{m2}} \right) \tag{70}$$

$$\bar{\varepsilon}_{13} = \frac{1}{(a+c)} \left(a\, \varepsilon_{13_{m1}} + c\, \varepsilon_{13_{m2}} \right) \tag{71}$$

$$\bar{\varepsilon}_{23} = \frac{1}{(a+b)(a+c)} \left(a^2\, \varepsilon_{23_f} + a\,b\, \varepsilon_{23_{m1}} + b\,c\, \varepsilon_{23_{m2}} + a\,c\, \varepsilon_{23_{m3}} \right) \tag{72}$$

The above micromechanics formulation for unidirectional composites has been employed to model the inelastic behavior of Metal-Matrix Composites (MMCs) (45-48). These studies have examined the effects of plasticity, viscoplasticity, and interfacial debonding on the composite's response to various load and temperature time histories. In the following chapters, the application of this model to such nonlinearities is presented as well as the extension of the model to include progressive interfacial failure (fiber/matrix interface possessing a finite strength) and nonlinear laminate analysis. More theoretical development will be required at each of these steps and is presented accordingly.

41

IV. Elastic-Plastic Behavior

Several forms of inelasticity may be exhibited by various materials such as plastic and viscoplastic behavior. In particular, most metals demonstrate elastic-plastic behavior where as long as the material is loaded below the yield stress, then it essentially behaves in a linear-elastic fashion, but once the yield stress is exceeded then the material becomes nonlinear. Many theories for plasticity have been proposed, but the present study will focus on theories that have been classically used with metals. For instance, the Von Mises yield criterion coupled with the Prandtl-Reuss flow rule (49). Also, in this chapter it is assumed that the nonlinear material properties are not dependent on time (viscoplasticity). That topic is discussed later in the following chapter.

An advantage in choosing the classical elastic-plastic approach for modeling nonlinear material behavior is that the required material constants are generally readily available or determined from a simple tensile test of the pure material. If the material is assumed elastic-perfectly plastic, then the yield stress remains constant throughout loading and will depend only upon temperature. Therefore, only a single parameter (yield stress) is required to define the plastic behavior. On the other hand, if the material is assumed elastic-plastic with work hardening, then only two parameters are required (Figure 10).

An additional topic which will be discussed is kinematic hardening, otherwise called the Bauschinger effect. The Bauschinger effect describes how some materials exhibit a shift of the yield surface origin in
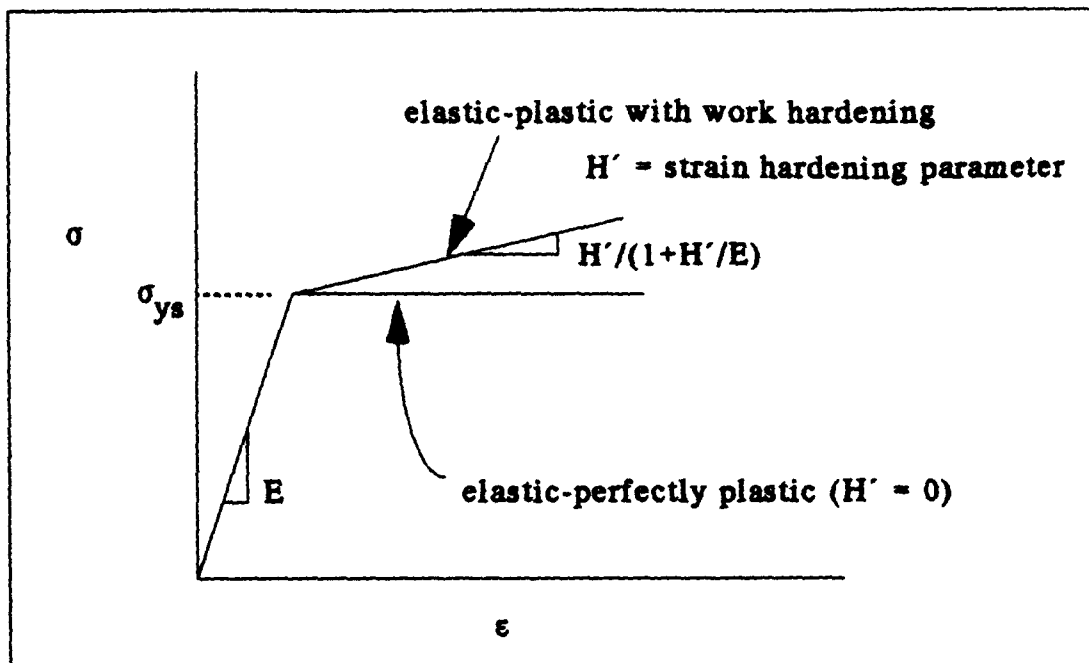
Figure 10. General Tensile Response of an Elastic-Plastic Material

stress space during plastic work hardening (49). An example is given in Figure 11 where the effect of kinematic hardening is compared to isotropic hardening. In isotropic hardening the yield surface expands while in kinematic hardening it experiences a shift of origin. The effect of this on the one-dimensional material response is to produce a yield stress in compression that is different from that in tension (Figure 11).

The present formulation will incorporate all these various plasticity effects. In addition, a combined approach is presented where a parameter between 0 and 1 is specified which controls the percent of hardening due to kinematic effects. The basic plasticity relations, method of solution, and results are presented and discussed in the following sections.
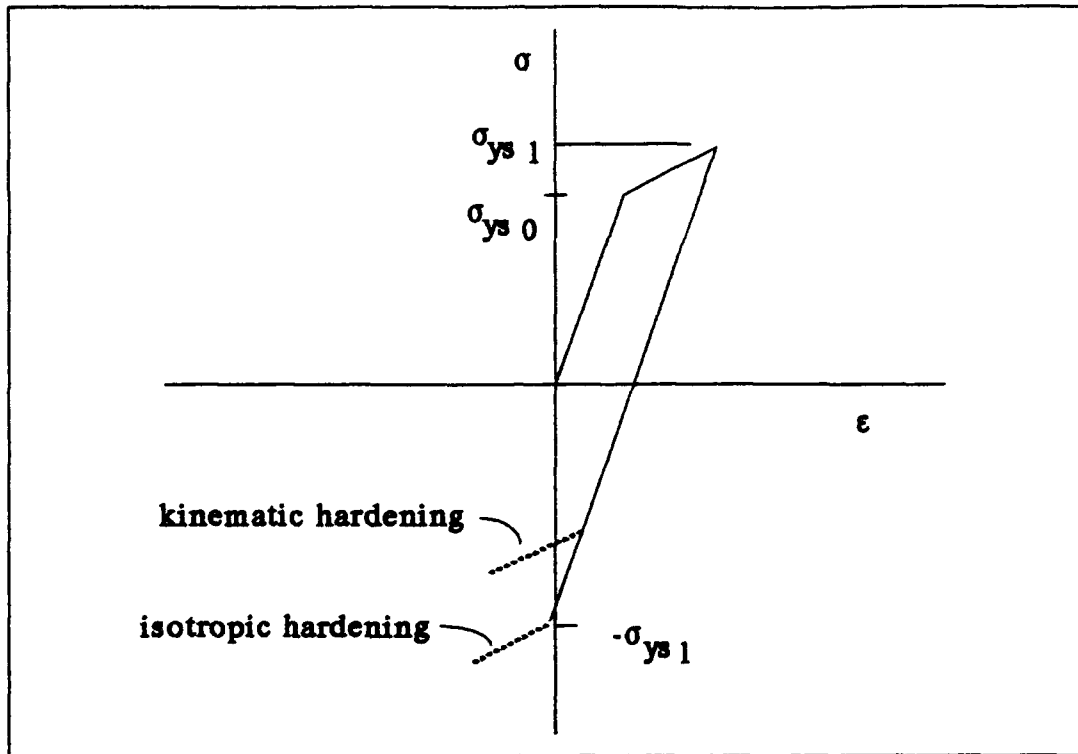
Figure 11. Kinematic and Isotropic Hardening

4.1 Plasticity Relations

The Von Mises yield criterion states that plasticity occurs when the second invariant of the deviatoric stress tensor, J_2, reaches a critical value. The deviatoric stress is defined by

$$\sigma'_{ij} = \sigma_{ij} - \delta_{ij}\frac{\sigma_{kk}}{3} \qquad (73)$$

where σ'_{ij} is the deviatoric stress and δ_{ij} is the Kronecker delta. The second invariant of the deviatoric stress tensor is given by

$$J_2 = \frac{1}{2} \sigma'_{ij} \sigma'_{ij} \tag{74}$$

The above relation when coupled with the critical value for J_2 controls the yielding of an elastic-plastic material. However, once yielding occurs, a relationship that describes the accumulation of plastic strain during load must be specified. Such relations are known as plastic flow rules, and for the present formulation, the Prandtl-Reuss flow rule which is normally associated with the Von Mises yield criterion is assumed. The Prandtl-Reuss flow rule states that the inelastic strain accumulated during any load increment may be related to the preexisting inelastic strain and the deviatoric stress as follows (49):

$$\varepsilon^I_{ij} = {}_0\varepsilon^I_{ij} + d\varepsilon^I_{ij} \tag{75}$$

where

$$d\varepsilon^I_{ij} = \sigma'_{ij} d\lambda \tag{76}$$

and ${}_0\varepsilon^I_{ij}$ is the preexisting inelastic strain prior to the load increment and $d\lambda$ is an incremental plastic multiplier.

Equations (73-76) are inherent to the elastic-plastic material approaches presented in this study. For instance, all the various types of behavior such as elastic-perfectly plastic, elastic-plastic with isotropic hardening, and elastic-plastic with kinematic hardening are accounted for by only slight modifications to the above equations.

4.1.1 Elastic-Perfectly Plastic

A perfectly plastic material experiences no hardening, and therefore, the yield stress remains unchanged throughout loading. Also, since the yield stress is constant, then the critical value of J_2 for yielding is constant and the yield surface remains fixed in stress space. However, rather than continuing to use the critical value of J_2, if an appropriate quantity is defined, then yielding in multi-dimensional stress space may be discussed in terms of the yield stress. This quantity is termed the effective stress, σ_{eff}, and is defined by

$$\sigma_{eff} = \sqrt{3 J_2} \qquad (77)$$

or in terms of the principal stresses, σ_1, σ_2, and σ_3 as

$$\sigma_{eff} = \sqrt{\frac{1}{2}\left[(\sigma_1 - \sigma_2)^2 + (\sigma_2 - \sigma_3)^2 + (\sigma_3 - \sigma_1)^2\right]} \qquad (78)$$

Yielding occurs once the effective stress exceeds the yield stress. Additional uses for the effective stress in material hardening are presented in section 4.1.2.

The yield surface may be visualized more readily in the principal stress axes system since only three stresses are required (Figure 12). If the full stress space is used, then either six or nine stresses are required depending on whether one is working in engineering or tensorial stress space. Further, by defining the variables given in Figures 12-15, the yield surface may be represented in two dimensions. If the material is

46
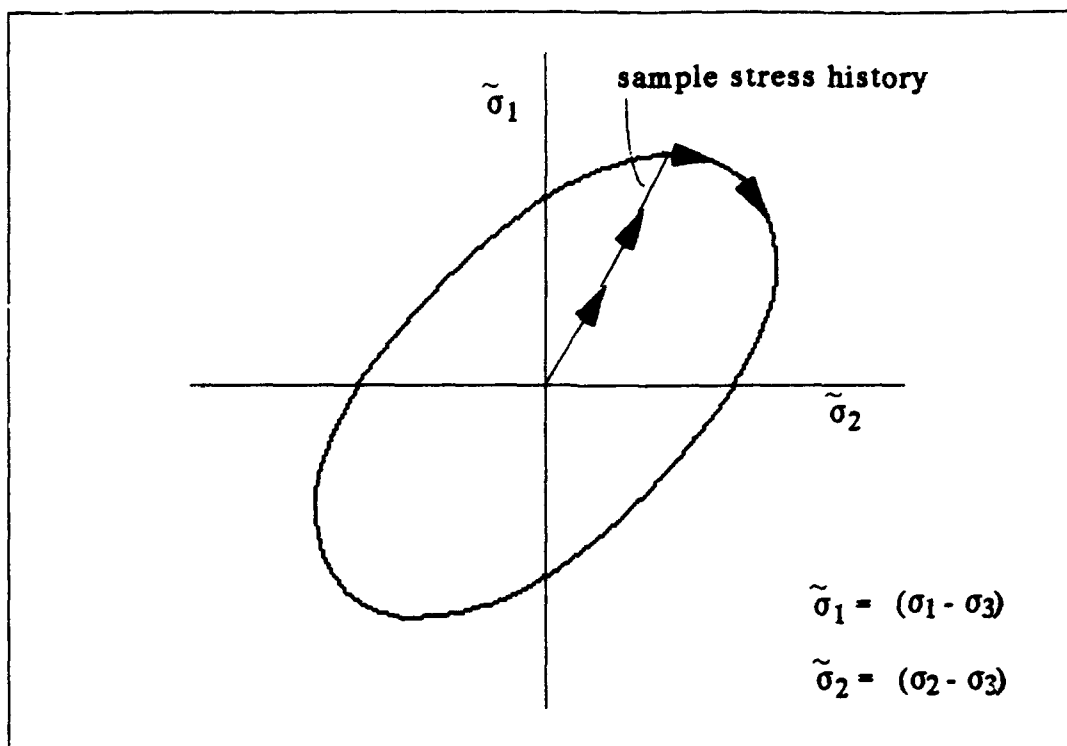
Figure 12. Yield Surface and Sample Stress History for Elastic-Perfectly Plastic Material

loaded such that its stress lies within the yield surface, then the material is elastic, but once it reaches yielding, then any further load increase will result in the stress state simply moving along the yield surface. Thus, the nonlinear solution is achieved by assuming linear-elastic behavior until the condition $\sigma_{eff} \leq \sigma_{ys}$ fails. Then an iterative procedure is used to solve for an appropriate value of the plastic multiplier, $d\lambda$, such that $\sigma_{eff} = \sigma_{ys}$ is satisfied.

4.1.2 Elastic-Plastic With Isotropic Hardening

The solution sequence for an elastic-plastic material with strain hardening is the same as for the perfectly plastic material except the yield surface is no longer fixed in stress space but expands as the body plastically deforms. This expansion is controlled by the strain hardening parameter, H′, which relates the incremental effective plastic strain, $d\varepsilon_{eff}^I$, to the yield stress by (49)

$$\frac{d\sigma_{ys}}{d\varepsilon_{eff}^I} = H' \tag{79}$$

where $d\varepsilon_{eff}^I$ is defined by

$$d\varepsilon_{eff}^I = \sqrt{\frac{2}{3}\, d\varepsilon_{ij}^I\, d\varepsilon_{ij}^I} \tag{80}$$

In this material model the solid body is once again assumed to behave linear-elastically until the condition $\sigma_{eff} \leq \sigma_{ys}$ fails. At this point the yield surface expands according to Eq (79) as the body plastically deforms. Hence, the solution is achieved by iterating around Eqs (73-77) and (79-80), along with the equilibrium and continuity relations until an appropriate plastic multiplier, dλ, is found that satisfies all requirements. The path an increasing load sequence might have in stress space is presented in Figure 13. If the material is unloaded after plastic deformation, then linear-elastic behavior persists as long as the stress

48
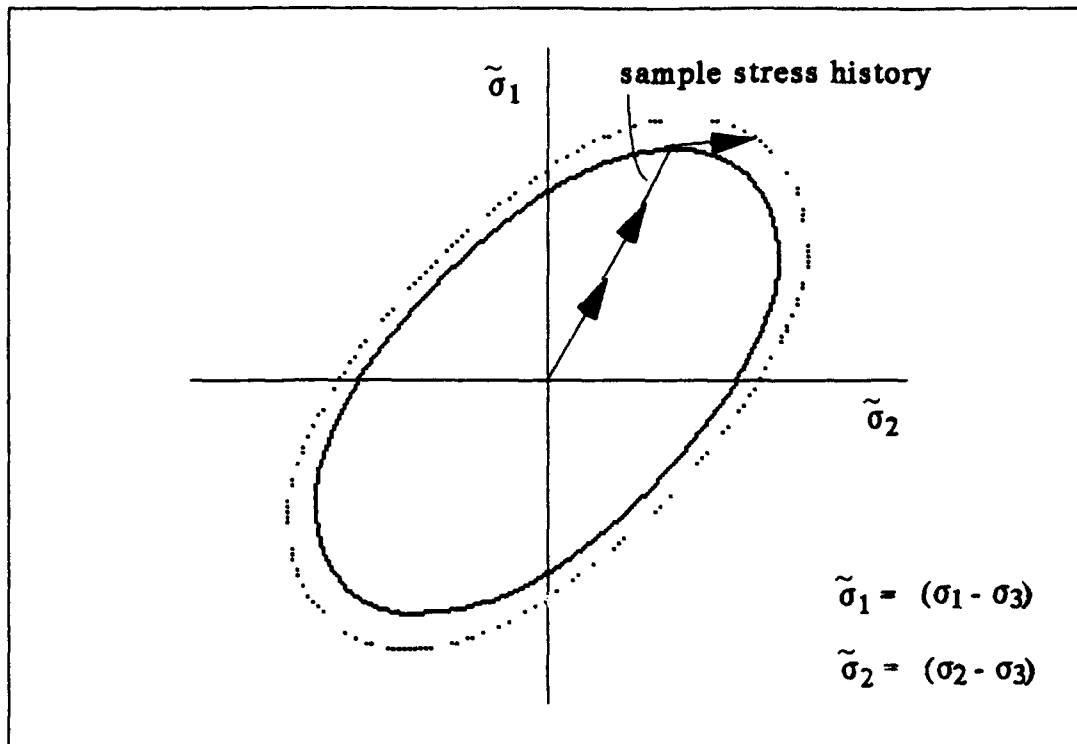
Figure 13. Yield Surface and Sample Stress History for Elastic-Plastic Material With Isotropic Hardening

lies within the new yield surface.

4.1.3 Elastic-Plastic With Kinematic Hardening

Kinematic hardening is accounted for in a similar manner as isotropic hardening except the yield surface origin is shifted (49) as opposed to its size expanding (Figure 14). In the present formulation a combined approach is presented where the percent of hardening due to kinematic effects is specified, and the yield surface both expands and shifts during plastic deformation (Figure 15). A kinematic hardening parameter, h_D, defined as a real number between 0 and 1 controls the percent of kinematic hardening, and the remainder is recognized as being due to isotro-

49
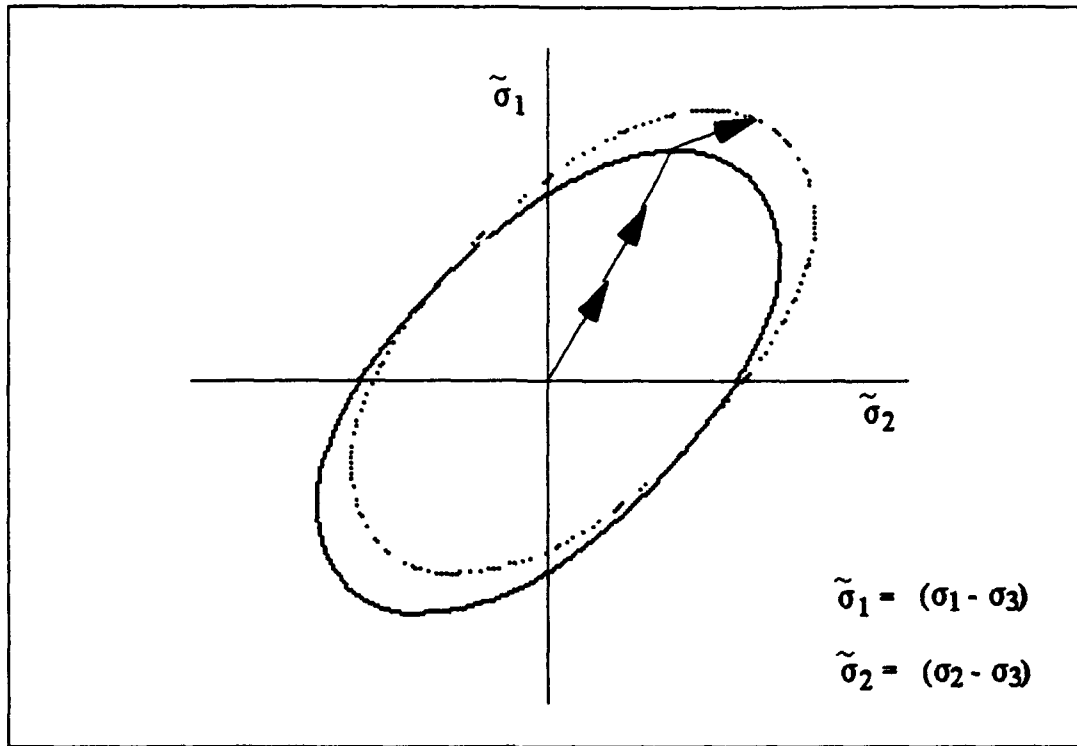
Figure 14. Yield Surface Shift Under Kinematic Hardening

pic hardening. Hence a single set of equations may then be developed that will allow both types of hardening.

To account for shifting of the yield surface a quantity which specifies the origin of the yield surface is required. This quantity is termed the back stress, Ω_{ij}, and is used to modify Eqs (74) and (76). Hence, Eq (74) is modified to become

$$K_2 = \frac{1}{2} \left(\sigma'_{ij} - \Omega_{ij} \right) \left(\sigma'_{ij} - \Omega_{ij} \right) \tag{81}$$

where K_2 is analogous to J_2, and Eq (76) becomes
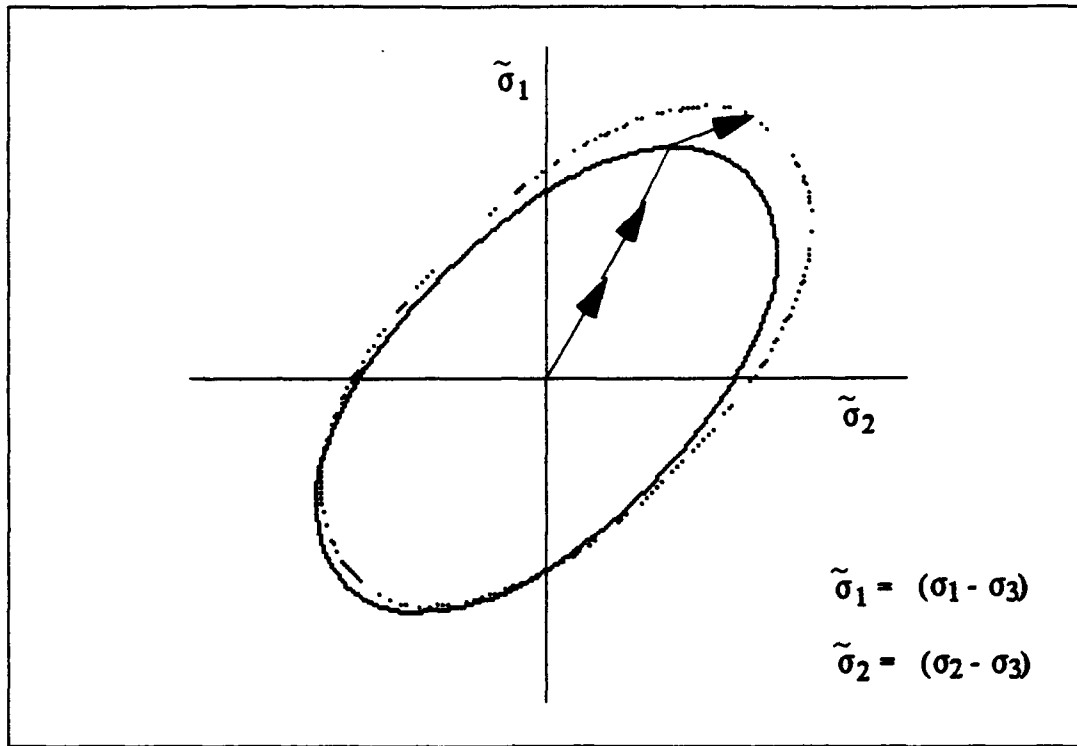
Figure 15. Yield Surface Shift and Expansion Under Combined Isotro-
pic-Kinematic Hardening

$$d\varepsilon_{ij}^{I} = \left(\sigma'_{ij} - \Omega_{ij}\right) d\lambda \qquad (82)$$

Also, the effective stress is now given in terms of the quantity, K_2,

as

$$\sigma_{eff} = \sqrt{3 K_2} \qquad (83)$$

and the increase in the size of the yield surface during an incremental
applied load as

$$\frac{d\sigma_{ys}}{d\varepsilon_{eff}^I} = (1 - h_D) H' \tag{84}$$

The shift in the yield surface origin is also controlled by the kinematic and strain hardening parameters and may be represented by

$$\frac{d\Omega_{ij}}{d\varepsilon_{ij}^I} = \sqrt{\frac{2}{3}} \, h_D H' \tag{85}$$

where the $\sqrt{2/3}$ results from the numerical factor in the definition of effective plastic strain.

Therefore, the above relations are used in a manner similar to that described for isotropic hardening. During plastic deformation an appropriate value of $d\lambda$ is sought that satisfies all requirements. The next section presents the numerical algorithm to solve for the nonlinear behavior of the micromechanics model. The algorithm was developed for the combined isotropic-kinematic hardening relations, and it is simply recognized that elastic-perfectly plastic behavior is achieved by setting $H' = 0$, isotropic hardening is achieved by setting $h_D = 0$, and pure kinematic hardening by setting $h_D = 1$.

4.2 Elastic-Plastic Algorithm

A synopsis of the algorithm that was employed to solve for the elastic-plastic behavior may be simply stated as initially assuming linear-elastic behavior for the given load increment, and then measuring the

52

distance between the resulting stresses and the yield surface. From this distance an approximation for $d\lambda$ is made and the elastic-plastic relations are solved to achieve a new stress state. This iteration is continued until the $d\lambda$ produces a stress state that is within a user specified tolerance from the yield surface.

Two problems must be guarded against when developing a stress-based elastic-plastic algorithm. First, the amount of plastic strain accumulated during a single load increment is not inherently limited as it is in strain-based algorithms. Hence, stress-based algorithms are more unstable, and must be supported with appropriate damping mechanisms. Also, if a plastic multiplier, $d\lambda$, is chosen that is greater than required, then the final stress state after the iteration may lie well within the yield surface as opposed to the desired condition of lying upon it. Therefore, this condition must also be checked at each iteration and recalculated if necessary.

The following sequence of steps were used to determine the strain of a single load increment and have been found to be very versatile in handling the above mentioned conditions:

(1) For the first iteration assume linear-elastic behavior. Therefore set the plastic multiplier for each region, r, to zero. Also, initialize the iteration counter, p.

$$^{0}d\lambda_{r} = 0 \quad \text{and} \quad p = 1 \tag{86}$$

Iterate

(2) Solve for the stresses in each region using the incremental plastic multiplier from the previous iteration and the micromechanics relations.

(3) Determine the deviatoric stresses of each region for the present iteration.

$$^{P}\sigma'_{ij_r} = {}^{P}\sigma_{ij_r} - \delta_{ij}\frac{^{P}\sigma_{kk_r}}{3} \tag{87}$$

(4) Determine the effective stress.

$$^{P}K_{2_r} = \frac{1}{2}\left(^{P}\sigma'_{ij_r} - {}^{P-1}\Omega_{ij_r}\right)\left(^{P}\sigma'_{ij_r} - {}^{P-1}\Omega_{ij_r}\right) \tag{88}$$

$$^{P}\sigma_{eff_r} = \sqrt{3\ ^{P}K_{2_r}} \tag{89}$$

(5) Check for a converged solution by testing if the following conditions are satisfied:

(a) For all regions check if

$$^{P}\sigma_{eff_r} \leq {}^{P-1}\sigma_{ys_r} \tag{90}$$

(b) For regions that have previously yielded during this load increment check if

54

$$\left(1 - \frac{{}^{P}\sigma_{eff_r}}{{}^{P-1}\sigma_{ys_r}}\right) > Fact_1 \qquad (91)$$

where $Fact_1$ is a user supplied tolerance.

(6) If the conditions of step 5 are satisfied, then stop iteration and calculate the region and composite strains. If the conditions are not satisfied, then continue iteration.

(7) Estimate the incremental plastic multiplier for the yielded regions.

$$^{P}d\lambda_r = \left(1 - \frac{{}^{P-1}\sigma_{ys_r}}{{}^{P}\sigma_{eff_r}}\right)\left(\frac{Fact_2}{E_{11_r} + H'_r}\right) \qquad (92)$$

where $Fact_2$ is a user supplied value that controls the instability and rate of convergence.

(8) Calculate the incremental inelastic strains.

$$^{P}d\varepsilon^{I}_{ij_r} = \left({}^{P}\sigma'_{ij_r} - {}^{P-1}\Omega_{ij_r}\right) {}^{P}d\lambda_r \qquad (93)$$

(9) Calculate the effective inelastic strain increment.

$$^{P}d\varepsilon^{I}_{eff_r} = \sqrt{\frac{4}{3} {}^{P}K_{2_r}} \; {}^{P}d\lambda_r \qquad (94)$$

55

(10) Calculate the change in the back stress.

$$^{p}\Omega_{ij_r} = {}^{p-1}\Omega_{ij_r} + \sqrt{\frac{2}{3}}\, h_D\, H'_r\, {}^{p}d\varepsilon_{ij_r} \qquad (95)$$

(11) Compute the change in the yield stress.

$$^{p}\sigma_{ys_r} = {}^{p-1}\sigma_{ys_r} + (1-h_D)\, H'_r\, {}^{p}d\varepsilon_{eff_r} \qquad (96)$$

(12) Set $p = p + 1$, and continue steps 2 through 12 until the conditions of step 5 are satisfied.

The above algorithm was found to be very robust at handling various types of mechanical and thermal loads, and for most calculations, the user supplied constants, Fact $_1$ and Fact $_2$, were given values of 0.005 and 1.0, respectively. A few of the calculations required either a modification from these initial values or a decrease in the size of the load increments to achieve convergence. Also, solutions were for the most part obtained in a matter of seconds on an Apple Macintosh IIx desktop computer.

4.3 Elastic-Plastic Results

In this section results from the present formulation are put forth and compared to published data from other models, finite element solutions, and experiments (45, 46). The purpose being to determine if the simplifying assumptions of the model are valid. First, linear-elastic results are

56

presented followed by nonlinear elastic-plastic solutions. The linear-elastic cases will demonstrate the model's capability for determining a composite's thermoelastic properties and constituent microstresses. Nonlinear elastic-plastic results will analyze the model's ability to capture the composite response to both thermal and mechanical loading and also demonstrate the effects of variation in the hardening condition from isotropic to a kinematic type. Also, whenever it is appropriate the material properties used in the model are considered functions of temperature.

Bigelow, Johnson, and Naik have compared various micromechanical models (1). The published data from their study along with calculations using the present analysis are presented in Tables 1 and 2 for the thermoelastic properties of Boron/Aluminum 6061-T0 and SCS-6/Ti-15-3. The constituent properties as listed in reference 1 were used in the calculations to provide for the direct comparison. The AGLPLY computer

Table 1. Unidirectional Laminate Properties for Boron/Aluminum as Calculated by the Present Model and Published Data from Existing Models and Finite Element Solutions (1)

	E_1(GPa)	E_2 (GPa)	G_{12} (GPa)	v_{12}	α_1(x10^{-5}/C°)	α_2(x10^{-5}/C°)
AGLPLY	218	118	42.1	0.240	0.824	1.77
EPC	219	132	49.0	0.233	0.860	1.67
METCAN	218	127	49.2	0.240	1.010	1.54
F.E.	217	146	- - -	0.230	0.871	1.64
4 - Reg model	219	144	55.6	0.233	0.860	1.67
8 - Reg model	219	149	56.1	0.228	0.879	1.63

Table 2. Unidirectional Laminate Properties for SCS_6 / Ti-15-3 as Calculated by the Present Model and Published Data from Existing Models and Finite Element Solutions (1)

	E_1(GPa)	E_2(GPa)	G_{12} (GPa)	v_{12}	α_1(x10^{-5}/C°)	α_2(x10^{-5}/C°)
AGLPLY	191	130	45.4	0.325	0.630	0.846
EPC	192	139	48.5	0.322	0.634	0.828
METCAN	192	134	48.5	0.324	0.691	0.776
F.E.	192	148	- - -	0.321	0.637	0.828
4 - Reg model	192	147	55.4	0.322	0.634	0.828
8 - Reg model	193	149	55.2	0.321	0.638	0.823

program utilizes the vanishing fiber diameter model of Bahei-El-Din (33), and the EPC program utilizes Aboudi's method of cells approach (42). A trend in the calculations of the transverse normal modulus, E_2, and in-plane shear modulus, G_{12}, is noted where the present approach yields values on the order of 5-15% stiffer than some of the existing micromechanics models. Nevertheless, when compared with the finite element solutions for transverse normal modulus, E_2, the present analysis agrees quite well. If the finite element results are assumed to be closer to the true solution as one might expect, then the present approach seems to provide an accurate representation of the transverse normal response. However, no finite element value for in-plane shear modulus was available in Bigelow, Johnson, and Naik's study. Therefore, to further evaluate the observed difference in in-plane shear modulus between the present model and the other listed models, a comparison of the in-plane shear modulus from the present approach, METCAN, and

58

the finite element solution of Crane and Adams for Glass/Epoxy unidirectional composite (50) was made (Table 3). The constituent properties used in the calculations were obtained from reference 50. Again, the present formulation provides a very good agreement with the finite element solution. Also, very little change in the calculated properties is noticed in going from the 4-region to the 8-region model. In fact, when compared with the finite element solutions, the greatly increased complexity of the 8-region model offers no noticeable improvement over the 4-region calculations.

Figures 16-19 display results for unidirectional Graphite/Epoxy at various fiber volume fractions. The present approach is compared to the method of cells and experiment (42). The same constituent properties as were used in reference 42 were employed. The effect of fiber volume fraction on the longitudinal modulus, the transverse modulus, the transverse Poisson's ratio, and the in-plane shear modulus are depicted. For this material the two analysis methods are indistinguishable when computing either the longitudinal or transverse modulus except for a slight difference with the 8-region model at the higher volume fractions. For

Table 3. Longitudinal Shear Modulus of Glass/Epoxy at Room Temperature Dry Conditions as Calculated by the Present Model, METCAN, and Crane and Adams (50)

	G_{12} (GPa)
METCAN	3.96
Finite Element	4.90
4-Reg Model	4.76
8-Reg Model	4.80
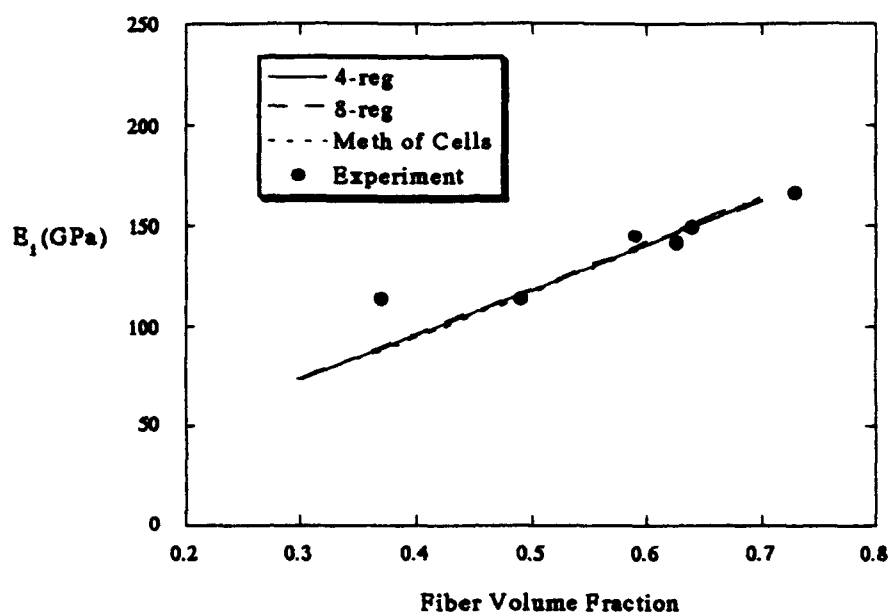
Figure 16. Longitudinal Modulus of Graphite/Epoxy (42)
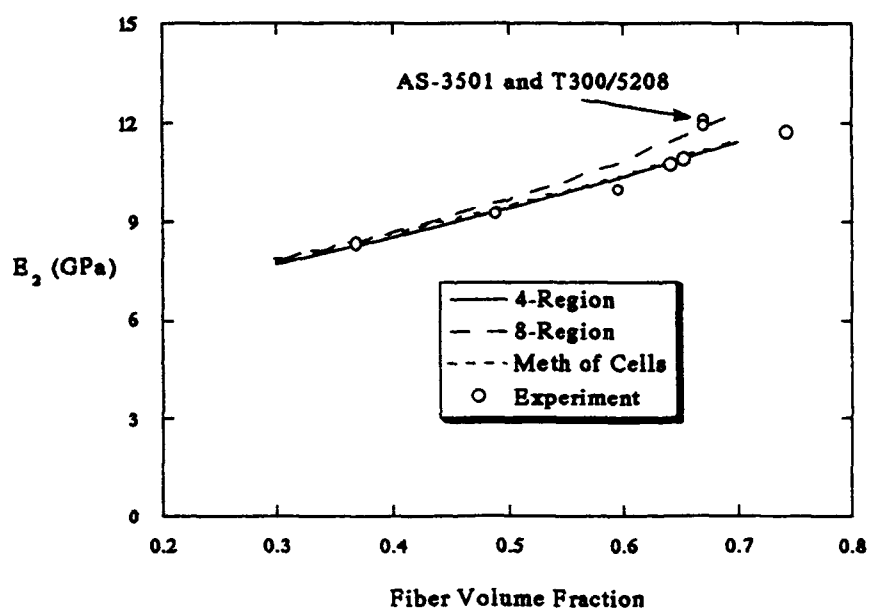
Figure 17. Transverse Modulus of Graphite/Epoxy (42)

60
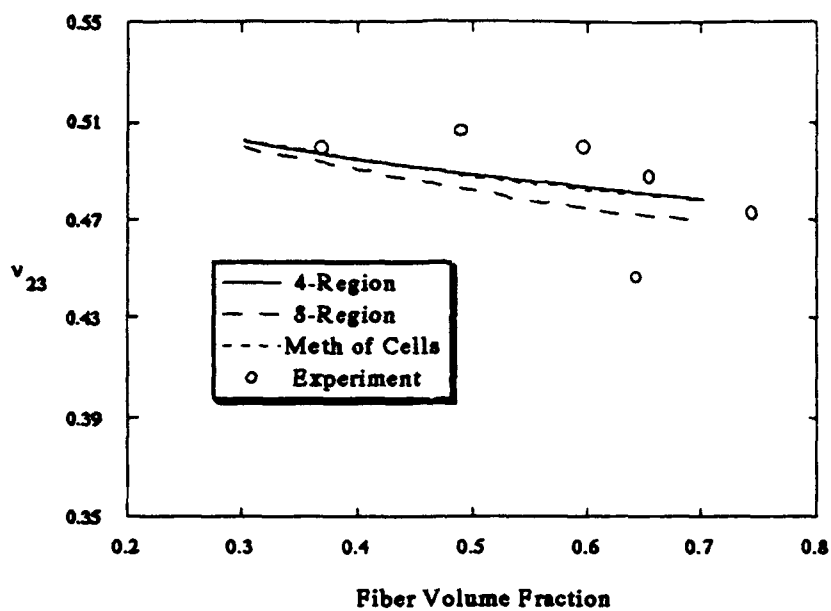
Figure 18. Transverse Poisson's Ratio for Graphite/Epoxy (42;
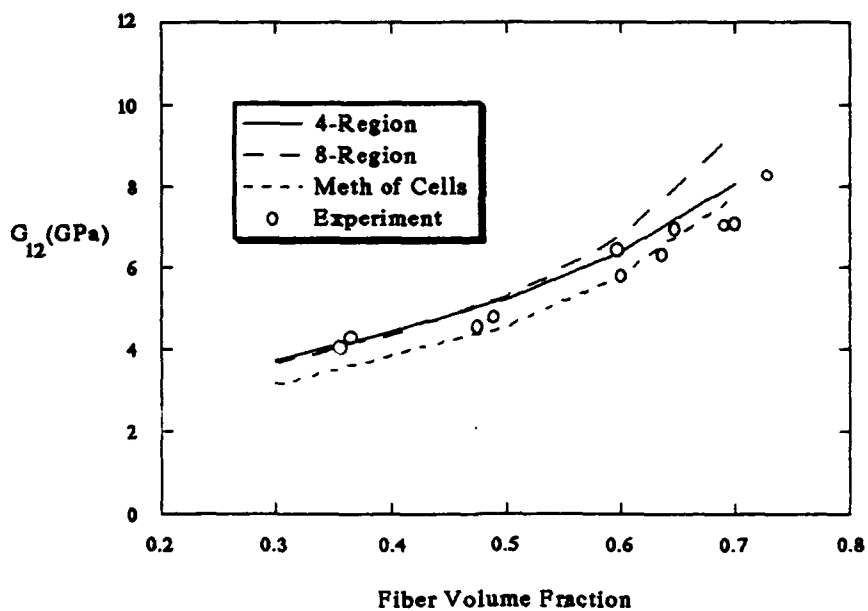
Figure 19. In-Plane Shear Modulus for Graphite/Epoxy (42)

61

in-plane shear modulus the present approach exhibits a modulus prediction that is on the order of 10% higher than the method of cells, but both models are within the scatter of the experimental data.

A comparison of stress calculations is demonstrated in Figures 20-23 where the effective stress, σ_{eff}, and the normal stress, σ_{33}, is presented for a titanium based metal matrix composite after cooldown from an assumed processing temperature of 1000°C to room temperature at 23°C. Results from a three-dimensional finite element solution as well as calculations using both 4 and 8 region micromechanics models are depicted. The finite element solution was performed using the MSC/NASTRAN code with 272 elements, and the constituent properties are listed in Table 4 (28). Although any of the micromechanical models discussed previously provide average stress calculations over a given region or phase, and hence, attempting to determine the stress field by such models has limited usefulness, nevertheless, the data provided in Figures 20-23 can furnish some insight into the overall residual thermal stresses in the fiber and matrix. Figures 20 and 21 present the stresses after cooldown only, and Figures 22 and 23 present the stresses resulting from an additional 200 MPa transverse load along the 2-axis. The stresses calculated by the present formulation were found to provide a good approximation to the average stress experienced by the equivalent areas in the finely discretized finite element solution.

Several comparisons involving nonlinear results of the present method with the experimental data of Kenaga, Doyle, and Sun (51) for Boron/Aluminum 6061-T0 have been performed . The constituent properties used for these calculations are given in Table 5. A zero stress
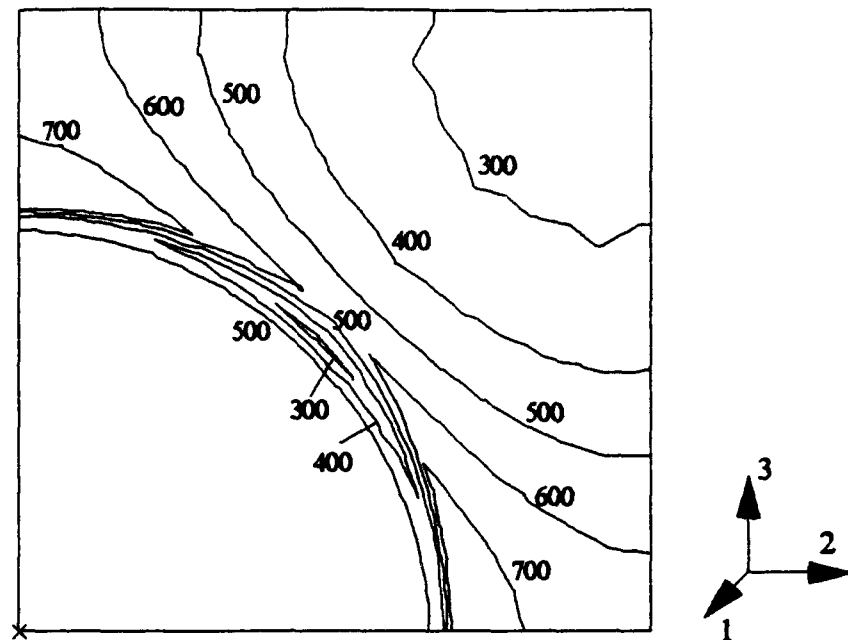
Units of Contour Labels: MPa
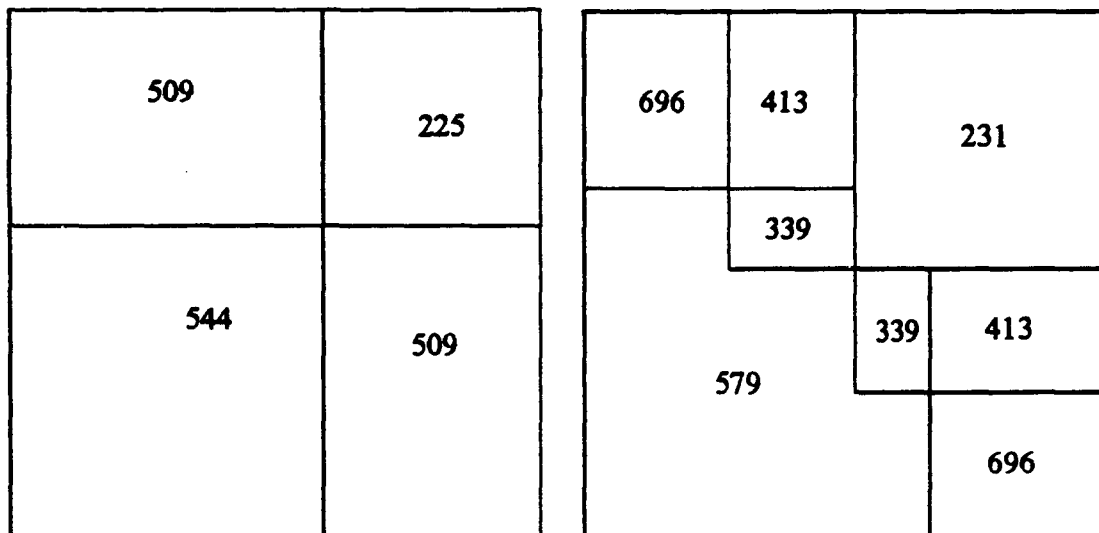
Figure 20. Effective Stress Contours after Cooldown (1000 to 23°C) from Finite Element Solution as Compared to 4 and 8 Region Solutions from the Present Formulation (28)

63
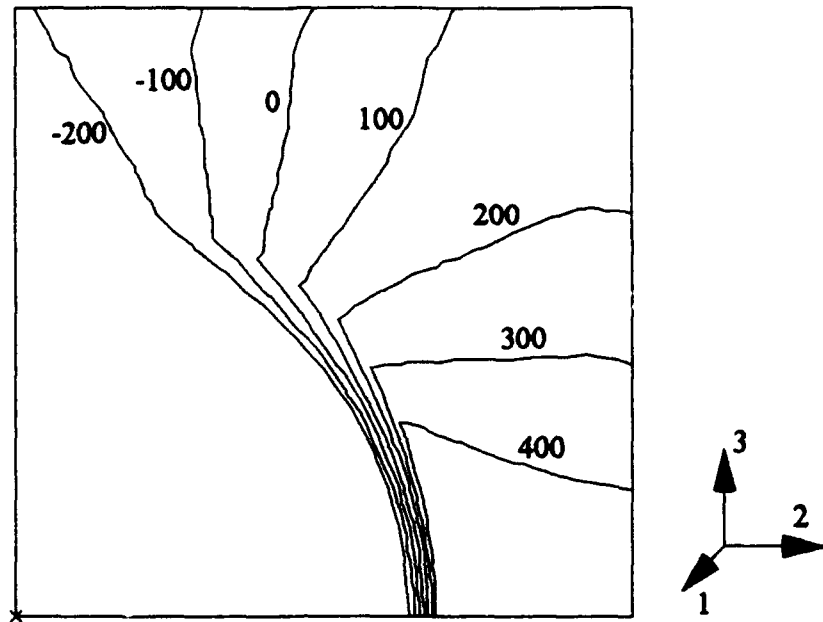
Units of Contour Labels: MPa

Figure 21. Normal Stress, σ_{33}, Contours after Cooldown (1000 to 23°C) from Finite Element Solution as Compared to 4 and 8 Region Solutions from the Present Formulation (28)

64
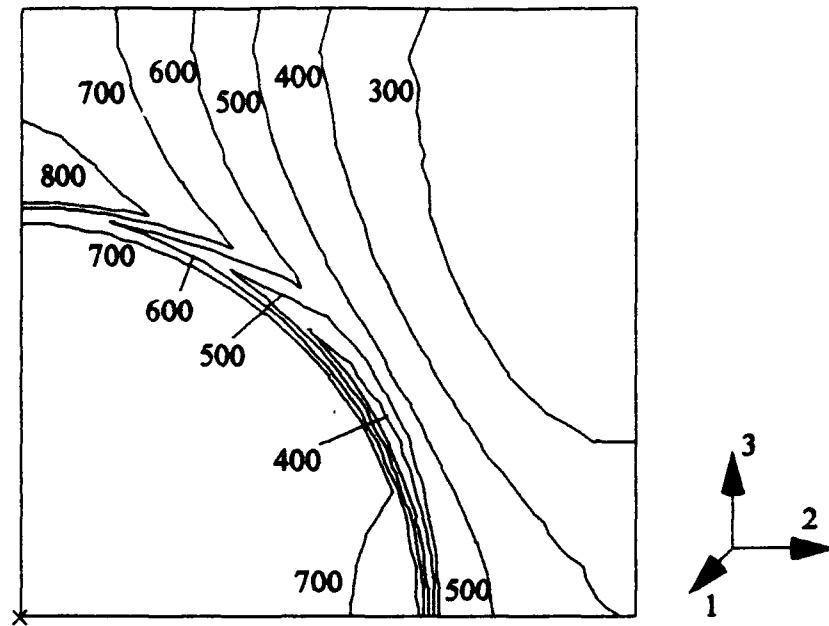
Units of Contour Labels: MPa

Figure 22. Effective Stress Contours after Cooldown (1000 to 23°C) and
200 MPa Transverse Load from Finite Element Solution as
Compared to 4 and 8 Region Solutions from the Present
Formulation (28)
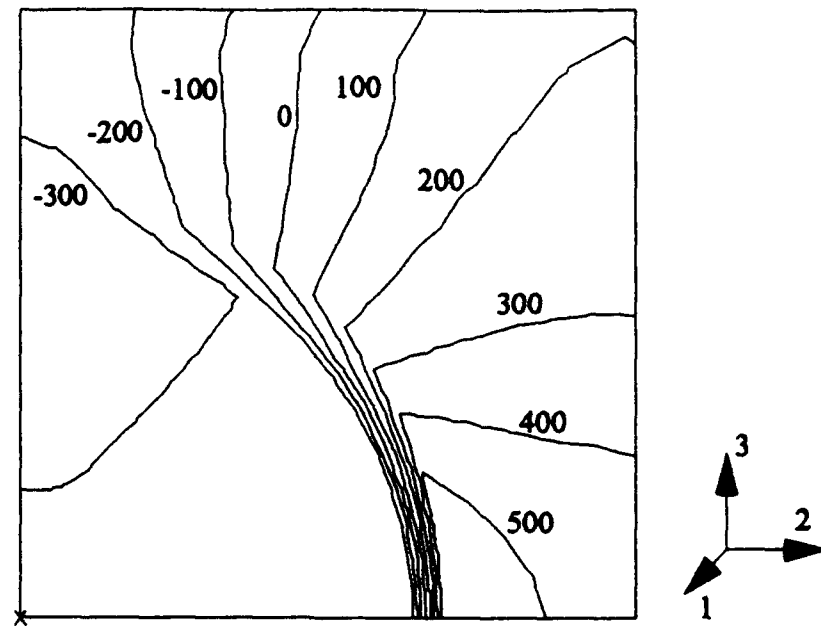
Units of Contour Labels: MPa
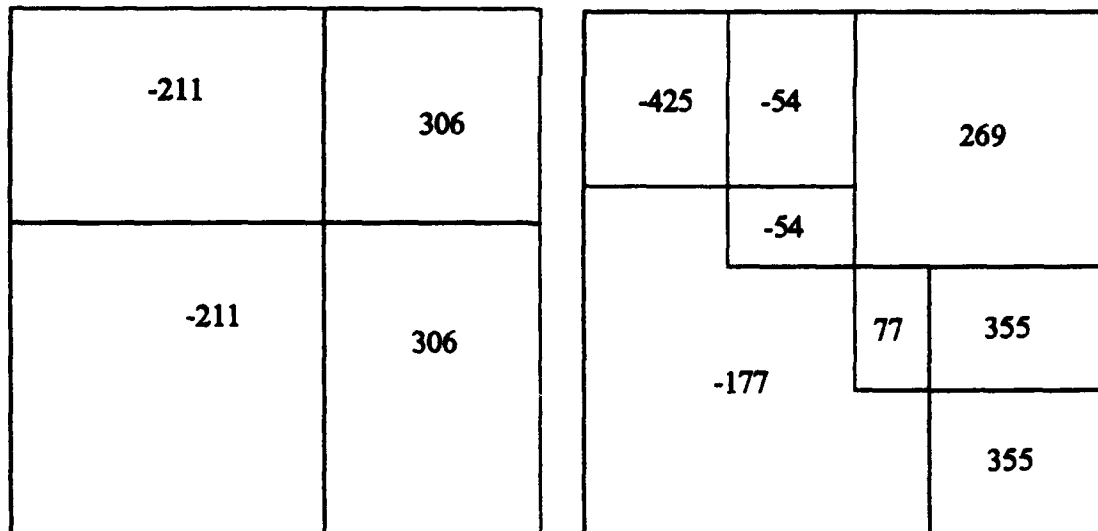
Figure 23. Normal Stress, σ_{33}, Contours after Cooldown (1000 to 23°C) and 200 MPa Transverse Load from Finite Element Solution as Compared to 4 and 8 Region Solutions from the Present Formulation (28)

Table 4. Constitutive Properties Used for the Calculations of Figures 20-23 (Fiber Volume Fraction = 0.35)

	E (GPa)	v	$\alpha \times 10^{-6}$ (°C)$^{-1}$
Matrix	100.	0.3	10.0
Fiber	400.	0.3	5.0

processing temperature of 370°C was assumed for the composite, and the fiber volume fraction is 0.475. Also, a combined hardening approach was assumed where 50% of the hardening takes place isotropically and 50% kinematically. The temperature at which mechanical loads were applied was assumed to be 21°C. Figure 24 depicts the stress-strain predictions for a 0°, and off-axis 10° and 20° lamina response. Calculations from both the 4 and 8 region micromechanics models are present-

Table 5. Constituent Properties for the Nonlinear Boron/Aluminum Calculations (31)

	Boron	Aluminum 6061-T0
E (GPa)	379.3	68.3
G (GPa)	172.4	26.2
v	0.1	0.3
α (1/°C)	8.1×10^{-6}	$23. \times 10^{-6}$
σys (MPa)	-	50.
H' (GPa)	-	1.17
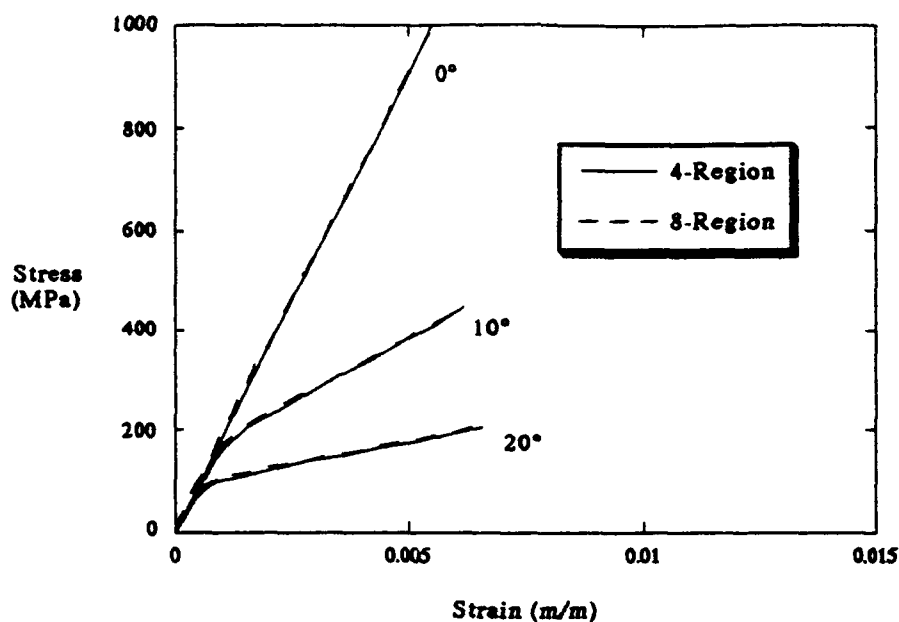
Figure 24. 0°, 10°, and 20° Off-Axis Predictions for Boron/Aluminum

ed, and in the same way as was observed in the linear-elastic cases, the additional complexity of the 8-region model produced little or no change in the overall response.

As to which formulation (4 or 8 region) is "better" at predicting a composite's response, the conclusion is that there is no appreciable difference. For instance, when compared with the experimental linear-elastic properties of Figures 16 through 19, the 8-region model seemed to exhibit a slightly stiffer response at the higher fiber volume fractions than observed in the experimental values. However, the analytical model is incapable of accounting for existent damage such as voids. Voids are more pronounced at the higher volume fractions since it is more difficult

68

for the matrix material to "wet" the fibers during processing. Therefore, the micromechanics solution should tend to produce stiffer results in comparison to its experimental counterpart; especially at the higher fiber volume fractions.

Although this last statement is simply speculation, it is apparent from experimental comparisons that the most one could say is that the eight-region model offers no improvement, and that both are within the scatter of the data. Rather than comparison with experiment, a more accurate measure of whether the four or eight-region model is "better" may be which model more closely approximates the solution to the mathematical problem defined by the unit cell approach. The exact solution to the unit cell problem has not been found, but if we assume that 3-D finite element results are a close approximation, then comparisons made so far (see Tables 1-3) indicate that the eight-region model offers either no improvement or slight improvement. For instance, additional 3-D finite element results performed with the finite element model used in Figures 20-23 predicts a transverse modulus of 156.0 GPa. The four-region model predicts 154.4 GPa and the eight-region model predicts 156.4 GPa for the same composite.

However, since the level of improvement in going from four to eight regions is small, and the mathematical complexity of the formulation is greatly increased, then continuing to carry along the eight-region model for other than comparison sake is questionable. Other researchers have found similar characteristics in the Hopkins and Chamis model where infinitely increasing the number of regions offered little or no improvement (52). Therefore, except for Figure 25, the remainder of the micro-

69

mechanics results were performed using the 4-region model.

Figure 25 presents comparisons between experimental results and the present formulation based on both 4 and 8 regions for 0°, and off-axis angles of 30° and 60° ply layups. Again, there is little or no difference between the 4 and 8 region models. In addition, the micromechanics results exhibit more of a bilinear response for the off-axis cases than is observed in the experiment. However, this is not surprising because the nonlinear material model used in the micromechanics formulation assumes an elastic-plastic bilinear matrix material, and therefore, the calculations will not be able to match exactly experimental results of composites that possess a matrix material that exhibits behavior other than bilinear elastic-plastic, so only general approximations of the experi-
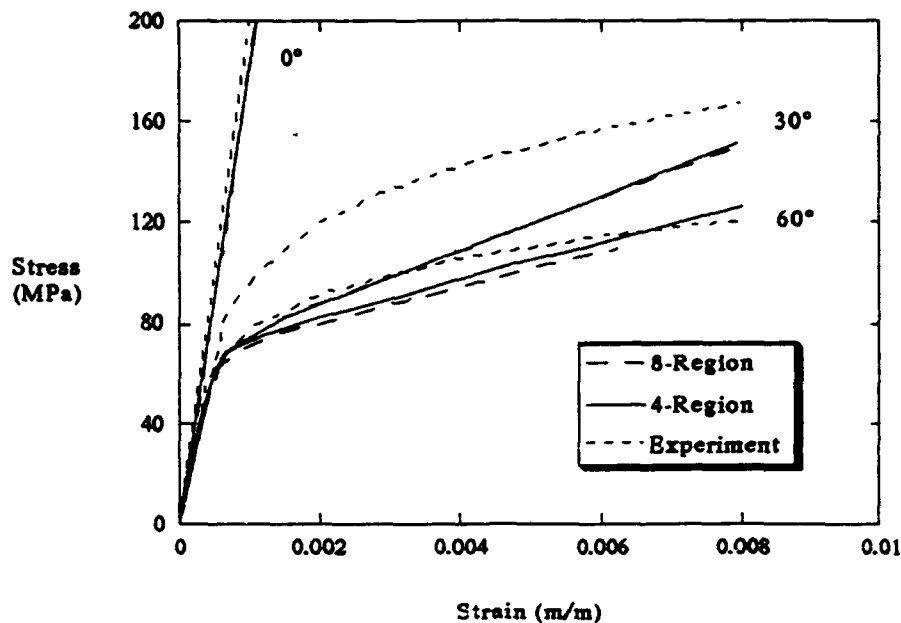
Figure 25. 0°, 30°, and 60° Off-Axis Predictions for Boron/Aluminum (51)

70

mental response is possible.

The cyclic response of a 0° Boron/Aluminum ply layup is presented in Figure 26. The applied mechanical loading consisted of four cycles to a maximum applied stress of 1310 MPa. The figure displays the cyclic data after completion of the initial cycle where both the micromechanics (4-region model) and experiment exhibit a material hysteresis. The only means for energy absorption in the micromechanics model is matrix plasticity, and therefore the material hysteresis observed in the model must be due to matrix plastic flow. After four cycles the micromechanics model indicated a shift of strain equal to only 0.000068 (m/m) from its original value at the zero stress state of the composite. Also, it is worth mentioning that when complete kinematic hardening is
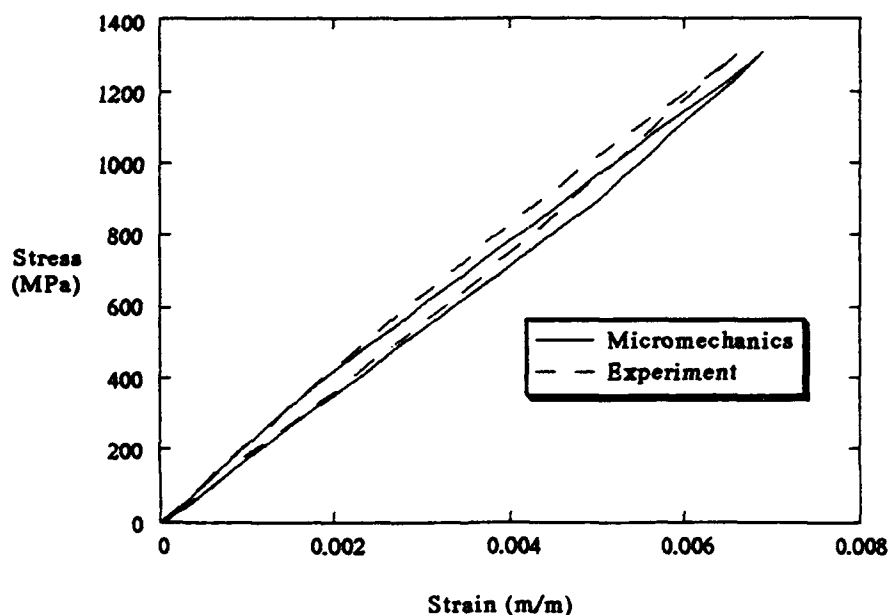
Figure 26. 0° Boron/Aluminum Cyclic Response to Mechanical Load (51)

assumed there is no shift in the zero stress strain state, but the calculations in the figure represent the results of assuming 50% of the hardening takes place kinematically and 50% isotropically.

Figure 27 presents the results of a 90° lamina with periodic unloading. In the calculations, the model was loaded until the strain at which each unloading point in the experiment was achieved and then unloaded. After four complete load and unload cycles the accumulated error in strain at zero applied stress is less than 0.00004 m/m. In addition, the micromechanics solution predicts the yield point and hardening characteristics very well.

Further comparisons involving elastic-plastic results from the present formulation as compared to results from other micromechanics
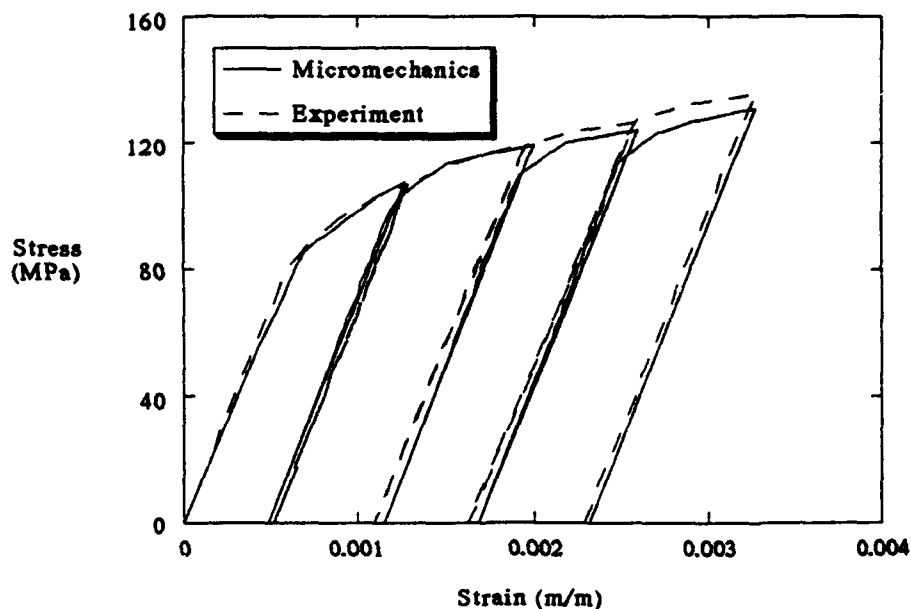
Figure 27. 90° Boron/Aluminum Response With Periodic Unloading (51)

models are exhibited in Figures 28-30. For example, the 0° response of SCS-6/Ti-15-3 at 650°C as calculated by the present formulation and the VISCOPLY program which incorporates the vanishing fiber diameter model (36) is displayed in Figure 28. The constituent elastic properties used were the same as listed in reference 36, but since the plastic capability of VISCOPLY utilizes a power law relation to define the plastic strain curve as opposed to the classical bilinear method, an appropriate yield stress of 150 MPa for the matrix was chosen to model the plastic behavior (53). Also, for this calculation the matrix strain hardening parameter was assumed to be zero. Excellent agreement between the two analysis methods is demonstrated for the 0° layup.

Figures 29 and 30 present results for a graphite/aluminum unidirectional composite layup undergoing a cooling and reheating cycle. The
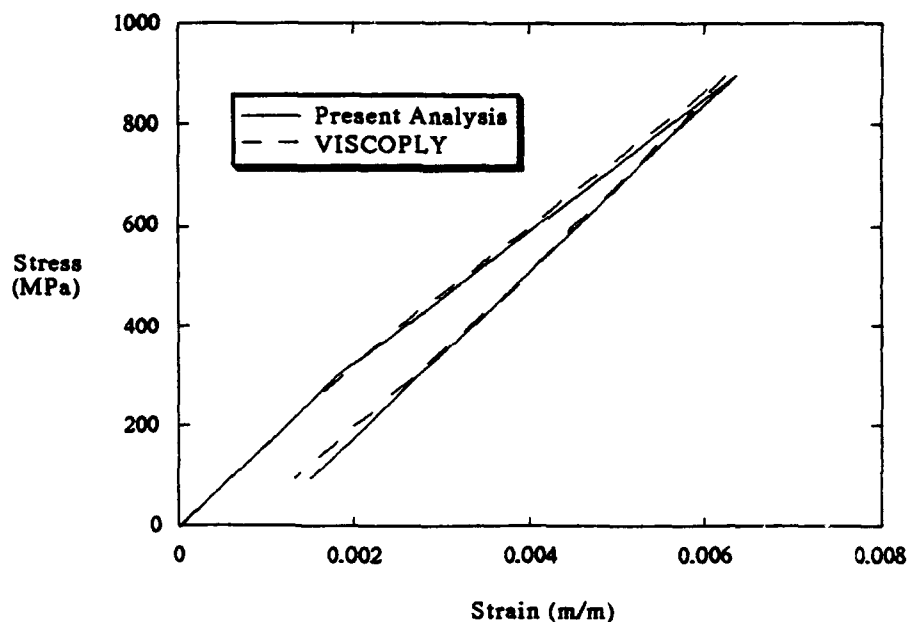
Figure 28. 0° SCS6/Ti-15-3 Predicted Response as Calculated by the Present Formulation and VISCOPLY (36)
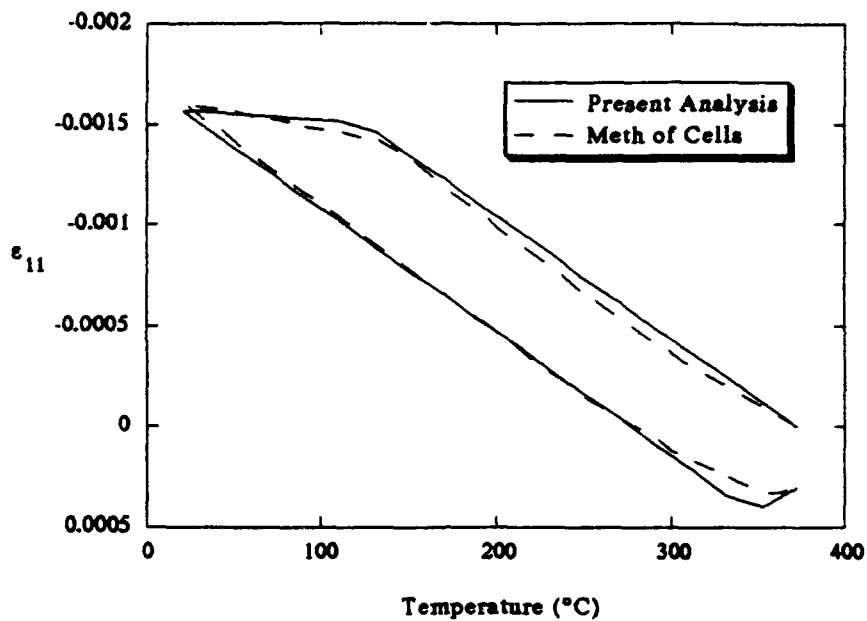
Figure 29. Longitudinal Strain for Graphite/Aluminum due to Thermal
Load (42)
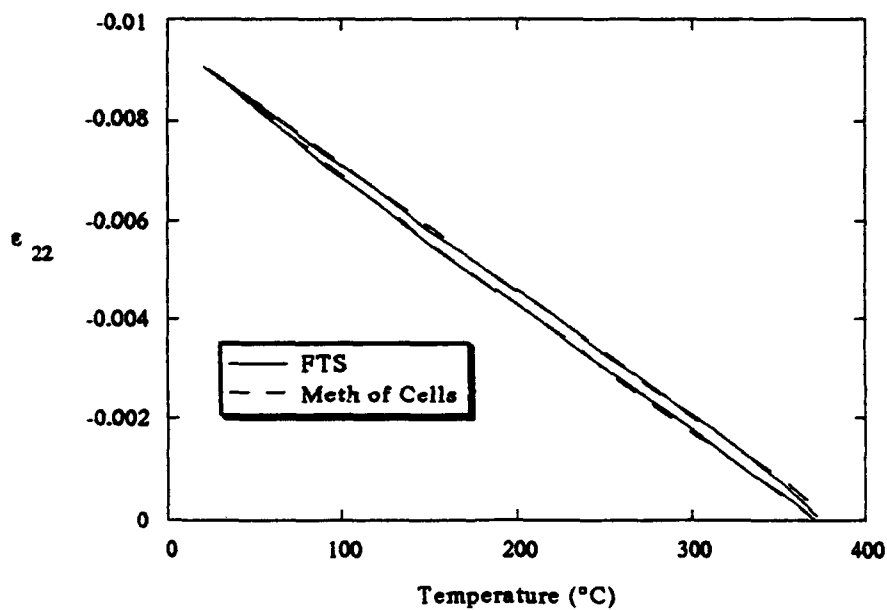
Figure 30. Transverse Strain for Graphite/Aluminum due to Thermal
Load (42)

present analysis is compared to Aboudi's method of cells, and the same constituent properties as employed in reference 42 are used. The temperature cycle consisted of cooldown to room temperature at 21°C from the stress free processing temperature of 371.1°C followed by reheating to the processing temperature. The longitudinal composite strain history, ε_{11}, is depicted in Figure 29, and the transverse composite strain history, ε_{22}, is displayed in Figure 30. The method of cells incorporates the unified theory of Bodner and Partom to model material nonlinearity, while the formulation presented in this chapter employs the classical elastic-plastic technique. In spite of this as well as the differing assumptions of the two models, the maximum difference in strain between the two models at any given point throughout the loading sequence is only 0.00008 m/m.

The capability for continuously varying the type of hardening from isotropic to kinematic was included in the micromechanics formulation developed in this chapter. An example depicting this effect of varying the hardening is shown in Figure 31. The constituent properties and temperature preload was the same as for Figures 24-27. A single ±124 MPa loading cycle for a 90° lamina was performed for the three cases: isotropic hardening, combined hardening (50% takes place isotropically and 50% kinematically), and pure kinematic hardening. The type of hardening is shown to have a pronounced effect on the response. Even the initial load to +124 MPa displays a different yield stress for all three cases. This is due to the fact that yielding occurs during cooldown from the processing temperature thereby causing the yield surface to expand in the isotropic hardening mode or its origin to shift in the kine-
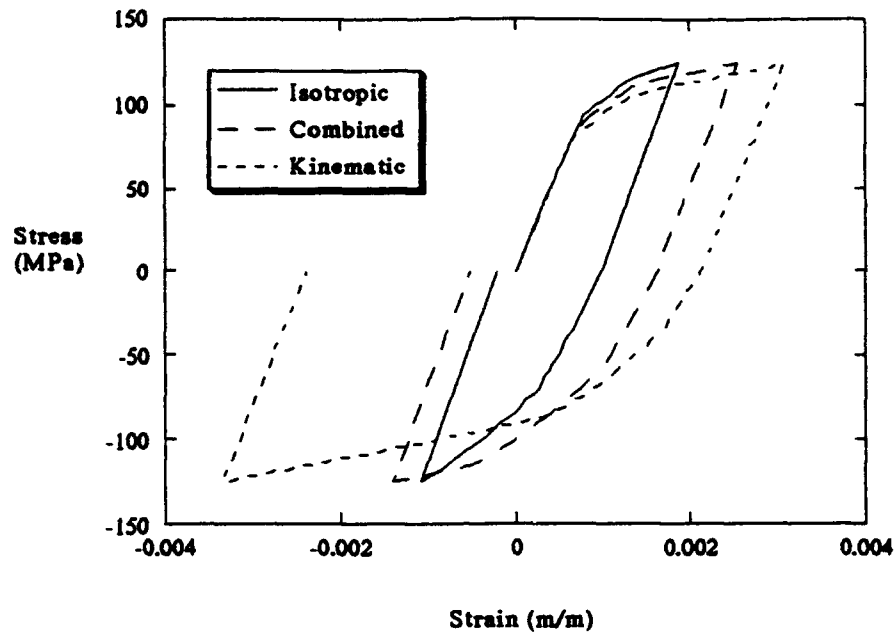
Figure 31. Boron/Aluminum 90° Lamina Predicted Response Under a
±124 MPa Load Assuming Isotropic, Kinematic, and Com-
bined Hardening

matic hardening mode. Likewise, the negative loading demonstrates the

effect of hardening where the negative strain at -124 MPa is almost

equal to the positive strain that was calculated at +124 MPa for the kine-

matic case. On the other hand, if there is isotropic hardening, then the

strain at minimum load (-124 MPa) is of a lower magnitude than that ex-

perienced at maximum positive load. Figure 32 provides further insight

in this direction where a 90° lamina under equivalent loading as in Fig-

ure 31 is subjected to a total of four cycles. For this case the matrix ma-

terial was assumed to possess a 95% kinematic hardening behavior.

Complete kinematic hardening would result in all cycles retracing the
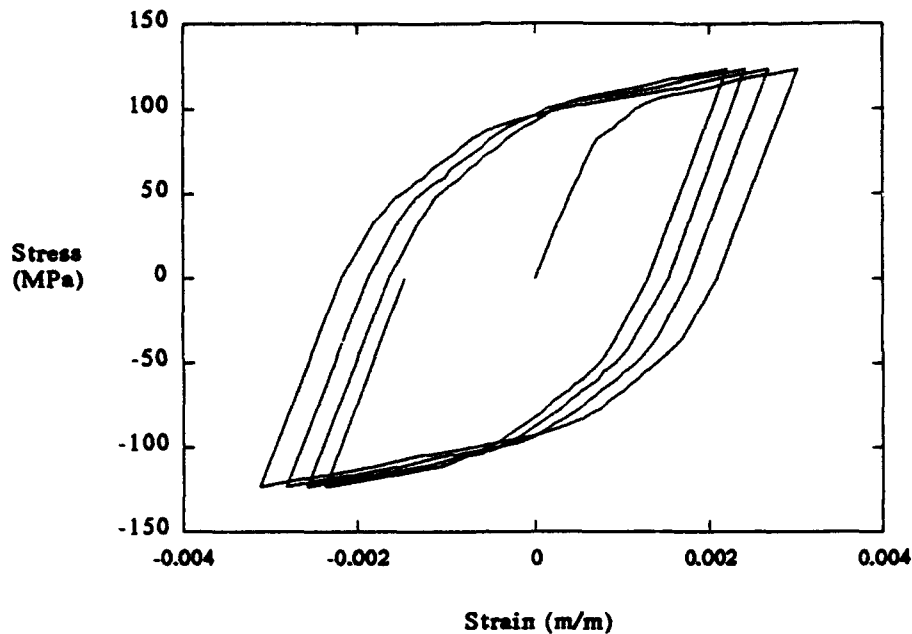
Figure 32. Boron/Aluminum 90° Lamina Predicted Cyclic Response (4 Cycles Displayed) for ±124 MPa Load Assuming 95% Kinematic Hardening

original curve, but with 5% of the hardening considered to be isotropic each subsequent cycle displays less of a difference between the maximum and minimum strains. Analytical results such as this when compared to experimental data could be used to characterize the composite's matrix hardening behavior.

As a final comparison for the elastic-plastic results, a weak fiber/matrix bond micromechanics model is used to calculate the 90° stress-strain response of SCS-6/Ti-6-4 at room temperature. Figure 33 exhibits this calculation along with a three-dimensional finite element solution and experimental result (20). The constituent properties are

77
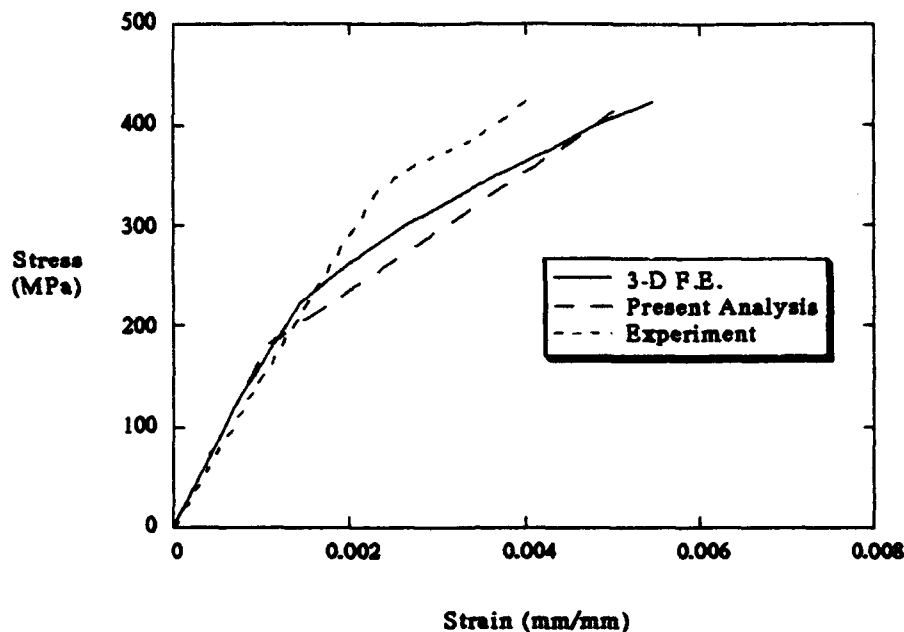
Figure 33. 90° Response of SCS6/Ti-6-4 Assuming Weak Interfacial Bond (20)

listed in reference 20 where a zero stress processing temperature of 900°C is used. Both numerical methods under-predict the experimental fiber/matrix separation point. Hence, there are additional mechanisms acting in the actual specimen that cannot be modeled with a weak bond alone. Also, it is worthy of note that although the finite element solution experienced some yielding from the onset of fiber/matrix separation and beyond, the micromechanics formulation did not experience matrix yield until 430 MPa which is just beyond the curve shown. This is expected since the stress is averaged over a greater area in the model, and hence yielding is delayed until a larger portion of the matrix has reached the yield stress.

78

In this chapter, several comparisons have been made with other micromechanics models, finite element solutions and experiment, and for the nonlinear cases the matrix material was modeled as elastic-plastic in terms of a yield stress and strain hardening parameter. This provides the capability to perform calculations on many composites since such properties are easily obtained from a simple uniaxial loading test as opposed to using power law relations where the necessary constants may be difficult to obtain. Additionally, the model possesses the capability to continuously vary the type of hardening from an isotropic to a kinematic type. Also, a weak fiber/matrix bond may be modeled by incorporating an equivalent interfacial compliance which provides the flexibility to model partial debonding as the compliance of the interface may be varied. The results from this model demonstrate excellent accuracy such as in determining elastic constants and the nonlinear behavior of 0° and 90° lamina.

Other micromechanics models that were discussed in chapter 2 such as the vanishing fiber diameter model incorporated into the VISCOPLY computer program and the multi-cell model used in the METCAN computer program represent one-dimensional formulations of the micromechanics equations (1). The present model provides additional capabilities when fiber/matrix interaction in the transverse direction (90° from the fiber) is important by incorporating the full three-dimensional equilibrium, continuity, and stress-strain relations for the representative volume element. Its simplicity allows the inclusion of various nonlinear effects such as the incorporation of time dependent plastic behavior in the form of the unified theory of Bodner and Partom, or the incorporation of

damage progression by modeling a failure of the fiber/matrix bond, and all this is accomplished while maintaining the ability to employ the micromechanics formulation into a laminate analysis. The remaining chapters will discuss these topics and present the results of their inclusion into the micromechanics formulation.

V. Viscoplastic Behavior

Development of reliable models for predicting the thermomechanical time-dependent characteristics of high temperature composites has received significant attention in the literature. This is mainly due to increased interest in high temperature composite applications for improved performance of air and spacecraft components where the loading may be highly cyclic. Several of these studies involve numerical models which incorporate the finite element or finite difference methods for solving the equilibrium and continuity relations. For instance, Mueller and Kolle used a general finite element approach to determine thermoelastic properties (54), and Coker, Ashbaugh, and Nicholas analyzed thermoelastic-plastic behavior with a finite difference technique (55). Other researchers have utilized the finite element method to analyze the effects of fiber/matrix debonding (56). Still others have employed the finite element method coupled with unified constitutive theory to model time-dependent behavior (57).

The main drawback in using the finite element method is its computational intensity. Further, modeling nonlinear temperature, time, and load dependent materials may require extensive iteration steps or computational effort to achieve convergence thereby limiting the number and type of solutions that may be obtained. Hence, more general models that are less problem specific and require fewer calculations than the finite element method are desired.

This chapter presents the details and results of the present microme-chanical analysis as applied to time-dependent inelastic problems (47, 48). To analyze time-dependent behavior the unified viscoplastic theory of Bodner has been incorporated into the micromechanics model (58). Several variations on the original Bodner viscoplastic material model have been proposed so that the theory could incorporate temperature and hardening effects more readily (59-61). The following sections will briefly describe some of these models and will detail how they were in-corporated into the micromechanics formulation.

5.1 Unified Viscoplastic Theory

Classical inelastic analysis separates the total strain into elastic, thermal, plastic, and creep strains where each component is determined from its own constituent elastic relation or flow rule. In contrast, viscoplasticity combines the plastic and creep strains into a single unified inelastic strain. Therefore, the total strain rate may be written as

$$\dot{\varepsilon}_{ij}^{TOT} = \dot{\varepsilon}_{ij}^{E} + \dot{\varepsilon}_{ij}^{TH} + \dot{\varepsilon}_{ij}^{I} \qquad (97)$$

where $\dot{\varepsilon}_{ij}$ represents a tensorial strain rate and the superscripts TOT, E, TH, and I denote the total, elastic, thermal, and inelastic components.

The inelastic strain rate term obeys a single flow rule designed to account for both plasticity and creep. Various flow rules and state vari-able evolution equations have been proposed for the unified theory, and

three such material models have been chosen for this study. All three are based on the original flow rule developed by Bodner and Partom (58), and have been used previously by other researchers to analyze metal matrix composites (42, 57, 62).

5.1.1 Bodner-Partom with Isotropic Hardening

The inelastic strain rate flow rule developed by Bodner and Partom (58) may be represented by

$$\dot{\varepsilon}_{ij}^{I} = D_o \exp\left[-\frac{(n+1)}{2n} \left(\frac{Z^2}{3\,J_2} \right)^n \right] \frac{\sigma'_{ij}}{\sqrt{J_2}} \tag{98}$$

where D_o and n are inelastic material parameters, σ'_{ij} is the deviatoric stress, J_2 is the second invariant of the deviatoric stress tensor, and Z is a state variable sometimes referred to as the drag stress. It describes the state of material hardening and is controlled by the evolution equation

$$\dot{Z} = m\dot{W}_p (Z_1 - Z) / Z_o \tag{99}$$

where m, Z_0, and Z_1 are parameters which characterize the material in the inelastic regime, and $\dot{W}_p$ is the rate of inelastic work given by

$$\dot{W}_p = \sigma_{ij}\,\dot{\varepsilon}_{ij}^{I} \tag{100}$$

This unified theory model has the fewest parameters out of all three models considered in this study, and it has also been incorporated into Aboudi's micromechanics method of cells model (42). Its main drawback is that it considers only the isotropic portion of hardening, and hence will have limited usefulness in characterizing behavior in cyclic loading environments.

5.1.2 Bodner-Partom with Back Stress

The Bodner-Partom flow rule has been modified by Ramaswamy et al. to include both isotropic and kinematic hardening behavior (60). The flow rule is given by

$$\dot{\varepsilon}_{ij}^I = D_o \exp\left[-\frac{1}{2}\left(\frac{Z^2}{3K_2}\right)^n\right] \frac{\sigma'_{ij} - \Omega_{ij}}{\sqrt{3K_2}} \qquad (101)$$

where Ω_{ij} is referred to as the back stress and is a state variable that controls the kinematic hardening behavior and K_2 performs the same function as J_2 in equation (98) and is expressed by Eq (81). The back stress evolution equation is represented by

$$\dot{\Omega}_{ij} = f_3 \dot{\sigma}'_{ij} + f_1 \dot{\varepsilon}_{ij}^I - f_1 \frac{3 \Omega_{ij}}{2 \Omega_s} \sqrt{\frac{2}{3} \dot{\varepsilon}_{ij}^I \dot{\varepsilon}_{ij}^I} \qquad (102)$$

where Ω_s is the maximum value of the back stress and is allowed to relax during creep loading. This saturation of the back stress is con-

84

trolled by the relation

$$\dot{\Omega}_s = -\hat{B}\left(\frac{\sqrt{3J_2}}{\sigma_o}\right)^r \left(\Omega_s - \Omega_{crp}\right) \tag{103}$$

Also, the drag stress evolution equation is given by

$$\dot{Z} = m\dot{W}_p(Z_1 - Z) - A_1(Z - Z_2)^P \tag{104}$$

The quantities D_o, n, f_1, f_3, $\hat{B}$, σ_o, r, Ω_{crp}, m, Z_1, A_1, Z_2, and p are material constants where all but D_o are temperature dependent.

5.1.3 Bodner-Partom with Directional Hardening

The directional hardening material model developed by Stouffer and Bodner (61) allows for kinematic hardening while avoiding the necessity of including a back stress in the flow rule. The directional hardening model used in this study is similar to that used by Chan and Lindholm (59) but with the further modifications incorporated by Neu (63). The flow rule is in the same form as the original Bodner model,

$$\dot{\varepsilon}_{ij}^I = D_o \exp\left[-\frac{1}{2}\left(\frac{(Z^I + Z^D)^2}{3J_2}\right)^n\right] \frac{\sigma'_{ij}}{\sqrt{J_2}} \tag{105}$$

where the state variable, Z, has been split into two components, Z^I and Z^D, which represent the hardening due to isotropic and directional char-

85

acteristics, respectively.

The isotropic hardening evolution equation is given by

$$\dot{Z}^I = m_1 \dot{W}_p \left(Z_1 - Z^I\right) - A_1 Z_1 \left(\frac{Z^I - Z_2}{Z_1}\right)^{r_1} + \dot{T} \left[\left(\frac{Z^I - Z_2}{Z_1 - Z_2}\right)\frac{\partial Z_1}{\partial T} + \left(\frac{Z_1 - Z^I}{Z_1 - Z_2}\right)\frac{\partial Z_2}{\partial T}\right] \quad (106)$$

and the directional hardening evolution is controlled by

$$Z^D = \beta_{ij} \, u_{ij} \quad (107)$$

where the variables β_{ij} and u_{ij} are determined by the equations

$$\dot{\beta}_{ij} = m_2 \dot{W}_p \left(Z_3 u_{ij} - \beta_{ij}\right) - A_2 Z_1 \frac{\beta_{ij}}{\sqrt{\beta_{kl} \beta_{kl}}} \left(\frac{\sqrt{\beta_{kl} \beta_{kl}}}{Z_1}\right)^{r_2} + \dot{T}\frac{\beta_{ij}}{Z_3}\frac{\partial Z_3}{\partial T} \quad (108)$$

and

$$u_{ij} = \frac{\sigma_{ij}}{\sqrt{\sigma_{kl} \, \sigma_{kl}}} \quad (109)$$

The temperature rate terms in the above equations allow for improved characteristics in the solution of nonisothermal loading. The constants D_o, n, m_1, m_2, Z_1, Z_2, Z_3, A_1, A_2, r_1, and r_2 are material parameters which must be determined experimentally. Also, in all the Bodner-Partom based models, D_o is independent of temperature and assumed to be 10^4 for all the calculations in this study. All other constants are temperature dependent parameters.

5.2 Viscoplastic Algorithm

The micromechanics equations listed in chapter 3 are formulated in a load-controlled format where the solution is obtained from the applied composite stress as opposed to an applied strain. This is advantageous from the standpoint that most cyclic or fatigue experiments are performed using load-control, but it produces difficulties when solving inelastic nonlinear problems because the solution is more likely to diverge. Therefore, damping mechanisms must be built into the numerical algorithm so that convergence may be achieved more easily. The algorithm employed for the present study improves the convergence characteristics by scaling the calculated change in the effective inelastic strain rate during a single iteration by a certain computed factor. This ensures that the effective inelastic strain rate will neither increase nor decrease from one iteration to the next by more than a given predetermined amount. The maximum change for a single iteration, $\delta \dot{\varepsilon}_{max}$, is determined for each region at the beginning of a load step. It is chosen based on the elastic strain rate, $\dot{\varepsilon}_{ij}^E$, calculated by assuming the load increment is completely elastic.

$$\delta \dot{\varepsilon}_{max} = \begin{cases} \sqrt{\frac{2}{3} \dot{\varepsilon}_{ij}^E \dot{\varepsilon}_{ij}^E} & \text{for } \sqrt{\frac{2}{3} \dot{\varepsilon}_{ij}^E \dot{\varepsilon}_{ij}^E} > 1. \times 10^{-8} \frac{1}{\text{sec}} \\ 1. \times 10^{-8} \frac{1}{\text{sec}} & \text{for } \sqrt{\frac{2}{3} \dot{\varepsilon}_{ij}^E \dot{\varepsilon}_{ij}^E} \leq 1. \times 10^{-8} \frac{1}{\text{sec}} \end{cases} \qquad (110)$$

Other parameters to scale the calculations may be used, but the above value was found to provide good convergence characteristics for a wide variety of calculations. The sequence of steps employed for computing the inelastic strain of a single load-time increment applied to the micro-mechanics model are given below (47):

(1) Determine the stresses in each region at time $t = t_0 + \Delta t$ by employing the micromechanics relations and assuming the load increment behaves as a completely elastic response (i.e. set $\varepsilon_{ij}^I = {}_0\varepsilon_{ij}^I$ where ${}_0\varepsilon_{ij}^I$ is the inelastic strain at $t = t_0$).

(2) Initialize the effective inelastic strain rate for each region, ${}^0\dot{\varepsilon}_{eff}^I$, and the iteration counter, p, to begin the iteration.

$$ {}^0\dot{\varepsilon}_{eff}^I = 0 \quad \text{and} \quad p = 1 \tag{111} $$

Iterate

(3) From the stresses that have just been calculated and the chosen unified viscoplastic theory material model calculate the inelastic strain rate, $\dot{\varepsilon}_{ij}^I$, for each region.

(4) Determine the calculated effective inelastic strain rate for each region by

$$ {}_{cal}\dot{\varepsilon}_{eff}^I = \sqrt{\frac{2}{3} \dot{\varepsilon}_{ij}^I \dot{\varepsilon}_{ij}^I} \tag{112} $$

(5) Determine the change in the effective inelastic strain rate, $\delta \dot{\varepsilon}_{eff}^I$,

88

for each region between the calculated value from step 4 and the value used in the previous iteration.

$$\delta \dot{\varepsilon}_{eff}^{I} = {}_{cal}\dot{\varepsilon}_{eff}^{I} - {}^{p-1}\dot{\varepsilon}_{eff}^{I} \tag{113}$$

(6) Calculate the scaling ratio, R, for each region by

$$R = \begin{cases} \dfrac{-\delta \dot{\varepsilon}_{eff}^{I}}{\delta \dot{\varepsilon}_{eff}^{I} - k \delta \dot{\varepsilon}_{max}} & \text{for } \delta \dot{\varepsilon}_{eff}^{I} < 0 \\[3mm] \dfrac{\delta \dot{\varepsilon}_{eff}^{I}}{\delta \dot{\varepsilon}_{eff}^{I} + k \delta \dot{\varepsilon}_{max}} & \text{for } \delta \dot{\varepsilon}_{eff}^{I} \geq 0 \end{cases} \tag{114}$$

where k is a user supplied constant (usually between 2 and 30) that controls the convergence stability. A larger value of k results in slower but more stable convergence.

(7) Set the effective inelastic strain rate of each region for the present iteration, p, by adding the scaled parameter.

$$^{p}\dot{\varepsilon}_{eff}^{I} = {}^{p-1}\dot{\varepsilon}_{eff}^{I} + R \, \delta \dot{\varepsilon}_{max} \tag{115}$$

(8) Calculate the inelastic strain rate for each region by

89

$$\dot{\varepsilon}_{ij}^{I} = \frac{3}{2} \, ^{p}\dot{\varepsilon}_{eff}^{I} \frac{\left(\sigma_{ij}' - \Omega_{ij}\right)}{\sqrt{3\,K_2}} \tag{116}$$

where for material models that do not contain a back stress it is recognized that $\Omega_{ij} = 0$

(9) Determine the inelastic strain for each region that exists at the end of the load-time increment.

$$\varepsilon_{ij}^{I} = \, _{o}\varepsilon_{ij}^{I} + \dot{\varepsilon}_{ij}^{I} \, \Delta t \tag{117}$$

(10) Determine the region stresses at the end of the load-time increment by employing the micromechanics relations and the inelastic strains calculated from step 9.

(11) Check for convergence by comparing the norm of the region stresses calculated before and after the iteration or by some other equivalent method. If convergence has not been achieved, then $p = p+1$ and repeat steps 3 through 11.

The above algorithm was found to be quite versatile for handling various loading conditions and for easily incorporating the three types of Bodner-Partom material models previously outlined. *All solutions were obtained on an Apple Macintosh IIx desktop computer.*

5.3 Viscoplastic Results

Representative results were obtained using each of the three material
models discussed above (47, 48). These results were compared with the
corresponding numerical solutions obtained by other methods such as
Aboudi's model and finite element solutions (42, 62). Also, solutions of
thermomechanical fatigue cyclic loading employing the material model
with directional hardening were analyzed and compared with available
experimental data (64, 65). The temperature dependent characteristics
of the material properties were incorporated, and the residual stresses
inherent in the composite after processing were accounted for by either
matching the processing temperature and cooldown procedures used by
other researchers in their calculations or estimating these conditions.
The fiber materials are assumed to be thermoelastic while the matrix ma-
terials are modeled with the unified viscoplastic theory.

5.3.1 Comparisons with Other Numerical Solutions

The original isotropic hardening Bodner-Partom material model has
been incorporated into the micromechanics method of cells developed by
Aboudi (42). Results from the Aboudi model and the present formula-
tion incorporating the Bodner-Partom isotropic hardening material
model for Boron/Aluminum are presented in Figures 34 and 35. The
material constants for a unidirectional composite consisting of a 6061-
T0 aluminum matrix with a 50% volume reinforcement of boron fibers
were employed (42). The transverse normal response of the composite is
presented in Figure 34, and the in-plane shear response is depicted in

Figure 35. Perfect bonding at the fiber/matrix contact was considered in the calculations of the present model, and the corresponding solutions plotted for Aboudi's model also assumed perfect bonding. The two micromechanics solutions are within 10% of each other for these calculations with the present model predicting a slightly stronger material response. This is consistent with the assumptions of the two models as the present model assumes the normal and shear stresses decouple, and therefore, any normal applied stress on the composite will not produce any shear stresses which might contribute to the deviatoric stress tensor. Such a model will likely produce a stiffer response in the inelastic regime than models which account for such coupling effects because the deviatoric stress tensor controls much of the behavior in this realm.
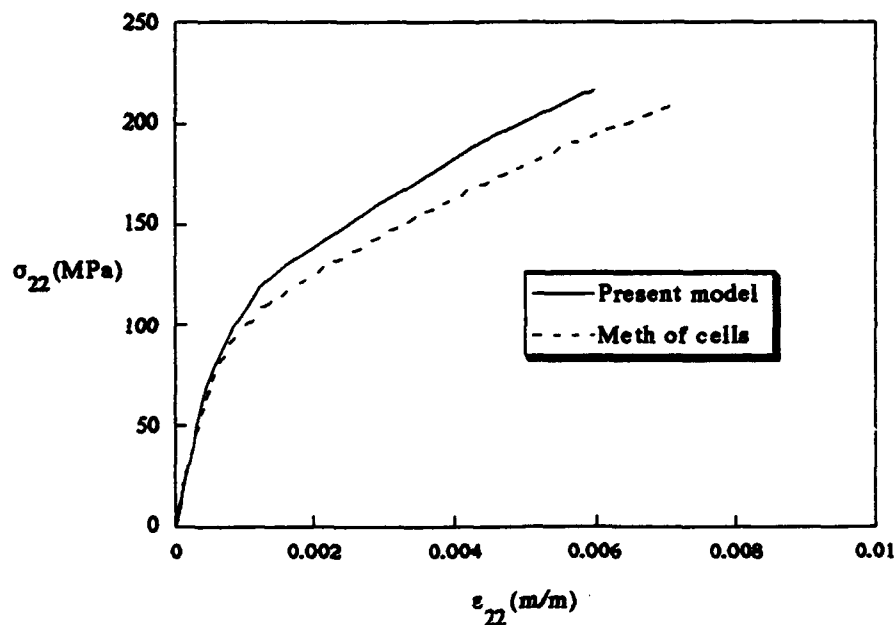
Figure 34. Unidirectional Boron/Aluminum Under Transverse Normal Loading as Calculated by the Present Model and the Method of Cells (42)

92
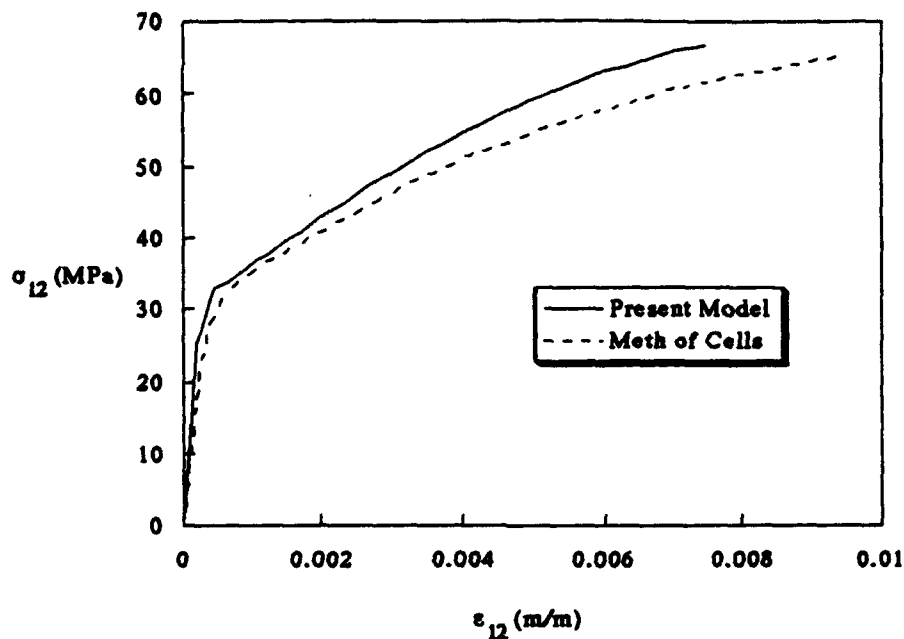
Figure 35. Unidirectional Boron/Aluminum In-Plane Shear Response as Calculated by the Present Model and the Method of Cells (42)

Also, the method of cells model assumes that continuity is satisfied on an average basis between subcells. Hence, overlap and gaps may occur between adjacent subcells while the average continuity condition remains satisfied. This would likely result in a weaker response than a model that maintains continuity all along the interface between adjacent regions.

A further comparison with Aboudi's method of cells is presented in Figure 36 where a graphite/aluminum unidirectional composite is considered. The material constants for 2024-T4 aluminum alloy and T-50 graphite fibers as employed by Aboudi were incorporated in the

calculations involving the present model with a 30% fiber volume rein-
forcement (42). The stress free state or processing temperature of the
composite is taken to be 371°C. This initial state is cooled to 21°C and
subsequently reheated to 371°C while maintaining a zero applied
composite stress. This is equivalent to the calculation presented in Fig-
ure 29, but here, the unified viscoplastic theory of Bodner (as was used
in Aboudi's calculations) is employed as opposed to the classical elas-
tic-plastic formulation. When the temperature reaches 150°C during the
cooldown phase, the calculations indicate that the microstresses are suf-
ficient to produce yielding in the matrix. Both methods are in agree-
ment on this as well as the on the remainder of the strain-temperature
profile.
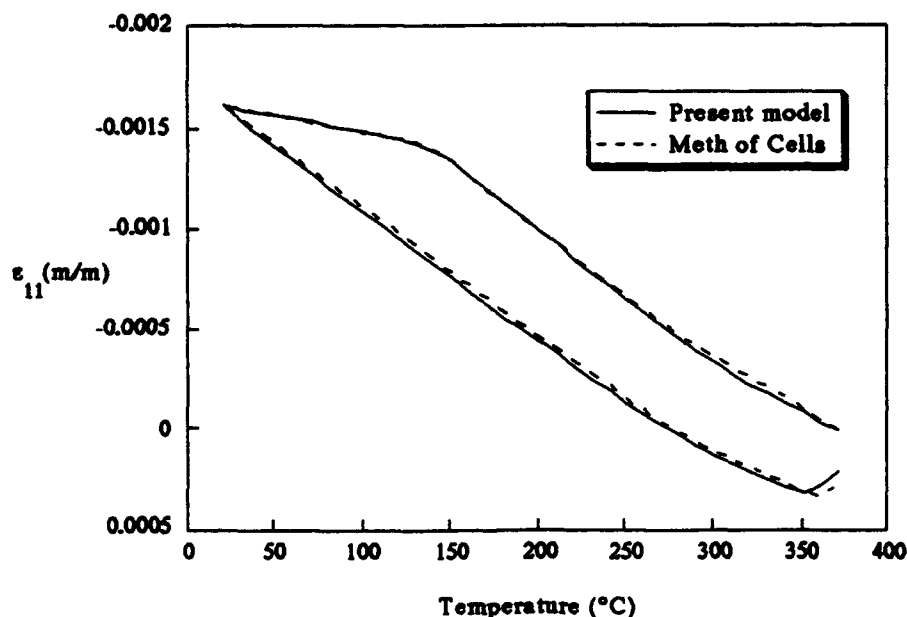
Figure 36. Longitudinal Strain History of Graphite/Aluminum Under
Thermal Load (Cooldown and Reheat) (42)

94

Three dimensional finite element solutions incorporating the unified theory with back stress have been performed by Sherwood and Quimby (66). The finite element program ADINA was modified to utilize the unified theory with back stress material model, and a unit fiber/matrix cell or RVE was analyzed to predict composite behavior. Comparisons between the micromechanics model of the present study and finite element solutions from Sherwood and Quimby are presented in Figures 37 and 38. The composite system analyzed consisted of a titanium based alloy, Ti-β21S, matrix material embedded with a 35% volume fraction of silicon carbide, SCS6, fibers. Constituent micros-tresses were assumed to be zero at a processing or cure temperature of 815°C, and calculations involving both a perfect fiber/matrix bond and
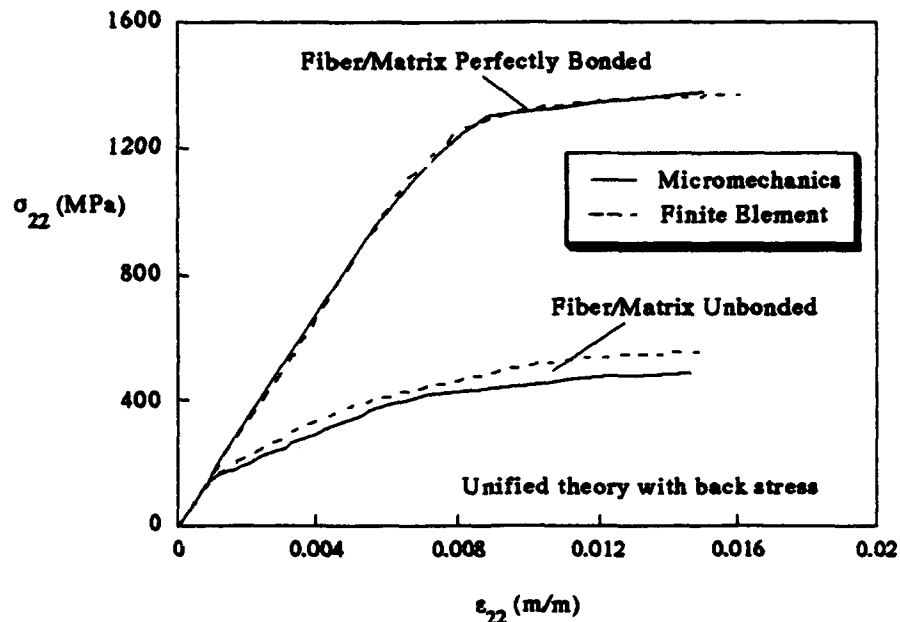
Figure 37. Predicted Transverse Normal Response of SCS6/Ti-β21S at 23°C Employing Bodner-Partom with Back Stress (66)
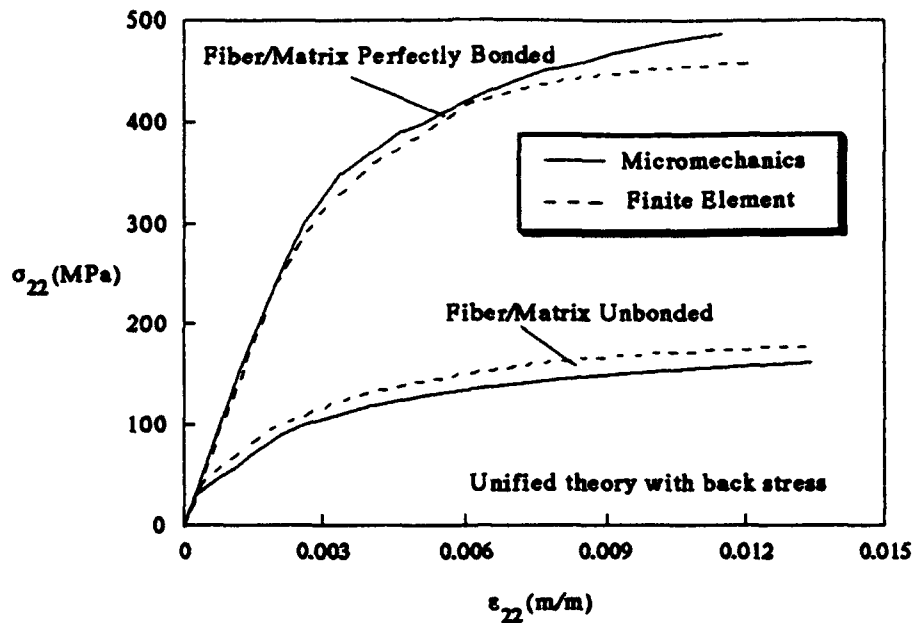
Figure 38. Predicted Transverse Normal Response of SCS6/Ti-β21S at 600°C Employing Bodner-Partom with Back Stress (66)

an unbonded fiber/matrix contact were performed. The nonlinear material model employed in the micromechanics solution was the unified theory with back stress material model earlier discussed which corresponded to that used in the finite element solutions.

The transverse normal stress-strain response at 23°C is depicted in Figure 37. As it is expected, the unbonded fiber/matrix interface demonstrates a considerably weaker response than a perfectly bonded interface for this type of loading. Residual thermal stresses due to cool down from the processing temperature prevent fiber/matrix separation from occurring until the applied stress reaches approximately 150 MPa. Once these residual stresses are overcome, the composite stiffness is

greatly reduced due to debonding. Yielding of the matrix begins to occur shortly thereafter at an applied composite stress of approximately 400 MPa. The perfectly bonded solution indicates that substantial matrix yielding does not occur until the applied stress reaches approximately 1300 MPa. Similar characteristics are observed in calculations where the mechanical load is applied at 600°C as in Figure 38. The lower yield stress of the matrix due to the elevated temperature produces a response that is considerably weaker than that at room temperature. Elevated temperatures also decrease the residual stresses which result in fiber/matrix separation occurring in the unbonded calculations at approximately 40 MPa. All these characteristics are captured equally well by both the micromechanics analysis and the finite element results displaying a very good agreement between the two. No greater than a 10% difference in stress is observed between the two methods at any point.

Further comparisons of the present formulation were done with finite element solutions incorporating the unified theory material model with the directional hardening. Kroupa and Neu have incorporated the directional hardening material model into ADINA and performed thermomechanical fatigue analysis by employing a unit cell or RVE approach (62). The constituent properties used in the calculations are listed in reference 63, but since extensive experimental comparisons will be made with this composite, the properties are also listed here for completeness. The constituent properties for the Ti-β21S matrix material are listed in Table 6, and the SCS6 fiber properties are presented in Table 7. A comparison between the present micromechanics model and finite element calcula-

tions of the Kroupa and Neu study using the properties of Tables 6 and 7 is presented in Figure 39. This plot parallels the calculations involving the back stress material model in Figures 37 and 38. A unidirectional SCS6/Ti-β21S composite consisting of a 35% fiber volume fraction with both an unbonded and a perfectly bonded fiber/matrix interface is considered and loaded perpendicular to the axis of the fiber. The processing temperature at which the microstresses were assumed to be zero was chosen to be 900°C, and during the cool down phase a heat treatment cycle was simulated where the composite was held at 621°C for

Table 6. Material Constants Used for the Ti-β21S Matrix Material (Viscoplastic Model: Bodner-Partom with Directional Hardening) (63)

Temp °C	E GPa	α (x10^{-6}) 1/°C	n	Z_2 MPa	Z_3 MPa	m_2 1/MPa	$A_1 = A_2$ 1/sec
23.	112.0	6.31	4.80	1550.	100.	0.35	0.00
260.	108.0	7.26	3.50	1300.	300.	0.35	0.00
315.	106.1	7.48	3.05	1251.	390.	1.50	0.00
365.	104.1	7.68	2.65	1205.	500.	2.55	0.00
415.	101.7	7.88	2.24	1160.	660.	3.60	.001
465.	99.1	8.09	1.84	1115.	960.	4.64	.005
482.	98.1	8.15	1.70	1100.	1100.	5.00	.008
500.	97.0	8.23	1.50	1089.	1300.	5.76	.012
525.	95.5	8.33	1.28	1074.	1670.	6.82	.020
550.	93.9	8.43	1.10	1060.	2100.	7.88	.034
575.	92.2	8.53	0.97	1045.	2600.	8.94	.056
600.	90.4	8.63	0.82	1030.	3700.	10.0	.089
650.	86.6	8.83	0.74	1000.	3800.	10.0	0.21
760.	77.2	9.27	0.58	600.	4000.	15.0	1.00
815.	72.0	9.49	0.55	300.	4100.	30.0	2.00

$$v = 0.36 \qquad D_0 = 10^4 \text{ sec}^{-1} \qquad m_1 = 0.0 \text{ MPa}^{-1}$$

$$r_1 = 3.0 \qquad r_2 = 3.0 \qquad Z_1 = 1300 \text{ MPa}$$

$$T_{ref} = 23°C$$

Table 7. Thermoelastic Properties of the Silicon Carbide (SCS-6)
Fiber ($v = 0.25$, $T_{ref} = 23°C$)

Temp (°C)	E (GPa)	α (x10^{-6} °C^{-1})
21.	393.	3.53
93.	390.	3.57
204.	386.	3.58
316.	382.	3.61
427.	378.	3.67
538.	374.	3.74
649.	370.	3.81
760.	365.	3.89
871.	361.	3.97
1093.	354.	4.10

eight hours before cool down to 25°C. Similar characteristics as previously observed in Figures 37 and 38 are present in the directional hardening material model calculations of Figure 39. Again, a very good agreement is observed here also between the present simplified micromechanics analysis and the computationally intensive finite element calculations.

Thermomechanical fatigue calculations were performed on the same composite material system. After the same cooldown procedures (as outlined in the previous paragraph) were simulated, the temperature and longitudinal stress parallel to the fiber axis were simultaneously increased to 150°C and 100 MPa, respectively. At this point the temperature and stress were cycled in-phase with a triangular waveform between temperatures of 150-650°C and longitudinal applied composite stresses of 100-1000 MPa. The time history of the average longitudinal matrix stress and strain during the first seven cycles as calculated by the present micromechanics model and the finite element solution of Kroupa
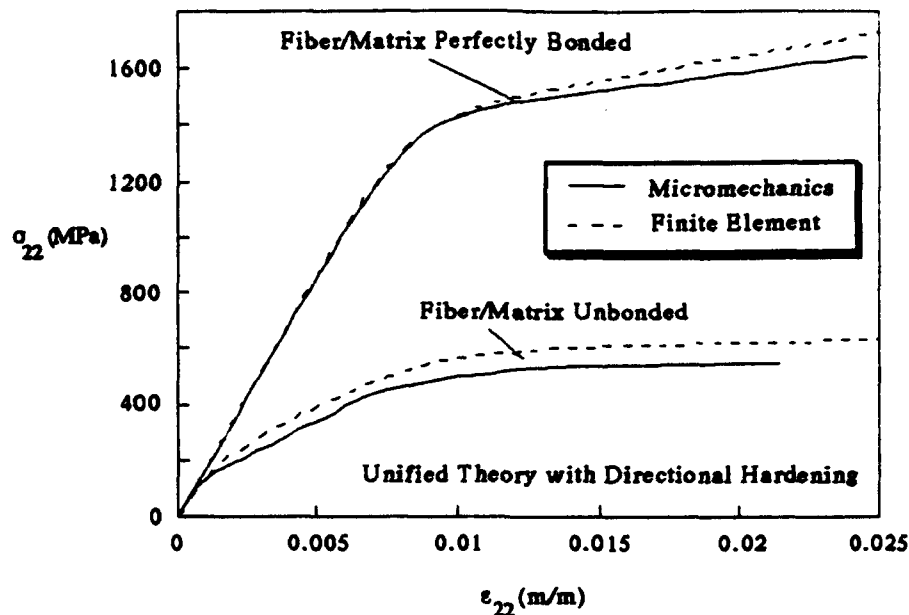
Figure 39. Predicted Transverse Normal Response of SCS6/Ti-β21S at 25°C Employing Bodner-Partom with Directional Hardening (62)

and Neu is displayed in Figure 40 where the zero strain reference point was taken to be 25°C (62). The two solutions are in excellent agreement and indicate that significant plastic deformation occurs during the first cycle while subsequent cycles demonstrate some plasticity as there is a gradual drift of increasing strain and a relaxation of the stress.

Simulations of an out-of-phase thermomechanical fatigue load is presented in Figure 41. The preload sequence for the out-of-phase case was similar to that for the in-phase loading except once the temperature and stress reached 150°C and 100 MPa, the stress was held constant while the temperature was increased to 650°C. The temperature and stress were then cycled out-of-phase between 150-650°C and 100-

100
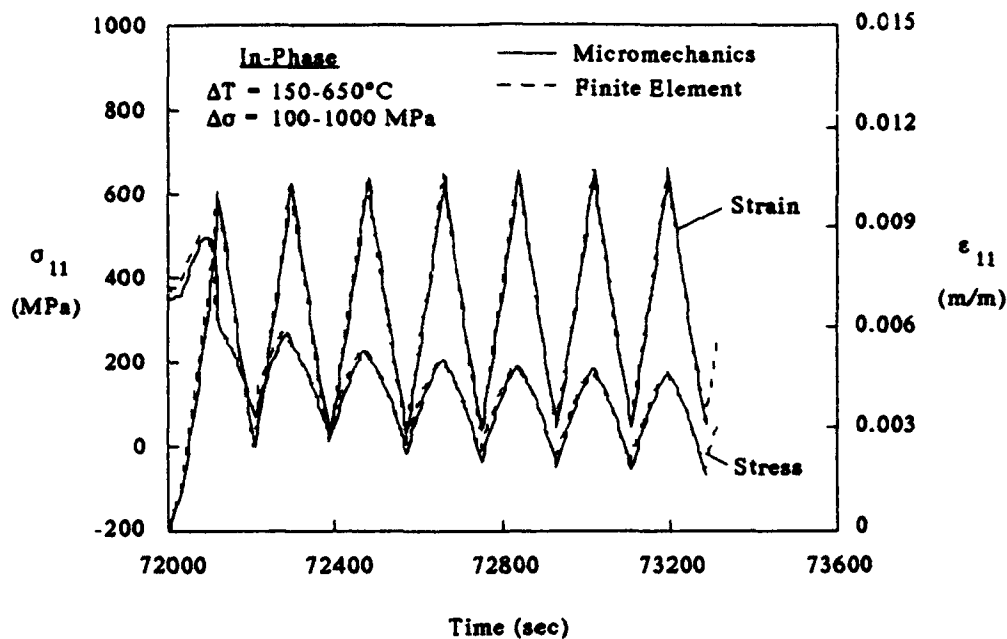
Figure 40. Time History of SCS6/Ti-β21S Average Matrix Stress and Total Strain Under Longitudinal In-Phase Thermomechanical Fatigue Loading (62)

1000 MPa. Once again both analysis methods are in excellent agreement. However, unlike the in-phase simulation, little or no plastic deformation was observed during the cycling.

5.3.2 Comparisons with Experiment

Validating the micromechanics model with other numerical solutions provided the means to determine if the calculations of the present micromechanics analysis and viscoplastic algorithm were performed correctly. This was accomplished in the previous section. Further validation with experimental data provides understanding into how well a micromechanics solution can actually predict a composite's behavior.

101
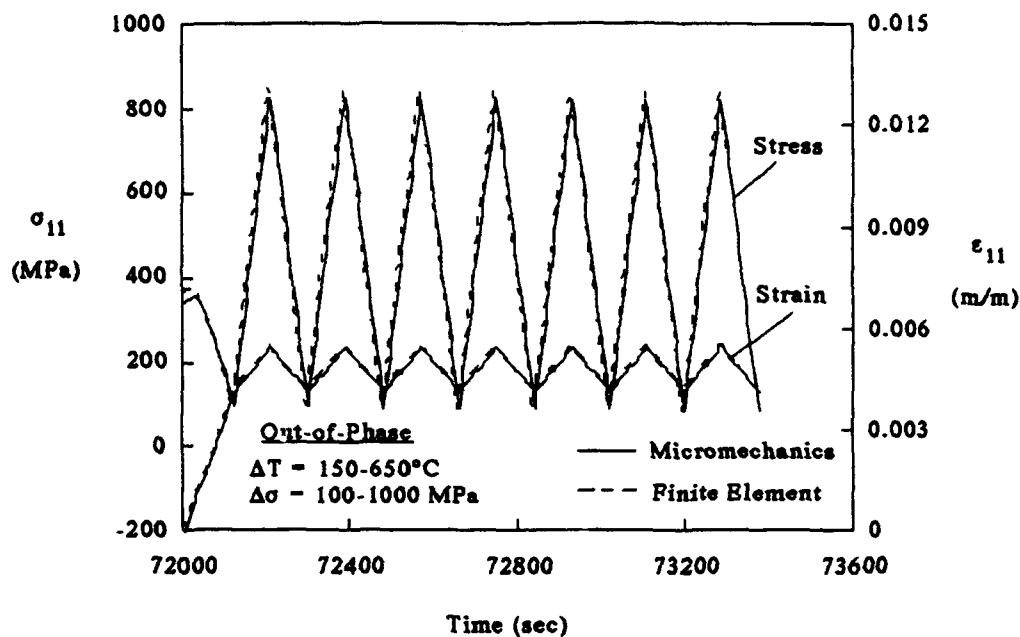
Figure 41. Time History of SCS6/Ti-β21S Average Matrix Stress and Total Strain Under Longitudinal Out-of-Phase Thermomechanical Fatigue Loading (62)

The SCS6/Ti-β21S composite system has been experimentally characterized (65). Therefore, the micromechanics model of the present study and the unified theory material model with directional hardening were employed together to compare with the experimental data obtained from other researchers (65, 67).

Figures 42 through 44 display 0° lamina tensile response at three temperatures. The micromechanics model assumed the microstresses were zero at 900°C, and then the model was cooled to room temperature at 25°C followed by reheating to the desired temperature. The fiber volume fraction of the tensile specimens were measured at 34.3% and matched in the micromechanics solutions. The tensile response is domi-

nated throughout by the fiber, but matrix nonlinearity is detectable in the composite response at high strains.

Not all physical mechanisms acting in the composite are accounted for in a micromechanics approach, such as fiber and matrix cracking. Also, the correct bond strength between fiber and matrix is usually unknown. Therefore, under conditions when such mechanisms are present any comparison between the micromechanics and experiment must be viewed with them in mind. In addition, there is experimental scatter which must also be considered. In spite of these differences, the present analysis is in good agreement with its counterpart from experiment as shown in Figures 42 through 44. Further insight into these differences is given in Figure 45 where the 90° response or the stress-strain re-
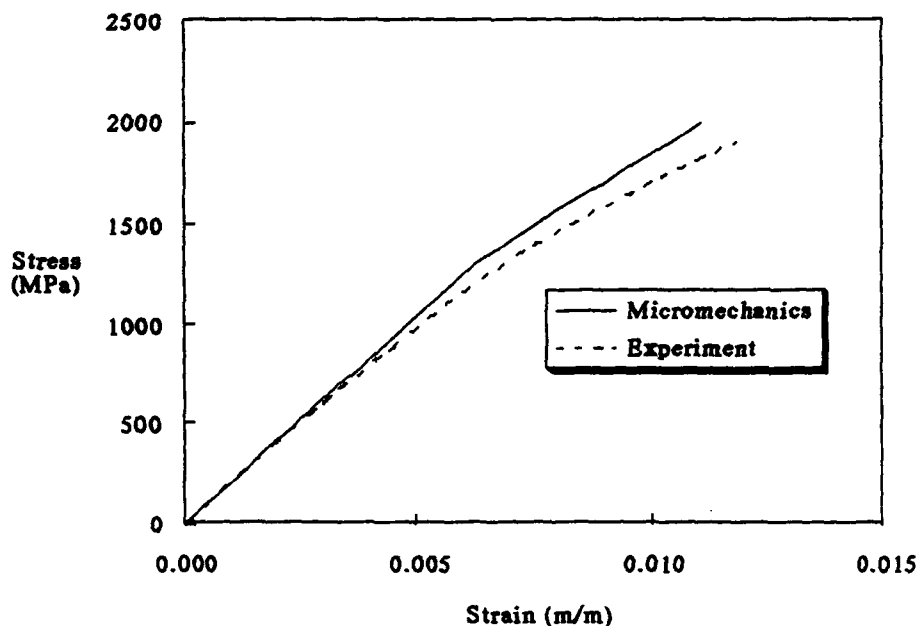
Figure 42. 0° SCS6/Ti-β21S Tensile Response at Room Temperature (25°C) (67)
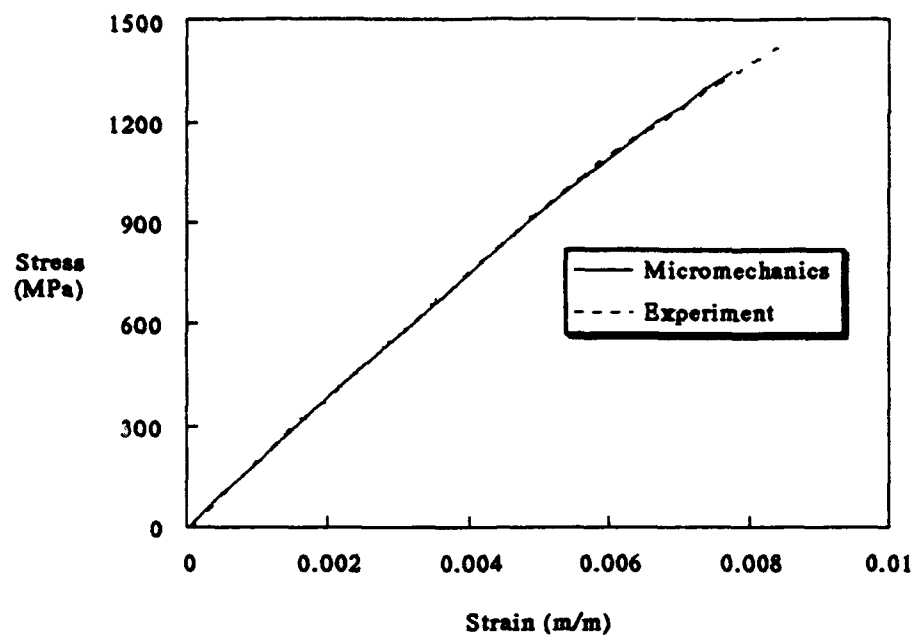
Figure 43.   0° SCS6/Ti-β21S Tensile Response at 500°C (67)
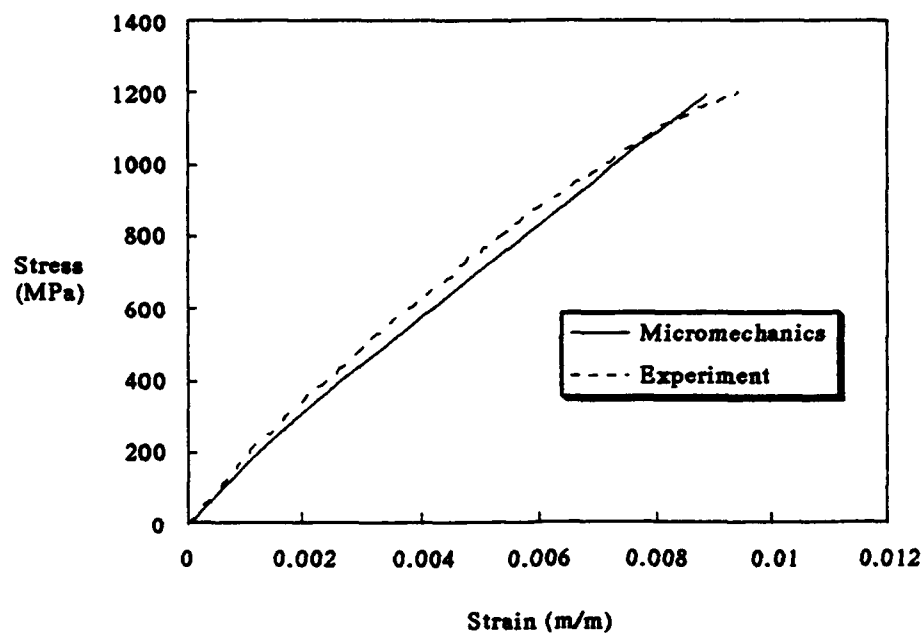
Figure 44.   0° SCS6/Ti-β21S Tensile Response at 650°C (67)
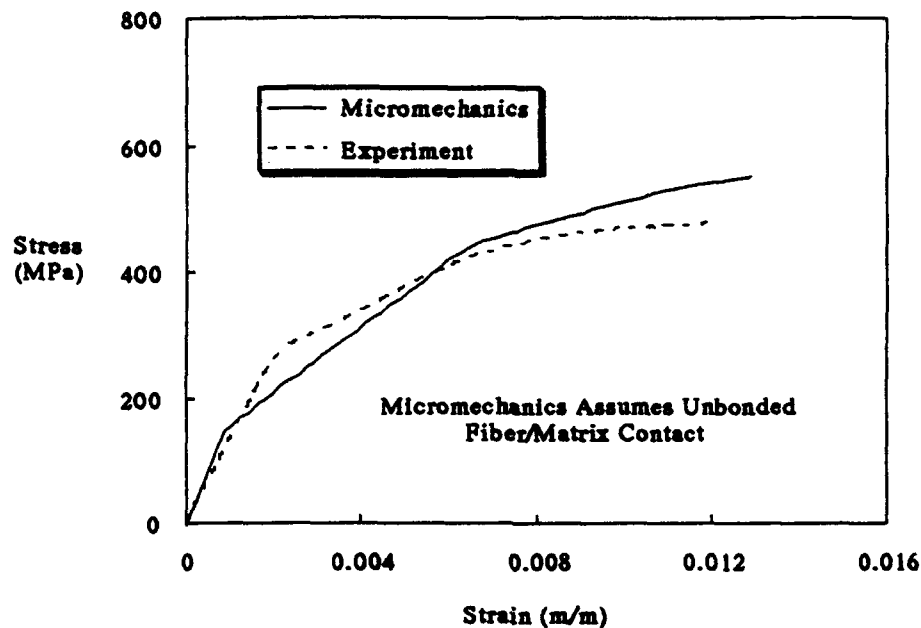
Figure 45. 90° SCS6/Ti-β21S at Room Temperature (25°C) (67)

sponse perpendicular to the fiber axis is depicted for the composite. The
micromechanics solution assumed an unbonded fiber/matrix interface,
and fiber/matrix separation occurs at about 150 MPa at which point the
first knee in the stress-strain response is observed. This is where the
applied load has overcome the residual stresses due to processing. The
experimentally observed point of initial nonlinearity does not occur until
approximately 280 MPa which indicates that the fiber/matrix bonds
throughout the composite possess a finite strength, and therefore, the
initial point of nonlinearity is delayed until these bonds begin to fail due
to the applied load. It should also be noted that finite element calcula-
tions of an unbonded fiber/matrix interface produce a fiber/matrix sepa-

105

ration point similar to that found from the micromechanics results (see Figures 37 through 39). Therefore, the difference between the fiber/matrix separation point as calculated by the micromechanics model and as observed in experiment is most likely due to a finite bond strength in the actual composite material rather than improper calculations of an unbonded interfacial contact in the micromechanics model. These features of interfacial debonding will be discussed at length in chapter 6.

In addition to the SCS6/Ti-β21S composite system, calculations performed in this study were compared with published experimental data of SCS6/Ti-15-3 composite (64, 68, 69, 70). The matrix material, Ti-15V-3Cr-3Al-3Sn alloy, undergoes a phase transformation at elevated temperature from the as received β-phase to the more stable α-phase which is accompanied by improved strength characteristics (71). However, due to the lack of experimental data characterizing the matrix material at all temperature ranges, the present study used thermoelastic and viscoplastic properties determined from studies involving both the as-received and heat treated material (29, 56, 69). Therefore, only a single set of constants were used in the analysis whether the comparison involved a heat treated specimen or not. The material properties developed from the experimental data for the matrix are presented in Table 8, and the properties for the silicon carbide fiber which is assumed to be thermoelastic are the same as were listed in Table 7. A plot of the matrix material response using the unified theory with directional hardening viscoplastic material model and the constants of Table 8 is presented in Figure 46 for a strain rate of 0.001/sec. The material characteristics exhibited in Figure 46 compare well with the previously published re-

sults (29, 56, 69). However, further improvement could be attained if two sets of constants were available depending on whether the application involved the heat treated material or not. This is not possible at the present time due to the lack of experimental data at all temperature regimes.

The stress-strain response for a 0° layup of this composite at both room and elevated temperature is depicted in Figures 47 and 48, respectively, where the composite was unloaded at approximately 75% of its ultimate strength at each temperature (69). Excellent agreement with the experiment is noted at these conditions. The nonlinear characteristics as observed in experiments are captured very well by the micromechanics approach, and an excellent agreement between predicted and experimental values of the permanent plastic strain upon unloading is ob-

Table 8. Material Constants Used for the Ti-15-3 Matrix Material (Viscoplastic Model: Bodner-Partom with Directional Hardening)

Temp °C	E GPa	$\alpha \, (\times 10^{-6})$ 1/°C	n	Z_2 MPa	Z_3 MPa	m_2 1/MPa	$A_1 = A_2$ 1/sec
25.	86.3	8.48	3.00	1200.	200.	3.0	0.00
315.	80.4	9.16	2.30	1070.	454.	4.9	0.06
482.	72.2	9.71	1.90	1000.	600.	6.0	0.10
538.	67.8	9.89	1.10	850.	1500.	8.0	0.30
566.	64.4	9.98	1.00	800.	2300.	10.0	0.50
649.	53.0	10.26	0.80	600.	3000.	20.0	2.00
900.	25.0	10.50	0.55	150.	5000.	50.0	3.00

$v = 0.36$ $D_0 = 10^4 \, \text{sec}^{-1}$ $m_1 = 0.0 \, \text{MPa}^{-1}$

$r_1 = 3.0$ $r_2 = 3.0$ $Z_1 = 1300 \, \text{MPa}$

$T_{ref} = 23°C$
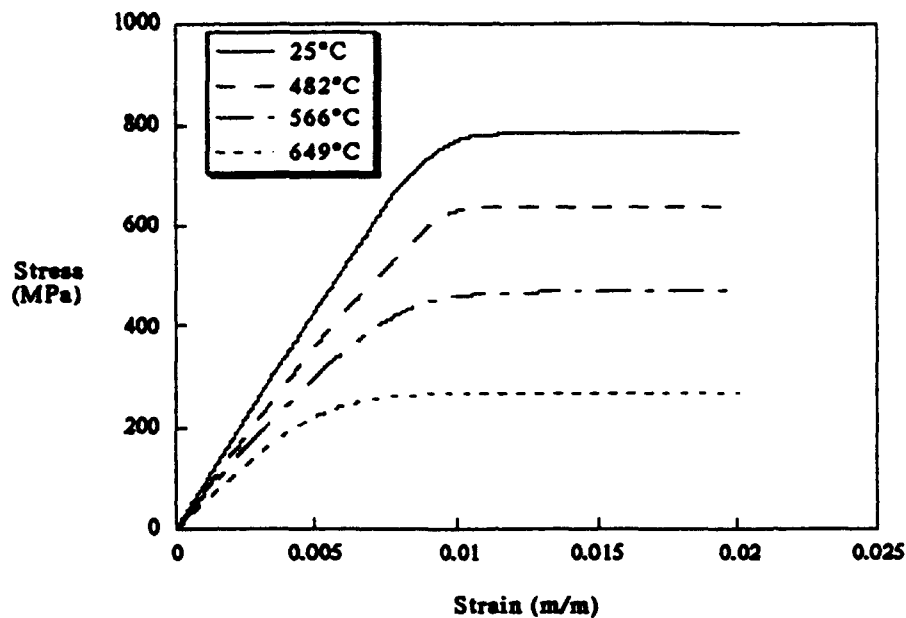
Figure 46. Ti-15-3 Alloy Matrix Material Response Using the Constants of Table 8 and a Strain Rate of 0.001/sec

tained. A further comparison of the effects of tension loading on a 0° layup is presented in Figures 49 and 50 where the longitudinal and transverse strains are plotted. The point in these curves where the slopes begin to increase is indicative of an increase in the Poisson's ratio which implies that plasticity has become prevalent (68). For the room temperature case, this occurs at a longitudinal strain of approximately 0.0055 m/m, and for the elevated temperature case, at a longitudinal strain of approximately 0.0035 m/m. Therefore, good predictions of both the onset of plasticity and the subsequent behavior were obtained by the micromechanics solution.
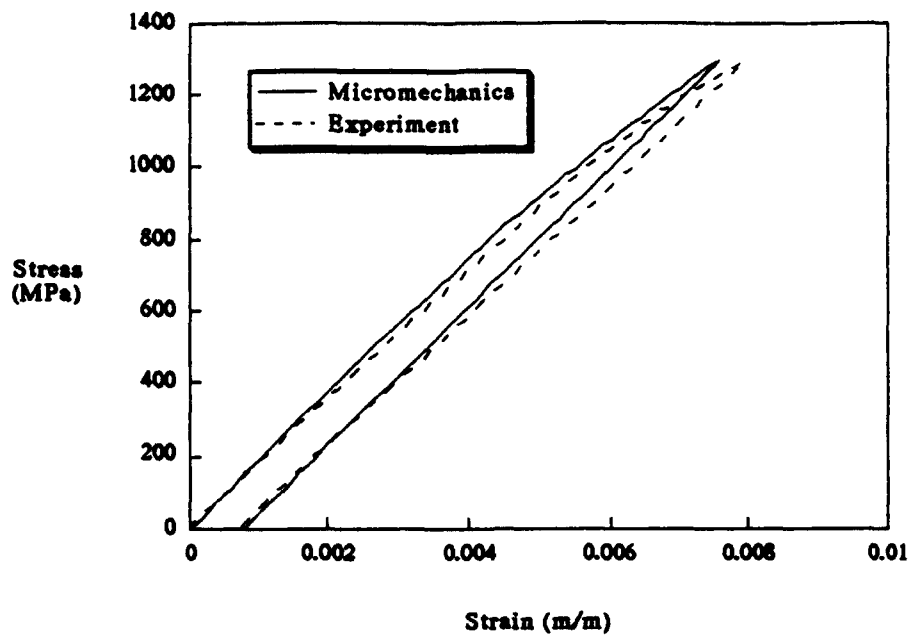
Figure 47   0° SCS6/Ti-15-3 Composite Layup at Room Temperature (69)
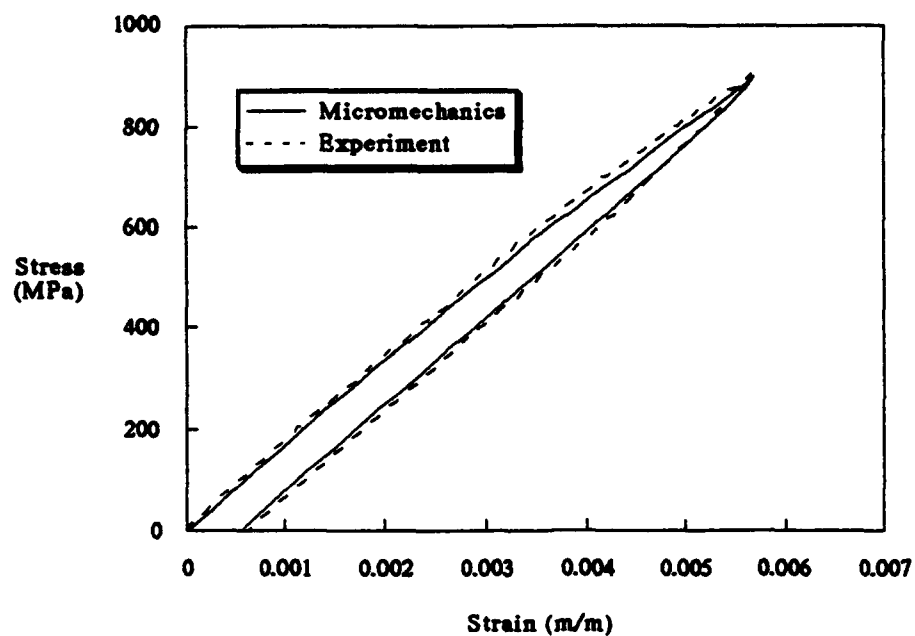
Figure 48   0° SCS6/Ti-15-3 Composite Layup at 538°C (69)
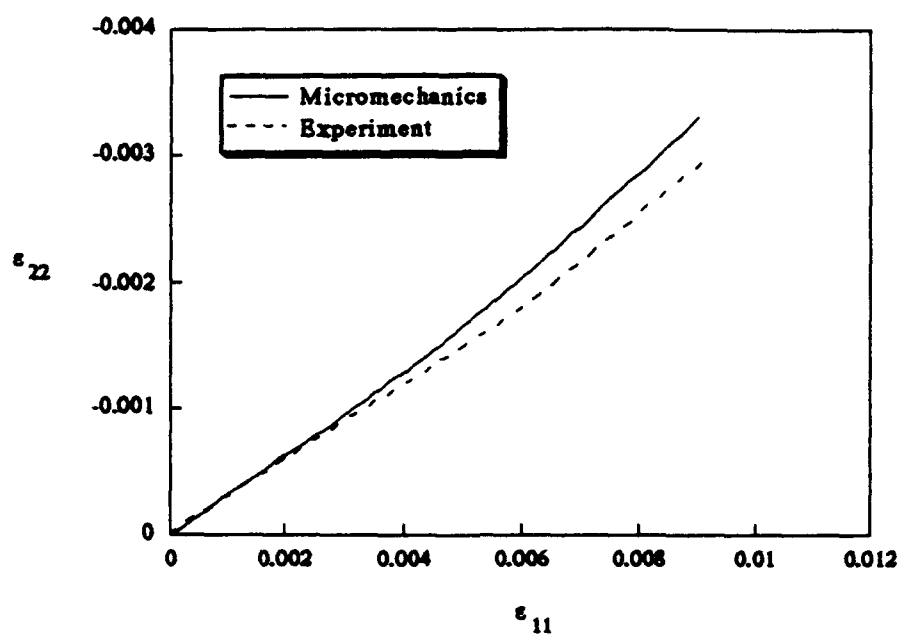
Figure 49. Transverse vs. Longitudinal Strain for 0° SCS6/Ti-15-3
Composite Layup at Room Temperature (68)
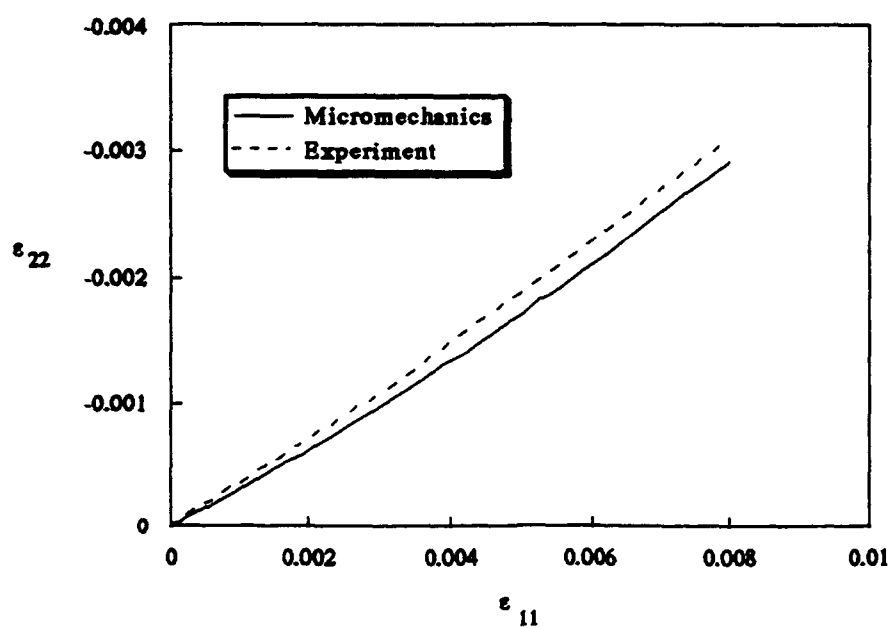
Figure 50. Transverse vs. Longitudinal Strain for 0° SCS6/Ti-15-3
Composite Layup at 538°C (69)

110

The stress-strain response under a 90° or transverse load condition at room and elevated temperature is displayed in Figures 51 and 52, respectively. As it was discussed previously for the SCS6/Ti-β21S system where the behavior under this type of load is dominated by the matrix and the fiber/matrix interface, the same applies for SCS6/Ti-15-3. Both compressive and tensile behavior are depicted in these figures, and there is a marked difference between their responses. This is due to the weak fiber/matrix bond strength of this composite. In tension, the fiber and matrix separate once the compressive residual thermal stress and interfacial bond strength are overcome. Therefore, the tensile response will demonstrate nonlinearity at a much lower level of applied stress. To account for this in the micromechanics, an unbonded interface was assumed where once the residual compressive stress at the interface was overcome, separation would occur. This method does not account for any interfacial bond strength, and as such, only the effects of residual stress were considered. The composite was assumed to be stress free at a processing temperature of 900°C for all the calculations involving the Ti-15-3 matrix material. Therefore, the room temperature tensile response exhibits nonlinearity at a higher stress level than the elevated temperature case due to the larger compressive interfacial stress. Also, the micromechanics exhibit nonlinearity at a lower stress level than the experiment. This is expected since the effect of a finite interfacial bond strength is not accounted for in the micromechanics solution, but this contingency will be discussed in the following chapter.

A compressive load is not effected by the weak interface, and therefore, the nonlinearity is a result of matrix plasticity. As shown in Fig-
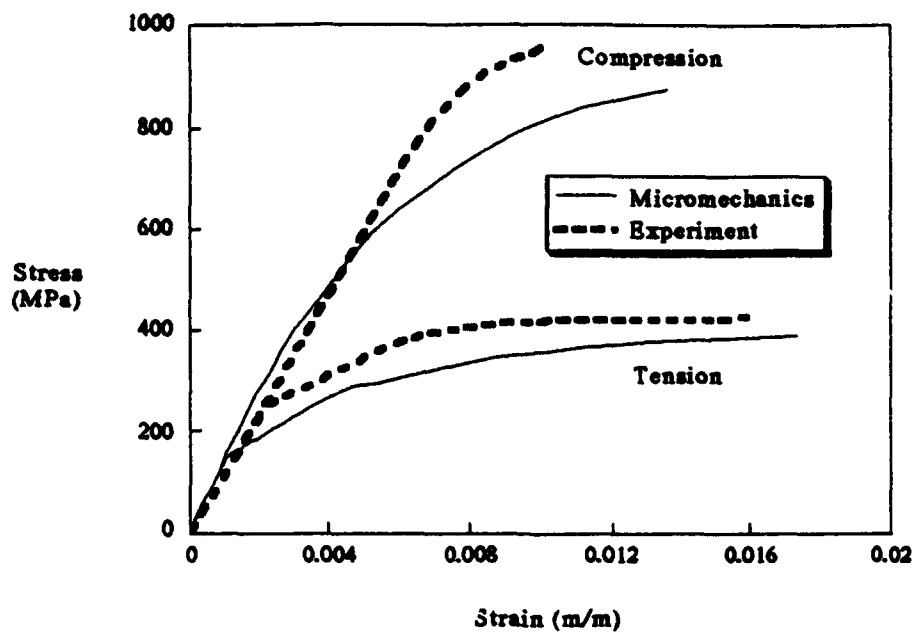
Figure 51. 90°SCS6/Ti-15-3 Composite Layup at Room Temp-
erature (70)
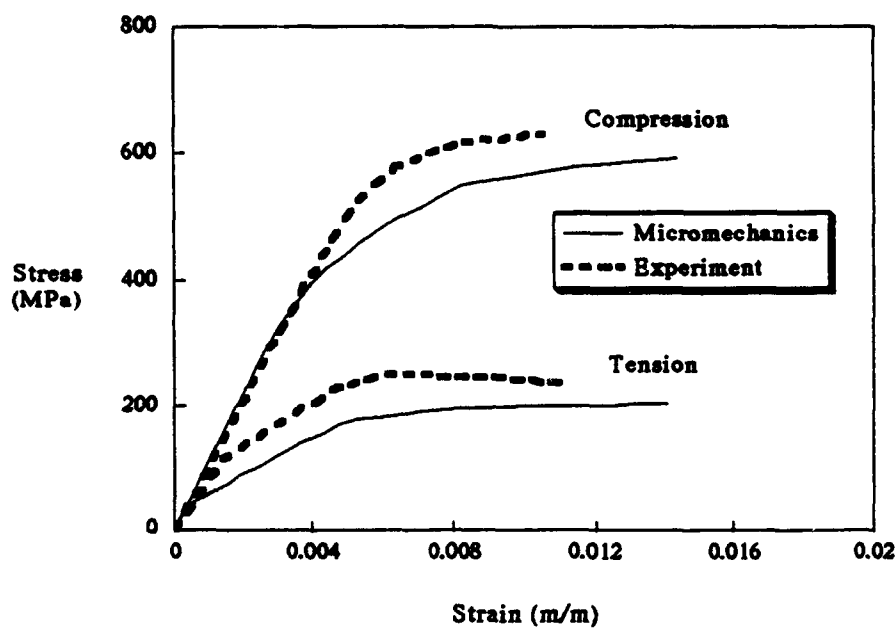
Figure 52. 90°SCS6/Ti-15-3 Composite Layup at 538°C (70)

112

ures 51 and 52, the micromechanics solution underpredicts the stress level at which plasticity becomes prevalent in compression. However, the matrix material constants employed in the unified theory (Table 8) were determined from the available tensile test data of the matrix. Also, most materials possess a yield stress in compression that is greater than their yield stress in tension, so it is not surprising that the micromechanics results display a lower compressive yield stress than the experiment. This clearly indicates that there is a need to characterize experimentally the matrix material in compression for accurate prediction of an MMC's response under compressive loading.

Figure 53 presents the longitudinal and transverse strains for a 90° laminate loaded in tension at room temperature. The decrease in slope indicates a decrease in the Poisson's ratio which verifies that the nonlinearity in the tensile response of Figure 51 is due to fiber/matrix separation as opposed to matrix plasticity which was observed in the 0° laminate (Figure 49). If the composite's response were dominated by matrix plasticity, then an increase in the Poisson's ratio would be observed. Also, the micromechanics solution was able to predict this behavior, and since the only two mechanisms for nonlinearity in the micromechanics solution were matrix plasticity and fiber/matrix debonding, then it is most likely that the behavior observed in experiment was due to fiber/matrix debonding.

Most high temperature applications involve thermomechanical fatigue or nonisothermal loading, and therefore, it is desirable for analytical methods to be able to encompass such loadings. Hence, the present micromechanics formulation was employed to predict the ther-
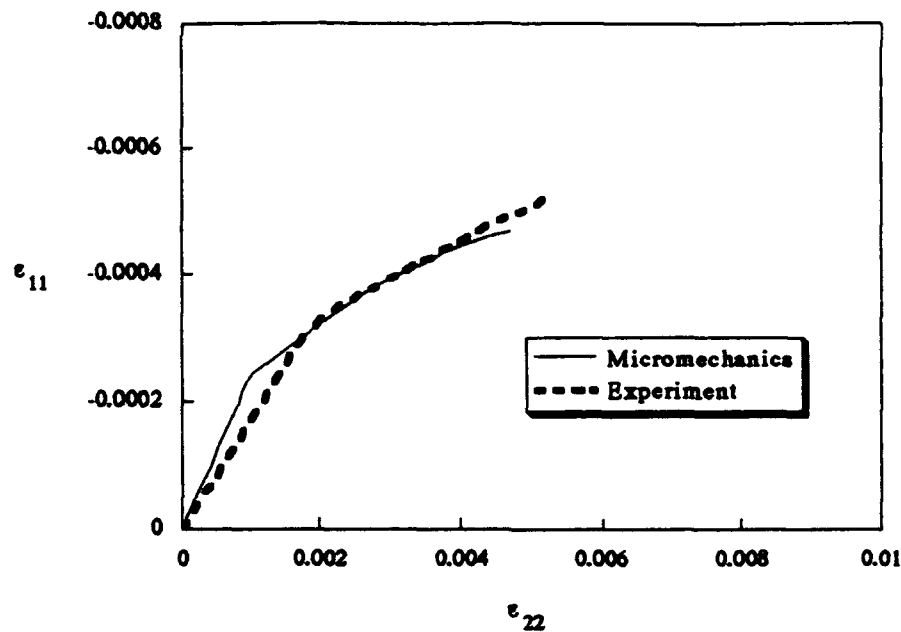
Figure 53. Longitudinal vs. Transverse Strain for SCS6/Ti-15-3 Loaded
90° to the Fiber at Room Temperature (68)

momechanical fatigue response of the titanium based MMCs discussed in this chapter.

For instance, comparisons with the experimental results of Castelli et al. (64) for unidirectional SCS6/Ti-15-3 are presented in Figure 54. Loading consisted of increasing the temperature and mechanical applied load simultaneously from 93°C to 538°C and from 44.8 MPa to 896 MPa in-phase followed by decreasing them in the same way using a sinusoidal waveform with a period of 180 seconds. A plot of the maximum and minimum total strains for the first 100 cycles is presented, and the micromechanics solution captures the overall behavior very well, but slightly overpredicts the maximum strain for the first few cycles by ap-

114
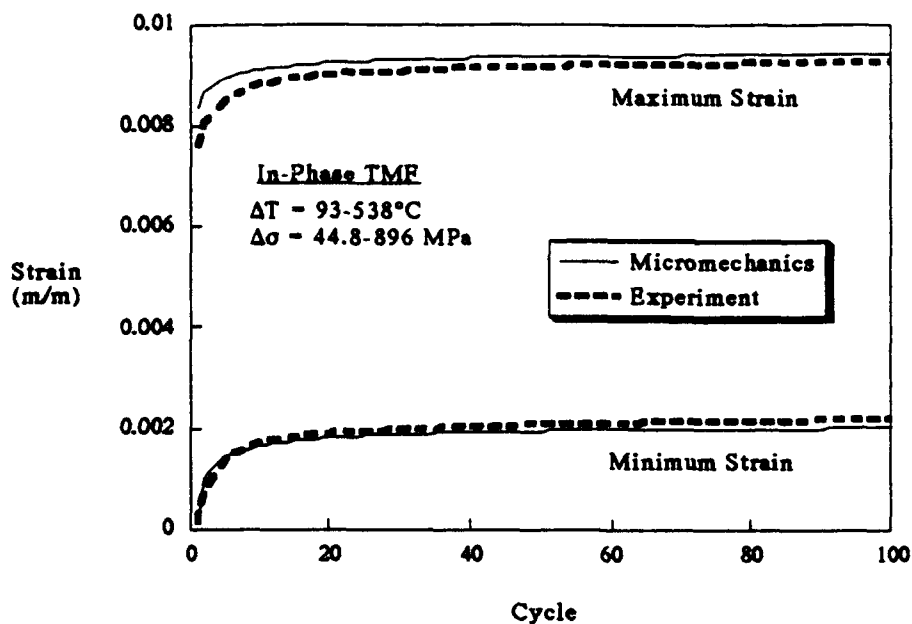
Figure 54. 0° SCS6/Ti-15-3 Max/Min Strain History for In-Phase Ther-
momechanical Fatigue (64)

proximately 10%. This can most likely be attributed to a change in the
mechanical properties due to a phase transformation after a specimen
has undergone heat treatment (71). For instance, in the temperature
range considered, the mechanical properties of the matrix used in the
micromechanics solution were determined for the most part from tests
involving no heat treatment. However, the specimen depicted in the ex-
perimental results underwent a heat treatment of 650°C for one hour
(64), and therefore experienced a change in the matrix mechanical prop-
erties.

A unidirectional 0° SCS6/Ti-β21S composite layup is considered
next. Extensive experimental results were available for this composite

115

(67), and the material constants for the Bodner-Partom with directional hardening model have been well validated (63). Both in-phase and out-of-phase thermomechanical fatigue loads were applied, but only the mechanical strains (i.e. excluding the thermal part) are depicted so that a better understanding of the mechanical response may be obtained. The calculations matched the experimental specimens' measured fiber volume fraction, and just as in the previous calculations, the temperature dependent properties of both the fiber and matrix are considered. Residual stresses were accounted for by assuming a 900°C cure temperature. The temperature was cycled between 150°C and 650°C for all calculations and maximum applied loads of 800 MPa and 1100 MPa were examined. Each temperature-load-time cycle consisted of a triangular applied thermomechanical waveform over a 180 second time interval.

The in-phase thermomechanical fatigue behavior during the first and tenth cycles for a maximum applied load of 1100 MPa is displayed in Figure 55. The calculations capture the permanent or creep strain extremely well and provide an accurate representation of the overall behavior. A slightly higher prediction of the modulus over that observed in the experiment (approximately 10%) is obtained. This is not surprising since at the peak stress of 1100 MPa the composite is close to its failure strength for that temperature of approximately 1250 MPa. Therefore, a significant amount of damage in the form of fiber breakage would be expected over the first few cycles which is not accounted for in the present micromechanics analysis (65).

The out-of-phase behavior at the 1100 MPa maximum load is depicted in Figure 56. The accumulated permanent strain after ten cycles is

116
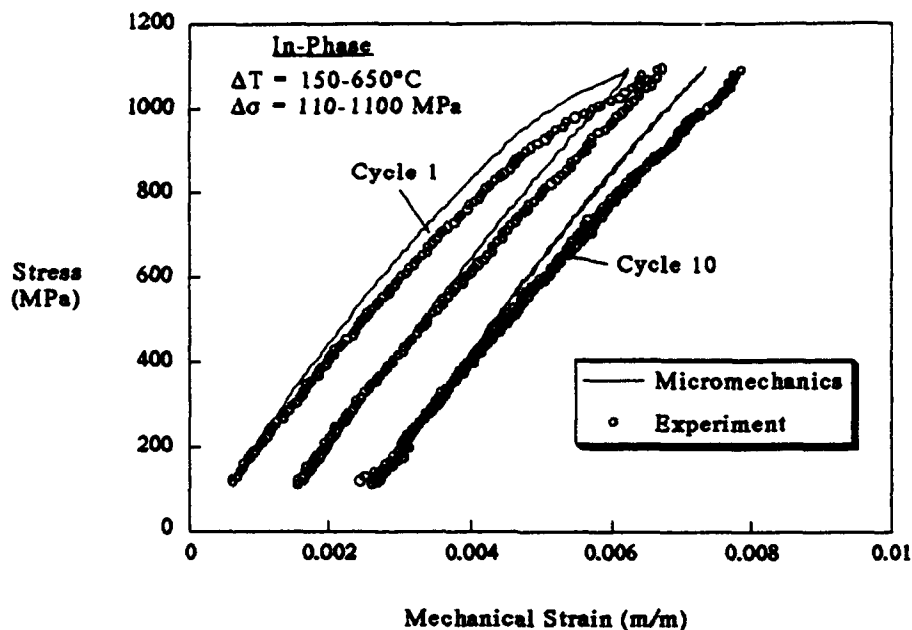
Figure 55. 0° SCS6/Ti-β21S Response to an In-Phase Load to 1100 MPa (67)

much less than was found with the in-phase loading, and the modulus determined from the calculations is in excellent agreement with experiment. This is as expected since the out-of-phase loading produces less damage than was experienced with the in-phase load (65).

Similar calculations involving a maximum applied stress of 800 MPa provide further insight. The behavior due to in-phase loading is presented in Figures 57 and 58. For the first ten cycles the micromechanics results match very well with the experimental results both in accumulated strain and modulus. As the fatigue loading continues, damage in the form of fiber and matrix cracking progresses in the specimen resulting in a larger accumulated strain than is calculated by the model (Figure

117
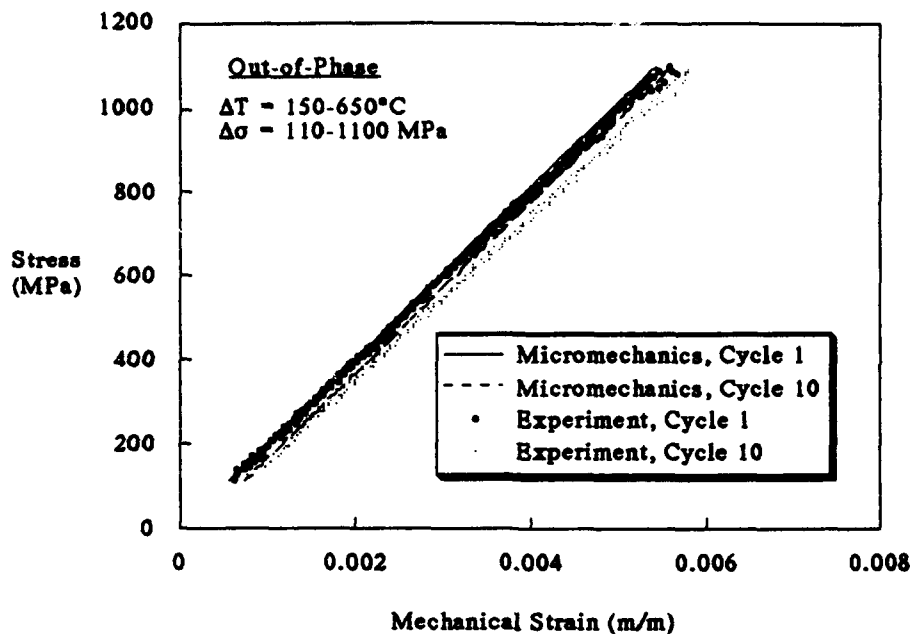
Figure 56. 0° SCS6/Ti-β21S Response to Out-of-Phase Load to 1100 MPa (67)

58). The micromechanics model accounts only for the viscoplastic be-
havior of the matrix material, but no damage. Therefore, the difference
between the calculations and experiment provides a measure of the
damage induced during cycling. On the other hand, the out-of-phase
results (Figure 59) demonstrate only a very modest strain accumulation
after 24 cycles.

An advantage of a reliable micromechanics solution is its ability to
calculate and track the constituent microstresses throughout loading.
Such results are useful for providing insight into the response of com-
posites, such as determining when the constituents are approaching their
respective failure strengths, etc. Examples are presented in Figures 60

118
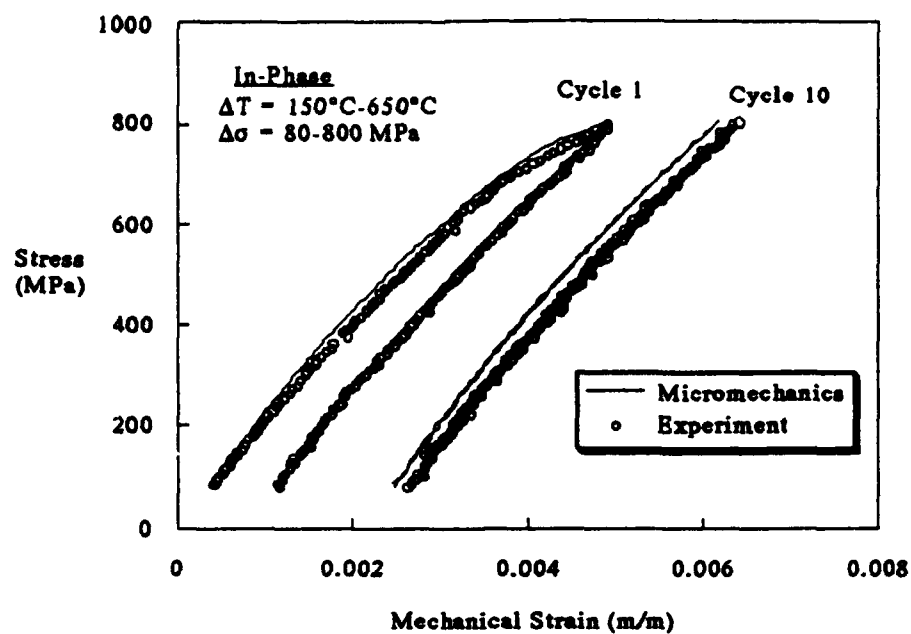
Figure 57. 0° SCS6/Ti-β21S Response to In-Phase Load to 800 MPa —
Cycles 1 & 10 (67)
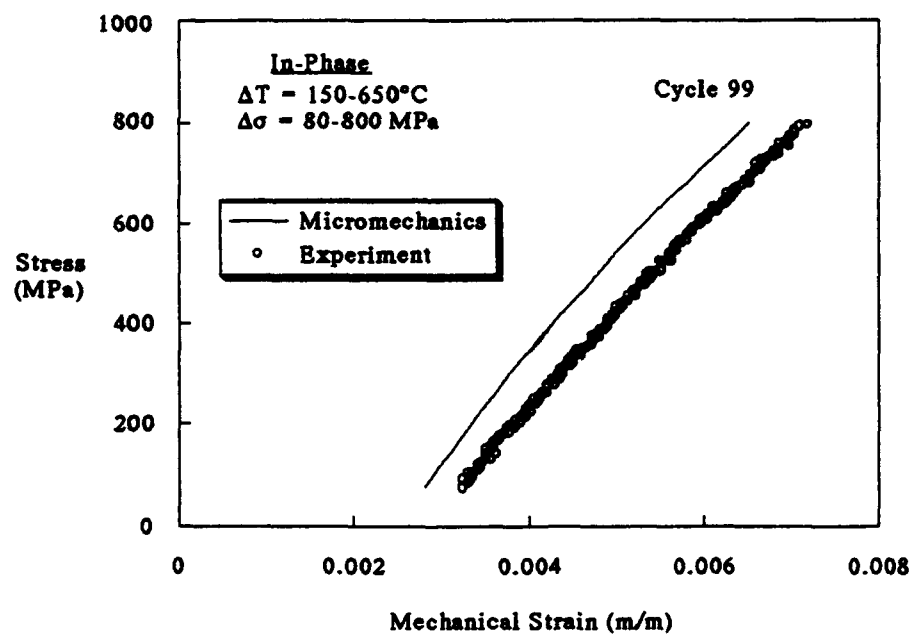
Figure 58. 0° SCS6/Ti-β21S Response to In-Phase Load to 800 MPa —
Cycle 99 (67)

119
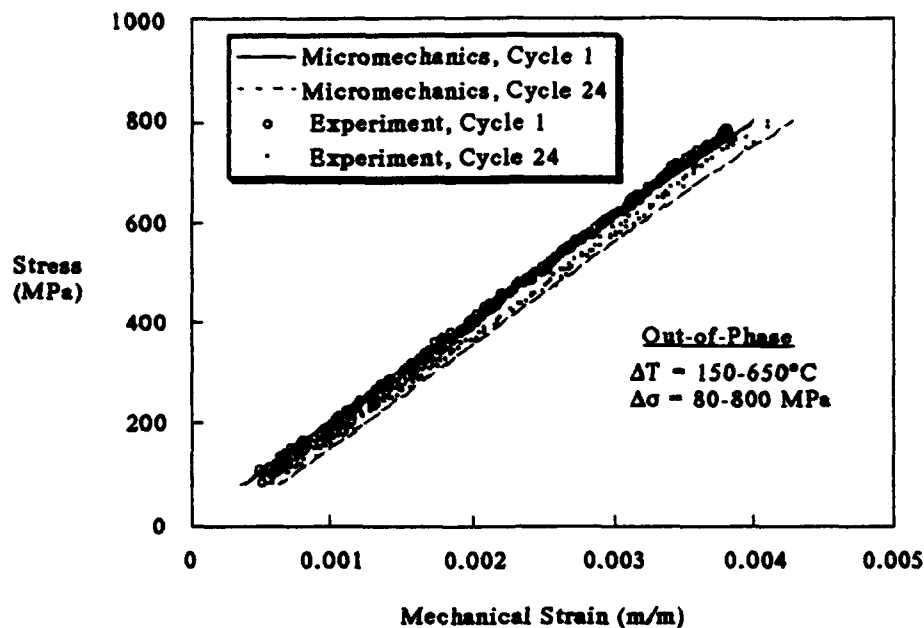
Figure 59. 0° SCS6/Ti-β21S Response to Out-of-Phase Load to 800 MPa (67)

and 61 where the average fiber and matrix stresses in the fiber direction are plotted for both in and out-of-phase thermomechanical loads. These plots represent the constituent results of the calculations previously presented in Figures 57 and 59, and it is noted that the in-phase loading produces a peak fiber stress that is approximately twice as large as with the out-of-phase load. In addition, the matrix stresses relax significantly for the in-phase loading within the first ten cycles, and the fiber stresses increase accordingly as the load is redistributed. Thus, fiber cracking should occur much sooner with the in-phase rather than the out-of-phase loading. This would result in a greater strain accumulation in the experiment than would be calculated by a micromechanics

120
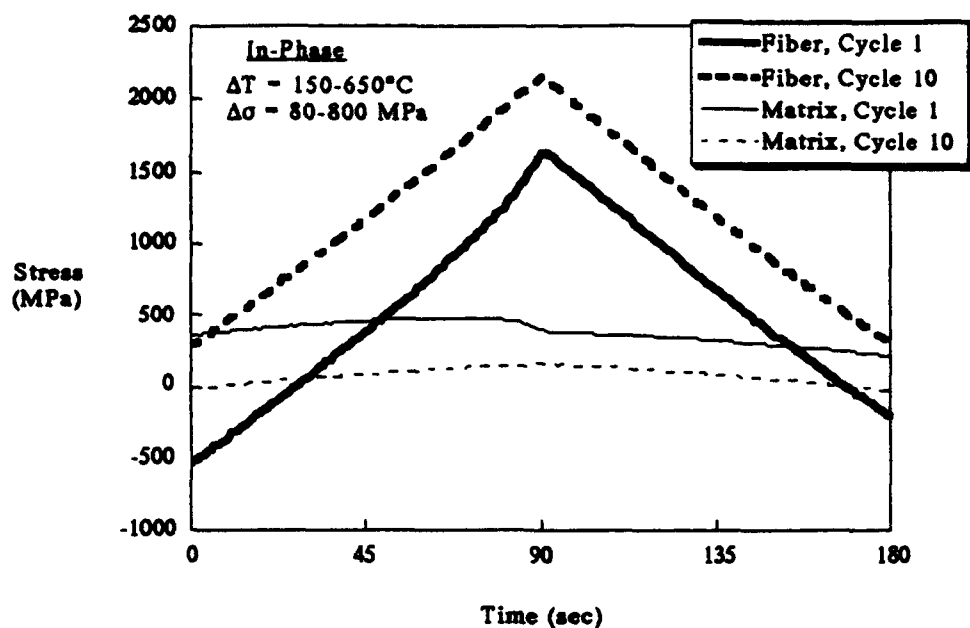
Figure 60. 0° SCS6/Ti-β21S Constituent Average Stress History for In-Phase Load to 800 MPa
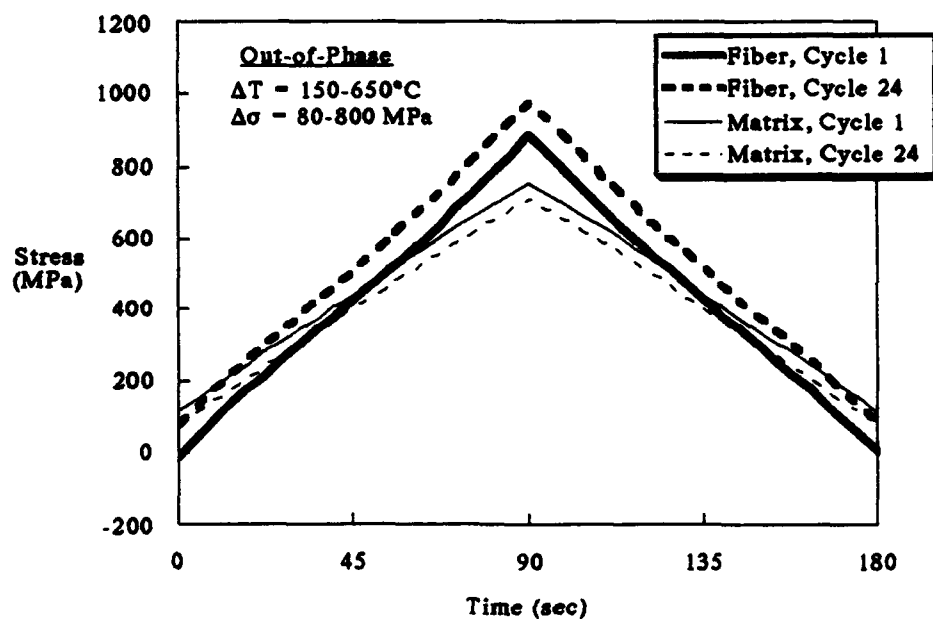
Figure 61. 0° SCS6/Ti-β21S Constituent Average Stress History for Out-of-Phase Load to 800 MPa

model. These characteristics have been observed in the previous figures when comparisons with experiments are made (65, 67).

The present model's capability to calculate reliable three-dimensional constituent microstresses allows for the incorporation of various three-dimensional unified viscoplastic theory models. The present chapter discussed the application of such viscoplastic models to the unidirectional composite micromechanics equations of chapter 3. A single algorithm was developed where all the examined material models could be easily adapted. This algorithm was found to be very stable and reliable for the calculations considered and provided a good basis from which the various unified theory material models could be added.

Results from the present micromechanics model closely matched with a previous micromechanical analysis (Aboudi's model) which incorporates the basic Bodner-Partom viscoplastic theory material model with isotropic hardening. Isotropic hardening material models are useful when composites are subjected to monotonic loading. However, in order to accurately model high temperature metal matrix composites under complex loading environments, more advanced material models which include kinematic hardening should be incorporated into the micromechanics analysis. The present formulation allowed for the inclusion of such material models with ease, and these results were compared with the corresponding available finite element and experimental results which showed that the present micromechanics analysis provides accurate calculations of a unidirectional composite's nonlinear response under various loading conditions including both monotonic loading and thermomechanical fatigue cycling. Also, an examination of the calculat-

ed constituent microstresses throughout the load-time history furnished a clearer understanding of the origins of damage progression under such loading conditions. Hence, reliable calculations of a composite material's constituent microstresses through the use of micromechanics techniques can equip the researcher with an additional tool to better understand the material's behavior.

Also, comparisons with experimental data provided further insight into the transverse response of a titanium alloy matrix composite. The results suggest that in addition to the effects of residual stresses, a finite bond strength exists at the fiber/matrix interface in the actual composite. A thorough discussion of the effects of a finite fiber/matrix bond strength and its associated failure on the composite behavior is given in the following chapter.

VI. Fiber/Matrix Interfacial Failure

The titanium-based MMCs discussed in the previous chapter have been found to possess low fiber/matrix bond strengths (68). This results in a pronounced effect on the transverse behavior as evidenced by Figures 45, 51 and 52. Previous researchers have attempted to mathematically model low fiber/matrix bond strengths by replacing the interface with a perfectly weak or unbonded fiber/matrix contact (56, 66). However, modeling the interface in such a way does not allow for a finite interfacial strength, and therefore the important point at which fiber/matrix separation occurs under transverse normal loading will be less in the analytical solution than in the actual observed behavior as shown in the previous chapter. Hence, MMCs exhibit behavior that cannot be modeled with either a perfectly weak or strong bond alone. Attempts have been made to correct this difficulty by modeling the interface as a thin third phase region possessing elastic-plastic properties with a relatively low yield stress (28). This type of an approach is sufficient for monotonic loads, but it meets with difficulty upon unloading and subsequent cycles since it is unable to account for the damaged interfaces which usually occurs in MMCs during the initial static load or under repeated loads.

The problem at hand is of a statistical nature and in order to accurately solve it, a statistical representation must be sought. Gayda and Gabb employed a one-dimensional model consisting of 128 elements of random fiber content to achieve a numerical approximation of progres-

sive interfacial failure under transverse normal load (72). Each successive load in the study contained elements of failed fiber/matrix bonds that may have been intact during the previous load. However, the computational intensity of such a method precludes its use for anything other than in a simplified one-dimensional method.

A unit cell or RVE approach to micromechanics as is put forth in the present study assumes that the entire composite will behave according to a single fiber/matrix cell possessing the average fiber volume fraction of the composite. Therefore, any associated material properties given to the RVE must be the composite average material properties and not just those associated with a single fiber and surrounding matrix. Moreover, to accurately model the effects of interfacial failure, an appropriate mathematical representation of the interface must be sought that reflects the average behavior of all interfaces throughout the composite.

The following discussion seeks to blend a statistical representation of fiber/matrix interfacial failure with the unit cell micromechanics equations already presented. First, a linear-elastic closed form statistical approach to analyze the effects of interfacial failure on the composite is introduced. Then, the average behavior of the interfacial failure from this approach is extracted and used in the nonlinear micromechanics technique discussed in the previous chapters.

6.1 A Statistical Model of Interfacial Failure

The statistical model is based on assuming a Gaussian distribution for the interfacial stresses, and hence, the fraction of interfaces which have failed at any given moment may be determined from the probability

density function and the interfacial failure strength. Figure 62 depicts a cross-section of the composite during a transverse applied load. Due to the random fiber packing and random interfacial failure strengths, all interfaces do not fail at the same moment. Initially, the majority of the interfaces are intact, but as the applied load is increased more interfaces fail as their respective failure strengths are exceeded.

As mentioned in the above paragraph, a Gaussian distribution for the interfacial stresses is assumed. Other researchers have performed similar analyses assuming a three parameter Weibull distribution (73). The advantage of the Gaussian distribution is that only two parameters are required thereby reducing the number of material constants which must be obtained from experimental data. Also, it is assumed that the effects of the random nature of the interfacial failure strengths may be included in the interfacial stress distribution, so only a single interfacial failure
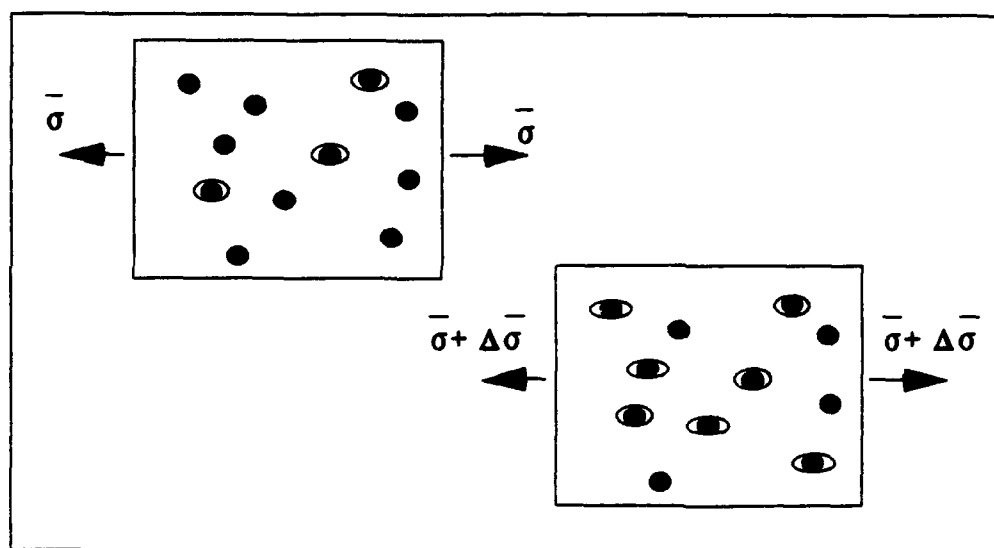
Figure 62. Schematic of Interfacial Failures During Transverse Load

126

strength need be specified. An example is presented in Figure 63 where the distribution of interfacial stresses, σ_I, is presented. All interfaces with stresses above the interfacial failure strength, σ_f, represent the fraction of interfaces that have failed. It is further assumed in the statistical model that interfacial failures do not effect the Gaussian distribution for the remaining intact interfaces. Therefore, the value, σ_m, in Figure 63 represents the mean of the Gaussian curve, and not the average interfacial stress which is given by the ensemble average of the unshaded area. Also, it is assumed that the standard deviation of the interfacial stresses remains constant as σ_m either increases or decreases. The final assumption in the development of the statistical model is that the fiber and matrix are linear-elastic. This last assump-
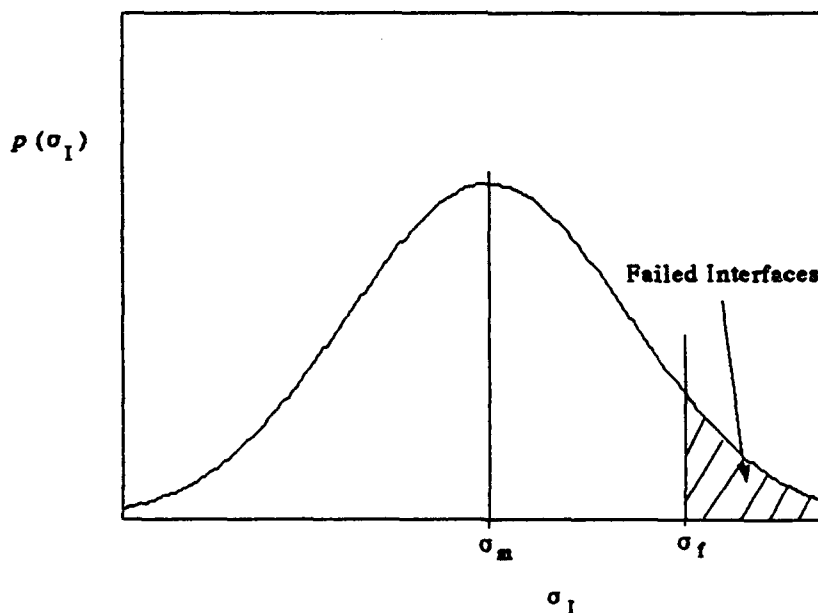
Figure 63. Distribution of Interfacial Stresses

127

tion will be abandoned when the mathematical model of the interface is adapted to the nonlinear micromechanics equations, but it is used in the initial formulation so that a concise set of equations may be developed to describe the average behavior of the interface.

6.1.1 Relations for Interfacial Failure

In this section, the above assumptions are used to develop a set of relations which describe interfacial failure under a static normal applied load. The Gaussian distribution of the interfacial stresses is given by

$$p(\sigma_I) = \frac{1}{S\sqrt{2\pi}} \exp\left[-\frac{(\sigma_I - \sigma_m)^2}{2S^2} \right] \quad \text{for} \quad -\infty < \sigma_I < \infty \tag{118}$$

where S is the standard deviation of the curve in Figure 63.

The portion of the curve that lies above σ_f represents all interfaces that have failed under the current load. The stress on the failed interfaces are considered to be zero since they are no longer capable of withstanding a tensile load. Therefore, the ensemble average of the interfacial stress for all interfaces may be represented by employing the unit step function, u, as given below

$$\sigma_{I_{AVG}} = \int_{-\infty}^{+\infty} [1 - u(\sigma_I - \sigma_f)] \, \sigma_I \, p(\sigma_I) \, d\sigma_I = \int_{-\infty}^{\sigma_f} \sigma_I \, p(\sigma_I) \, d\sigma_I \tag{119}$$

128

which may be solved to give the general form of the average interfacial stress as

$$\sigma_{I_{AVG}} = \frac{-S}{\sqrt{2\pi}} \exp\left[-\frac{(\sigma_f - \sigma_m)^2}{2S^2}\right] + \frac{\sigma_m}{2}\left(1 + \text{erf}\left[\frac{\sigma_f - \sigma_m}{S\sqrt{2}}\right]\right) \qquad (120)$$

where

$$\text{erf}[t] = \frac{2}{\sqrt{\pi}} \int_0^t \exp(-x^2)\, dx \qquad (121)$$

To determine the relative interfacial displacements, further assumptions on their behavior must be made. For instance, it is assumed that the displacement of all failed interfaces are proportional to the stress at the interface if it had not failed. In other words, the displacement of a failed interface is linearly related to how far above σ_f that particular failed interface is in Figure 63. This assumption for the displacements of all the failed interfaces is analogous to Hooke's law for elastic materials. In addition, the displacement of all intact interfaces are assumed to be zero. Therefore, the displacement of any interface may be given by

$$u_I = \begin{cases} 0 & \text{for } \sigma_I < \sigma_f \\ C_u \sigma_I & \text{for } \sigma_I \geq \sigma_f \end{cases} \qquad (122)$$

129

where C_u is a constant related to the elastic properties of the material and is therefore temperature dependent.

The general form for the average displacement of all interfaces may now be determined. Taking the ensemble average and substituting Eq (122) results in

$$u_{I_{AVG}} = \int_{-\infty}^{+\infty} u_I \, p(\sigma_I) \, d\sigma_I = \int_{\sigma_f}^{+\infty} C_u \, \sigma_I \, p(\sigma_I) \, d\sigma_I \tag{123}$$

which may be rewritten as

$$u_{I_{AVG}} = C_u \left[\int_{-\infty}^{+\infty} \sigma_I \, p(\sigma_I) \, d\sigma_I - \int_{-\infty}^{\sigma_f} \sigma_I \, p(\sigma_I) \, d\sigma_I \right] \tag{124}$$

The first integral inside the brackets of Eq (124) represents the mean of the curve in Figure 63, σ_m, and the second integral is the same as was already solved in Eqs (119) and (120). Therefore, the general form for the average displacement of all interfaces is given by

$$u_{I_{AVG}} = C_u \left\{ \frac{S}{\sqrt{2\pi}} \exp\left[-\frac{(\sigma_f - \sigma_m)^2}{2S^2} \right] + \frac{\sigma_m}{2} \left(1 - \text{erf}\left[\frac{\sigma_f - \sigma_m}{S\sqrt{2}} \right] \right) \right\} \tag{125}$$

130

From the assumption that the material is dominated by linear-elastic behavior it is inferred that the mean stress, σ_m, of the Gaussian curve is linearly related to the composite applied stress, $\bar{\sigma}$, and the change in temperature from the zero stress state, ΔT. Therefore,

$$\sigma_m = C_I \bar{\sigma} + C_T \Delta T \qquad (126)$$

where C_I and C_T are temperature dependent constants.

The above formulation presents five constants (C_u, C_I, C_T, σ_f, and S) that are necessary to describe the interfacial damage progression under a statically applied load. The first three, C_u, C_I, and C_T are simply mathematical constants from the linear-elastic assumption and may be determined from a micromechanical analysis. Therefore, only two parameters, σ_f and S, are composite interfacial properties which must be determined experimentally.

In order to evaluate these last two constants, comparisons must be made with appropriate experimental data. The method chosen in the present study was to compare experimental stress-strain curves of monotonically increasing load with similar results obtained from the above analysis. To do this, a relation is needed which relates the composite stress to the composite strain. Therefore, such a relation is developed from the linear-elastic material assumption by first assuming the composite possesses only intact or strong interfacial bonds. The composite strain, $\bar{\varepsilon}$, for such a material may be linearly related to the interfa-

cial stress and the change in temperature by

$$\bar{\varepsilon} = C_\varepsilon^\sigma \sigma_{I_{AVG}} + C_\varepsilon^T \Delta T \qquad (127)$$

Likewise, the composite strain for a material that possesses only failed or unbonded interfaces may be related to the interfacial displacement and change in temperature by

$$\bar{\varepsilon} = C_\varepsilon^u u_{I_{AVG}} + C_\varepsilon^T \Delta T \qquad (128)$$

where C_ε^σ, C_ε^T, and C_ε^u are elastic constants of the particular composite and may be determined through a micromechanical analysis. Therefore, if the mechanical portions of strain for the two types of material are summed, then a general relation may be obtained for a composite possessing both intact and failed interfaces which is given by

$$\bar{\varepsilon} = C_\varepsilon^u u_{I_{AVG}} + C_\varepsilon^\sigma \sigma_{I_{AVG}} + C_\varepsilon^T \Delta T \qquad (129)$$

This equation along with Eqs (120) and (125-126) are used in the following section to demonstrate the characteristics of the statistically based model and compare with linear-elastic experimental results. Also, it should be noted that a similar development may be followed for longitudinal shear along the interface. Almost identical equations will result for longitudinal shear in a unidirectional composite with the only excep-

tion being the absence of the terms involving temperature.

6.1.2 Characteristics of the Statistical Interface Model

A micromechanical analysis using the formulation of chapter 3 under transverse normal load was performed on the SCS6/Ti-15-3 material with a 35% fiber volume fraction to determine the elastic constants C_u, C_I, C_T, C_ε^σ, C_ε^T, and C_ε^u, the results of which are listed in Table 9. These constants were then used in conjunction with an interfacial failure strength, σ_f, of 250 MPa, and a standard deviation of interfacial stresses, S, of 60 MPa which produced the best match to the experimental composite behavior under a monotonically increasing load. The change in temperature from the stress free state was chosen at -875°C which simulates a cooldown from 900°C to 25°C. The results of the model as compared to the experimental data of Majumdar (68) for room temperature SCS6/Ti-15-3 is presented in Figure 64. The composite is apparently

Table 9.   Interfacial Elastic Constants for SCS6/Ti-15-3 as Determined from a Micromechanical Analysis

$$C_u = 1.954 \times 10^{-5} \frac{\text{fiber dia.}}{\text{MPa}} \qquad C_\varepsilon^\sigma = 5.369 \times 10^{-6} \frac{1}{\text{MPa}}$$

$$C_I = 1.25 \qquad C_\varepsilon^T = -9.141 \times 10^{-6} \frac{1}{°C}$$

$$C_T = 0.1965 \frac{\text{MPa}}{°C} \qquad C_\varepsilon^u = 0.5976$$
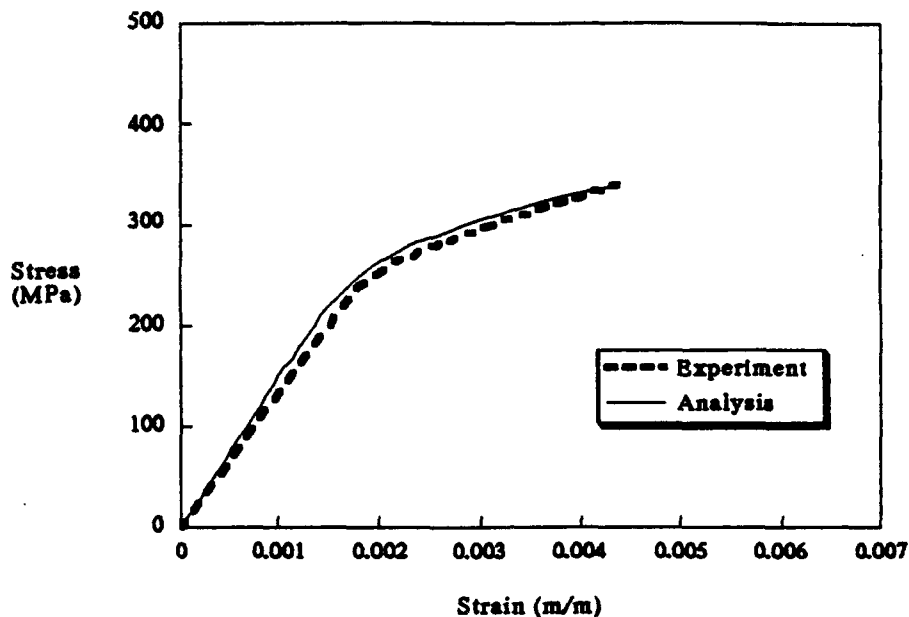
Figure 64. 90° SCS6/Ti-15-3 Response at 25°C as Predicted by the Linear-Elastic Statistical Interface Model and Experiment (68)

still in the elastic regime at the load levels presented since the experiment and analysis do no⁺ deviate from one another under these conditions. Even though the composite's response is nonlinear, the matrix has not yet exceeded its yield stress, and the nonlinearity is a result of the interfacial failure.

Further insight into the characteristics of the model may be gleaned by examining the average interfacial stress, $\sigma_{I_{AVG}}$, and average interfacial displacement, $u_{I_{AVG}}$, throughout the loading sequence as calculated by the mathematical model. Such a plot is presented in Figure 65 for the same conditions as in the previous figure only in this case the loading was continued until near complete interfacial failure (450 MPa applied

134
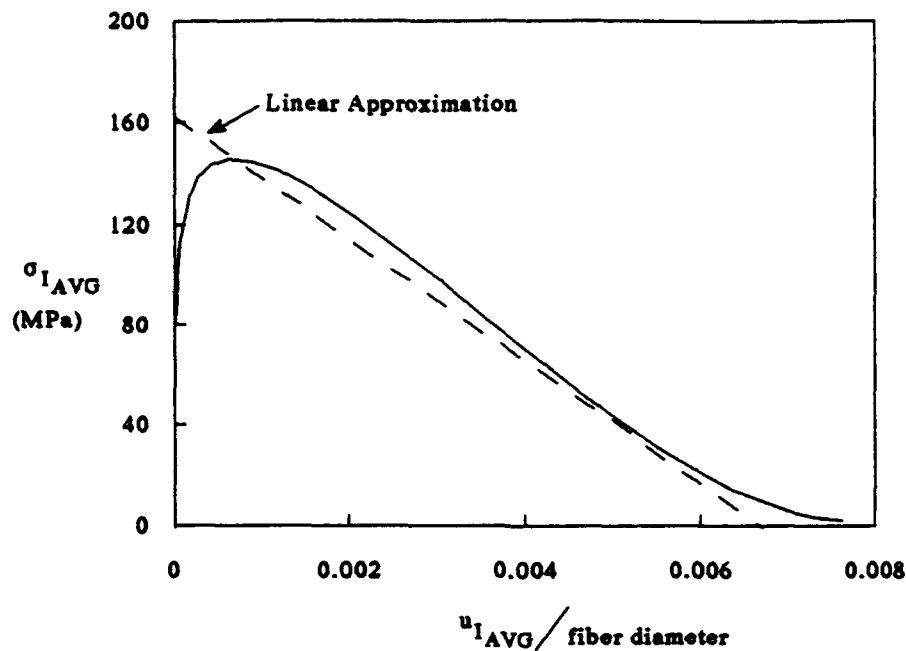
Figure 65. Average Interfacial Displacement and Stress for 90°
SCS6/Ti-15-3 at 25°C

composite load) had occurred. Several features of this curve are note-
worthy. First, no appreciable displacement occurs at the interfaces until
the average interfacial stress reaches approximately 120 MPa. Also, the
average interfacial stress is never greater than 150 MPa even though the
interfacial failure strength is 250 MPa. This is due to the statistical rep-
resentation where all points in the random distribution above 250 MPa
are said to have failed, and hence their associated stress drops immedi-
ately to zero resulting in an average interfacial stress for the composite
much less than the interfacial failure strength. In addition, except for
the regions near the axes, the curve in Figure 65 could be approximated
by a straight line extending from the average interfacial stress axis at

135

approximately 160 MPa to the average interfacial displacement axis at approximately 0.0065 fiber diameter as shown by the dashed line. This characteristic will be employed later when the interfacial model is adapted to the inelastic nonlinear micromechanics model.

The above discussion presents the characteristics of the statistical interface model under monotonically increasing load. Similarly, it is important how well the model captures the effects of interfacial failure during unloading. Therefore, appropriate relations must be developed that control the average interfacial behavior during unloading. The only assumption required is that while the interfacial stress is decreasing, no new interfacial failures occur until the interface is loaded to its previous maximum value. Hence, no displacement occurs at all intact interfaces and interfaces where the normal stress, σ_I, is less than zero which represent the interfaces that have reclosed under a compressive load. A new quantity is now defined which describes the stress point in the random distribution at which all separated interfaces begin. This quantity is termed the separation stress, σ_{sep}, and is defined by the following relation:

$$\sigma_{sep} = \begin{cases} \sigma_f & \text{for} & \sigma_{m_{max}} \leq \sigma_m < \infty \\ \sigma_m + \left(\sigma_f - \sigma_{m_{max}}\right) & \text{for} & -\left(\sigma_f - \sigma_{m_{max}}\right) \leq \sigma_m < \sigma_{m_{max}} \\ 0 & \text{for} & -\infty \leq \sigma_m < -\left(\sigma_f - \sigma_{m_{max}}\right) \end{cases} \quad (130)$$

where σ_m is a function of time, t, and $\sigma_{m_{max}}$ is its maximum through the present time, t_0

136

$$\sigma_{m_{max}} = \max\left[\sigma_m(t)\right] \qquad 0 \le t \le t_0 \qquad (131)$$

The separation stress, σ_{sep}, of Eq (130) now replaces σ_f in Eqs (120) and (125) for all calculations. This new value is more general than the original formulation and will apply throughout the loading sequence for both loading and unloading. An example is depicted in Figure 66 where the composite is loaded monotonically to 320 MPa followed by complete mechanical unload to 0 MPa and then reload to 340 MPa. The arrows in the figure are to avoid confusion in visualizing the correct load-unload path. The initial increasing load follows the original path already depicted in Figure 64, but upon unloading the response traces out a new
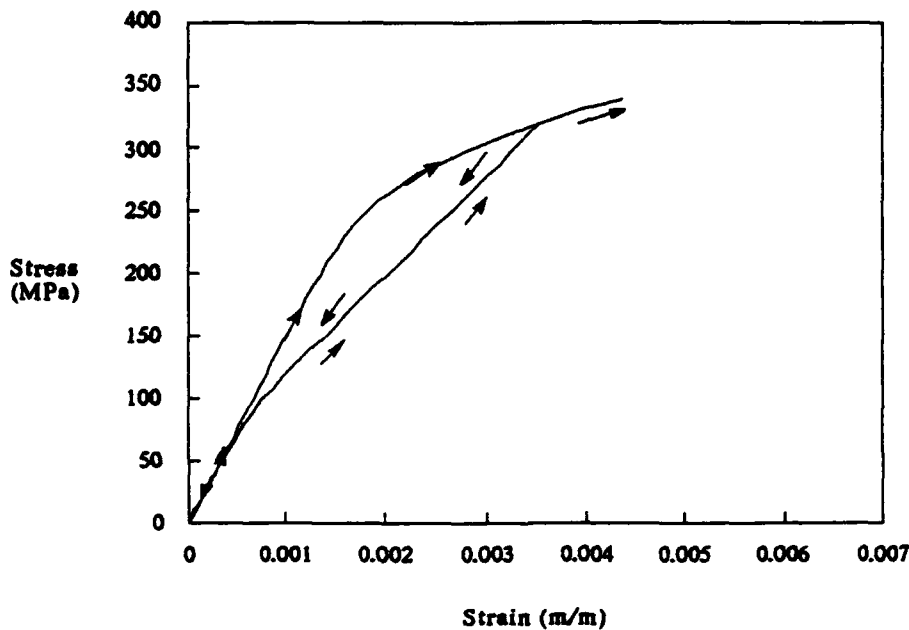
Figure 66. 90° SCS6/Ti-15-3 Response as Predicted by the Linear-Elastic Statistical Model for a Load-Unload Sequence

137

curve that falls below the original one. Once the vast majority of the separated interfaces reconnect through compressive stresses, then the unloading curve rejoins the original response. Upon further reload, the response again follows the previous unloading curve until all curves rejoin at the 320 MPa applied stress level where interfacial failure occurs once again. The hysteresis in the load-unload sequence represents the energy absorbed through interfacial bond failure. Therefore, the composite is initially elastic during unloading and reload since no energy is absorbed through the failure of new interfaces. However, once interfacial failure again becomes prevalent upon further reload, then inelastic behavior is observed.

The average interfacial stress and average interfacial displacement for the above load-unload sequence is presented in Figure 67. This curve exhibits similar behavior as observed in the composite response. During the initial increasing load the interfacial stress and displacement follows the original curve of Figure 65, but upon unload it follows a different path that is elastic and approximately linear until it reconnects with the stress axis. As before, reloading follows the unload curve until it finally rejoins with the original curve. It is worthy of note that the unloading curve does not intersect the stress axis at 0 MPa, but rather at a negative stress of approximately -80 MPa. This is due to the random distribution of stresses so that even while the average interfacial stress is zero a portion of the interfaces will still possess positive displacement. An additional illustration is given in Figure 68 where the average interfacial stress and displacement are plotted for three consecutive load-unload sequences to 320 MPa, 360 MPa, and 400 MPa, respective-
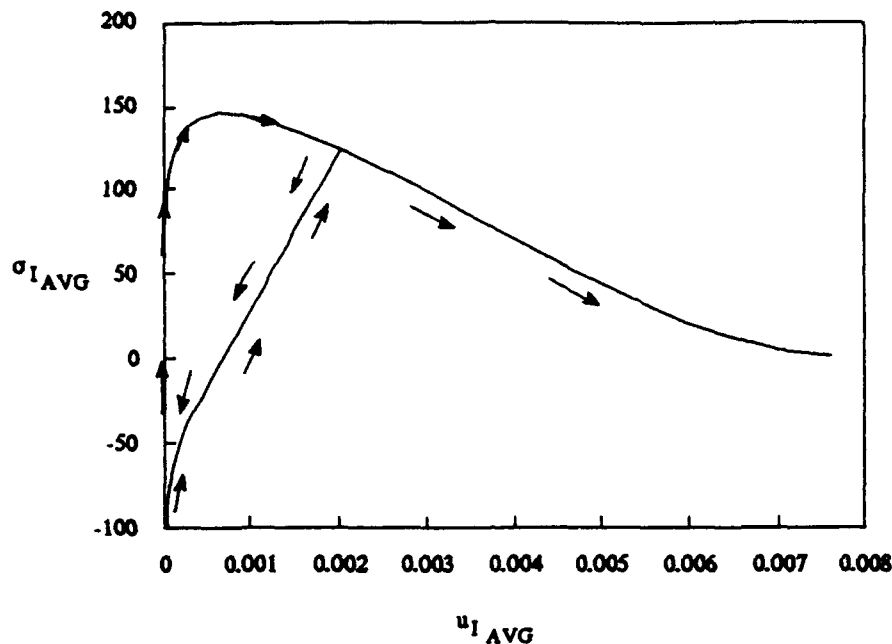
Figure 67. Average Interfacial Displacement and Stress for 90°
SCS6/Ti-15-3 at 25°C with Load-Unload Sequence

ly, followed by a final loading to 450 MPa. Each unloading curve re-
turns to approximately the same point on the stress axis with only a de-
crease in slope occurring for each successive step.

This last observation will be used in the adaptation of the above
statistical model for an elastic material to the nonlinear inelastic micro-
mechanics relations already developed. The micromechanics formula-
tion of chapter 3 operates on a unit cell approach which approximates
the composite by assuming a representative fiber/matrix cell possessing
average properties. Therefore, to incorporate the effects of interfacial
failure, the appropriate average behavior of the interface is desired, and
Figure 68 presents such a plot of the average interfacial behavior. Fur-
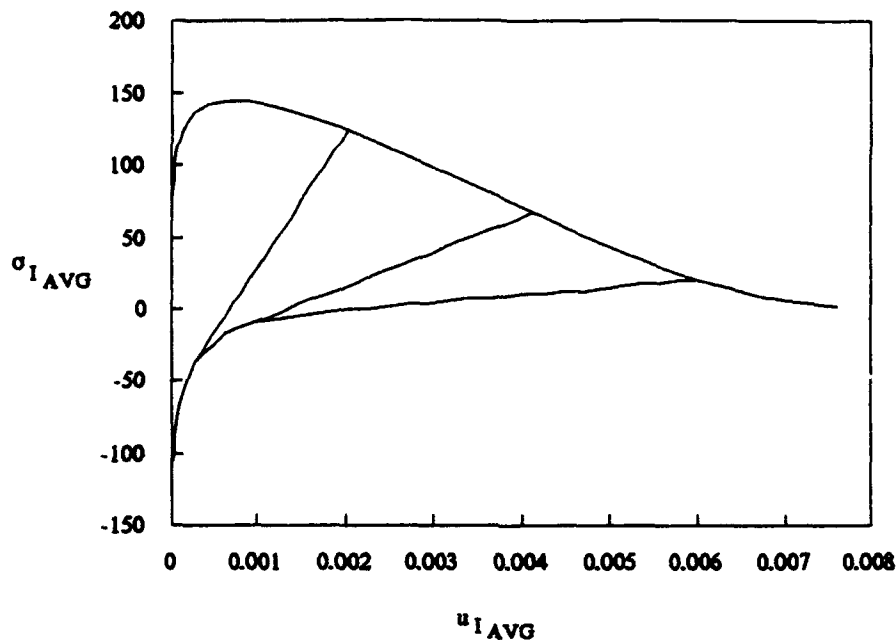
Figure 68. Average Interfacial Displacement and Stress for 90°
SCS6/Ti-15-3 at 25°C with Three Consecutive Load-Unload
Sequences

ther simplifications are desired so the computational requirements will
not be so intense. The inelastic micromechanics computations
sometimes require hundreds of iterations per load point, and the full sta-
tistical representation of the interface would be too limiting for such.

6.2 Statistical Interface Applied to the Micromechanics Formulation

The application of the interfacial failure model of the previous sec-
tion to the micromechanics formulation requires both a simplification of
the statistical interfacial model and a numerical algorithm for
incorporating the nonlinear effects of the interface into the microme-
chanics solution. The algorithm should be computationally efficient,

140

and it must not produce instabilities in the already existent nonlinear material algorithms described in chapters 4 and 5 for the elastic-plastic and elasic-viscoplastic materials. The basic assumption for applying the interfacial failure model to the micromechanics solution is that the basic behavior of the average interfacial stress and displacement is not greatly affected by the inelastic deformation of the matrix material.

Simplifying the average interfacial behavior involved approximating the characteristics exhibited in Figure 68 by a series of straight lines. Three quantities, σ_{I_f}, σ_{I_c}, and u_{I_f}, are specified to control where the lines intersect with the axes. An example is shown in Figure 69 where the interface remains intact until interfacial failure begins to occur at σ_{I_f}. Then the interfacial stress drops and the interfacial displacement
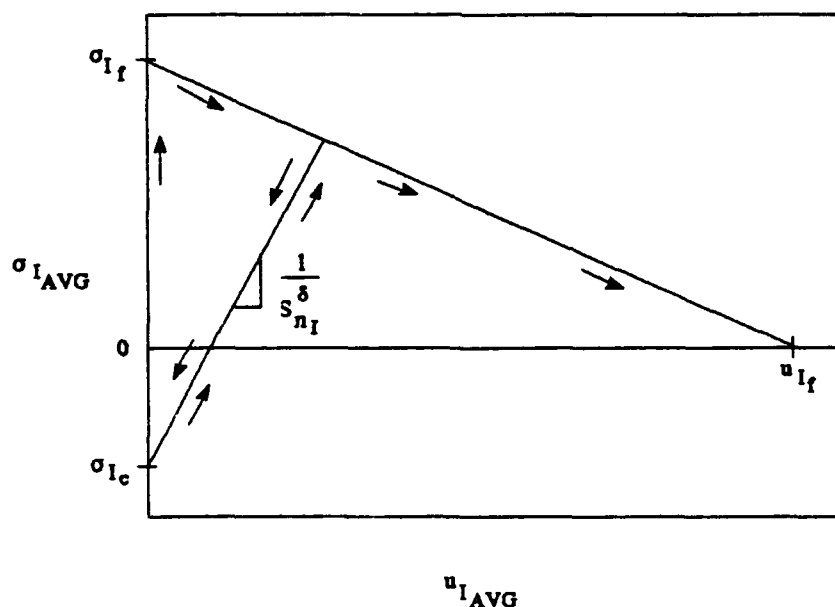
Figure 69. Simplified Interfacial Behavior for the Micromechanics Formulation

141

increases to follow the failure line that intersects the displacement axis at u_{If}. If the interface experiences unloading, then the response is modeled as linear-elastic behavior between the point along the failure line where unloading began and the point σ_{I_c} on the stress axis. The slope of the unloading curve is simply the inverse of the interfacial separation compliance normal to the interface, S_{Sep}^{δ}, where the equation for the displacement of the interface originally defined in Eq (11) is modified to include the effects of σ_{I_c} as

$$\delta_{n_r} = aS_{n_r}^{\delta}(\sigma_{n_r} - \sigma_{I_c}) \qquad S_{n_r}^{\delta} = \begin{cases} 0 & \sigma_{n_r} < \sigma_{I_c} \\ S_{Sep}^{\delta} & \sigma_{n_r} \geq \sigma_{I_c} \end{cases} \qquad (132)$$

where all quantities except σ_{I_c} are the same as originally defined in Eq (11).

The original equation for the longitudinal shear displacement of the interface along the fiber, Eq (12), remains unchanged. However, shear failure of the interface may occur under either positive or negative stress, so therefore, the interfacial failure model under these conditions will possess a failure curve similar to the one depicted in Figure 69 only with an additional curve that is its mirror image for negative stress (Figure 70).

The nonlinear micromechanics formulation may now be achieved in the same manner as was described in chapter 3. The resulting equations are the same as were already derived except for Eq (43) which is now
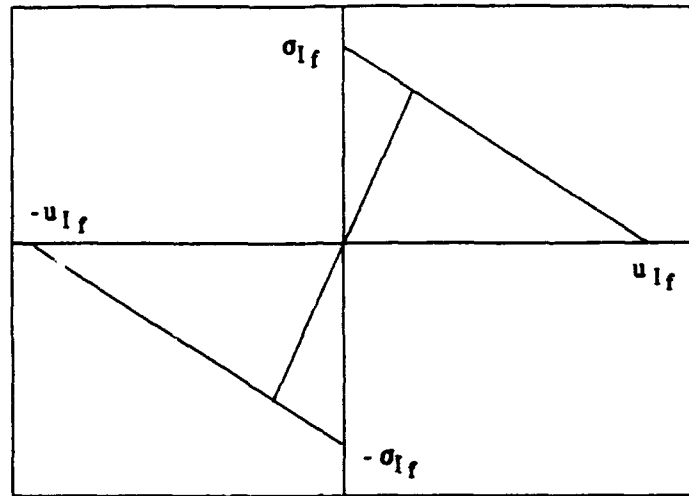
Figure 70. Simplified Interfacial Failure Model for Longitudinal Shear

modified to read

$$
\left[\begin{array}{c} P \\ 6x6 \end{array}\right] \left\{\begin{array}{c} \sigma_{11_f} \\ \sigma_{22_f} \\ \sigma_{33_f} \\ \sigma_{11_{m1}} \\ \sigma_{33_{m1}} \\ \sigma_{11_{m2}} \end{array}\right\} = \left\{\begin{array}{c} (\alpha_{1_m} - \alpha_{1_f})\Delta T \\ a(\alpha_{2_m} - \alpha_{2_f})\Delta T + a S_{m_{11}}^{\delta}\sigma_{I_c} \\ a(\alpha_{3_m} - \alpha_{3_f})\Delta T + a S_{m_{12}}^{\delta}\sigma_{I_c} \\ \bar{\sigma}_{11} \\ \bar{\sigma}_{22} \\ \bar{\sigma}_{33} \end{array}\right\} - \left[\begin{array}{c} P_I \\ 6x9 \end{array}\right] \left\{\begin{array}{c} \varepsilon_{m1}^I \\ \varepsilon_{m2}^I \\ \varepsilon_{m3}^I \end{array}\right\}
$$

(133)

where all quantities are as defined in chapter 3.

143

The solution of these equations requires the defining of an additional parameter which controls the failure point of the interface (Figure 71). The quantity, $u_{k_s}^c$, and its associated intercept point on the failure line, $\sigma_{k_s}^c$, defines the maximum point of linear-elastic behavior for an interface before further failure will occur. This represents the upper end of the linear-elastic unloading curve whose intercept along the stress axis will be σ_{I_c} for the normal direction and zero for the tangent or shear failure direction.

The numerical algorithm for solving the interfacial failure model coupled with an inelastic matrix material using the micromechanics relations is presented below. It represents the solution sequence employed to achieve convergence for a single load increment.
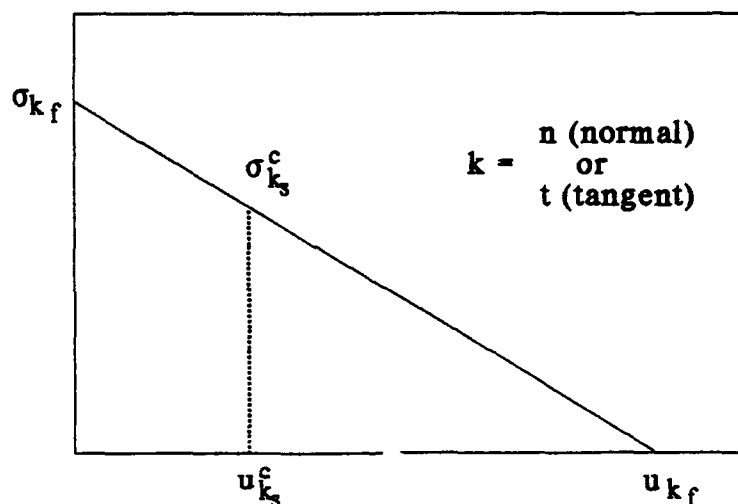
Figure 71. Sample Critical Point of Failure for Each Interface Region, s

(1) Assume linear-elastic behavior and no interfacial failure for the first iteration. Therefore, set

$$\varepsilon_{ij_r} = {}_0\varepsilon_{ij_r} \tag{134}$$

and

$$u^c_{k_s} = {}_0u^c_{k_s} \tag{135}$$

for each matrix region, r, and each interface region, s, where the subscript, o, indicates the value from the previously converged point.

(2) Calculate compliance values, $S^{\delta}_{k_s}$, for each interface, s, by

$$\sigma^c_{k_s} = \sigma_{k_f}\left(1 - \frac{u^c_{k_s}}{u_{k_f}}\right) \qquad k = n, t \tag{136}$$

$$S^{\delta}_{n_s} = \frac{u^c_{n_s}}{a\left(\sigma^c_{n_s} - \sigma_{I_c}\right)} \tag{137}$$

$$S^{\delta}_{t_s} = \frac{u^c_{t_s}}{a\,\sigma^c_{t_s}} \tag{138}$$

(3) Solve for all region stresses using the micromechanics relations.

145

(4) Initialize the iteration counter to one, and the change in the critical failure point, $\delta u_{k_s}^c$, to zero.

$$\delta u_{k_s}^c = 0 \quad \text{and} \quad p = 1 \tag{139}$$

Iterate

(5) Check if interfacial failure occurs during this load increment.

(a) For all interfacial regions, s, that satisfy

$$\sigma_{n_s} - \sigma_{n_s}^c \leq 0 \quad \text{and} \quad \delta u_{n_s}^c = 0 \tag{140}$$

set

$$\delta u_{n_s}^c = 0 \tag{141}$$

otherwise set

$$\delta u_{n_s}^c = a f_I S_{n_s}^\delta \left(\sigma_{n_s} - \sigma_{n_s}^c \right) \tag{142}$$

(b) For all interfacial regions, s, that satisfy

$$\left| \sigma_{t_s} \right| - \left| \sigma_{t_s}^c \right| \leq 0 \quad \text{and} \quad \delta u_{t_s}^c = 0 \tag{143}$$

set

146

$$\delta u_{t_s}^c = 0 \tag{144}$$

otherwise set

$$\delta u_{t_s}^c = a f_I S_{t_s}^{\delta} \left(\sigma_{t_s} - \sigma_{t_s}^c \right) \tag{145}$$

where f_I is a user supplied convergence parameter between 0 and 1.

(6) Determine new critical point along failure curve for all interface regions, s.

$$^P u_{k_s}^c = {}^{P-1} u_{k_s}^c - \delta u_{k_s}^c \qquad k = n, t \tag{146}$$

(7) Determine new inelastic strain, ε_{ij_r}, for all matrix regions using the appropriate algorithms described in chapters 4 and 5.

(8) Calculate new interfacial compliance values, $S_{k_s}^{\delta}$, for each interface, s, by Eqs (134-136).

(9) Solve for all region stresses using the micromechanics relations.

(10) Check for convergence by comparing the norm of the region stresses calculated before and after the iteration or by some

147

other equivalent method. If convergence has not been achieved, then $p = p+1$ and repeat steps 5 through 10. If convergence has been achieved, then stop iteration and calculate all remaining stresses and strains.

The above algorithm meshed well with the inelastic matrix material algorithms of chapters 4 and 5, and it for the most part did not add significantly to the number of iterations required to achieve convergence. The unidirectional composite solutions were normally obtained in a matter of seconds even under highly nonlinear loading conditions.

6.3 Micromechanics Solutions of Interfacial Failure

The viscoplastic material properties from the SCS6/Ti-15-3 composite were employed with the interfacial model of the previous section and comparisons were made with available experimental data. The effects of interfacial damage on the composite behavior is most prevalent in the transverse normal (90° to the fiber axis) and longitudinal shear (shear parallel to the fiber axis responses. Unfortunately, very little experimental data is available for the transverse normal response, and none for the longitudinal shear. Majumdar and Newaz (68) have characterized the response of 90° SCS6/Ti-15-3 at room and elevated temperature. The room temperature response is presented in Figure 72 where the micromechanics solutions of an unbonded fiber/matrix contact and the interfacial failure model described in the previous section are compared to two experimental test results of the Majumdar and Newaz study (68). The micromechanics model possessing a finite interfacial bond strength

148

with progressive failure provides a more exact representation of the experimental results. If an unbonded interface is assumed, then the characteristic "knee" in the stress-strain response occurs at approximately 150 MPa which is 100 MPa lower than is observed in the experimental data. The micromechanics solution that contains the interfacial failure model delays the nonlinearity, providing a more realistic approximation to the actual behavior. The interfacial properties employed for the SCS6/Ti-15-3 composite normal to the interface are listed in Table 10. These properties were approximated from the room temperature (25°C) and elevated temperature (538°C) monotonic response and were used for all the various calculations. The parameter, a, used in Table 10 to normalize the failure intercept on the displacement axis, u_{n_f}, is the char-
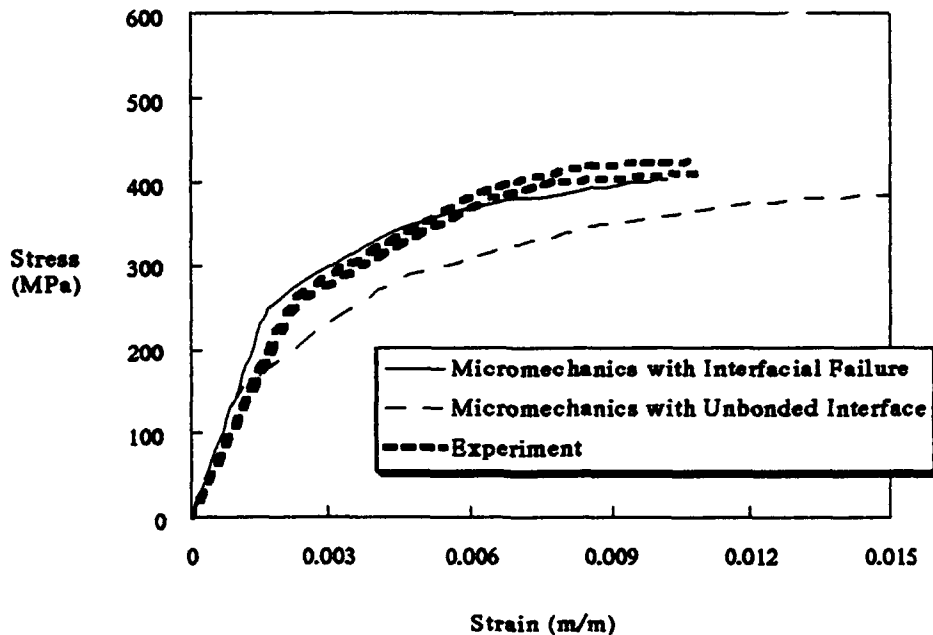
Figure 72. 90° SCS6/Ti-15-3 Monotonic Response at 25°C — Inelastic Micromechanics and Experiment (68)

Table 10. Normal Interfacial Properties Employed for the SCS6/Ti-15-3 Composite

	σ_{n_f}	σ_{I_c}	u_{n_f}/a
25°C	130 MPa	-75 MPa	0.04
538°C	100 MPa	-75 MPa	0.04

acteristic fiber dimension of Figure 9.

Additional understanding of the constituent interaction may be obtained by analyzing the constituent microstresses. Figure 73 presents the average stress in the fiber and matrix as functions of the composite strain, and the calculations were performed using the micromechanics relations with interfacial failure. The stress plotted is the volumetric average for each constituent in the direction of loading or perpendicular to the fiber. Initially, the fiber is experiencing a compressive stress of 184 MPa and the matrix a tensile stress of 95 MPa. As the composite is loaded, the compressive stress of the fiber is replaced by a tensile stress that reaches 130 MPa before interfacial failure begins to occur and causes a gradual decrease in the average fiber stress. The average stress in the matrix continues to increase throughout loading. Since the fiber is prevented from carrying the load due to failure of the interface, more load is carried by the matrix than if the interface had remained intact. Also, since the average matrix stress is approaching 600 MPa, it is likely that a substantial amount of the matrix material has locally exceeded its yield stress of 800 MPa even though the composite is loaded well below this value.
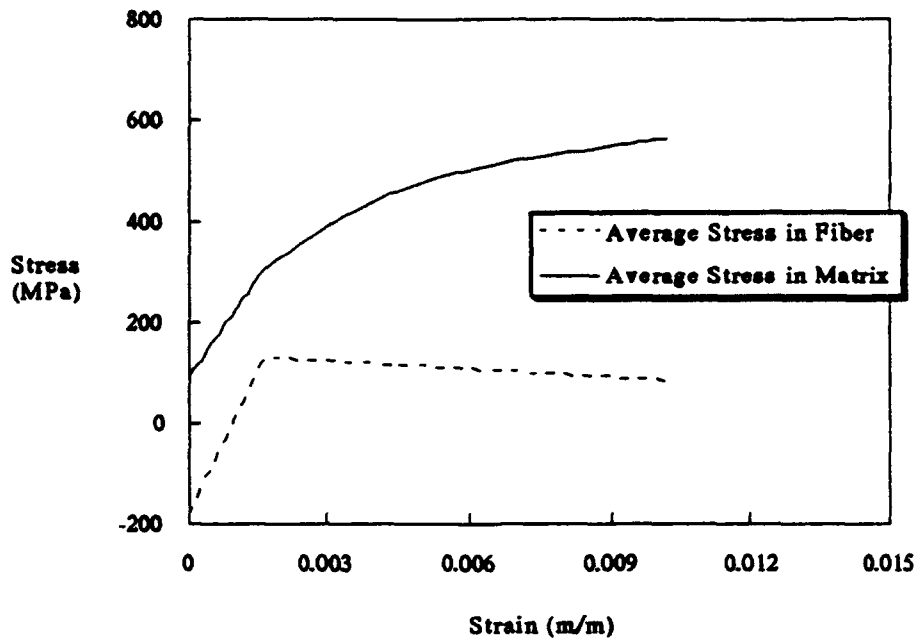
**Figure 73. Average Constituent Transverse Normal Stresses for 90°
SCS6/Ti-15-3 at 25°C for Monotonically Increasing Load**

The longitudinal and transverse strain is presented in Figure 74 for the monotonic loading at room temperature. Additional experimental data from Lerch and Saltsman (74) is also plotted to display the inherent experimental error existent when attempting to measure the strain in the fiber direction, ε_{11}, while loading perpendicular to it in the direction of the transverse strain, ε_{22}. The strains in the fiber direction are an order of magnitude smaller than those in the loading direction and this measurement is normally taken over a specimen of very limited width. However, the micromechanics solution is in good agreement with the two experimental results over the strain range presented. The decrease in the slope is indicative of damage as opposed to plasticity. This is as

151
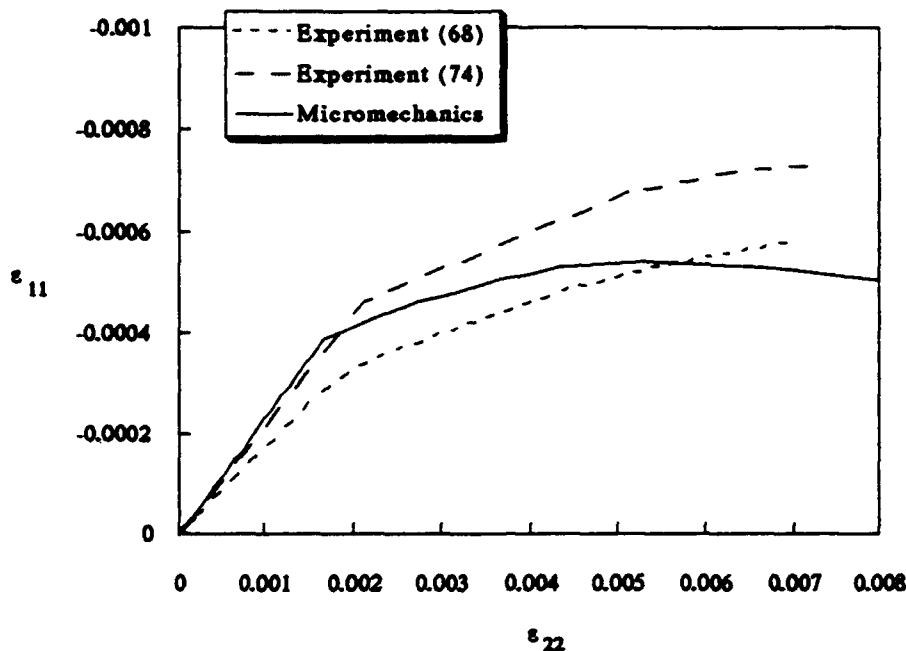
Figure 74. Longitudinal vs. Transverse Strain for 90° SCS6/Ti-15-3 at 25°C Loaded Monotonically (68, 74)

expected since failure of the interface dominates the transverse behavior.

Comparison to experimental data at 538°C is presented in Figure 75. Just as was observed in the room temperature case, the unbonded micromechanics solution under-predicts the point where the initial "knee" in the curve is seen. The difference between the unbonded and interfacial failure model is more pronounced in this elevated temperature case because the residual thermal stresses are not as large.

The constituent microstresses presented in Figure 76 also exhibit similar behavior as was observed in the room temperature calculations. The main difference is that the residual thermal stresses in the fiber and
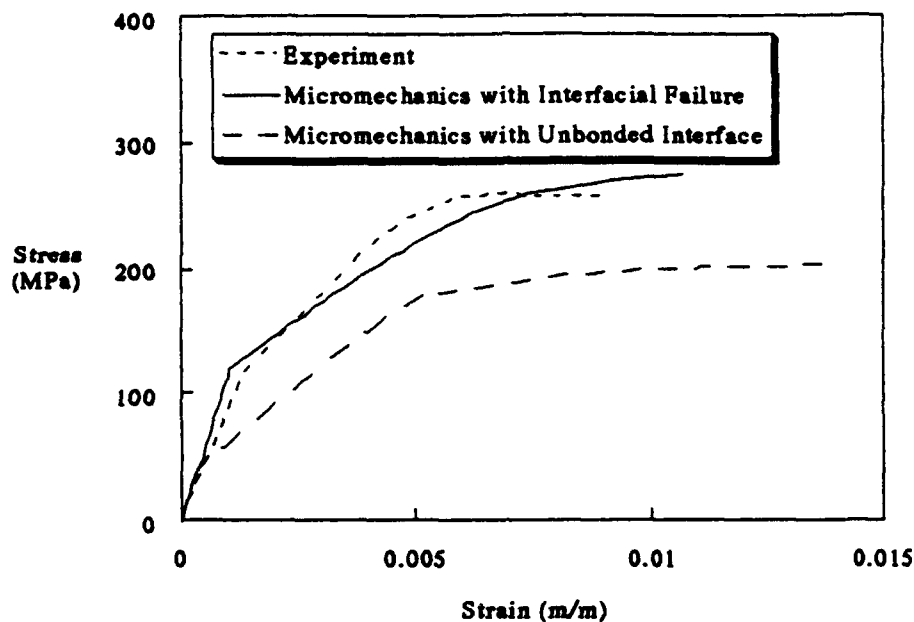
Figure 75. 90° SCS6/Ti-15-3 Response at 538°C — Inelastic Micromechanics and Experiment (70)

matrix at the beginning of the applied mechanical load are much smaller and the average stress in the matrix at the maximum applied load does not achieve as large a value than in the room temperature results. The yield stress for the matrix at this temperature is approximately 400 MPa. Therefore, since the average matrix stress is close to this value at the end of loading, then it is apparent that most of the matrix has yielded.

The effect of interfacial failure on the through-the-thickness strain, ε_{33}, is presented in Figure 77 for both room and elevated temperatures. Both curves may be characterized by three stages. The first stage is limited to linear-elastic behavior of the composite where the ratio of the strains are controlled by the elastic Poisson's ratio. The second stage

153
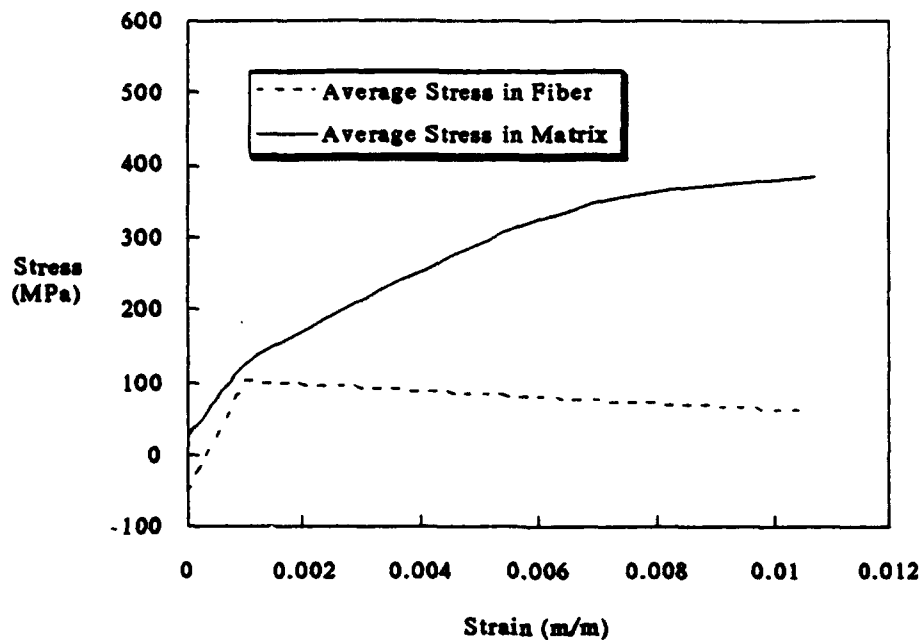
Figure 76. Average Constituent Transverse Normal Stresses for 90°
SCS6/Ti-15-3 at 538°C
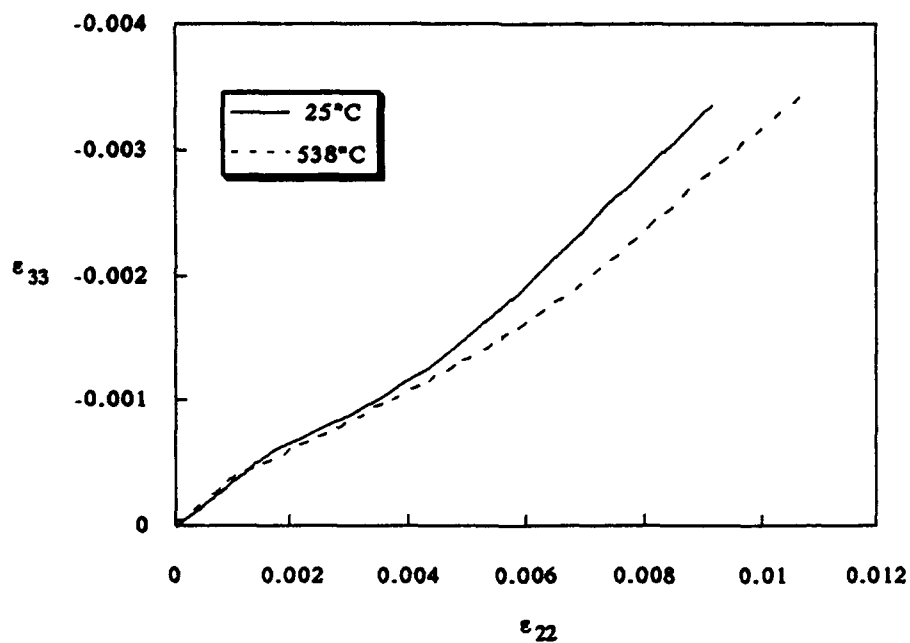
Figure 77. Transverse and Through-the-Thickness Strain for Monotoni-
cally Transverse Loaded SCS6/Ti-15-3

154

commences when a decrease in the slope is observed. This is where interfacial failure is predominant, thus, resulting in a reduced Poisson's ratio. In the final stage the slope increases due to the plastic deformation of the matrix. The Poisson's ratio in the matrix approaches the plastic value of one-half, and as a result, the Poisson's ratio of the composite necessarily increases according to the constituent interaction.

The inelastic composite response during unloading is also effected by interfacial failure as it was for the elastic material (see Figure 66). An example of some micromechanics calculations during mechanical load and unload sequences as compared to experimental data at room temperature is displayed in Figure 78. The maximum strain observed in the experiment for each loading sequence was attained in the microme-
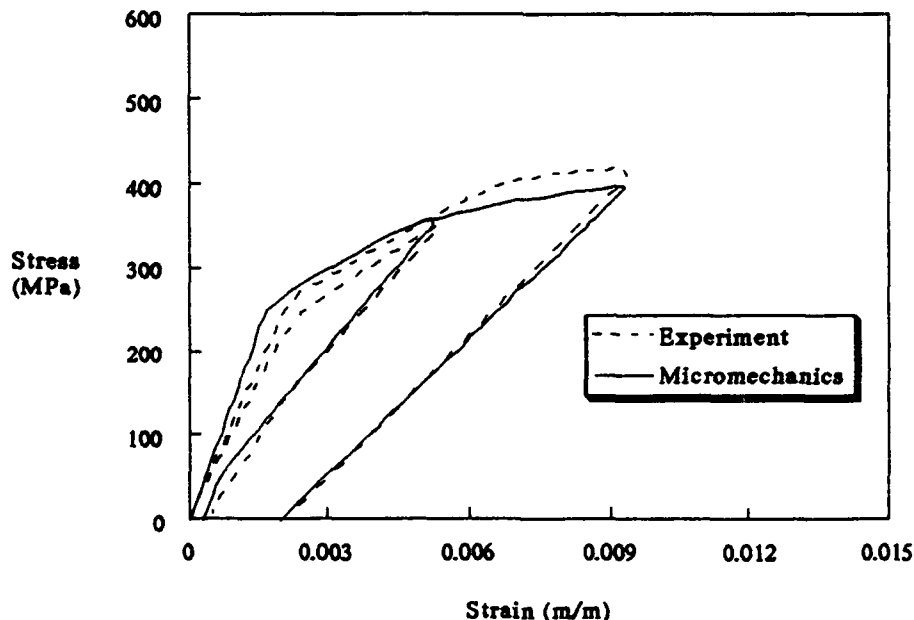
Figure 78. 90° SCS6/Ti-15-3 Response to Load/Unload Sequences at 25°C (68)

chanics solution before beginning the unloading portion. The return slope realized in the experiment is matched very well in the microme- chanics results. This return slope is effected by the amount of interfa- cial failure that has occurred during increasing load. If very little inter- facial failure occurs, then the unloading response will be very stiff with a return slope similar to that experienced during the initial elastic por- tion of the curve. If a significant amount of interfacial failure does occur, then the unloading response will be much weaker than the initial elastic modulus. Such characteristics are observed in both the microme- chanics solution and experimental results (68). A further comparison of a load-unload sequence at the elevated temperature of 538°C is dis- playe d in Figure 79, and it exhibits similar characteristics as in the room
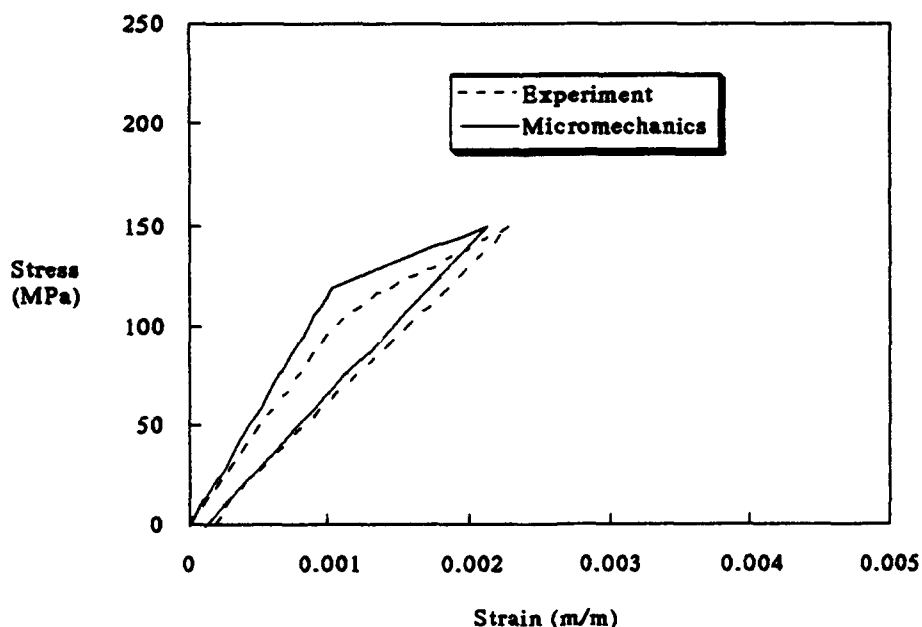
Figure 79. 90° SCS6/Ti-15-3 Response to a Load/Unload Sequence at 538°C (69)

temperature results

The modified statistical interfacial failure model that has been developed and incorporated into the inelastic unidirectional micromechanics formulation as described in section 6.2 has been shown to provide good agreement with available experimental data for characterizing the fiber/matrix interface. In addition, previous chapters have presented the application of the unidirectional micromechanics formulation to both elastic-plastic and elastic-viscoplastic materials with temperature dependent properties. Therefore, the groundwork is well laid for the development of a nonlinear laminated composite analysis that can examine the effects of all these various phenomena on the macromechanical behavior of laminated composites. Such a formulation is presented in the following chapter, and where it is appropriate, comparisons are made with previously published analytical or experimental data.

VII. Nonlinear Laminate Analysis

Very few applications involve the use of unidirectional fiber rein-
forced composites; rather, laminated layups are used where the fibers of
each individual unidirectional ply are oriented at different angles from
other plies. Therefore, it is important for a micromechanics analysis to
address this and attempt to relate the micromechanics to the macrome-
chanical behavior of the laminate. For linear-elastic cases this may be
accomplished by simply employing the linear-elastic classical laminated
plate (CLP) theory for composites (3). CLP theory takes the elastic
orthotropic material properties of each lamina or ply and assembles them
through various linear transformations to produce an approximation of
the elastic material properties of the entire layup or laminate. More-
over, if only linear-elastic behavior is desired, then the linear-elastic
properties of the unidirectional ply may be obtained from the microme-
chanics formulation and employed in the CLP theory. However, this is
not possible if a nonlinear analysis of the macromechanical behavior of
the laminate is desired.

A nonlinear analysis requires a direct formulation from the microme-
chanics level to the laminate. Other micromechanics formulations such
as Aboudi's method of cells (42) accomplish this indirectly by calculat-
ing the laminate elastic properties and equivalent plastic forces and
moments from the micromechanics after each load increment. The in-
elastic strains from the previous increment are used to determine the
equivalent plastic forces and moments. The accumulated error from this

158

process is assumed to be slight for small increments. Such an approach is very versatile but greatly increases the computational requirements due to the small load increments which must be used. The present formulation will eliminate this difficulty through direct assembly of the micromechanics equations up through to the laminate level.

7.1 Basic Nonlinear Formulation for Laminates

The basic tenant of the laminate formulation in the present analysis as well as several previous formulations by other researchers is that the CLP theory assumptions for strain throughout the laminate still apply (35, 38, 42). This is a reasonable supposition because it is the initial assumption made in the CLP theory and not tied to the linear-elastic equations. It simply states that any plane perpendicular to the midplane before deformation remains both plane and perpendicular to the midplane after deformation. Therefore, the strain at any point in the laminate may be related to the strain at the midplane by a curvature vector and the distance that point is from the midplane. The succeeding sections present the micromechanics to macromechanics formulation that was applied to the micromechanics equations of chapter 3 to provide for the direct calculation of nonlinear composite laminate behavior.

7.1.1 Basic Assumptions for Laminate Analysis

A composite laminate with its associated applied in-plane forces is presented in Figure 80. The condition that all planes perpendicular to the midplane before deformation remain perpendicular after deformation

requires that the out-of-plane shear strains are zero (3). Therefore,

$$\gamma_{xz} = \gamma_{yz} = 0 \qquad (147)$$

Also, at the laminate level it is assumed that the through-the-thickness normal stress can be neglected. In other words, a state of plane stress exists, so therefore,

$$\sigma_{zz} = 0 \qquad (148)$$

Equations (147) and (148) imply that only the in-plane stresses and strains are necessary in determining the response of a laminate to an applied load. However, it should be noted that Eq (148) does not imply
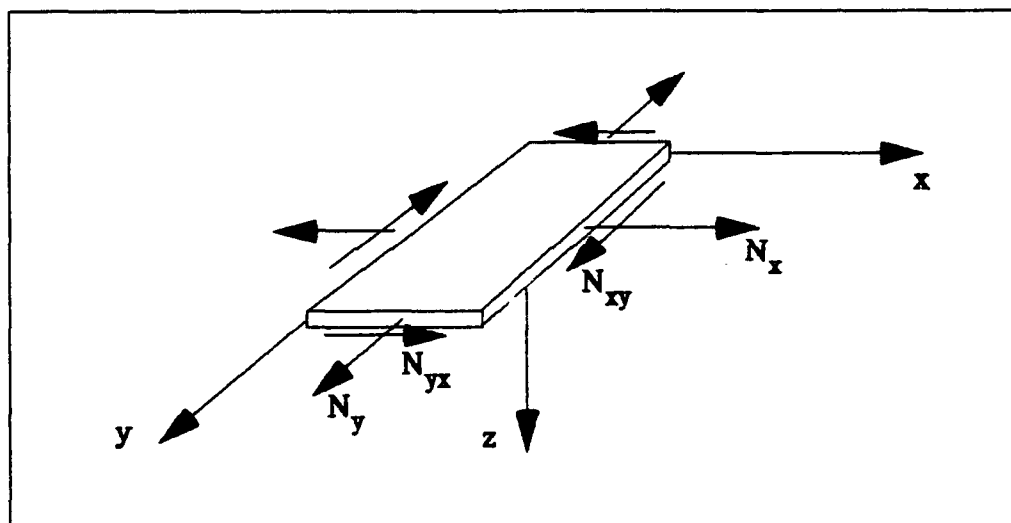
Figure 80. In-plane Forces on a Composite Laminate

that the constituents possess no through-the-thickness stress, for a state of plane stress certainly does not exist at the microscopic or micromechanics level. However, at the laminate and ply level Eq (148) is assumed to be valid, and hence, the stresses and strains for the laminate and each ply may be examined from a two-dimensional standpoint and can be expressed as

$$\{\varepsilon\} = \begin{Bmatrix} \varepsilon_x \\ \varepsilon_y \\ \gamma_{xy} \end{Bmatrix} \qquad \text{and} \qquad \{\sigma\} = \begin{Bmatrix} \sigma_x \\ \sigma_y \\ \tau_{xy} \end{Bmatrix} \tag{149}$$

In addition to the in-plane applied loads, there may exist applied moments at the edges of the laminate such as are depicted in Figure 81. These moments at the edges of the laminate as well as the in-plane loads are specified on a per unit length basis, and upon adopting a similar notation as is used in Eq (149), the laminate in-plane loads and moments are expressed as

$$\{N\} = \begin{Bmatrix} N_x \\ N_y \\ N_{xy} \end{Bmatrix} \qquad \text{and} \qquad \{M\} = \begin{Bmatrix} M_x \\ M_y \\ M_{xy} \end{Bmatrix} \tag{150}$$

The CLP theory assumption for strain at any point in the laminate may be given by the following equation
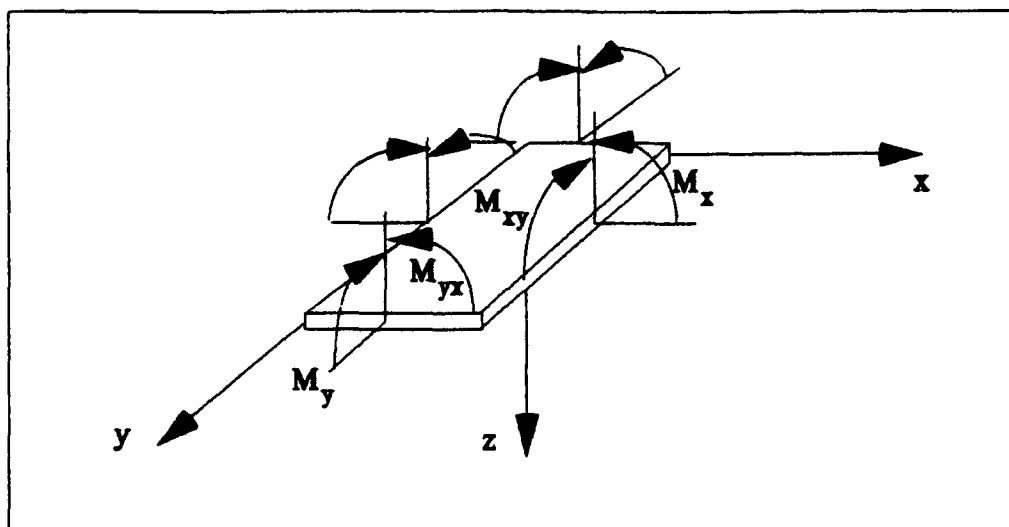
Figure 81. Moments on a Composite Laminate

$$\left\{ \begin{array}{c} \varepsilon_x \\ \varepsilon_y \\ \varepsilon_{xy} \end{array} \right\} = \left\{ \begin{array}{c} _o\varepsilon_x \\ _o\varepsilon_y \\ _o\varepsilon_{xy} \end{array} \right\} + z \left\{ \begin{array}{c} \kappa_x \\ \kappa_y \\ \kappa_{xy} \end{array} \right\} \qquad (151)$$

or simply as

$$\{\varepsilon\} = \{_o\varepsilon\} + z\{\kappa\} \qquad (152)$$

where the prescript, o, indicates the value of strain at the midplane and κ is the curvature of the laminate surface.

The stress in the laminate may be related to the applied forces and moments by invoking equilibrium through various cross-sections of the laminate and integrating. Performing such an exercise results in the following integral relationships for the applied forces and moments and the

162

laminate stress:

$$\{N\} = \int_{-t/2}^{t/2} \{\sigma\} \, dz = \sum_{k=1}^{n} \int_{z_{k-1}}^{z_k} \{\sigma\}_k \, dz \tag{153}$$

$$\{M\} = \int_{-t/2}^{t/2} \{\sigma\} \, z \, dz = \sum_{k=1}^{n} \int_{z_{k-1}}^{z_k} \{\sigma\}_k \, z \, dz \tag{154}$$

where t is the thickness of the laminate, n is the number of plies and z_k is as defined in Figure 82.

If it is assumed that the stress in each ply is approximately constant, then the stress vectors may be pulled outside the integrals in the above equations, and the applied forces and moments can be related to the ply
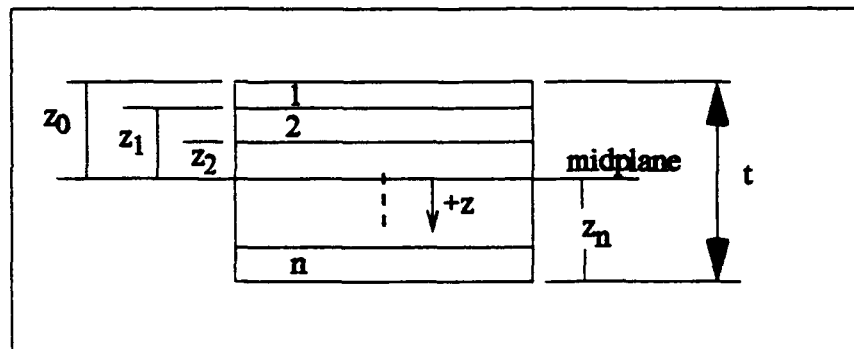
Figure 82. Ply Numbering Sequence and Distances from Midplane

163

stresses through the matrix equation

$$\left\{ \begin{matrix} N \\ M \end{matrix} \right\} = \begin{bmatrix} A_1 & A_2 & A_n \\ B_1 & B_2 & B_n \end{bmatrix} \left\{ \begin{matrix} \{\sigma\}_1 \\ \{\sigma\}_2 \\ \vdots \\ \{\sigma\}_n \end{matrix} \right\} \tag{155}$$

where if the 3x3 identity matrix is represented by I, then

$$A_k = (z_k - z_{k-1}) I \tag{156}$$

$$B_k = \frac{1}{2} \left(z_k^2 - z_{k-1}^2 \right) I \tag{157}$$

Equation (155) cannot be inverted in its present form. Therefore, the vector of applied forces and moments on the left-hand side is extended by the ply stresses in ply numbers 3 to n, and the matrix is extended by placing a unit matrix in the lower right-hand corner that begins in the 7th row and column. Thus, a square matrix, H, is developed which may be inverted to relate the applied forces and moments to the various ply stresses.

$$\left\{ \begin{matrix} N \\ M \\ \{\sigma\}_3 \\ \vdots \\ \{\sigma\}_n \end{matrix} \right\} = \begin{bmatrix} & H & \end{bmatrix} \left\{ \begin{matrix} \{\sigma\}_1 \\ \{\sigma\}_2 \\ \{\sigma\}_3 \\ \vdots \\ \{\sigma\}_n \end{matrix} \right\} \tag{158}$$

where

$$
\begin{bmatrix} H \end{bmatrix} = \begin{bmatrix} A_1 & A_2 & A_3 & & A_n \\ B_1 & B_2 & B_3 & & B_n \\ 0 & 0 & I & 0 & 0 \\ 0 & 0 & 0 & & 0 \\ \vdots & & & & \\ 0 & 0 & 0 & \cdots & I \end{bmatrix} \qquad (159)
$$

Equations (152) and (159) are formulated in the global or laminate coordinate system, but the micromechanics formulation is based on the individual ply or lamina coordinate system which is determined by the fiber direction. Figure 83 depicts the two coordinate systems and the angle, θ, used to transform between the laminate coordinate system and the ply coordinate system. The linear transformation of coordinates must be made at each iteration, and therefore, this transformation is embedded in the formulation because it must be calculated at each step. The transformation of ply stresses may be given by

- x-y is the laminate coordinate system

- 1-2 is the ply coordinate system

- The z and 3 axes always point in the same direction (out of the plane)
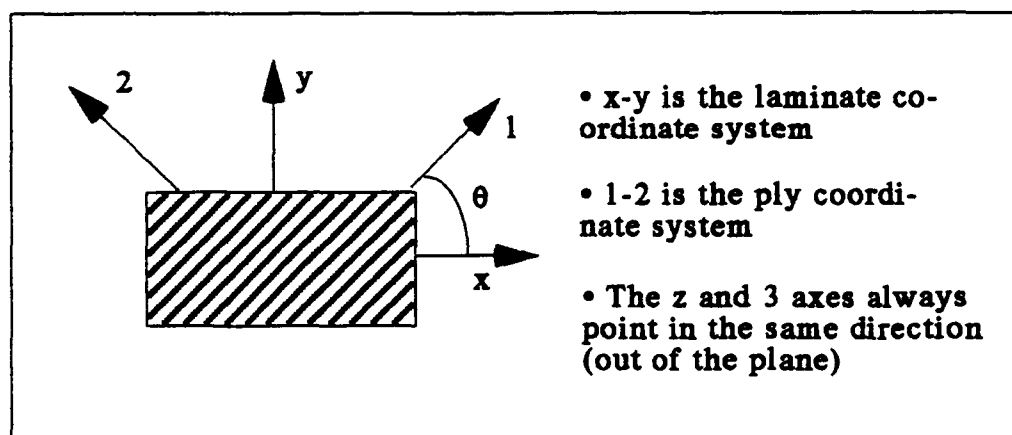
Figure 83. Laminate and Ply Coordinate Systems

$$\begin{Bmatrix} \sigma_{11} \\ \sigma_{22} \\ \tau_{12} \end{Bmatrix} = \begin{bmatrix} & T & \end{bmatrix} \begin{Bmatrix} \sigma_{xx} \\ \sigma_{yy} \\ \tau_{xy} \end{Bmatrix} \tag{160}$$

where

$$\begin{bmatrix} & T & \end{bmatrix} = \begin{bmatrix} \cos^2\theta & \sin^2\theta & 2\sin\theta\cos\theta \\ \sin^2\theta & \cos^2\theta & -2\sin\theta\cos\theta \\ -\sin\theta\cos\theta & \sin\theta\cos\theta & \cos^2\theta - \sin^2\theta \end{bmatrix} \tag{161}$$

Also, the transformation of strain is accomplished similarly as

$$\begin{Bmatrix} \varepsilon_{11} \\ \varepsilon_{22} \\ \dfrac{\gamma_{12}}{2} \end{Bmatrix} = \begin{bmatrix} & T & \end{bmatrix} \begin{Bmatrix} \varepsilon_{xx} \\ \varepsilon_{yy} \\ \dfrac{\gamma_{xy}}{2} \end{Bmatrix} \tag{162}$$

The relations presented in this section apply to the various plies of a single laminate. The micromechanics equations must be assembled together with these equations to provide for a nonlinear micro to macromechanics analysis. The following section presents the micromechanics equations with the necessary modifications required for inclusion in a laminate analysis, and then a subsequent section discusses the assembly of all these equations to produce a general laminate analysis.

166

7.1.2 Micromechanics Equations for Laminate Analysis

The micromechanics equations presented in chapter 3 must be presented in a different format when applying them to a laminate analysis from the format already given because certain conditions apply which were not considered in the unidirectional case. For instance, the normal stress, σ_{33}, of the composite is always assumed to be zero. In addition, the through-the-thickness shear strains, γ_{13} and γ_{23}, are also zero. These as well as other requirements must necessarily be incorporated into the micromechanics relations.

The condition that the normal stress, σ_{33}, of the composite is always zero implies that the normal stress, σ_{33}, on each ply is also zero. Therefore, the unidirectional micromechanics equations must reflect this, and so Eq (30) is now simply

$$a\,\sigma_{33_{m3}} + b\,\sigma_{33_{m2}} = 0 \tag{163}$$

where it is recognized that the stresses listed as composite stresses in the unidirectional formulation of chapter 3 now become the ply stresses.

In addition, all the equations involving the through-the-thickness shear strains, γ_{13} and γ_{23}, do not need to be considered because these are assumed to be zero in accordance with the laminated plate theory assumptions. All other equilibrium and continuity conditions remain unchanged.

However, the equation simplification at the micromechanics level takes a slightly different path for the laminate analysis than it did for

the unidirectional investigation. For example, even though the shear stresses and strains decouple from the normal stresses and strains at the micromechanics level, they do not at the laminate level, and hence, the shear stresses and strains in the 1-2 direction must be included in the overall formulation and cannot be considered separately as was done for the unidirectional formulation of chapter 3. Also, the stress and strain for a single ply is interrelated to the stress and strain in all other plies, so all these values must also be related. Therefore, the micromechanics equations may be reduced to the following general form for a single ply

$$
\begin{bmatrix} P \\ 8x8 \end{bmatrix}
\begin{Bmatrix}
\bar{\varepsilon}_{11} \\
\bar{\varepsilon}_{22} \\
\bar{\gamma}_{12} \\
\sigma_{11_f} \\
\sigma_{22_f} \\
\sigma_{11_{m1}} \\
\sigma_{33_{m1}} \\
\sigma_{11_{m2}}
\end{Bmatrix}
=
\begin{Bmatrix} f \\ \bar{\sigma} \end{Bmatrix}
-
\begin{bmatrix} P_1 \\ 8x12 \end{bmatrix}
\begin{Bmatrix}
\varepsilon_{m1}^I \\
\varepsilon_{m2}^I \\
\varepsilon_{m3}^I
\end{Bmatrix}
\tag{164}
$$

where the inelastic strain term for each region, r, is represented by

$$
\varepsilon_r^I =
\begin{Bmatrix}
\varepsilon_{11}^I \\
\varepsilon_{22}^I \\
\varepsilon_{33}^I \\
\gamma_{12}^I
\end{Bmatrix}_r
\tag{165}
$$

and the forcing vector by

$$
\left\{ \frac{f}{\bar{\sigma}} \right\} = \left\{ \begin{array}{c} \alpha_{1_f}\Delta T \\ -\left(a\,\alpha_{2_f}+b\,\alpha_{2_m}\right)\Delta T + a\,S_{\eta_{11}}^{\delta}\,\sigma_{I_c} \\ \left(\alpha_{1_m}-\alpha_{1_f}\right)\Delta T \\ a\left(\alpha_{2_m}-\alpha_{2_f}\right)\Delta T + a\,S_{\eta_{11}}^{\delta}\sigma_{I_c} \\ a\left(\alpha_{3_m}-\alpha_{3_f}\right)\Delta T + a\,S_{\eta_{12}}^{\delta}\sigma_{I_c} \\ \bar{\sigma}_{11} \\ \bar{\sigma}_{22} \\ \bar{\tau}_{12} \end{array} \right\} \tag{166}
$$

The first five columns of the matrix, P, are

$$
\begin{bmatrix}
1 & 0 & 0 & -S_{11_f} & -S_{12_f} \\[2ex]
0 & -(a+b) & 0 & a\,S_{12_f} & a\,S_{22_f}+b\,S_{22_m}+a\,S_{\eta_{11}}^{\delta} \\[2ex]
0 & 0 & 0 & S_{11_f} & S_{12_f}\!-\,S_{12_m} \\[2ex]
0 & 0 & 0 & a\,S_{12_f} & a\left(S_{22_f}\!-\,S_{22_m}+S_{\eta_{11}}^{\delta}\right) \\[2ex]
0 & 0 & 0 & a\,S_{12_f} & a\left(S_{23_f}\!-\,S_{23_m}\right) \\[2ex]
0 & 0 & 0 & \dfrac{a^2}{(a+b)(a+c)} & 0 \\[2ex]
0 & 0 & 0 & 0 & 1 \\[2ex]
0 & 0 & \dfrac{(a+b)}{S_{44_m}\!\left(a\dfrac{A}{B}+b\right)} & 0 & 0
\end{bmatrix} \tag{167}
$$

169

and the last three columns are

$$
\begin{bmatrix}
0 & \dfrac{b}{a}S_{12_f} & 0 \\[2em]
bS_{12_m} & b\left(S_{23_m} - S_{23_f}\right) & 0 \\[2em]
-S_{11_m} & -S_{12_m} - \dfrac{b}{a}S_{12_f} & 0 \\[2em]
C - aS_{12_m} & -(a+b)\dfrac{S_{12_m}^2}{S_{11_m}} + b\left(S_{23_m} - S_{23_f}\right) & -C \\[2em]
-aS_{12_m} & D & 0 \\[2em]
\dfrac{ab}{(a+b)(a+c)} & \dfrac{cS_{12_m}}{(a+c)S_{11_m}} & \dfrac{c}{(a+c)} \\[2em]
\dfrac{cS_{11_m}}{(a+c)S_{12_m}} & 0 & \dfrac{-cS_{11_m}}{(a+c)S_{12_m}} \\[2em]
0 & 0 & 0
\end{bmatrix}
\qquad (168)
$$

where the values A, B, C, and D are given by

$$
A = \left(1 + \frac{c}{a}\right)\left(S_{44_f} + S_{t_{11}}^{\delta}\right)
\qquad (169)
$$

$$
B = S_{44_m} + \frac{c}{a}\left(S_{44_f} + S_{t_{11}}^{\delta}\right)
\qquad (170)
$$

$$C = (a+b)\left(S_{12_m} - \frac{S_{11_m}S_{22_m}}{S_{12_m}}\right) \qquad (171)$$

$$D = \left(c+\frac{bc}{a}\right)\left(\frac{S_{12_m}^2}{S_{11_m}} - S_{22_m}\right) - aS_{22_m} - b\left(S_{22_f} + S_{n_{12}}^\delta\right) \qquad (172)$$

The first four columns of the matrix, P_I, are

$$
\begin{bmatrix}
0 & 0 & 0 & 0 \\
0 & b & 0 & 0 \\
-1 & 0 & 0 & 0 \\
-(a+b)\dfrac{S_{22_m}}{S_{12_m}} & b & 0 & 0 \\
0 & 0 & -a & 0 \\
0 & 0 & 0 & 0 \\
\dfrac{c}{(a+c)\,S_{12_m}} & 0 & 0 & 0 \\
0 & 0 & 0 & \dfrac{-b}{\left(a\dfrac{A}{B}+b\right)\left(1+\dfrac{c}{a}\right)S_{44_m}}
\end{bmatrix}
\qquad (173)
$$

The second four columns of the matrix, P_I, are

171

$$
\begin{bmatrix}
0 & 0 & 0 & 0 \\
0 & 0 & 0 & 0 \\
0 & 0 & 0 & 0 \\
(a+b)\dfrac{S_{22_m}}{S_{12_m}} - a\dfrac{S_{12_m}}{S_{11_m}} & -b & 0 & 0 \\
c\dfrac{S_{12_m}}{S_{11_m}} & 0 & -c & 0 \\
\dfrac{ac}{(a+b)(a+c)S_{11_m}} & 0 & 0 & 0 \\
\dfrac{-c}{(a+c)S_{12_m}} & 0 & 0 & 0 \\
0 & 0 & 0 & \dfrac{-b\,c/a}{\left(a\dfrac{A}{B}+b\right)\left(1+\dfrac{c}{a}\right)S_{44_m}}
\end{bmatrix}
\qquad (174)
$$

and the last four columns of the matrix, P_I, are

$$
\begin{bmatrix}
0 & 0 & 0 & 0 \\[2ex]
0 & 0 & 0 & 0 \\[2ex]
0 & 0 & 0 & 0 \\[2ex]
a\dfrac{S_{12_m}}{S_{11_m}} & -a & 0 & 0 \\[2ex]
-c\dfrac{S_{12_m}}{S_{11_m}} & 0 & c & 0 \\[2ex]
\dfrac{-ac}{(a+b)(a+c)S_{11_m}} & 0 & 0 & 0 \\[2ex]
0 & 0 & 0 & 0 \\[2ex]
0 & 0 & 0 & \dfrac{-a\left(1-\dfrac{S_{44_m}}{B}\right)}{\left(a\dfrac{A}{B}+b\right)\left(1+\dfrac{c}{a}\right)S_{44_m}}
\end{bmatrix}
\tag{175}
$$

The above relations are now assembled in the subsequent section by employing the laminate relations outlined previously for the stresses and strains in a laminated composite under any arbitrary angle layup.

7.1.3 Micro to Macromechanics Equation Assembly

In order to avoid confusion between the use of the two coordinate systems (laminate and ply), a convention will be adopted and followed throughout this section where all stresses and strains that are in the global or laminate coordinate system will be written using Greek symbols and all stresses and strains that are in the local or ply coordinate system will be written in English symbols. Therefore, the micromechanics equations from the previous section may be rewritten as follows:

$$\begin{bmatrix} P \\ 8\times8 \end{bmatrix}_k \begin{Bmatrix} \bar{e}_k \\ s_k^{reg} \end{Bmatrix} = \begin{Bmatrix} f_k \\ \bar{s}_k \end{Bmatrix} - \begin{bmatrix} P_I \\ 8\times12 \end{bmatrix}_k \begin{Bmatrix} e_k^I \end{Bmatrix} \tag{176}$$

where the subscript, k, denotes the particular ply, and the ply stresses and strains have been separated out in the vectors where they appear. Hence, s_k^{reg} and f_k represent 5x1 vectors where the former is all the region stresses of Eq (164) and the latter is the vector, f, in Eq (166). Also, the vector of inelastic strains contains all the matrix regions for a single ply.

From Eq (162) it can be shown that

$$\{\bar{e}_k\} = [T]^{-T} \{\bar{\epsilon}_k\} \tag{177}$$

Also, if the first three columns of the P matrix in Eq (176) are separated out, then by employing Eqs (177) and (160)

174

$$\begin{bmatrix} P_A \\ 8x3 \end{bmatrix}_k [T]_k^{-T} \{\bar{\varepsilon}_k\} + \begin{bmatrix} P_B \\ 8x5 \end{bmatrix}_k \{s_k^{reg}\} = \begin{Bmatrix} f_k \\ [T]_k \bar{\sigma}_k \end{Bmatrix} - \begin{bmatrix} P_I \\ 8x12 \end{bmatrix}_k \{e_k^I\} \quad (178)$$

where the ply stresses and strains have been transformed into the global or laminate coordinate system.

Further, by employing equation (152) the micromechanics relations of Eq (178) may be cast in terms of the laminate midplane strain and curvature as

$$\begin{bmatrix} P_A \\ 8x3 \end{bmatrix}_k [T]_k^{-T} \begin{bmatrix} 1 & \tilde{z}_k \end{bmatrix} \begin{Bmatrix} {}_o\varepsilon \\ \kappa \end{Bmatrix} + \begin{bmatrix} P_B \\ 8x5 \end{bmatrix}_k \{s_k^{reg}\} =$$

$$\begin{Bmatrix} f_k \\ [T]_k \bar{\sigma}_k \end{Bmatrix} - \begin{bmatrix} P_I \\ 8x12 \end{bmatrix}_k \{e_k^I\} \quad (179)$$

where $\tilde{z}$ is the distance from the midplane of the laminate to the center of the given ply, k.

Eq (179) applies for each individual ply. Therefore, a larger set of equations for all plies of the composite system may be assembled. Such a set of equations for all plies 1 through n of a given composite system are given below in a single matrix format as

$$
\begin{bmatrix}
PT_1 & P_{B_1} & 0 & \cdots & 0 \\
PT_2 & 0 & P_{B_2} & \cdots & 0 \\
\vdots & \vdots & & & \\
PT_n & 0 & 0 & \cdots & P_{B_n}
\end{bmatrix}
\begin{Bmatrix}
{}_o\varepsilon \\ \kappa \\ s_1^{reg} \\ s_2^{reg} \\ \vdots \\ s_n^{reg}
\end{Bmatrix}
=
\begin{Bmatrix}
f_1 \\ 0 \\ f_2 \\ 0 \\ \vdots \\ f_n \\ 0
\end{Bmatrix}
+
$$

$$
\begin{bmatrix}
0 & 0 & \cdots & 0 \\
T_1 & 0 & \cdots & 0 \\
0 & 0 & \cdots & 0 \\
0 & T_2 & \cdots & \\
 & 0 & & \\
 & & & 0 \\
0 & & \cdots & T_n
\end{bmatrix}
\begin{Bmatrix}
\bar\sigma_1 \\ \bar\sigma_2 \\ \bar\sigma_3 \\ \vdots \\ \bar\sigma_n
\end{Bmatrix}
-
\begin{Bmatrix}
[P_{I_1}]e_1^I \\
[P_{I_2}]e_2^I \\
[P_{I_3}]e_3^I \\
\vdots \\
[P_{I_n}]e_n^I
\end{Bmatrix}
\tag{180}
$$

where the quantity, PT, is defined as

$$
[PT]_k = [P_A]_k [T]_k^{-T} [\; I \;\; I\tilde{z}_k \;]
\tag{181}
$$

Also, from Eq (158) it is recognized that

$$
\begin{Bmatrix}
\bar\sigma_1 \\ \bar\sigma_2 \\ \bar\sigma_3 \\ \vdots \\ \bar\sigma_n
\end{Bmatrix}
=
\begin{bmatrix}
& H &
\end{bmatrix}^{-1}
\begin{Bmatrix}
N \\ M \\ \bar\sigma_3 \\ \vdots \\ \bar\sigma_n
\end{Bmatrix}
\tag{182}
$$

Therefore, substituting Eq (182) into Eq (180) results in

176

$$\begin{bmatrix} PT_1 & P_{B_1} & 0 & \cdots & 0 \\ PT_2 & 0 & P_{B_2} & \cdots & 0 \\ \vdots & \vdots & \vdots & \ddots & \vdots \\ PT_n & 0 & 0 & \cdots & P_{B_n} \end{bmatrix} \begin{Bmatrix} _o\varepsilon \\ \kappa \\ s_1^{reg} \\ s_2^{reg} \\ \vdots \\ s_n^{reg} \end{Bmatrix} = \begin{Bmatrix} f_1 \\ 0 \\ f_2 \\ 0 \\ \vdots \\ f_n \\ 0 \end{Bmatrix} +$$

(183)

$$\begin{bmatrix} & TH & \end{bmatrix} \begin{Bmatrix} N \\ M \\ \bar{\sigma}_3 \\ \vdots \\ \bar{\sigma}_n \end{Bmatrix} - \begin{Bmatrix} [P_{I_1}]e_1^I \\ [P_{I_2}]e_2^I \\ [P_{I_3}]e_3^I \\ \vdots \\ [P_{I_n}]e_n^I \end{Bmatrix}$$

where

$$\begin{bmatrix} & TH & \end{bmatrix} = \begin{bmatrix} 0 & 0 & \cdots & 0 \\ T_1 & 0 & \cdots & 0 \\ 0 & 0 & \cdots & 0 \\ 0 & T_2 & \cdots & \vdots \\ & 0 & & \\ \vdots & & \ddots & 0 \\ 0 & & \cdots & T_n \end{bmatrix} \begin{bmatrix} & H & \end{bmatrix}^{-1}$$

(184)

Each zero term in Eq (184) represents a 5x3 zero matrix, so considering that [H] is a 3n x 3n matrix as defined by Eq (159), then the matrix [TH] is an 8n x 3n matrix. If all but the first six columns of the [TH] matrix are moved to the left-hand side of the equation, then a final form for the micro to macromechanics equations is obtained which relates the composite strain and region and ply stresses to the applied thermome-

177

chanical load and existing inelastic material strain of each region. The general form of this relation is

$$
\begin{bmatrix}
PT_1 & P_{B_1} & 0 & \cdots & 0 & TH_{13} & TH_{14} & \cdots & TH_{1n} \\
PT_2 & 0 & P_{B_2} & \cdots & 0 & TH_{23} & TH_{24} & \cdots & TH_{2n} \\
\vdots & \vdots & \vdots & & \vdots & \vdots & \vdots & & \vdots \\
PT_n & 0 & 0 & \cdots & P_{B_n} & TH_{n3} & TH_{n4} & \cdots & TH_{nn}
\end{bmatrix}
\begin{Bmatrix}
{}_o\varepsilon \\
\kappa \\
s_1^{reg} \\
s_2^{reg} \\
\vdots \\
s_n^{reg} \\
\bar{\sigma}_3 \\
\bar{\sigma}_4 \\
\vdots \\
\bar{\sigma}_n
\end{Bmatrix}
=
$$

$$
\begin{Bmatrix}
f_1 \\
0 \\
f_2 \\
0 \\
\vdots \\
f_n \\
0
\end{Bmatrix}
+
\begin{bmatrix}
TH_{11} & TH_{12} \\
TH_{21} & TH_{22} \\
\vdots & \\
TH_{n1} & TH_{n2}
\end{bmatrix}
\begin{Bmatrix} N \\ M \end{Bmatrix}
-
\begin{Bmatrix}
[P_{I_1}] e_1^I \\
[P_{I_2}] e_2^I \\
[P_{I_3}] e_3^I \\
\vdots \\
[P_{I_n}] e_n^I
\end{Bmatrix}
\qquad (185)
$$

where each TH term represents an 8x3 matrix, each P_B term is an 8x5 matrix, and each PT term is an 8x6 matrix defined by Eq (181). Therefore, the controlling matrix premultiplying the vector on the left-hand side of the equation is an 8n x 8n matrix which may be inverted to obtain the overall laminated composite inelastic response.

Equation (185) when coupled with the micromechanics equations of chapter 3 as modified in section 7.1.1 and the nonlinear formulations of chapters 4 through 6 results in a very versatile three-dimensional nonlin-

ear micromechanics formulation which may easily be applied to the mac-romechanical behavior of laminated composites. The method is compu-tationally efficient as the load is automatically distributed between the various plies according to the classical laminated plate theory assump-tions by assembling a matrix formulation that extends from the microme-chanics all the way through the laminate level.

7.2 Laminate Analysis Results

A computer program has been developed in conjunction with this study which solves for nonlinear composite behavior of symmetric lami-nates by assembling the equations described in the previous section and employing the various nonlinear material and interfacial failure models of chapters 5 and 6 along with their respective algorithms. Results from the present formulation were compared with Aboudi's method of cells (75), the finite element and experimental results of Lerch and Melis (76), and the experimental results of Nicholas et. al. (67).

First, results from monotonic quasi-static loading was investigated and compared with available data. Then, a parametric investigation was undertaken to examine the effects of various types of loading on the in-elastic composite behavior. For instance, the effect of different levels of interfacial failure on the strain accumulation during cyclic loading as well as the effect of various loading rates on the composite response. Also, the effects of in-phase and out-of-phase thermomechanical fatigue (TMF) loading on the laminate behavior was also investigated. Lastly, comparisons with experimental data from TMF tests and fatigue life pre-dictions using the present approach coupled with the Linear Life Frac-

tion Model (LLFM) are made (77).

7.2.1 Quasi-Static Results

Investigations into the inelastic behavior of various SCS6/Ti-15-3 layups have recently been conducted (75, 76). The present formulation is compared to some of the results of these studies to validate the analysis. For instance, Figure 84 presents the longitudinal response of a $[0/\pm 15]_s$ SCS6/Ti-15-3 layup as calculated by the present method and Aboudi's method of cells. Both analyses predict essentially the same response. The matrix material was assumed to behave according to the Bodner-Partom unified viscoplastic theory with isotropic hardening.

Figure 84. $[0/\pm 15]_s$ SCS6/Ti-15-3 Longitudinal Response as Calculated by the Present Analysis and Aboudi's Model (75)

This material model is the only one presently available in Aboudi's model, and hence, was employed with the present analysis along with the same material constants that were used in Aboudi's study so that a direct comparison could be made. Cooldown was simulated by a change in temperature of -1111.°C before the mechanical load was applied.

A further comparison with the $[0/\pm15]_s$ layup is presented in Figure 85 for the in-plane shear response of the laminate. The two approaches again show excellent agreement with a maximum percent deviation between the two of less than 10% at any point. Both methods predict the onset of inelastic behavior at approximately 450 MPa, and the same trend is observed here in the laminate analysis as was found in the unidi-
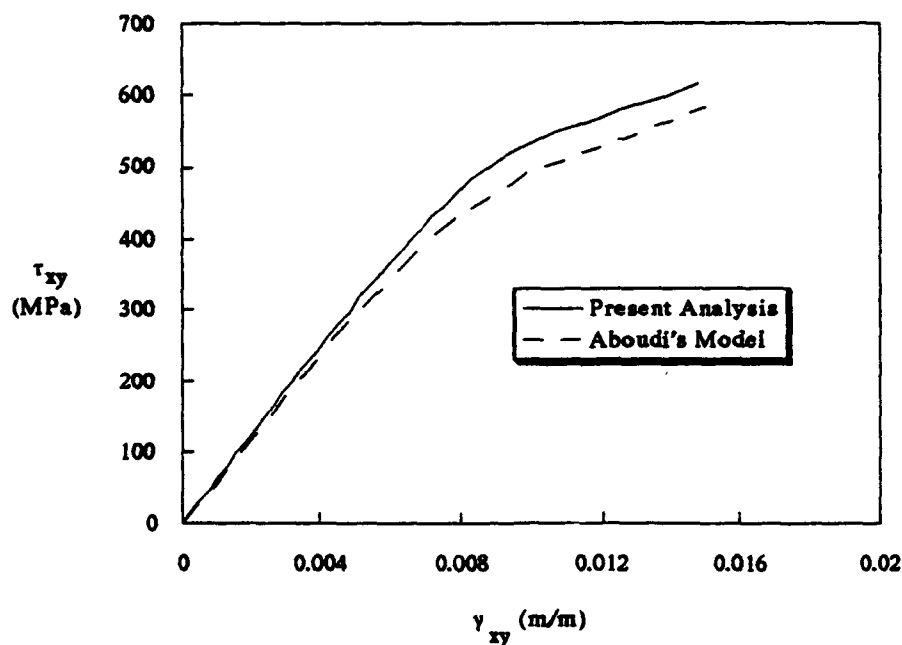
Figure 85. $[0/\pm15]_s$ SCS6/Ti-15-3 In-Plane Shear Response as Calculated by the Present Analysis and Aboudi's Model (75)

rectional results of chapters 4 and 5 when in-plane shear solutions were compared between the present formulation and Aboudi's method of cells model. The present analysis predicts a slightly stiffer response than the method of cells for in-plane shear, but as was discussed in these earlier chapters, this is consistent with the assumptions of the two models.

Results from a $[0/\pm45]_s$ laminate is displayed in Figure 86, and just as for the $[0/\pm15]_s$ case, the two mathematical models are in excellent agreement. The slightly weaker response of Aboudi's model is most likely due to the 45° plies which contribute to the overall composite response largely through shear, and therefore, will produce a weaker response in Aboudi's model as was previously observed for in-plane shear.
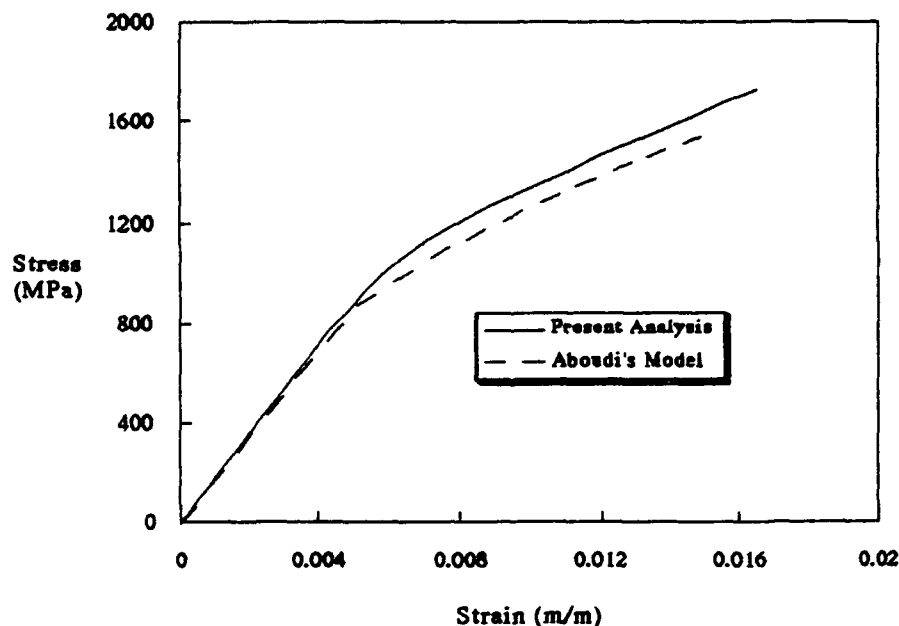
Figure 86. $[0/\pm45]_s$ SCS6/Ti-15-3 Longitudinal Response as Calculated by the Present Analysis and Aboudi's Model (75)

182

A final comparison with Aboudi's method of cells model is made in Figure 87. A quasi-isotropic layup, $[0/\pm45/90]_s$, is considered and comparisons were made for its longitudinal response. The calculations employed a change in temperature of -1111.°C followed by the mechanically applied load. The method of cells approach assumes a perfect fiber/matrix contact or strong interface. Therefore, two calculations were performed with the present analysis. First, a strong interface was assumed to compare with Aboudi's model, and then, calculations were performed using the progressive interfacial failure model developed in chapter 6 with the same interfacial parameters that were employed in the
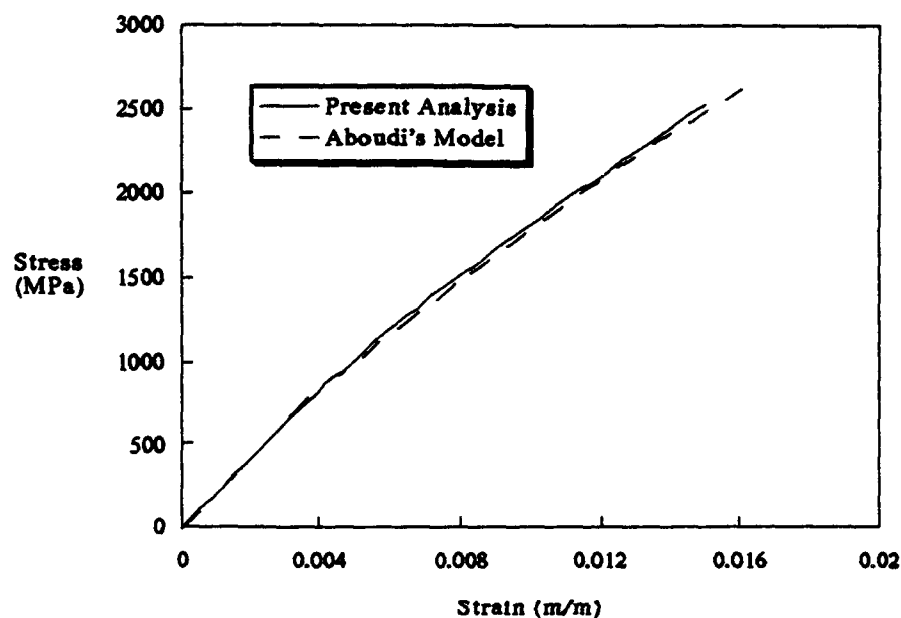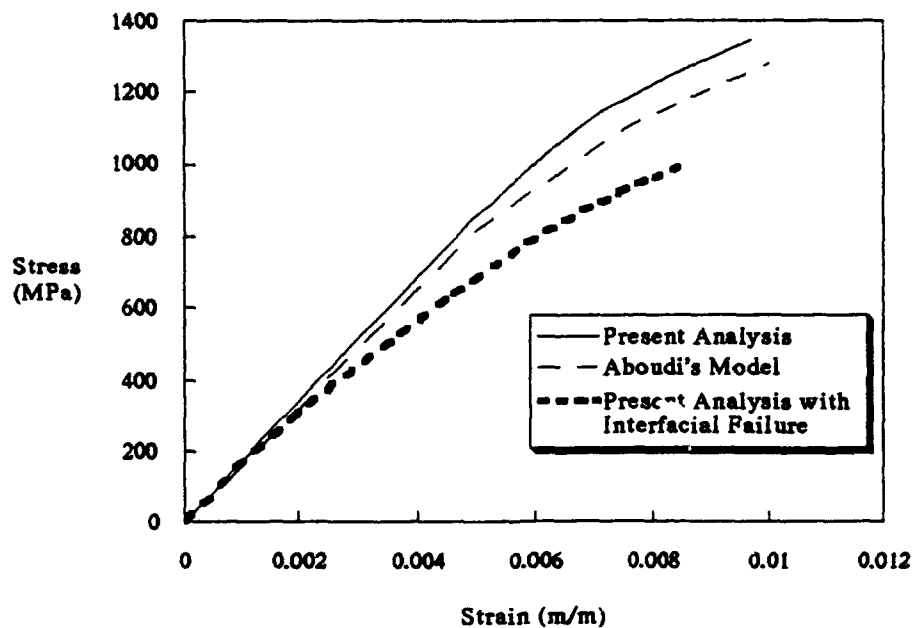
Figure 87. $[0/\pm45/90]_s$ SCS6/Ti-15-3 Longitudinal Response as Calculated by the Present Analysis and Aboudi's Model (75)

183

previous chapter for SCS6/Ti-15-3. Only failure normal to the fiber was assumed to occur, so shear failure in the 45° plies are not accounted for in the calculations of Figure 86. The results demonstrate that the inclusion of interfacial failure has a pronounced effect on the behavior. If shear failure along the fiber was also considered, then there would be even a greater difference between the strong fiber/matrix contact calculations and the calculations possessing interfacial failure. Therefore, for composite systems that exhibit less than perfect fiber/matrix bonding, an analytical model that employs some method for interfacial failure should be used.

A limited amount of finite element data has been published for laminated composites. Developing a reasonable finite element grid for various layups is very difficult, and therefore, solutions from very simple layups such as crossply laminates, $[0/90]_s$, are generally the most that can be accomplished. Lerch and Melis (76) have performed nonlinear finite element calculations of an SCS6/Ti-15-3 crossply laminate with a 432 element grid on a CRAY YMP and compared their results to experimental data. Figure 88 displays their results along with calculations using the laminate analysis of the present study. The loading sequence consisted of cooldown from 705°C which was assumed to be the stress free state to 21°C followed by monotonic loading. The finite element calculations employed an elastic-plastic material model for the matrix and assumed an unbonded fiber/matrix interface. The present analysis employed the unified viscoplastic theory of Bodner and Partom with directional hardening for the matrix and the interfacial failure model of the previous chapter for the interface. In this case, the present formula-
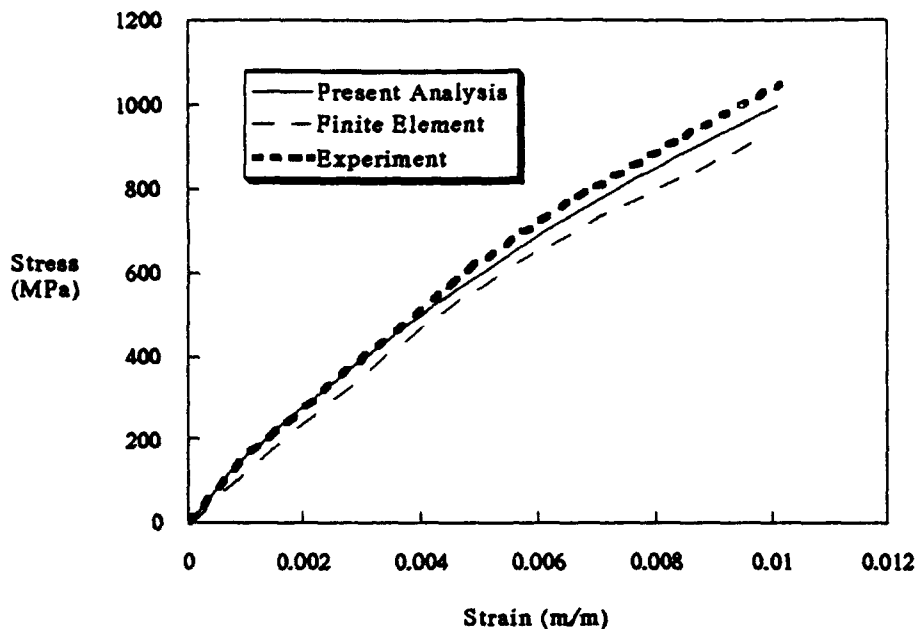
Figure 88. [0/90]ₛ SCS6/Ti-15-3 Longitudinal Response as Calculated
by the Present Analysis with Comparisons to Experiment
and Finite Element Data (76)

tion agrees with the experimental results better than does the computa-
tionally intensive finite element calculations. The present formulation
assumes a more exact model of the fiber/matrix interface than the finite
element solution which assumes it to be perfectly weak. Therefore, sep-
aration of the fiber/matrix contact in the 90° plies occurs very early in
the finite element solution while it is delayed in the present analysis due
to the finite fiber/matrix bond strength until it more reasonably approxi-
mates the experiment.

A comparison of the transverse strain during loading for the crossply
laminate of the previous paragraph is presented in Figure 89. Just as
was observed for the longitudinal strain, the experimental transverse

185
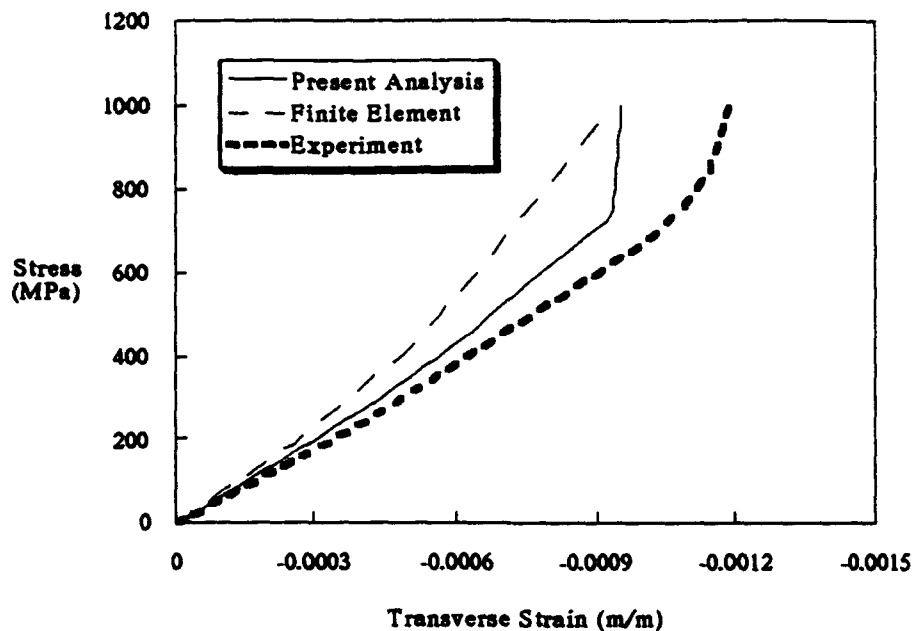
Figure 89. [0/90]ₛ SCS6/Ti-15-3 Transverse Strain Under Longitudinally Applied Load as Calculated by the Present Analysis and Compared to Experiment and Finite Element Data (76)

strain is more closely approximated by the present analysis than by the finite element approach. In addition, both the present analysis and experiment indicate a sharp decrease in the incremental transverse strain during load at approximately 700 MPa. This corresponded to complete interfacial failure in the micromechanics which would result in a decreased Poisson's ratio, and hence, less transverse strain during increased load. Also, failure of the composite in the experiment occurred at 1060 MPa which is beyond the point of complete interfacial failure as predicted by the micromechanics. Therefore, if complete interfacial failure is a mechanism that occurs in these types of composites before

186

failure of the material, then a means of estimating when composite failure is imminent may be achieved by accurately predicting the interfacial failure.

Moreover, the present micro to macromechanics formulation can reliably predict nonlinear laminated composite behavior under monotonic and quasi-static loading conditions. Attempting to model the composite behavior with what some would consider to be a more mathematically rigorous approach such as the finite element method meets with grave difficulty due to the computational intensity and inability to produce representative finite element grids. This was demonstrated in the Lerch and Melis (76) study whose results are given in Figures 88 and 89. In their study the nonlinear finite element results for a simple crossply symmetric laminate under monotonically increasing load required the use of a CRAY-YMP supercomputer. If more complex composite layups or cyclic thermomechanical loading was desired, then the use of the finite element method would be prohibitive. All calculations of the present analysis presented so far were performed on an Apple Macintosh IIx desktop computer and for the majority of the remaining solutions presented in the following sections with the exception of a few calculations which were carried out to several thousand cycles and performed on a SUN 4 workstation.

7.2.2 A Parametric Study of MMC Laminates

Now that a reliable analytical tool is available for predicting the nonlinear behavior of MMC laminates, the effects of various parameters such as the type of layup, loading rate, and type of loading on the com-

posite behavior and constituent microstresses may be examined. Thus, a better understanding of the composite characteristics may be achieved without the necessity of performing extensive experimental work. The present section will look at the effects of these parameters, and in the next section, some of the characteristics that were observed here will be verified with comparison to available experimental data.

Figures 90 through 93 compare the effects of two types of loading on the characteristics of a [0/90]$_s$ crossply laminate. In-phase, and out-of-phase thermomechanical fatigue loads were applied to an SCS6/Ti-β21S composite layup. For both cases the composite was assumed to be stress free at a processing temperature of 900°C and then cooled to room temperature at 25°C followed by increasing the temperature to the desired starting temperature for the loading. For the in-phase case this consisted of 150°C and for the out-of-phase case it was further heated to 650°C. Each case was then loaded to 30 MPa before beginning the cyclic loading which corresponded to a triangular waveform for both the mechanical load and temperature with a period of 180 seconds. The mechanical applied load was cycled between 30 and 300 MPa, and the temperature was cycled between 150 and 650°C. Figures 90 and 91 present the stress-strain histories for the first and tenth cycles for both types of loading. The thermal strain has been subtracted out so that only the mechanical strain is plotted in each figure. A 35% fiber volume fraction was assumed, and a weak interface was assumed so that fiber/matrix separation occurs once the compressive residual stress at the interface is overcome. The matrix material was assumed to behave according to the Bodner-Partom unified viscoplastic theory with direc-
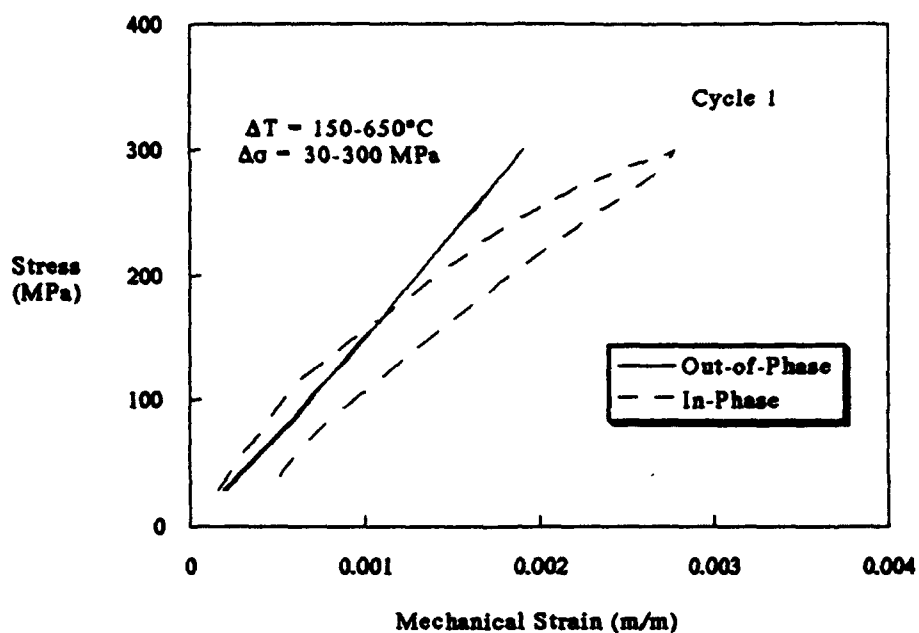
Figure 90. [0/90]$_s$ SCS6/Ti-β21S TMF Response to In-Phase and Out-of-Phase Load — Cycle 1
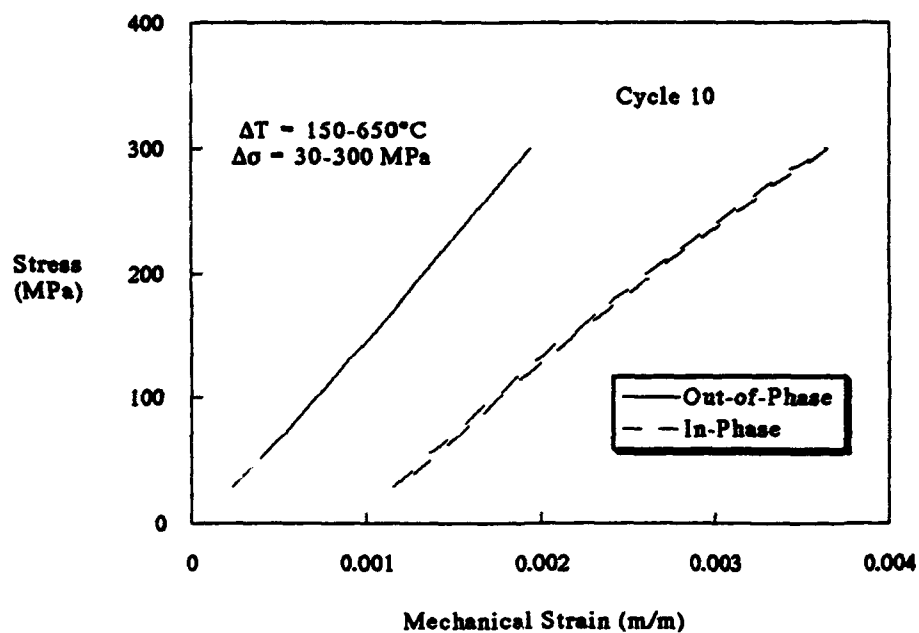
Figure 91. [0/90]$_s$ SCS6/Ti-β21S TMF Response to In-Phase and Out-of-Phase Load — Cycle 10

189

tional hardening and the material constants for the model were the same as used in chapter 5 where similar cyclic data were obtained for the unidirectional composite. The trends that were observed in the unidirectional calculations for in-phase and out-of-phase loading are very similar to what is presented for the crossply laminate. The out-of-phase response is essentially linear elastic while the in-phase solution exhibits significant viscoplastic deformation within the first cycle and accumulates considerable permanent strain after ten cycles. Further insight is gained by examining the maximum and minimum mechanical strain for each cycle as plotted in Figure 92. The out-of-phase results produce very little plastic strain accumulation over one thousand cycles. Therefore, any strain accumulation that might be observed in an experiment
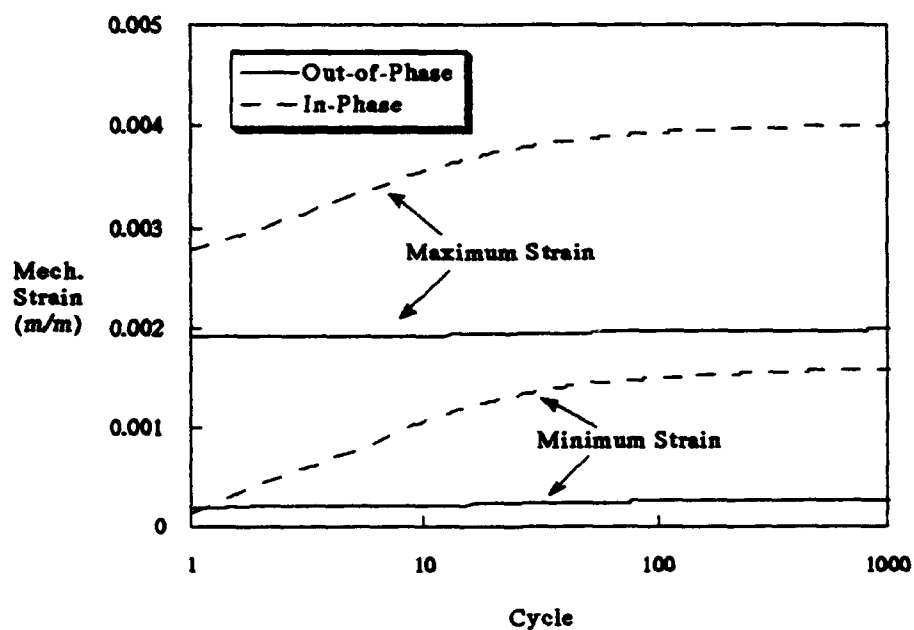
Figure 92. [0/90]$_s$ SCS6/Ti-β21S TMF In-Phase and Out-of-Phase Maximum and Minimum Strain Histories

190

would most likely be due to damage progression in the form of fiber or matrix cracks rather than any viscoplastic relaxation of the material. On the other hand, the viscoplastic effects for the in-phase load is very prevalent up through the first one hundred cycles at which point the stress relaxation of the matrix through viscoplasticity is nearly complete.

The maximum constituent microstresses in the direction of load for the 0° ply is plotted in Figure 93. The most dominant characteristic observed in the microstresses is the difference in the maximum stress in the fiber between in-phase and out-of-phase loads. For the in-phase calculations the maximum fiber stress approaches 1300 MPa while for the out-of-phase case the fiber is under mild compression throughout. In
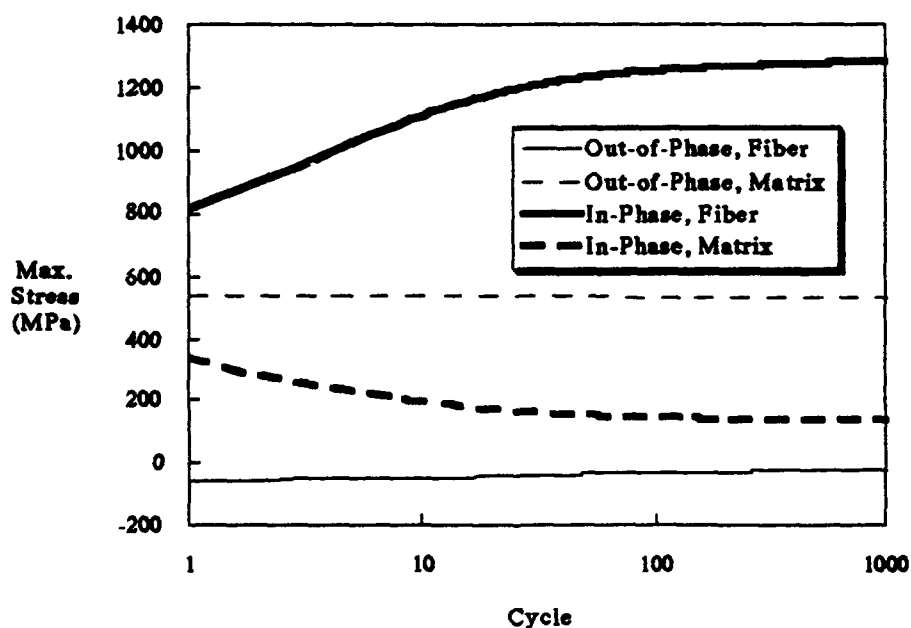
Figure 93. [0/90]ₛ SCS6/Ti-β21S Constituent Microstresses in 0° Ply for In-Phase and Out-of-Phase Loads

191

addition, the matrix experiences a much larger stress level in the out-of-phase solutions than it does for the in-phase load. Therefore, matrix cracking would most likely be the dominant mode of failure under out-of-phase loads while fiber cracking would be the dominant mode under in-phase loads.

The effect of varying the cycle frequency on the in-phase TMF load described in the previous paragraphs is plotted in Figures 94 and 95. Increasing and decreasing the loading rate was found to have a pronounced effect on the composite response. Although the initial stress-strain response during increasing load on the first cycle is unaffected by varying the cycle period, once viscoplasticity becomes prevalent at approximately 280 MPa, the strain accumulation for the longer cycles increases sig-
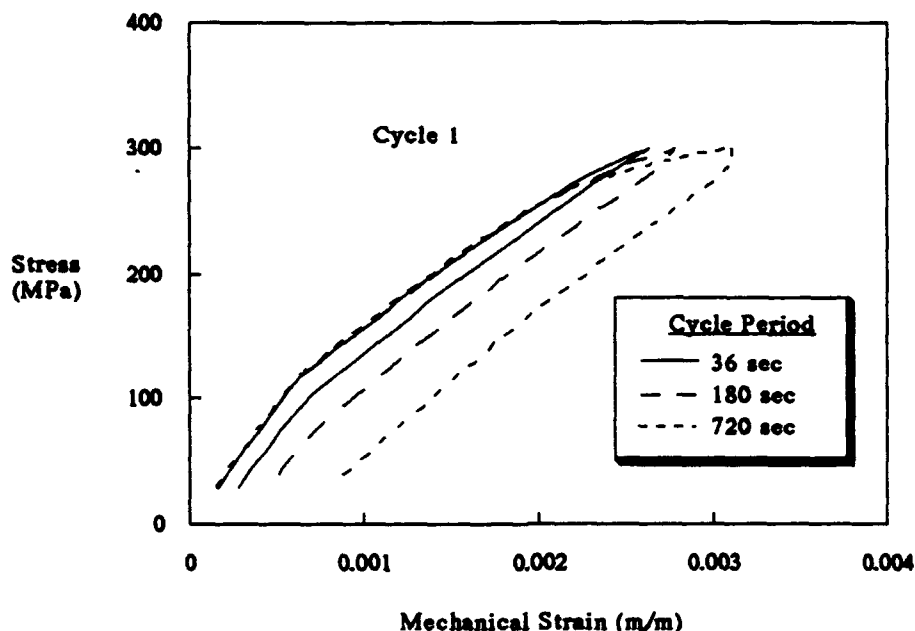
Figure 94. Effect of Cycle Period on the In-Phase TMF Stress-Strain Response of [0/90]$_s$ SCS6/Ti-β21S
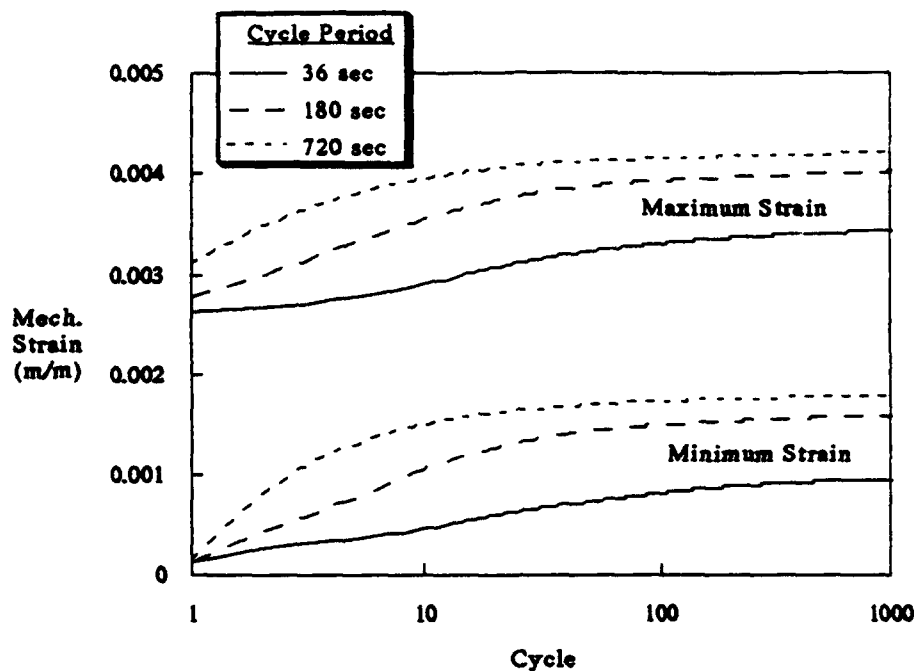
Figure 95. Effect of Cycle Period on the In-Phase TMF Strain History of [0/90]$_s$ SCS6/Ti-β21S

nificantly. For the 36 second cycle, the unloading portion of the curve also possesses a knee which corresponds to the fiber and matrix in the 90° ply again coming in contact upon unload. In addition, the maximum and minimum strain histories (Figure 95) show that the effect of varying the loading rate is still prevalent even after one thousand cycles at which point the strain accumulation per cycle for all three cases is very small. For instance, if the number of cycles is greatly increased for the short cycle time (36 sec) case, then the strain accumulation per cycle on a logarithmic plot becomes approximately linear as it approaches 50,000 cycles (Figure 96).
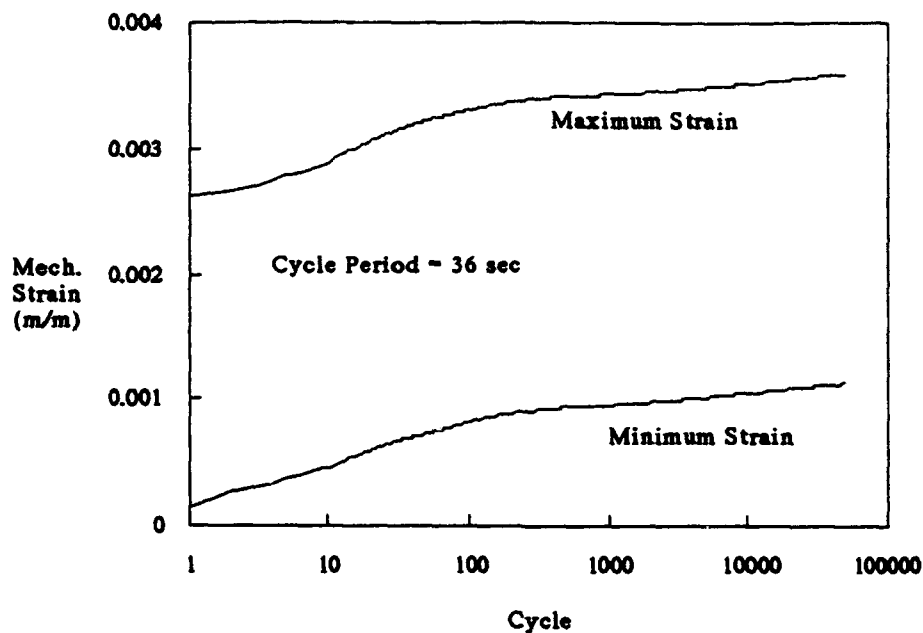
Figure 96. In-Phase TMF Strain History of [0/90]ₛ SCS6/Ti-β21S to 50,000 Cycles

The effect of a quasi-isotropic composite layup, $[0/\pm45/90]_s$, as opposed to the crossply composite layup already discussed is depicted in Figures 97 and 98. The same in-phase and out-of-phase loading sequences with the 180 sec cycle period were performed for the quasi-isotropic layup as were performed for the crossply laminate. Similar results were observed in the first cycle behavior for both composites. For example, the out-of-phase response is essentially linear elastic while the in-phase load experiences significant plastic deformation in the first cycle. In addition, the stress-strain response of the quasi-isotropic laminate almost traces that of the crossply over the first cycle for both types of loading. However, when the maximum and minimum strain history of

194
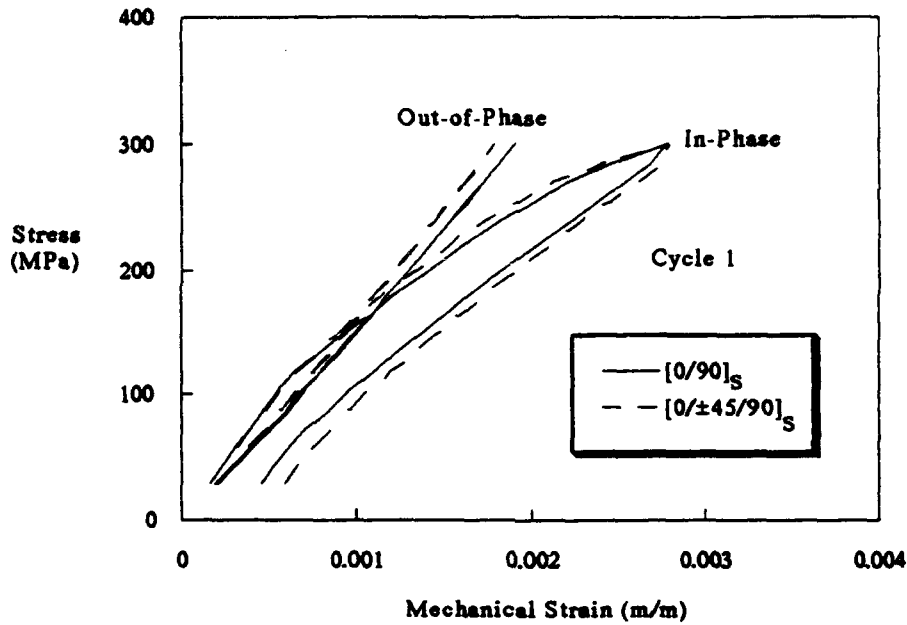
Figure 97. Effect of Composite Layup on First Cycle Stress-Strain Response
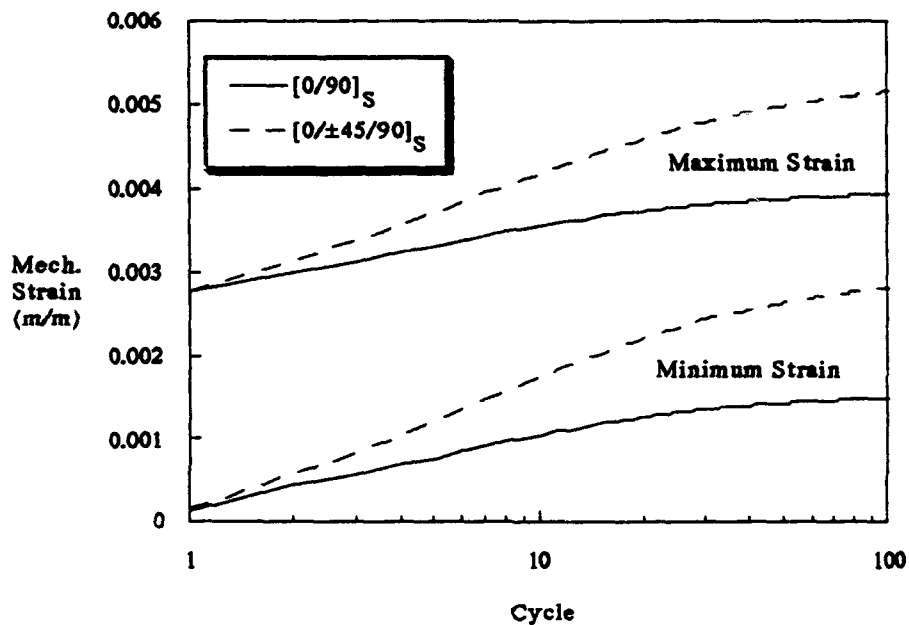
Figure 98. Effect of Composite Layup on the Strain History for an In-Phase TMF Load

195

the two laminates for the in-phase cases are compared as in Figure 98, it is found that the quasi-isotropic laminate experiences a much greater accumulation of strain over one hundred cycles. The maximum and minimum strain history for the out-of-phase cases are not plotted since they are basically linear elastic and experience little or no strain accumulation with subsequent cycles.

The effect of employing the interfacial failure model of chapter 6 on the strain accumulation of a crossply SCS6/Ti-15-3 laminate for two in-phase TMF load profiles is presented in Figures 99 and 100. The solutions from a strong interface and also a weak interface are plotted alongside for comparison. Figure 99 presents results from an in-phase TMF cycle whose maximum stress is well above the point at which interfacial
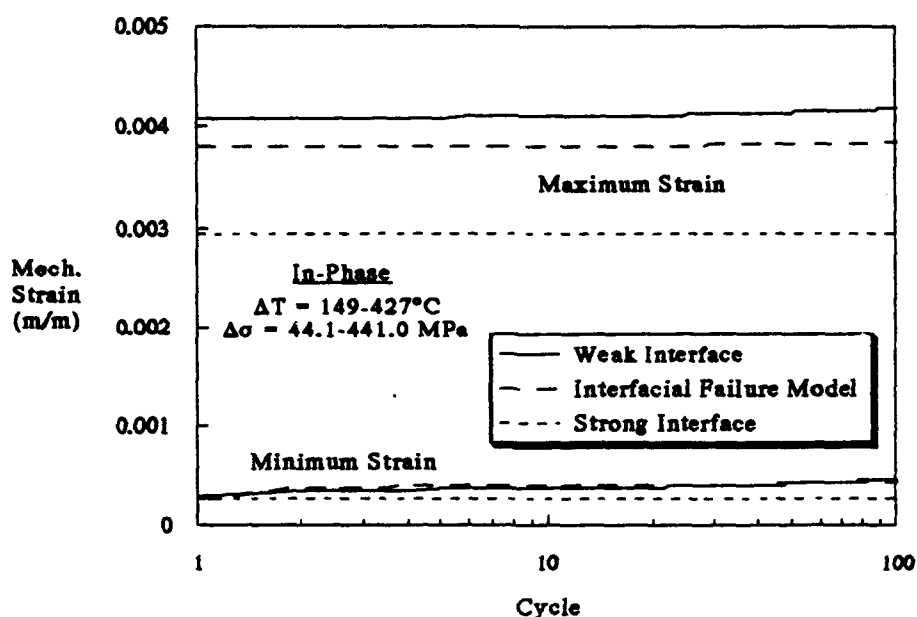
Figure 99. Effect of Interfacial Failure on the Strain History of [0/90]$_s$ SCS6/Ti-15-3 — High Stress Range (441 MPa Max.)
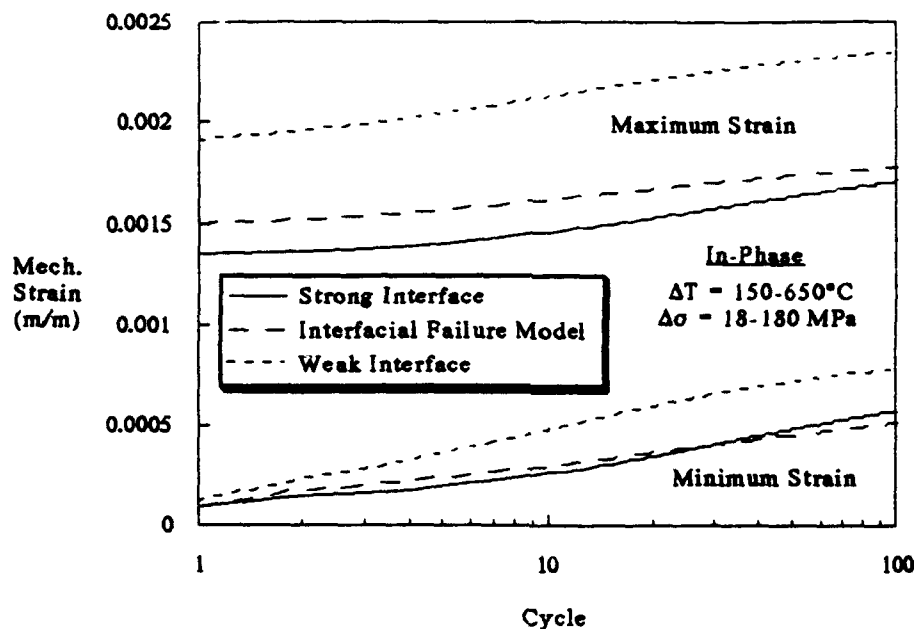
Figure 100. Effect of Interfacial Failure on the Strain History of [0/90]ₛ
SCS6/Ti-15-3 — Low Stress Range (180 MPa Max.)

failure begins, and therefore, may be approximated by assuming the in-
terface is weak. In addition, very little viscoplastic strain accumulation
from cycle to cycle is observed for this TMF sequence which possesses a
lower maximum temperature (427°C) and shorter period (48 sec) than
most of the previous TMF cycles presented in this section. On the other
hand, Figure 100 presents the results of an in-phase TMF cycle charac-
terized by more extensive viscoplastic deformation due to a higher maxi-
mum temperature (650°C) and longer cycle period (180 sec). The maxi-
mum stress of this cycle is very close to the point at which interfacial
failure begins to occur in the composite, and therefore, the microme-
chanics solution with the interfacial failure model behaves similarly to

197

the strong interface calculations. However, the calculations of Figure 99 for the interfacial failure model were closer to a weak interface. This indicates that before assuming either a strong or weak interface for a given composite, the loading environment must also be considered.

7.2.3 Experimental Comparisons and Fatigue Life

Experimental data for crossply and quasi-isotropic layups of the SCS6/Ti-β21S composite are compared in this section to the computational results of the micromechanics equations for laminates presented in section 7.1. Just as in the previous section, in-phase and out-of-phase TMF cycles are examined, but in this instance they are compared to experimental work (67).

Results from an in-phase TMF cycle are presented in Figures 101 and 102. The cycle consisted of simultaneously increasing both the temperature and applied load to their respective maximum values and then decreasing them simultaneously back to their minimum values over a 180 sec time interval. This included a change in temperature from 150°C to 650°C and a change in applied stress from 40 MPa to 400 MPa. The fiber/matrix interface was assumed to be weak normal to its face, and the temperature preload sequence was the same as employed in the previous section. The micromechanics demonstrates excellent agreement for the first few cycles of this TMF load. For instance, the calculations match the stress-strain plot of the first cycle very well, and continue to capture the slope of the stress-strain curve through the tenth cycle with only a slight 0.0003 m/m offset in strain which is most likely due to damage in the actual composite. The results plotted in Figure 102
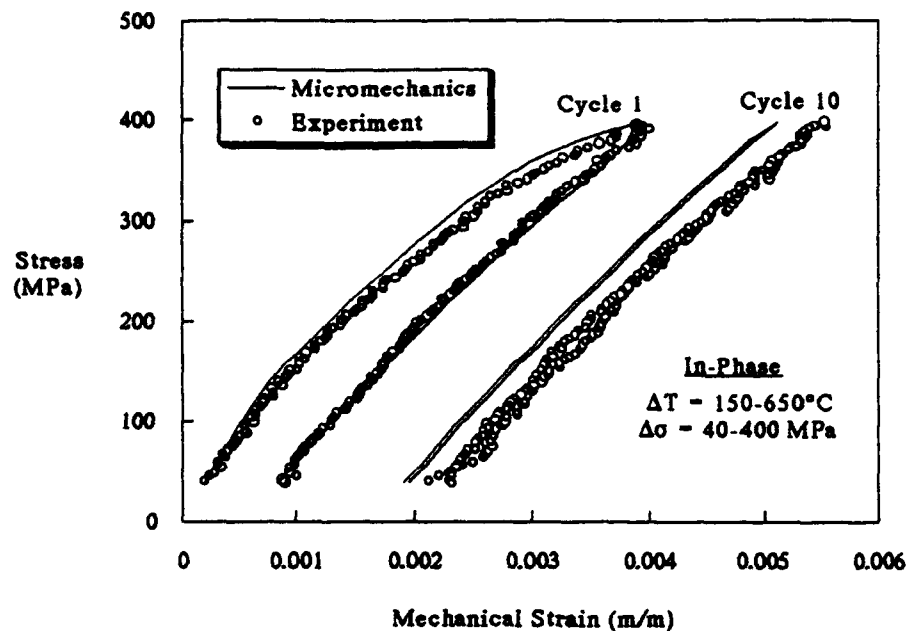
Figure 101. [0/90]ₛ SCS6/Ti-β21S Stress-Strain Response to In-Phase TMF — Comparison to Experiment (67)

also show this trend as the experimental data displays a greater accumulation of strain with increasing cycles. On the other hand, the micromechanics results show that the viscoplastic effects die out around 100 cycles causing the calculated strain accumulation to level off.

A comparison with an out-of-phase TMF cycle is presented in Figure 103 for the crossply laminate. The cycle time and change in temperature were the same as for the in-phase results of Figure 101 and 102, but the mechanically applied load was cycled between 30 MPa and 300 MPa out-of-phase with the temperature. Also, just as was observed in all previous out-of-phase results, the stress-strain response was essentially linear-elastic. Therefore, the maximum and minimum strain histories over
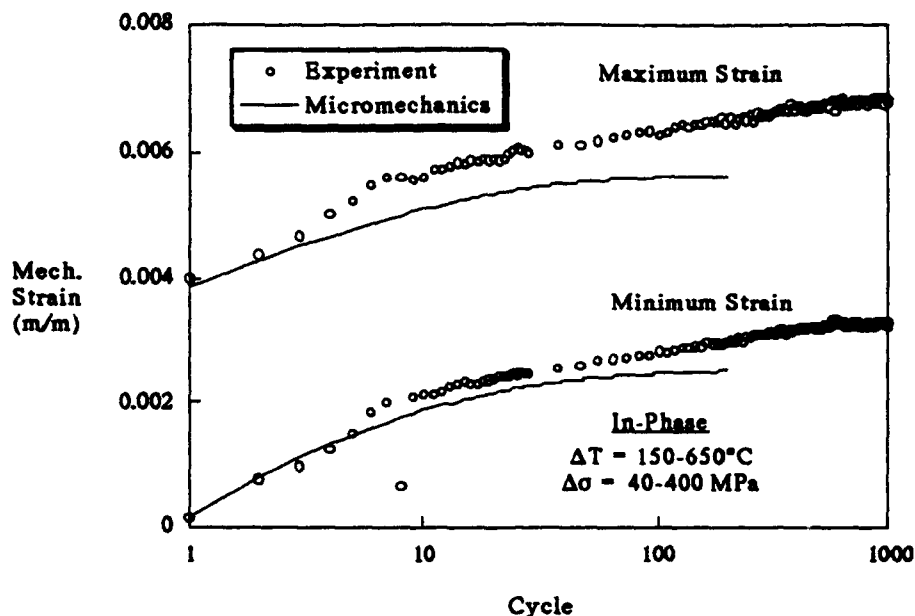
Figure 102. [0/90]$_s$ SCS6Ti-β21S Max-Min Strain History for an In-Phase TMF — Comparison to Experiment (67)

several cycles are not presented since very little strain accumulation occurs. The micromechanics results once again demonstrate excellent agreement with the experimental data.

In addition to the crossply, experimental results from a quasi-isotropic laminate were also compared to the micromechanics model. Figure 104 presents the composite stress-strain results of the first cycle for an in-phase TMF load. The cycle time and temperature were the same as for the crossply, but the applied load was cycled between 26 MPa and 260 MPa. The interface was assumed to be perfectly weak normal to its face, and three separate micromechanics calculations were made with each possessing its own unique properties tangential to the interface.

200
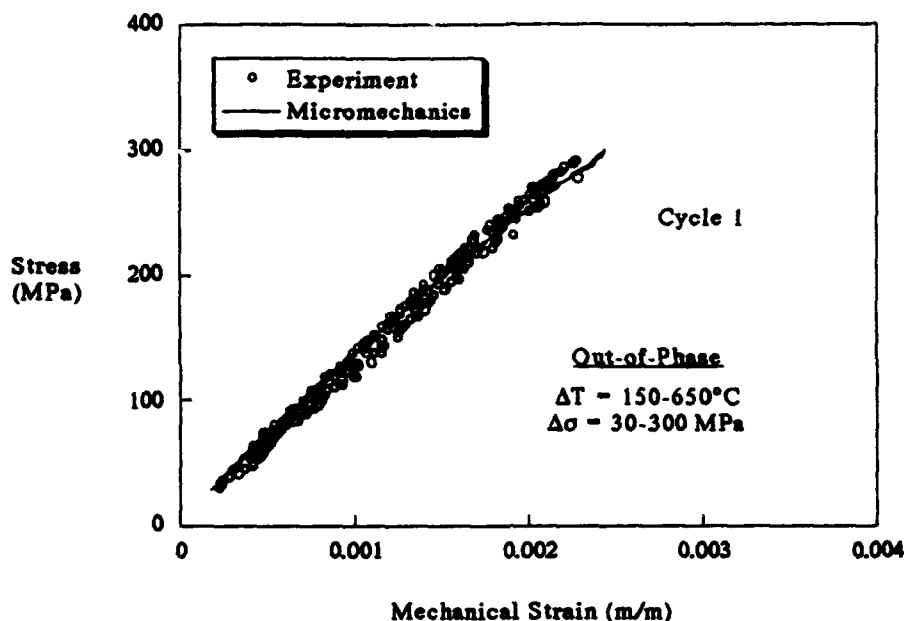
Figure 103. [0/90]₃ SCS6/Ti-β21S Stress-Strain Response to Out-of-Phase TMF — Comparison to Experiment (67)

These properties effect the laminate behavior for the quasi-isotropic layup because the 45° plies experience shear longitudinally along the fiber. First, a strong interface in shear was assumed which translates to no slip longitudinally between the fiber and matrix, and then a weak interface in shear was assumed which allowed unrestrained slip along the interface, and lastly, the interfacial failure model of the previous chapter was employed with the tangential interfacial constants of $\sigma_{tf} =$ 100 MPa and $u_{tf}/a = 0.01$. The results of Figure 104 demonstrate that the interfacial failure model does an excellent job of capturing the effects of the experimental response.
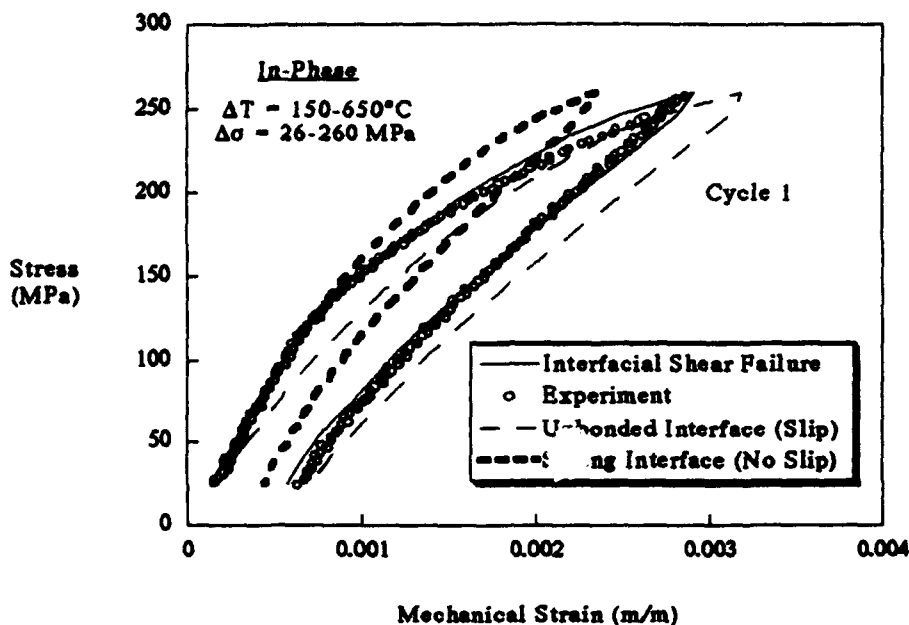
Figure 104. [0/±45/90]ₛ SCS6/Ti-β21S Stress-Strain Response to In-Phase TMF — Comparison to Experiment (67)

Additional results are plotted in Figure 105 for the accumulated strain history of the in-phase TMF on the quasi-isotropic layup. The micromechanics were performed with the interfacial failure parameters given in the previous paragraph, and the first few cycles agree quite well with the experimental data. After this, the experiment displays a greater accumulation of strain with increasing cycles which could be attributed to damage.

Also, the results from an out-of-phase TMF load for the quasi-isotropic laminate were compared to experiment. Figure 106 presents the first cycle stress-strain response of the composite where the interfacial fail-
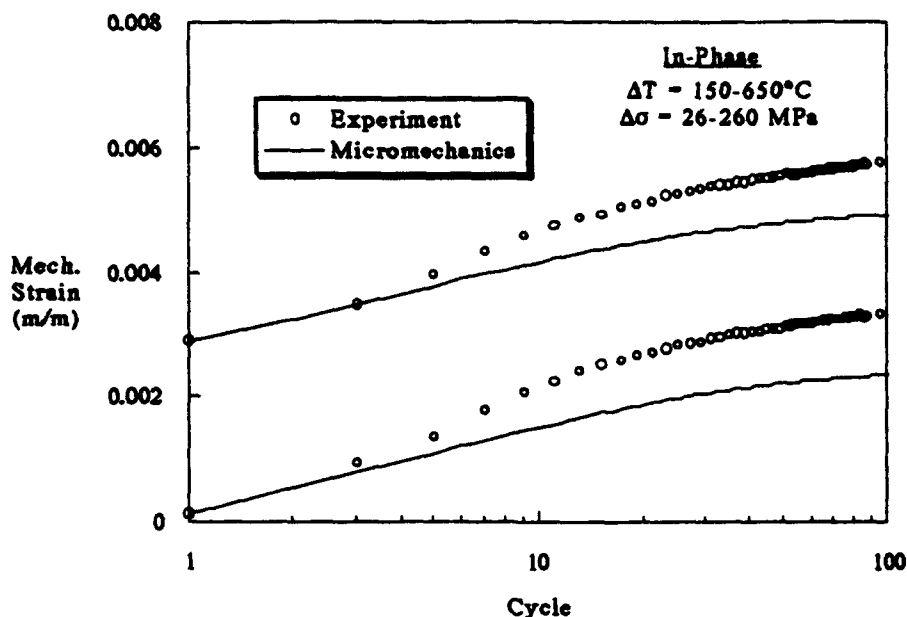
Figure 105. [0/±45/90]ₛ SCS6/Ti-β21S Max-Min Strain History for an In-Phase TMF — Comparison to Experiment (67)

ure parameters from the in-phase calculations are once again used. The out-of-phase results display a material hysteresis in the first cycle response where the strain begins and ends at approximately the same point even though the unloading curve does not match the response during increasing load. The micromechanics solution indicated that this hysteresis was due to interfacial failure because very little viscoplasticity was found to occur, yet some interfacial failure did occur in the 45° plies. Therefore, the energy dissipation displayed in the first cycle in the form of material hysteresis was due to interfacial shear failure. Further insight may be gained by examining Figure 107 which indicates
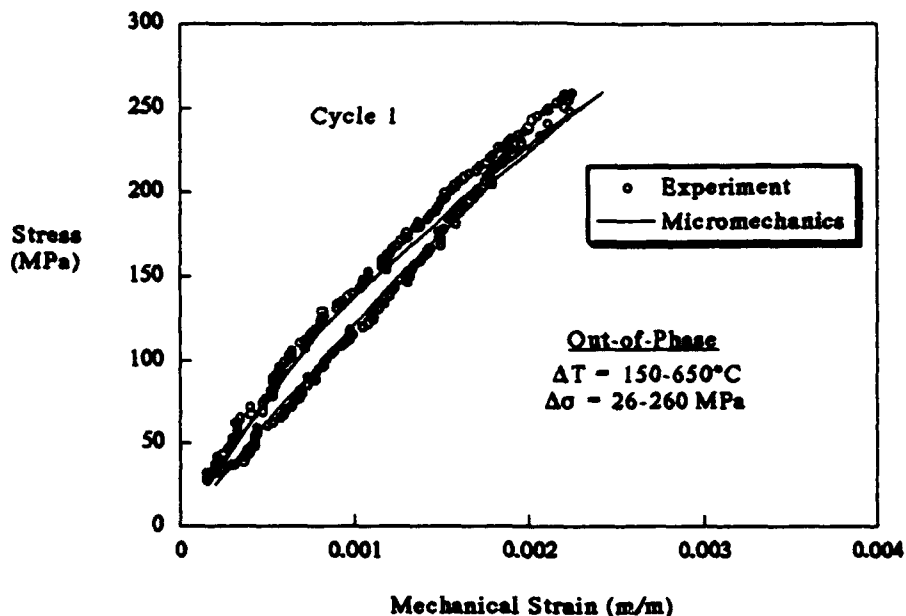
Figure 106. [0/±45/90]$_s$ SCS6/Ti-β21S Stress-Strain Response to an Out-of-Phase TMF — Comparison to Experiment (67)

very little viscoplastic strain accumulation through 100 cycles.

It is worthy of note that additional errors between experiment and a micromechanics solution may result from other than composite damage in the form of fiber and matrix cracks. For instance, it is very difficult to achieve an accurate TMF cycle empirically because a sophisticated control system is required to regulate both the temperature and mechanical load simultaneously. One of the difficulties that arise from this is a phase shift between the temperature and mechanical load. Such a phase shift is normally most prevalent in the first few cycles. However, in the micromechanics solution, it is very easy to achieve the exact
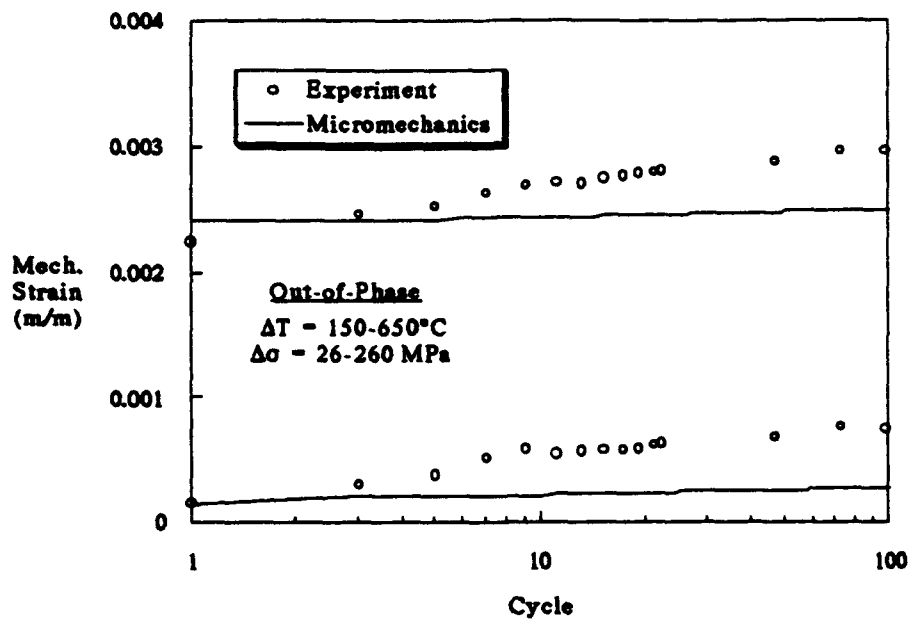
Figure 107. [0/±45/90]ₛ SCS6/Ti-β21S Max-Min Strain History for an
Out-of-Phase TMF — Comparison to Experiment (67)

cycle desired, so the computational results may depict a load sequence
that was in reality never achieved in the actual composite. In an effort
to evaluate the potential size of this error, two micromechanics solutions
are displayed in Figure 108 for the crossply laminate already discussed
in this section. One solution is for a perfectly in-phase TMF with a
cycle period of 180 seconds while the other contains a 10 second phase
shift between the temperature and mechanical load where the stress level
led the temperature such that the stress achieved its maximum of 400
MPa when the temperature had only reached 600°C. The results indicate
little effect on the response except at maximum strain where the error in

205
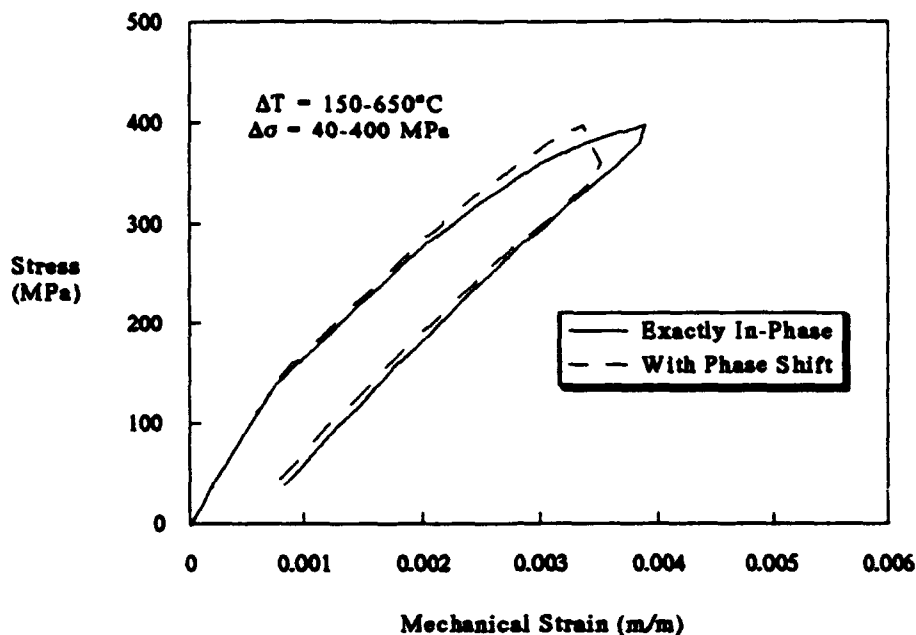
Figure 108. [0/90]ₛ SCS6/Ti-β21S Effect of Phase Shift on Stress-Strain Response

strain is approximately 8%. Therefore, errors such as these must be considered when comparing the micromechanics to experimental data.

Determining the fatigue life or cycles to failure under a given set of loading conditions is of prime importance for composite applications, but a tremendous number of experiments would be required to characterize the material for all types of load conditions. Therefore, attempts have been made to consolidate the results so that only a few parameters need be obtained to predict the fatigue life (77). A model proposed by Russ et. al. assumes that the failure of the composite is controlled by a fiber dominated mode and a matrix dominated mode which may be com-

bined through the following relation (77):

$$\frac{1}{N_f} + \frac{1}{N_m} = \frac{1}{N} \qquad (186)$$

where N_f and N_m are the cycles to failure due solely to either the fiber or matrix, and N is the combined cycles to failure. It is further assumed that the matrix failure mode is a function of the matrix stress range for the cycle and the fiber failure mode is a function of the maximum fiber stress (77, 78). This Linear Life Fraction Model (LLFM) has been further modified by Hart and Mall who assumed that N_f and N_m are controlled by the following power law relations:

$$N_m = B\left[\left(\Delta\sigma_m\right)^{-m} - 1 \right] + A \qquad (187)$$

$$N_f = K\left[\left(\sigma_{max}/\sigma_*\right)^{-m} - 1 \right] + A \qquad (188)$$

where A, B, K, and m are constants which must be determined experimentally. σ_* is the maximum fiber stress at tension failure under static load at the maximum temperature of the cycle, σ_{max} is the maximum axial stress in the 0° fibers for a given maximum applied stress level, and $\Delta\sigma_m$ is the axial stress range in the matrix.

The fatigue life of quasi-isotropic SCS6/Ti-15-3 laminates under isothermal, in-phase, and out-of-phase TMF cyclic loading has been ex-

perimentally characterized by Hart and Mall (78). They also employed Eqs (186) through (188) in conjunction with a linear micromechanics analysis using METCAN to predict the fatigue life. However, a linear analysis will not account for stress relaxation and redistribution within the constituents due to plasticity. Therefore, the present study will employ the nonlinear micromechanics analysis which has been heretofore developed and presented in this study to determine the microstresses required for Eqs (187) and (188) and compare the fatigue life results to the experiment (78). The microstresses were examined for the tenth and hundredth cycles of the 420 MPa in-phase TMF load, and it was found that 80% of the viscoplastic stress relaxation took place within the first ten cycles. Therefore, it was assumed that the microstresses employed for the LLFM fatigue model could be taken from the tenth cycle with a high degree of confidence that little further stress relaxation would occur. Also, Table 11 presents the constants A, B, K, and m that were found to best correlate the LLFM fatigue model with the experiment.

Figure 109 displays the LLFM fatigue life predictions using the microstresses from the nonlinear laminate analysis developed in this study as compared to the experimental cycles to failure. The loading consisted of 48 sec cycles at 427°C for the isothermal case and 149-427°C for the in-phase and out-of-phase TMF cases. In addition, a maximum to minimum applied stress ratio of 0.1 was used for all cases, and the stress-free processing temperature was assumed to be 900°C. The results indicate excellent agreement with the experimental data for the loading conditions plotted in the figure.

Table 11. Constants Employed for the LLFM Predictions of Quasi-Isotropic SCS6/Ti-15-3

	A	K	B	m
Isothermal				
N_f	400.	1.15e-6	---	19.7
N_m	2.55e5	---	1.5e6	0.03
In-Phase				
N_f	400.	1.15e-6	---	17.0
N_m	2.55e5	---	1.5e6	0.03
Out-of-Phase				
N_f	1500.	1.15e-6	---	17.0
N_m	2.55e5	---	1.5e6	0.03
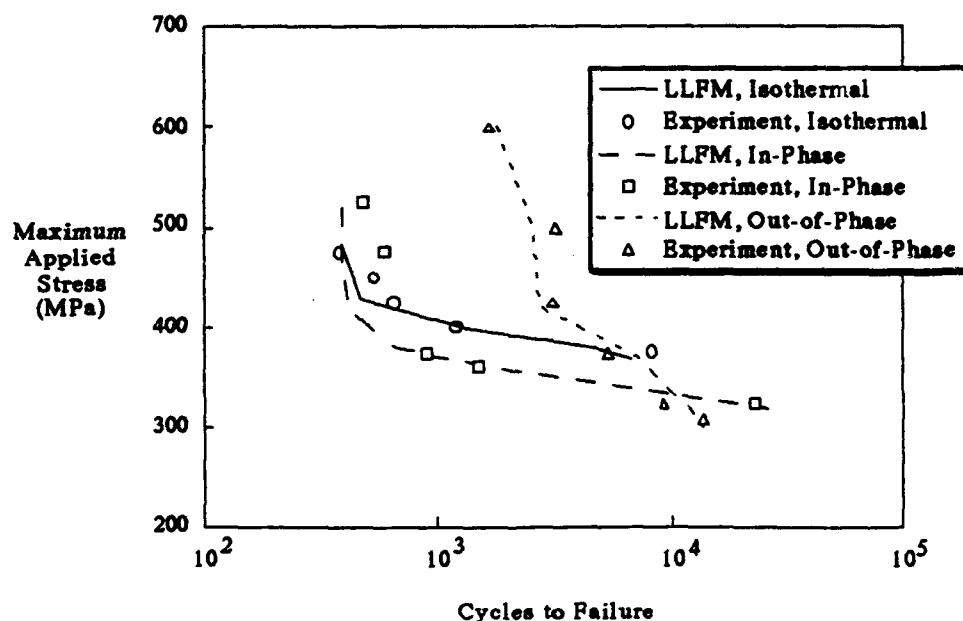
Figure 109. $[0/\pm45/90]_s$ SCS6/Ti-15-3 Fatigue Life as Predicted by LLFM and Experiment (78)

Moreover, the nonlinear micromechanics to laminate analysis presented in this chapter has displayed excellent agreement with the available experimental data for various loading conditions. The application of the model to both monotonic and cyclic thermomechanical loads as well as its ability to calculate strain accumulation and constituent stress relaxation due to viscoplastic effects and interfacial failure demonstrates its versatility. In addition, the accurate determination of ply stresses and constituent microstresses enables the researcher to pinpoint potential failure mechanisms and perform fatigue life predictions of the composite.

VIII. Summary and Conclusions

Composite materials designed for high temperature applications such as metal-matrix composites (MMCs) display various types of nonlinearities. Temperature dependent properties, plasticity and damage all play a role in the processing and loading regimes which these composites are likely to experience. An extensive three-dimensional nonlinear micromechanics model that accounts for all the various types of nonlinearities and provides the tool to investigate how the composite's behavior is affected by them is not available. Hence, the research and development of such a model has been undertaken and presented in the preceding document.

To develop this model, a proper foundation of three-dimensional stress-strain, equilibrium and continuity relationships for an appropriate representative volume element (RVE) was first established. This foundation was chosen with sufficient complexity to provide for accurate calculations of the constituent interaction and microstresses while maintaining enough simplicity to allow for the inclusion of numerous nonlinearities and the extension of the model into a general laminate analysis. To accomplish this, the RVE is partitioned into separate regions, each of constant stress, which for the majority of the calculations consisted of a single fiber region and three matrix regions. Then, the equilibrium of tractions and continuity of displacements between these regions were formulated such that all shear stresses decouple from the normal stresses within the RVE. This provides a computationally efficient means of

determining the three-dimensional constituent microstresses in and around the fiber so that various nonlinearities may be easily added. Figure 110 lays out a tree structure of the micromechanics model with all the types of nonlinearities that are presently included in this formulation. A brief summary of the model and some of the conclusions gained by it are presented in this chapter, and more detailed discussions of par-
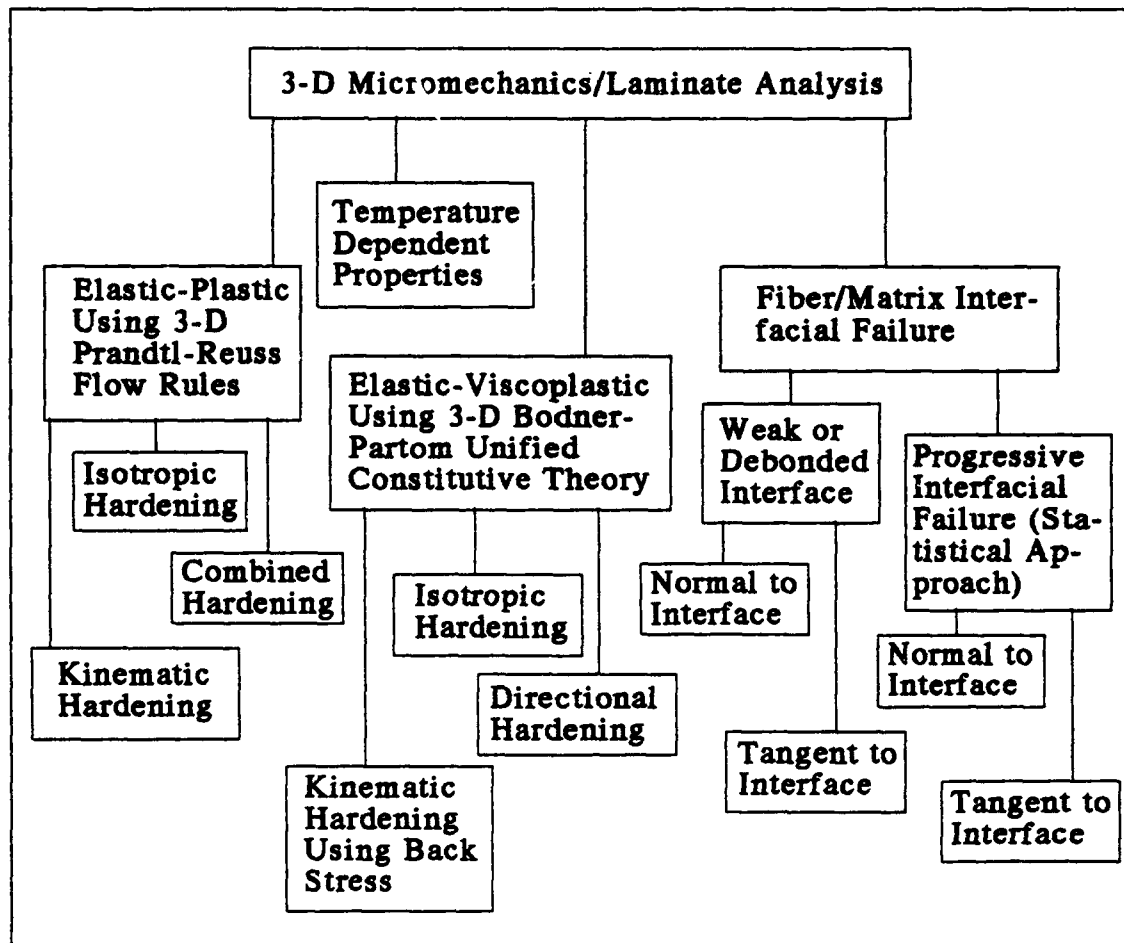
Figure 110. Tree Structure of Nonlinearities in the Micromechanics/Laminate Analysis

ticular topics which were presented in the preceding chapters are referred to.

The elastic-plastic analysis employed the Prandtl-Reuss flow rule along with a Von Mises yield criterion (section 4.1), and the elastic-viscoplastic analysis employed the unified constitutive theory of Bodner and Partom (section 5.1). Several versions of these theories which exploit various types of hardening effects were included for a more accurate representation of the cyclic material behavior. Also, damage at the fiber/matrix interface was accomplished by assuming either a completely weak/debonded interface or by using the interfacial failure/damage progression scheme based on a statistical representation of interfacial failure that was developed as a part of this research (sections 6.1 and 6.2). Numerical algorithms for each of these nonlinear phenomena were developed and were found to possess excellent convergence characteristics.

The analysis was extended into the laminate composite realm by employing the classical laminated plate theory assumptions. The nonlinear micromechanics were then formulated through linear transformations of each ply's stress and strain by its associated ply angle to produce a set of matrix equations equal to the number of plies. These could then be assembled into an expanded matrix equation and related to the applied composite load by invoking equilibrium between the ply stresses and the applied load (section 7.1).

The analysis was verified at each step of the development by comparing it with either other micromechanics models, finite element analysis, or experiments. The most extensive comparisons were made with

213

experimental data because much of the capabilities included in the present model are unavailable with the other analytical methods. Also, in addition to monotonic loading, a majority of the results included cyclic load-time-temperature profiles to examine the effects of plasticity and interfacial damage on strain accumulation and constituent stress relaxation in titanium based metal matrix composites when subjected to thermomechanical fatigue (TMF).

Unidirectional linear-elastic comparisons with preexisting micromechanics models, finite element analysis, and experiment as presented in chapter 4 indicate that the present formulation does an excellent job of predicting a composite's overall properties. Also, comparison of the constituent microstresses as calculated by 3-D finite element solutions and the present formulation demonstrated the model's usefulness for examining the constituent interaction. The confidence gained in the model by such linear-elastic results were further substantiated with the elastic-plastic analysis. Experimental results of unidirectional boron/aluminum were employed to validate the elastic-plastic formulation for various off-axis loads. The experimental longitudinal and transverse response of the MMC were closely matched by the present micromechanics model, and the capability to include either isotropic hardening, kinematic hardening, or a combination of the two was demonstrated (section 4.3).

Additional comparisons using the viscoplastic formulation were accomplished by employing three types of Bodner-Partom viscoplastic theories in the present micromechanics model (section 5.1). Results from Aboudi's method of cells micromechanics model were employed to verify the isotropic hardening calculations while finite element solutions

214

were used to verify both the back stress and the directional hardening forms of the Bodner-Partom theory (section 5.3.1). Experimental TMF results from unidirectional SCS6/Ti-β21S were compared with the micromechanics model to test the strain accumulation features of the present formulation under a TMF load (section 5.3.2). The microme- chanics solution agreed very well with its counterpart from experiment)r the first few cycles, but as might be expected, upon further cyclic loading, the experiment displays a greater strain accumulation than the micromechanics since the actual composite experiences damage in the form of fiber and matrix cracks. This provides a means of separating out and measuring the effects of viscoplasticity and damage which is im- possible using an experiment alone. In addition, the ability to calculate the constituent microstresses after stress relaxation due to viscoplastici- ty through the first few cycles was demonstrated to identify the sources of fiber and matrix cracking.

The effects of interfacial debonding were first modeled with an equivalent compliance at the interface which is zero in compression and a finite positive value in tension (infinite for perfectly weak). This in- terfacial model allowed for the analysis of different effects such as the thermal residual stresses on interfacial debonding (section 5.3). Com- parisons of this interfacial model with experimental transverse stress- strain curves indicated that the actual composite possesses a finite inter- facial failure strength in addition to the effects of residual thermal stresses. Therefore, an interfacial failure model that applies a progres- sive failure scheme for the interface was developed (section 6.1). This interfacial failure model is based on a statistical representation of the

interfacial stresses in a composite where a Gaussian distribution is assumed, and the fraction of interfaces that have failed are controlled by the portion of the random distribution that lies above a given failure strength. Results from this formulation demonstrated excellent agreement with the available experimental data which indicates that it provides a more reasonable method of modeling the fiber/matrix interface (section 6.3).

A general purpose micromechanics formulation is not complete without the ability to analyze various laminate composite layups. Therefore, the present formulation was extended to the laminate analysis and extensive comparisons were made with other numerical methods and experiments. Results from Aboudi's method of cells and some limited finite element data of a crossply laminate were also used to compare with the present model which showed an excellent agreement (section 7.2.1). This as well as the extensive experimental comparisons assured the validity of the present micromechanics to laminate analysis formulation (section 7.2.3). Additionally, a parametric study on the effects of various conditions such as loading rate, ply layup, interfacial strength, and type of loading was presented to demonstrate the effectiveness of the model as a supplement and in some instances a substitute for experimental work where it may be cost prohibitive to perform an extensive number of experiments at all the various conditions (section 7.2.2). Also, in order to accurately predict the life of a composite, the constituent microstresses must be reliably determined, but the effects of nonlinearities such as viscoplasticity and interfacial failure which can occur very early in the cyclic loading sequence may contribute to a redistribution of the

constituent stresses. Hence, a micromechanics formulation such as the present one which accounts for such nonlinearities through a three-dimensional stress formulation would provide such information as the constituent microstresses with accuracy. An example of the use of the present model in this regard was given in the last chapter.

Many aerospace applications of composite materials involve extremely high temperatures (i.e. engine components, NASP, etc.), and the titanium-based MMCs targeted for such applications exhibit the various nonlinearities previously discussed. Therefore, the present micromechanics formulation provides an excellent tool for analyzing these types of composites as it has been confirmed throughout this study. On the other hand, it is also capable of analyzing any type of continuously fiber reinforced composite, and it possesses a formulation that has been shown to allow for the inclusion of many material nonlinearities.

A reliable micromechanics analysis can provide both the design and laboratory engineer with an invaluable tool for selecting classes of composites by predicting their response when subjected to different temperatures and loading regimes, ranging from monotonic loading to thermal-mechanical cycling. Also, a better understanding of the observed experimental behavior of a these composites are often required. The present formulation was developed to provide such a tool, and its accuracy and potential for these applications was established in this study.

In addition, consideration should be given in future investigations for further application of the present formulation to model additional nonlinearities. For instance, damage of unidirectional composites in the form of fiber and matrix cracks is a very prevalent phenomena, and ex-

panding the model to include this would be of great benefit. Also, the effects of such types of damage on various laminated composite layups and how ply orientation may effect the acceleration this damage would be additionally worthwhile.

Appendix: Eight-Region Model Equations

The determination of the region dimensions and the equilibrium and continuity relations employed for the unidirectional micromechanics eight-region model are presented here. Results from the eight-region model are presented in chapter 4.

Figure 111 displays the region configuration and labeling which will be used throughout the Appendix, and when it is compared with the four-region model, the number of matrix regions for the eight-region model have been increased from three to seven while the number of in-
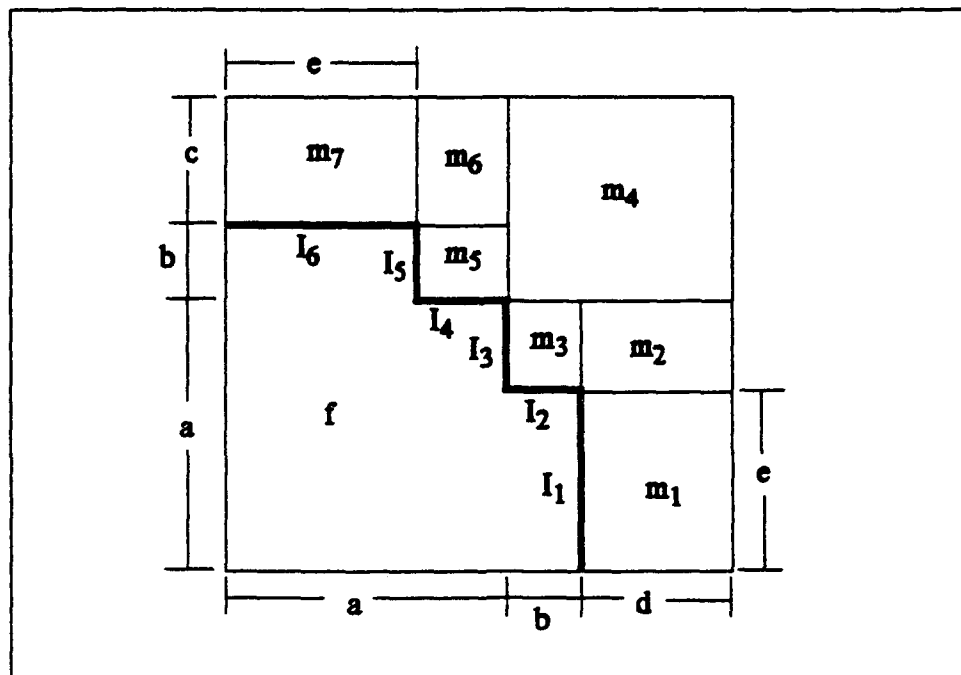
Figure 111. Region Configuration and Labeling for the Eight-Region
Micromechanics Model

terfaces have been increased from two to six. The dimensions of the
fiber region are chosen such that the overall shape will most closely
match that of a quarter-circle. Figure 112 compares the fiber region of
the micromechanics to a circular fiber, and it is recognized that the area
traced out by each must be the same. Hence,

$$2be + a^2 = \frac{\pi}{4}r^2 \qquad (189)$$

The most optimum dimensions for the prismatic fiber region are
those that will minimize the shaded area depicted in Figure 112. There-
fore, if a general representation of this shaded area is obtained then the
most optimum dimensions may be obtained through elementary calculus.
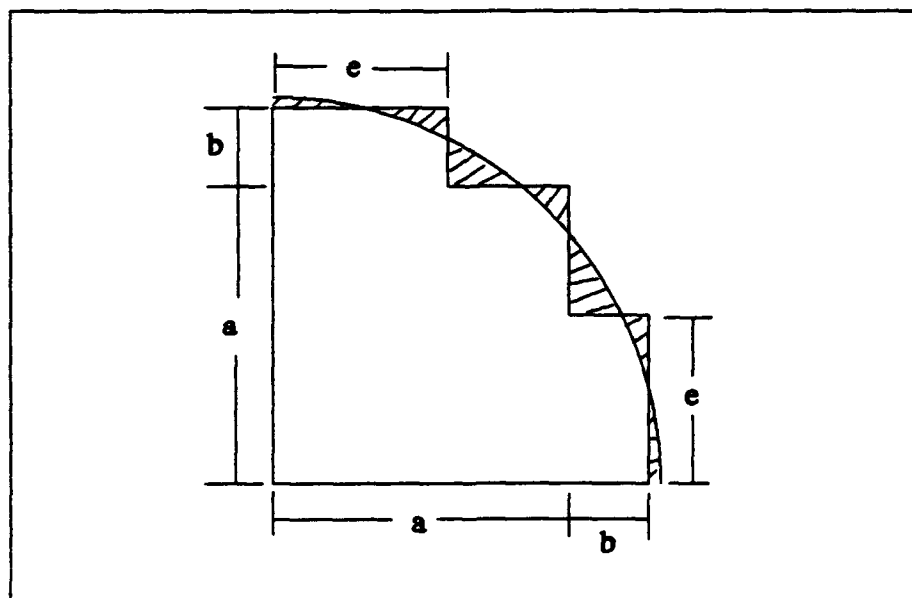
Figure 112. Fiber Region Dimensions

220

The shaded area may be represented by

$$A_s = 2\left[rd - \int_0^e \sqrt{r^2 - x^2}\, dx + \int_e^{r\sqrt{1 - a^2/r^2}} \sqrt{r^2 - x^2}\, dx \right.$$

$$\left. - 2ar\sqrt{1 - a^2/r^2} + ae + \frac{a^2}{2} + \frac{r^2}{2} - \int_{r\sqrt{1 - a^2/r^2}}^{r/\sqrt{2}} \sqrt{r^2 - x^2}\, dx \right] \qquad (190)$$

where A_s is the shaded area in Figure 112. Therefore, the two additional equations which must be satisfied to optimize the fiber region dimensions are

$$\frac{\partial A_s}{\partial a} = 0 \qquad (191)$$

$$\frac{\partial A_s}{\partial e} = 0 \qquad (192)$$

The solution to Eqs (184) through (187) is

$$a = 0.7862\, r \qquad (193)$$

$$b = 0.1860\, r \qquad (194)$$

$$e = 0.4499\, r \qquad (195)$$

and the dimension r is simply the fiber radius. The other dimensions in

221

Figure 111 are determined from the fiber volume fraction of the composite and the fiber spacing aspect ratio.

The analysis cell dimensions are now used in the following pages where the equilibrium and continuity equations that were employed for the eight-region micromechanics model are listed. The method of solution of these equations is the same as for the four-region model outlined in chapter 3.

Equilibrium:

$$\left(a^2 + 2be\right)\sigma_{11_f} + d\,e\,\sigma_{11_{m_1}} + d\,(a\text{-}e)\,\sigma_{11_{m_2}} + b\,(a\text{-}e)\,\sigma_{11_{m_3}} + (b\text{+}c)(b\text{+}d)\,\sigma_{11_{m_4}} \tag{196}$$
$$+ b\,(a\text{-}e)\,\sigma_{11_{m_5}} + c\,(a\text{-}e)\,\sigma_{11_{m_6}} + c\,e\,\sigma_{11_{m_7}} = (a\text{+}b\text{+}c)(a\text{+}b\text{+}d)\,\overline{\sigma}_{11}$$

$$e\,\sigma_{22_{m_1}} + (a\text{-}e)\,\sigma_{22_{m_3}} + b\,\sigma_{22_{m_5}} = (a\text{+}b)\,\sigma_{22_f} \tag{197}$$

$$\sigma_{22_{m_1}} = \sigma_{m_1} \tag{198}$$

$$\sigma_{22_{m_3}} = \sigma_{22_{m_2}} \tag{199}$$

$$\sigma_{22_{m_3}} = \sigma_{m_3} \tag{200}$$

$$b\,\sigma_{22_{m_5}} + c\,\sigma_{22_{m_6}} = (b\text{+}c)\,\sigma_{22_{m_4}} \tag{201}$$

$$\sigma_{22_{m_5}} = \sigma_{m_5} \tag{202}$$

$$\sigma_{22_{m_6}} = \sigma_{22_{m_7}} \tag{203}$$

222

$$(b+c)\,\sigma_{22_{m_4}} + (a-e)\,\sigma_{22_{m_2}} + e\,\sigma_{22_{m_1}} = (a+b+c)\,\bar{\sigma}_{22} \tag{204}$$

$$e\,\sigma_{33_{m_7}} + (a-e)\,\sigma_{33_{m_5}} + b\,\sigma_{33_{m_3}} = (a+b)\,\sigma_{33_f} \tag{205}$$

$$\sigma_{33_{m_7}} = \sigma_{m_6} \tag{206}$$

$$\sigma_{33_{m_6}} = \sigma_{33_{m_5}} \tag{207}$$

$$\sigma_{33_{m_5}} = \sigma_{m_4} \tag{208}$$

$$b\,\sigma_{33_{m_3}} + d\,\sigma_{33_{m_2}} = (b+d)\,\sigma_{33_{m_4}} \tag{209}$$

$$\sigma_{33_{m_3}} = \sigma_{m_2} \tag{210}$$

$$\sigma_{33_{m_2}} = \sigma_{33_{m_1}} \tag{211}$$

$$(b+d)\,\sigma_{33_{m_4}} + (a-e)\,\sigma_{33_{m_6}} + e\,\sigma_{33_{m_7}} = (a+b+d)\,\bar{\sigma}_{33} \tag{212}$$

$$e\,\tau_{12_{m_1}} + (a-e)\,\tau_{12_{m_2}} + (b+c)\,\tau_{12_{m_4}} = (a+b+c)\,\bar{\tau}_{12} \tag{213}$$

$$(a+b)\,\tau_{12_f} + c\,\tau_{12_{m_7}} = (a+b+c)\,\bar{\tau}_{12} \tag{214}$$

$$b\,\tau_{t_{I_5}} + (a-e)\,\tau_{t_{I_3}} + e\,\tau_{t_{I_1}} = (a+b)\,\tau_{12_f} \tag{215}$$

$$b\,\tau_{t_{I_5}} + c\,\tau_{12_{m_7}} = b\,\tau_{12_{m_5}} + c\,\tau_{12_{m_6}} \tag{216}$$

$$(a-e)\,\tau_{t_{I_3}} + b\,\tau_{12_{m_5}} + c\,\tau_{12_{m_6}} = (a-e)\,\tau_{12_{m_3}} + (b+c)\,\tau_{12_{m_4}} \tag{217}$$

$$e \, \tau_{13_{m_7}} + (a\text{-}e) \, \tau_{13_{m_6}} + (b\text{+}d) \, \tau_{13_{m_4}} = (a\text{+}b\text{+}d) \, \bar{\tau}_{13} \qquad (218)$$

$$(a\text{+}b) \, \tau_{13_f} + d \, \tau_{13_{m_1}} = (a\text{+}b\text{+}d) \, \bar{\tau}_{13} \qquad (219)$$

$$b \, \tau_{t_{l_2}} + (a\text{-}e) \, \tau_{t_{l_4}} + e \, \tau_{t_{l_6}} = (a\text{+}b) \, \tau_{13_f} \qquad (220)$$

$$b \, \tau_{t_{l_2}} + d \, \tau_{13_{m_1}} = b \, \tau_{13_{m_3}} + d \, \tau_{13_{m_2}} \qquad (221)$$

$$(a\text{-}e) \, \tau_{t_{l_4}} + b \, \tau_{13_{m_3}} + d \, \tau_{13_{m_2}} = (a\text{-}e) \, \tau_{13_{m_5}} + (b\text{+}d) \, \tau_{13_{m_4}} \qquad (222)$$

$$\tau_{23_f} = \tau_{23_{m_1}} = \tau_{23_{m_2}} = \tau_{23_{m_3}} = \tau_{23_{m_4}} = \tau_{23_{m_5}} = \tau_{23_{m_6}} = \tau_{23_{m_7}} = \bar{\tau}_{23} \qquad (223)$$

Continuity:

$$\varepsilon_{11_f} = \varepsilon_{11_{m_1}} = \varepsilon_{11_{m_2}} = \varepsilon_{11_{m_3}} = \varepsilon_{11_{m_4}} = \varepsilon_{11_{m_5}} = \varepsilon_{11_{m_6}} = \varepsilon_{11_{m_7}} = \bar{\varepsilon}_{11} \qquad (224)$$

$$(a\text{+}b) \, \varepsilon_{22_f} + \delta_{m_{l_1}} + d \, \varepsilon_{22_{m_1}} = (a\text{+}b\text{+}d) \, \bar{\varepsilon}_{22} \qquad (225)$$

$$b \, \varepsilon_{22_f} + \delta_{m_{l_1}} + d \, \varepsilon_{22_{m_1}} = \delta_{m_{l_3}} + b \, \varepsilon_{22_{m_3}} + d \, \varepsilon_{22_{m_2}} \qquad (226)$$

$$(a\text{-}e) \, \varepsilon_{22_f} + \delta_{m_{l_3}} + b \, \varepsilon_{22_{m_3}} + d \, \varepsilon_{22_{m_2}} = \delta_{m_{l_5}} + (a\text{-}e) \, \varepsilon_{22_{m_5}} + (b\text{+}d) \, \varepsilon_{22_{m_4}} \qquad (227)$$

$$e \, \varepsilon_{22_f} + \delta_{m_{l_5}} + (a\text{-}e) \, \varepsilon_{22_{m_5}} = e \, \varepsilon_{22_{m_7}} + (a\text{-}e) \, \varepsilon_{22_{m_6}} \qquad (228)$$

$$(a\text{+}b) \, \varepsilon_{33_f} + \delta_{m_{l_6}} + c \, \varepsilon_{33_{m_7}} = (a\text{+}b\text{+}c) \, \bar{\varepsilon}_{33} \qquad (229)$$

224

$$b\,\varepsilon_{33_f} + \delta_{n_{I_6}} + c\,\varepsilon_{33_{m_7}} = \delta_{n_{I_4}} + b\,\varepsilon_{33_{m_5}} + c\,\varepsilon_{33_{m_6}} \tag{230}$$

$$(a\text{-}e)\,\varepsilon_{33_f} + \delta_{n_{I_4}} + b\,\varepsilon_{33_{m_5}} + c\,\varepsilon_{33_{m_6}} = \delta_{n_{I_2}} + (a\text{-}e)\,\varepsilon_{33_{m_3}} + (b\text{+}c)\,\varepsilon_{33_{m_4}} \tag{231}$$

$$e\,\varepsilon_{33_f} + \delta_{n_{I_2}} + (a\text{-}e)\,\varepsilon_{33_{m_3}} = e\,\varepsilon_{33_{m_1}} + (a\text{-}e)\,\varepsilon_{33_{m_2}} \tag{232}$$

$$(b\text{+}d)\,\gamma_{12_{m_4}} + (a\text{-}e)\,\gamma_{12_{m_6}} + e\,\gamma_{12_{m_7}} = (a\text{+}b\text{+}d)\,\bar{\gamma}_{12} \tag{233}$$

$$\gamma_{12_{m_6}} = \gamma_{12_{m_5}} \tag{234}$$

$$e\,\gamma_{12_{m_7}} = e\,\gamma_{12_f} + \delta_{t_{I_5}} \tag{235}$$

$$e\,\gamma_{12_{m_7}} + (a\text{-}e)\,\gamma_{12_{m_6}} = a\,\gamma_{12_f} + \delta_{t_{I_3}} \tag{236}$$

$$\gamma_{12_{m_3}} = \gamma_{12_{m_4}} \tag{237}$$

$$\gamma_{12_{m_2}} = \gamma_{12_{m_4}} \tag{238}$$

$$\delta_{t_{I_3}} + b\,\gamma_{12_{m_3}} + d\,\gamma_{12_{m_2}} = b\,\gamma_{12_f} + \delta_{t_{I_1}} + d\,\gamma_{12_{m_1}} \tag{239}$$

$$(b\text{+}c)\,\gamma_{13_{m_4}} + (a\text{-}e)\,\gamma_{13_{m_2}} + e\,\gamma_{13_{m_1}} = (a\text{+}b\text{+}c)\,\bar{\gamma}_{13} \tag{240}$$

$$\gamma_{13_{m_2}} = \gamma_{13_{m_3}} \tag{241}$$

$$e\,\gamma_{13_{m_1}} = e\,\gamma_{13_f} + \delta_{t_{I_2}} \tag{242}$$

225

$$e\,\gamma_{13_{m_1}} + (a\text{-}e)\,\gamma_{13_{m_2}} = a\,\gamma_{13_f} + \delta_{t_{l_4}} \qquad (243)$$

$$\gamma_{13_{m_5}} = \gamma_{13_{m_4}} \qquad (244)$$

$$\gamma_{13_{m_6}} = \gamma_{13_{m_4}} \qquad (245)$$

$$\delta_{t_{l_4}} + b\,\gamma_{13_{m_5}} + c\,\gamma_{13_{m_6}} = b\,\gamma_{13_f} + \delta_{t_{l_6}} + c\,\gamma_{13_{m_7}} \qquad (246)$$

$$\left(2be+a^2\right)\gamma_{23_f} + de\,\gamma_{23_{m_1}} + d(a\text{-}e)\,\gamma_{23_{m_2}} + b(a\text{-}e)\,\gamma_{23_{m_3}} + (b+d)(b+c)\,\gamma_{23_{m_4}}$$
$$+ b(a\text{-}e)\,\gamma_{23_{m_5}} + c\,(a\text{-}e)\,\gamma_{23_{m_6}} + ce\,\gamma_{23_{m_7}} = (a+b+c)(a+b+d)\,\bar{\gamma}_{23} \qquad (247)$$

Bibliography

1. Bigelow, C. A., Johnson, W. S., and Naik, R. A., "A Comparison of Various Micromechanics Models for Metal Matrix Composites," Presented at the Third Joint ASCE/ASME Mechanics Conference, La Jolla, CA, July 1989.

2. Chamis, C. C. and Sendeckyj, G. P., "Critique on Theories Predicting Thermelastic Properties of Fibrous Composite," *Journal of Composite Materials*, July 1968, pp. 332-358.

3. Jones, Robert M., *Mechanics of Composite Materials*, Hemisphere Publishing Corporation, New York, NY, Washington D.C., and Philedelphia, PA, 1975.

4. Hill, R., "Theory of Mechanical Properties of Fibre-Strengthened Materials III: Self-Consistent Model," *Journal on the Mechanics and Physics of Solids*, Vol. 13, No. 4, 1965, pp. 189-198.

5. Gramoll, K. C., Freed, A. D., and Walker, K. P., "An Overview of Self-Consistent Methods for Fiber Reinforced Composites," NASA TM 103713, January 1991.

6. Hashin, Zvi, "The Elastic Moduli of Heterogeneous Materials," *Journal of Applied Mechanics*, March 1962, pp. 143-150.

7. Lee, Y. S., Gungor, M. N., and Liaw, P. K., "Modeling of Transverse Mechanical Behavior of Continuous Fiber Reinforced Metal-Matrix Composites," *Journal of Composite Materials*, Vol. 25, May 1991, pp. 536-555.

8. Muskhelishvili, N. I., *Some Basic Problems of the Mathematical Theory of Elasticity, 4th ed.*, P. Noordhoff, Ltd., Goningen, The Netherlands, pp. 218.

9. Pagano, N. J. and Tandon, G. P., "Modeling of Imperfect Bonding in Fiber Reinforced Brittle Matrix Composites," *Mechanics of Materials*, Vol. 9, No. 1, May 1990, pp. 49-64.

10. Tandon, G. P. and Pagano, N. J., "On the Effective Transverse Shear Modulus of Debonding Composites," American Society for Composites, Proceedings of the 5th Technical Conference, East Lansing, MI, June 12-14, 1990, Technomic Publishing Co., pp. 319-325.

11. Tandon, G. P., and Pagano, N. J., "A Study of Fiber-Matrix Interfacial Modeling," Proceedings of the 4th Japan-U.S. Conference on Composite Materials, Washington D.C., June 27-29, 1988, Technomic Publishing Co., Lancaster, PA, pp. 191-200.

12. Pagano, N. J. and Tandon, G. P., "Elastic Response of Multi-directional Coated-Fiber Composites," *Composites Science and Technology*, Vol. 31, 1988, pp. 273-293.

13. Halpin, J. C., and Tsai, S. W., "Effect of Environmental Factors on Composite Materials," AFML-TR 67-423, June, 1969.

14. Adams, D. F., and Tsai, S. W., "The Influence of Random Filament Packing on the Transverse Stiffness of Unidirectional Composites, *Journal of Composite Materials*, Vol. 3, July 1969, pp. 368-380.

15. Foye, R. L., "An Evaluation of Various Engineering Estimates of the Transverse Properties of Unidirectional Composites," Proceedings of the Tenth National SAMPE Symposium — Advanced Fibrous Reinforced Composites, November 1966.

16. Adams, D. F., and Doner, D. R., "Longitudinal Shear Loading of a Unidirectional Composite," *Journal of Composite Materials*, Vol. 1, 1967, pp. 4-17.

17. Adams, D. F., and Doner, D. R., "Transverse Normal Loading of a Unidirectional Composite," *Journal of Composite Materials*, Vol. 1, 1967, pp. 152-164.

18. Adams, D. F., "Inelastic Analysis of a Unidirectional Composite Subjected to Transverse Normal Loading," *Journal of Composite Materials*, Vol. 4, 1970, pp. 310-328.

19. Adams, D. F., "Elastoplastic Crack Propagation in a Transversely Loaded Unidirectional Composite," *Journal of Composite Materials*, Vol. 8, January 1974, pp. 38-54.

20. Nimmer, R. P., Bankert, R. J., Russell, E. S., Smith, G. A., and Wright, P. K., "Micromechanical Modeling of Fiber/Matrix Interface Effects in Transversely Loaded SiC/Ti-6-4 Metal Matrix Composites," *Journal of Composites Technology & Research*, Vol. 13, No. 1, Spring 1991, pp. 3-13

21. Zhu, H., and Achenbach, J. D., "Effect of Fiber-Matrix Interphase Defects on Microlevel Stress States at Neighboring Fibers," *Journal of Composite Materials*, Vol. 25, March 1991, pp. 224-238.

22. Folias, E. S., "On the Prediction of Failure at a Fiber/Matrix Interface in a Composite Subjected to a Transverse Tensile Load," *Journal of Composite Materials*, Vol. 25, July 1991, pp. 869-886.

23. Caruso, J. J., and Chamis, C. C., "Interfacial Effects on the Behavior of Partially Bonded Metal Matrix Composite Properies," Presented at the 35th International SAMPE Symposium, April 2, 1990.

24. Clyne, T. W., and Watson, M. C., "Interfacial Mechanics in Fibre-Reinforced Metals," *Composites Science and Technology*, Vol. 42,

1991, pp. 25-55.

25. Evans, A. G., Zok, F. W., and Davis, J., "The Role of Interfaces in Fibre-Reinforced Brittle Matrix Composites," *Composites Science and Technology*, Vol. 42, 1991, pp. 3-24.

26. Johnson, W. S., Lubowinski, S. J., and Highsmith, A. S., "Mechanical Characterization of Unnotched SCS6/Ti-15-3 Metal Matrix Composites at Room Temperature," Presented at the ASTM Symposium — Thermal and Mechanical Behavior of Ceramic and Metal Matrix Composites, Atlanta, GA, November, 1988.

27. Nimmer, R. P., "Fiber-Matrix Interface Effects on the Presence of Thermally Induced Residual Stresses," *Journal of Composites Technolgy & Research*, Vol. 12, No. 2, Summer 1990, pp. 65-75.

28. Robertson, D. D., and Mall, S., "Fiber-Matrix Interphase Effects Upon Transverse Behavior in Metal Matrix Composite," *Journal of Composites Technolgy & Research*, Vol. 14, No. 1, Spring 1992, pp. 3-11.

29. Rogacki, J. R., and Tuttle, M. E., "A Combined Experimental Analytical Methodology for Characterizing the Thermoviscoplastic Deformation of a Metal Matrix Composite," Prepared for NASA-Langley Research Center under Grant No. NAG-1-97?, August, 1992.

30. Sun, C. T., and Chen, J. L., "A Simple Flow Rule for Characterizing Nonlinear Behavior of Fiber Composites," *Journal of Composite Materials*, Vol. 23, October 1989, pp. 1009-1020.

31. Sun, C. T., and Chen, J. S., "A Micromechanical Model for Plastic Behavior of Fibrous Composites," *Composites Science and Technology*, 1990, pp. 115-129.

32. Sherwood, J. A., and Boyle, M. J., "Investigation of the Thermomechanical Response of a Titanium-Aluminide/Silicon-Carbide Composite Using a Unified State Variable Model and the Finite Element Method," Presented at the Winter Annual Meeting of the American Society of Mechanical Engineers, Dallas, TX, Nov 25-30, 1990.

33. Bahei-El-Din, Y. A., "Plastic Analysis of Metal-Matrix Composite Laminates," Ph.D. Dissertation, Duke University, 1979.

34. Dvorak, G. J., and Bahei-El-Din, Y. A., "Plasticity Analysis of Fibrous Composites," *Journal of Applied Mechanics*, Vol. 49, 1982, pp. 327-335.

35. Bahei-El-Din, Y. A., "Plasticity Analysis of Fibrous Composite Laminates Under Thermomechanical Loads," *Thermal and Mechanical Behavior of Ceramic and Metal Matrix Composite*, ASTM STP 1080, Kennedy, J. M., Moeller, H. H., and Johnson, W. S., eds., American Society for Testing and Materials, Philadelphia, 1990, pp.

20-39.

36. Mirdamadi, M., Johnson, W. S., Bahei-El-Din, Y. A., and Castelli, M. G., "Analysis of Thermomechanical Fatigue of Unidirectional Titanium Metal Matrix Composites," NASA TM 104105, July 1991.

37. Hopkins, D. A., and Chamis, C. C., "A Unique Set of Micromechanics Equations for High Temperature Metal Matrix Composites," NASA TM 87154, 1987.

38. Chamis, C. C., and Hopkins, D. A., "Thermoviscoplastic Nonlinear Constitutive Relationships for Structural Analysis of High Temperature Metal Matrix Composites," NASA TM 87291, 1987.

39. Aboudi, J. A., "A Continuum Theory for Fiber-Reinforced Elastic-Viscoplastic Composites," *International Journal of Engineering Science*, Vol. 20, 1982, pp. 605-621.

40. Aboudi, Jacob, "Damage in Composites — Modeling of Imperfect Bonding," *Composites Science and Technology*, Vol. 28, 1987, pp. 103-128.

41 Aboudi, J. A., "Closed Form Constitutive Equations for Metal-Matrix Composites," *International Journal of Engineering Science*, Vol. 25, 1987, pp 1229-1240.

42. Aboudi, Jacob, "Micromechanical Analysis of Composites by the Method of Cells," *Applied Mechanics Review*, Vol. 42, No. 7, July 1989, pp. 193-221.

43. Paley, M., and Aboudi, J., "The Overall Instantaneous Properties of Metal-Matrix Composites," *Composites Science and Technology*, Vol. 41, 1991, pp. 411-429.

44. Bodner, S. R., "Review of a Unified Elastic-Viscoplastic Theory," *Unified Constitutive Equations for Plastic Deformation and Creep of Engineering Alloys*, Miller, A. K., ed., Elsvier Applied Science Publishers, England, 1987.

45. Robertson, D. D., and Mall, S., "Micromechanical Relations for Fiber-Reinforced Composites Using the Free Transverse Shear Approach," *Journal of Composites Technology & Research*, Vol. 15, No. 3, Fall 1993, pp. 181-192.

46. Robertson, David D., and Mall, Shankar, "A Three-Dimensional Micromechanical Model for Nonlinear Behavior of Fibrous Composites," presented at the Ninth International Conference of Composite Materials, ICCM9, Zargoza, Spain, July 12-16, 1993.

47. Robertson, D., and Mall, S., "Micromechanical Analysis for Thermoviscoplastic Behavior of Unidirectional Fibrous Composites," accepted for publication in *Composites Science and Technology*, 1993.

48. Robertson, David D., and Mall, Shankar, "A Micromechanical Approach for Predicting Time-Dependent Nonlinear Material Behavior of a Metal Matrix Composite," to be presented at the Symposium on Thermomechanical Behavior of Advanced Structural Materials, ASME Winter Annual Meeting, New Orleans, LA, November 28 - December 3, 1993.

49. Owen, D. R. J., and Hinton, E., *Finite Elements in Plasticity: Theory and Practice*, Pineridge Press Limited, Swansea, U.K., 1980, pp. 215-264.

50. Crane, D. A., and Adams, D. F., "Finite Element Micromechanical Analysis of a Unidirectional Composite Including Longitudinal Shear Loading," Final Report Under Contract No. DAAG46-79-C-0076, Prepared for Army Materials and Mechanics Research Center, AMMRC TR 81-7, February 1981.

51. Kenaga, D., Doyle, J. F., and Sun, C. T., "The Characterization of Boron/Aluminum Composite in the Nonlinear Range as an Orthotropic Elastic-Plastic Material," *Journal of Composite Materials*, Vol. 21, June 1987, pp. 516-531

52. Craddock, J. N., and Kocher, C. G., "Micromechanical Models for the Transverse Properties of High Temperature Metal Matrix Composites," *Composites Design, Manufacture, and Application*, Tsai & Springer, Stanford, CA, from the Proceedings of the 7th Interrational Conference on Composite Materials, ICCM/VII, July 15-19, 1991, pp 29-A-1 to 29-A-10.

53. Rogacki, J., and Tuttle, M., "Thermoviscoplastic Behavior of SCS6/Ti Metal Matrix Composites," Presented at the 1990 Society of Experimental Mechanics, SEM, Spring Conference, Albequerque, NM, June 6-8, 1990

54. Mueller, A. C., and Kolle, J. J., "General Approach to Finite Element Analysis of Composite Micromechanics," *Composites Design, Manufacture, and Application*, Tsai & Springer, Stanford, CA, from the Proceedings of the 7th International Conference on Composite Materials, ICCM/VII, July 15-19, 1991, pp 29-E-1 to 29-E-13.

55. Coker, D., Ashbaugh, N. E., and Nicholas, T., "Analysis of Thermomechanical Cyclic Behavior of Unidirectional Metal Matrix Composites," Proceedings of the Symposium on Thermomechanical Fatigue Behavior of Materials, San Diego, CA, October 16, 1991.

56. Santhosh, U., Ahmad, J., and Nagar, A., "Non-Linear Micromechanics Analysis Prediction of the Behavior of Titanium-Alloy Matrix Composites," *Fracture and Damage*, ASME, Vol 27, 1992.

57. Sherwood, J. A., and Boyle, M. J., "Investigation of the Thermomechanical Response of a Titanium Aluminide/Silicon Carbide Com-

posite Using a Unified State Variable Model in ADINA," *Computers & Structures*, Vol. 40, No. 2, 1991, pp. 257-269.

58. Bodner, S. R., and Partom, Y., "Constitutive Equations for Elastic Viscoplastic Strain Hardening Materials," ASME *Journal of Applied Mechanics*, Vol. 42, 1975, pp. 385-389.

59. Chan, K. S., and Lindholm, U. S., "Inelastic Deformation Under Nonisothermal Loading," *Journal of Engineering Materials and Technology*, Vol. 112, 1990, pp. 15-25.

60. Ramaswamy, V. G, Stouffer, D. C., and Laflen, J. H., "A Unified Constitutive Model for the Inelastic Uniaxial Response of Ren'e 80 at Temperatures Between 538 C and 982 C," ASME *Journal of Engineering Materials and Technology*, Vol. 112, 1990, pp. 280-286.

61. Stouffer, D. C., and Bodner, S. R., "A Constitutive Model for the Deformation Induced Anisotropic Plastic Flow of Metals," *International Journal of Engineering Science*, Vol. 17, 1979, pp. 757-764.

62. Kroupa, Joseph L., and Neu, Richard, W., "Implementation of a Nonisothermal Unified Inelastic-Strain Theory into ADINA 6.0 for a Titanium Alloy — User Guide," WL-TR-93-4005, 1993.

63. Neu, R. W., "Nonisothermal Material Parameters for the Bodner-Partom Model," to be presented at the Symposium on Parameter Estimation for Modern Constitutive Equations, ASME Winter Annual Meeting, New Orleans, LA, November 28 - December 3, 1993.

64. Castelli, M. G., Ellis, J. R., and Bartolotta, P. A., "Thermomechanical Testing Techniques for High Temperature Composties: TMF Behavior of SiC(SCS6)/Ti-15-3," NASA TM 103171, 1990.

65. Neu, R. W., and Nicholas, T., "Effect of Laminate Orientation on the Thermomechanical Fatigue Behavior of a Titanium Matrix Composite," submitted to the *Journal of Composites Technology & Research*, 1993.

66. Sherwood, J. A., and Quimby, H. M., "Damage Modeling in Fiber Reinforced Composites," accepted for publication in ASME *Fracture and Damage*, 1993.

67. Nicholas, T., Neu, R., Ashbaugh, N., and Russ, S., personal communication with members of the Material Directorate, Wright Laboratory, Wright-Patterson AFB, OH, January - June 1993.

68. Majumdar, B. S., and Newaz G. M., "Inelastic Deformation of Metal Matrix Composites: Plasticity and Damage Mechanisms," *Philosophical Magazine A*, Vol. 66, No. 2, 1992, pp. 187-212.

69. Majumdar, B. S., and Newaz, G. M., "Inelastic Deformation of Metal

Matrix Composites: Plasticity and Damage Mechanisms — Part II,"
NASA CR 189096 — Part II, December 1992.

70. Majumdar, B. S., Newaz, G. M., and Brust, F. W., "Constitutive Be-
havior of Metal Matrix Composites," *Constitutive Behavior of High-
Temperature Composites*, ASME MD-Vol. 40, Majumdar, B. S.,
Newaz, G. M., and Mall, S., eds., pp. 77-90.

71. Tuttle, M. E., and Rogacki, J., "Thermoviscoplastic Response of Ti-
15-3 Under Various Loading Conditions," NASA CR 187621, 1991.

72. Gayda, John, and Gabb, Timothy P., "Isothermal Fatigue Behavior of
a [90]$_8$ SiC/Ti-15-3 Compsote at 426°C," NASA TM 103686, Janu-
ary 1991

73. Kyono, Tetsuyuki, Hall, Ian W., and Taya, Minoru, "The Effect of
Isothermal Exposure on the Transverse Properties of a Continuous
Fibre Metal-Matrix Composite," *Journal of Material Science*, Vol.
21, 1986, pp. 4269-4280

74. Lerch, B. A., and Saltsman, J., "Tensile Deformation in SiC Rein-
forced Ti-15V-3Cr-3Al-3Sn," NASA TM 103620, 1991

75. Aboudi, J., Hidde, J. S., and Herakovich, C. T., "Thermo-mechanical
Response Predictions for Metal Matrix Composite Laminates,"
Mechanics of Composites at Elevated and Cryogenic Temperatures,
ASME, AMD-Vol. 118, 1991, pp. 1-8

76. Lerch, Bradley, A., and Melis, Matthew, E., "Experimental and Ana-
lytical Analysis of Stress-Strain Behavior in a [90/0]$_{2s}$ SiC/Ti-15-3
Laminate," NASA TM 104470, August 1991.

77. Russ, S. M., Nicholas, T., Bates, M., and Mall, S., "Thermo-mechan-
ical Fatigue of SCS6/Ti-24Al-11Nb Metal Matrix Composite," *Fail-
ure Mechanisms in High Temperature Composite Materials*, ASME,
AMD-Vol. 122, 1991, pp. 37-43.

78. Hart, K. A., and Mall, S., "Thermomechanical Fatigue Behavior of a
Quasi-Isotropic SCS6/Ti-15-3 Metal Matrix Composite," submitted
for publication, 1993.

Vita

Captain David D. Robertson was born on 28 May 1961 in Joplin, Missouri. He received his Bachelor of Science Degree in Mechanical Engineering from the University of Missouri - Columbia in May 1983, and that same month, received a commission in the USAF through the ROTC program. He was initially assigned to the Air Force Satellite Control Facility, Onizuka AFB, California, as engineer for satellite recovery systems. Later, in December 1986, he was assigned to NASA-Ames Research Center, Moffett Field, California, under the Air Force Office of Scientific Research's laboratory associate program. He was then accepted into the Air Force Institute of Technology's graduate engineering program in Aeronautical Engineering in May 1989 and received his Master of Science Degree in December 1990. Subsequently, he was selected to continue his education at the Institute's resident doctoral engineering program in January 1991. He and his wife, Diane, have three children, Emily (6 yr.), Daniel (4 yr.), and Drew (2 yr.).

Permanent Address: 501 West 3rd Street

Lamar, Missouri 64759

REPORT DOCUMENTATION PAGE

Public reporting burden for this collection of information is estimated to average 1 hour per response, including the time for reviewing instructions, searching existing data sources, gathering and maintaining the data needed, and completing and reviewing the collection of information. Send comments regarding this burden estimate or any other aspect of this collection of information, including suggestions for reducing this burden, to Washington Headquarters Services, Directorate for Information Operations and Reports, 1215 Jefferson Davis Highway, Suite 1204, Arlington, VA 22202-4302, and to the Office of Management and Budget, Paperwork Reduction Project (0704-0188), Washington, DC 20503.

1. AGENCY USE ONLY (Leave blank)	2. REPORT DATE November 1993	3. REPORT TYPE AND DATES COVERED Doctoral Dissertation

4. TITLE AND SUBTITLE A Nonlinear Three-Dimensional Micromechanics Model for Fiber-Reinforced Laminated Composites	5. FUNDING NUMBERS
6. AUTHOR(S) David D. Robertson, Capt, USAF	

7. PERFORMING ORGANIZATION NAME(S) AND ADDRESS(ES) Air Force Institute of Technology Wright-Patterson AFB OH 45433-6583	8. PERFORMING ORGANIZATION REPORT NUMBER AFIT/DS/AA/93-3

9. SPONSORING/MONITORING AGENCY NAME(S) AND ADDRESS(ES) AFOSR/NA, Dr. Walter Jones Bolling AFB, D.C. 20332-0001	10. SPONSORING/MONITORING AGENCY REPORT NUMBER

11. SUPPLEMENTARY NOTES

12a. DISTRIBUTION/AVAILABILITY STATEMENT Approved for public release; distribution unlimited	12b. DISTRIBUTION CODE

13. ABSTRACT (Maximum 200 words)

In this study, a three-dimensional micromechanics model is developed. The present capabilities of the model include both unidirectional and laminated composite layups with various types of nonlinear analysis such as a thermoelastic-plastic analysis employing the Prandtl-Reuss flow relations, a thermoviscoplastic analysis using Bodner-Partom unified constitutive theory, and an interfacial damage progression scheme based on a statistical interfacial failure criteria. Such nonlinearities are critical factors during thermomechanical fatigue (TMF) loading of high temperature composites.

Solutions were obtained and extensive comparisons performed with existing micromechanics models, finite element analysis, and experiment with excellent results. In addition, the analysis was developed to require minimal computer resources. For instance, the majority of problems may be accomplished on a personal computer in a matter of seconds.

14. SUBJECT TERMS Micromechanical Modeling, Thermomechanical Fatigue High Temperature Composites, Damage Modeling	15. NUMBER OF PAGES 255
	16. PRICE CODE

17. SECURITY CLASSIFICATION OF REPORT Unclassified	18. SECURITY CLASSIFICATION OF THIS PAGE Unclassified	19. SECURITY CLASSIFICATION OF ABSTRACT Unclassified	20. LIMITATION OF ABSTRACT UL